University of Alberta

Ultrafast Imaging of Terahertz Pulses

by

Zhenyou Wang

A thesis submitted to the Faculty of Graduate Studies and Research
in partial fulfilment of the requirements for the degree of

Doctor of Philosophy

Department of Physics

Abstract

The main purpose of this thesis is to develop terahertz (THz) generation, detection, and spectroscopy techniques via ultrafast imaging methods.

Sampling THz pulse waveforms with a noncollinear imaging technique was carried out. Full-field images of the THz electric field waveforms sampled in E-mode can be used to perform THz spectroscopy, but multi-shots are required. On the other hand, the square of the THz electric field waveforms is obtained in a single shot in E^2-mode, which enables single-shot THz spectroscopy of the transmitted THz power spectra.

In order to study the THz generation process by optical rectification in $LiNbO_3$ crystals, we developed a novel transverse imaging technique to image the THz Cherenkov wave in side-view mode and top-view mode. Based on the images of the THz Cherenkov wave generated by the point focused optical pump pulse, parameters including the Cherenkov angle and group and phase velocities of the optical pump pulse and THz pulse, respectively, are measured directly. A transition-like radiation generated at the crystal boundary is imaged for the first time. Imaging distortions due to the transverse imaging geometry are simulated and a correction chart is made.

We also imaged THz pulses generated with the titled-pulse-front excitation technique in real time. The real time visualization of THz pulse generation and

propagation in $LiNbO_3$ crystals enables us to optimize the THz pulse generation efficiency in a more direct way. Based on the transverse imaging technique, THz pulse reflection, transmission, and tunneling in various conditions are imaged, which may be useful in physics teaching demonstrations. Applications of the transverse imaging technique to image THz generation in periodically poled lithium niobate (PPLN), air plasmas generated by femtosecond laser pulses, and nonlinear optical Kerr effect signals induced by femtosecond laser pulses in CS_2, quartz, water, methanol, and THF are explored.

Finally, a new type of free-standing, frameless carbon nanotube array THz polarizer is fabricated and tested.

Acknowledgments

As this thesis marks the end of my five and a half year Ph. D. program, I would like to give my sincerest thanks to those people who helped me to go through it.

First and foremost, I'm extremely grateful to my Ph. D. supervisor, Professor Frank A. Hegmann for his tremendous help to mentor me to be an experimental physicist. His serious attitudes towards academic research show me what a scientist should be. His enthusiasm in my research progress inspires me to keep on exploring in the lab. I enjoy my various discussions with Frank because I can always get some new ideas or learn some new things from him. I also really appreciate his patience, understanding, and support when things do not go well.

I also would like to thank Dr. Fu Hai Su for his invaluable help during my unprecedented difficult period of the Ph. D. project. He acted as a kind of co-supervisor for not only teaching me various skills, but also giving me lots of important advice on my project. I memorize the two and a half years we spent together in the lab and treasure the friendship between us. I'm very happy to know that Fu Hai has got enough funding to build his terahertz lab in China and wish him a great future.

I want to thank Dr. Jianbo Gao, a former Ph. D. graduate student, who takes care of me like a brother in both my research and private life.

It has also been a great time to work with Dr. Lyuba Titova, Dr. Tyler Cocker, and Ayesheshim K. Ayesheshim. We joined the lab almost at the same time. We helped, encouraged each other for the past five years. I'm proud to work with you guys and will always miss the wonderful time we were together.

I want to thank other former and current group members including Dr. Amin Kabir, Glenda De los Reyes, Sijia Xu, and Vedran Jelic for their kind help. Especially, I would like to thank former summer students Eric Epp, Graham

Table of Contents

List of Tables

List of Figures

Chapter 2

the electric field is parallel to $[1\bar{1}0]$, the index ellipsoid is tilted by 45 °relative to [110] direction.

Figure 2.8: Illustration of the phase shift induced by the birefringence. The electric field components in the fast axis and the slow axis propagate at different speeds

Figure 2.9: The refractive index ellipsoid of $LiNbO_3$ crystals without an electric field (solid line) and with a THz electric field that is parallel to the *c*-axis (z axis) (dashed line).

Figure 2.10: Experimental setup for THz waveforms sampling in E^2 *-mode*.

Figure 2.11: Experimental setup for THz waveforms sampling in *E-mode*.

Figure 2.12: Schematic diagram of the Talbot imaging setup. The period of the phase structure object is *d*, the distance between the phase structure object and the object plane of the camera is *y*.

Figure 2.13: Schematic illustration of (a) collinear, (b) near-collinear, (c) transverse imaging geometries.

Chapter 3

Figure 3.1:   Illustration of sampling THz pulses with the noncollinear imaging technique. The optical probe pulse and THz pulse propagate noncollinearly through a ZnTe crystal.

Figure 3.2: Schematic of the experimental setup. 1: low power imaging beam; 2: medium power optical pump beam; 3: high power beam for THz pulse generation; 4: THz beam; ZnTe: zinc telluride crystal; BP: black polyethylene; PM: parabolic mirror; L: lens; GaAs: gallium arsenide sample; P1: polarizer; P2: analyzer; λ/4: quarter-wave plate (inserted for *E*-mode, removed for E^2-mode); DDG: Digital delay

generator (Stanford Research System, DG 645); ICCD: intensified CCD camera with relay lens for imaging the THz waveform in the ZnTe detection crystal. For multi-shot, the gate of the ICCD camera system is trigged directly by a laser trigger and opens when every optical probe pulse comes in. While for single shot, A DDG is connected between the laser trigger and the ICCD gate. It is used to open the ICCD camera gate just one time, and the CCD only integrates one optical probe pulse. The inset shows the THz detection principle.

Figure 3.3: Sample imaging of the THz electric field waveform in *E-mode* in multi-shot. (a) Signal image captured with a THz modulation. (b) Background image taken without a THz modulation. (c) Background-subtracted image. The solid red rectangle defines the area for the THz waveform sampling.

Figure 3.4: Sample imaging of the square of the THz electric field waveform in E^2-*mode* in single shot. (a) Imaging with a THz modulation. (b) Imaging without a THz modulation. (c) Background-subtracted image. The solid red rectangle defines the window used for THz waveform sampling.

Figure 3.5: (a) THz electric field waveforms taken in *E-mode* with single shot and multi-shot (400,000). (b) Waveform of the square of the THz electric field in E^2-*mode* in single shot.

Figure 3.6: Images of the THz waveform at different time delays. The images are taken at delay stage positions of (a) 49.90 mm, (b) 50.00 mm, (c) 50.10 mm, and (d) 50.15 mm.

Figure 3.7: The change of the peak position with the delay stage position.

Figure 3.8: Background-subtracted multi-shot-averaged images of the electric field waveforms of the THz pulses that are transmitted through (a) the unexcited (reference) and (b) excited (pumped) GaAs sample in the *E*-mode configuration. The time scale is 45 pixels/ps and the arrows denote the direction of motion of the THz pulses. The solid red rectangles define the binning windows used for obtaining the THz waveforms.

(c) THz reference and pumped waveforms obtained in images (a) and (b). (d) The real (black symbols) and imaginary (red symbols) components of the THz conductivity measured in the photoexcited GaAs sample. A Drude model fit to the data (blue lines) is also shown.

Figure 3.9: Single-shot images of a transmitted THz pulse through (a) the unexcited GaAs sample, (b) the excited GaAs sample. (c) Extracted THz single-shot waveforms for the unexcited and excited GaAs. Thick lines depict the average of 10 single-shot THz waveforms. The arrow indicates the relative level of the background light that was subtracted from the original images. (d) The square of the THz waveforms in Figure 3.8(c).

Figure 3.10: Single-shot and multi-shot THz power transmission spectra through photoexcited GaAs. The thin lines represent single-shot power transmission spectra obtained from the single-shot E^2-mode THz waveforms in Figure 3.9(c). Line A (thick red line) is obtained from the power spectra of the E-mode THz waveforms in Figure 3.8(c). Line B (thick blue line) is obtained from the amplitude spectra of the E^2-mode 10-shot-averaged reference and pumped THz waveforms in Figure 3.9(c). Line C (thick green line) is the calculated power transmission spectrum based on the Drude fit in Figure 3.8(d).

Chapter 4

Figure 4.1: (a) Illustration of the THz Cherenkov wave. The Cherenkov angle θ_c is determined by the velocities of the optical pump pulse and the THz pulse. (b) Imaging the THz Cherenkov wave using the collinear imaging method, in which a probe pulse propagates collinearly with the pump pulse. (c) Imaging the THz Cherenkov wave using the transverse imaging method, in which a probe pulse propagates perpendicularly to the pump pulse.

Figure 4.2: Illustration of the transverse imaging setup. (a) and (b), The side-view imaging of the THz Cherenkov wave, the probe pulse propagates parallel to the *c*-axis of the crystal. (c) and (d), Top-view imaging of the THz Cherenkov wave, the probe pulse propagates perpendicular to the *c*-axis of the crystal.

Figure 4.3: (a) Experimental setup in side-view mode. An amplified Ti:sapphire laser pulse (100 fs, 800 nm, 0.9 mJ, 1 kHz) is split into two parts. The pump pulse (7.4 µJ) is focused by a lens (focal length 500 mm) onto the $LiNbO_3$ crystal (or $LiTaO_3$) to generate a THz wave. The probe pulse is frequency doubled through a BBO crystal and further spatially filtered and expanded to obtain a clean and uniform 400 nm probe beam. The expanded 400 nm probe pulse is transmitted through the crystal from the side (parallel to the *c*-axis). A filter after the crystal is used to remove the scattering from the 800 nm optical pump pulse. L1, L2, and L3 are optical lenses, L4 is the imaging microscope of the camera. F1 and F2 are bandpass coloured glass filters, BBO is β-Barium borate crystal, SF is the spatial filter, P is the polarizer, $\lambda/2$ is the half-wave plate, LN is the sample crystal ($LiNbO_3$ or $LiTaO_3$), and ICCD means Intensified CCD camera. (b) Detailed geometry of the optical pump and probe beams in the crystal. The pump polarization is controlled by a half-wave plate. The probe polarization is 54 °relative to the pump-probe intersection plane (actually, the measurement is independent on the probe polarization). L, H, and W are the size of the crystal, θ is the cutting angle. (c) Diagram of the index ellipsoid of the $LiNbO_3$ and $LiTaO_3$ crystal in the presence of the THz electric field which is parallel to the *c*-axis. The refractive index n_o is isotropic in the plane that is perpendicular to the *c*-axis and the change of the refractive index "n_o'-n_o" is proportional to the THz electric field [34]. (d) Background-subtracted image of the THz Cherenkov wave obtained from the ICCD.

Figure 4.4: Background-subtracted images of the THz pulse inside the **LN1** crystal captured at time delays of (a) 10 ps, (b) 20 ps, (c) 30 ps, and (d) 40 ps, respectively. (e) Overlay image of (a), (b), (c), and (d). (f) An illustration of the THz Cherenkov wave and the THz Cherenkov angle. The optical pump polarization is parallel to the *c*-axis of the crystal and the *c*-axis is pointing out of the paper plane.

Figure 4.5: (a)-(c) Schematic illustration of how the probe pulse wavefront (grey square plane) gets modulated by the THz Cherenkov cone when the optical pump pulse and the probe pulse propagate perpendicular to each other. (d) The THz cone and its Cherenkov angle in the probe image plane is 64 °, the cone is squeezed due to different refractive indices at different propagation directions. The red dashed line shows the observed cone edge in the image. (e) Simulation results of the image using 3ds Max. (f) Experimental image with an observed Cherenkov angle of 60.2 °. (g) Schematic diagram of the Cherenkov cone. The cone is squeezed with major radius *a* and minor radius *b*.

Figure 4.6: (a)-(c) Side-view images of the THz Cherenkov wave in the $LiNbO_3$ crystal captured at time delays of (a) 0 ps, (b) 12 ps, and (c) 24 ps, respectively. (d)-(f) Side-view images of the THz Cherenkov wave in the $LiTaO_3$ crystal captured at time delays of (d) 0 ps, (e) 12 ps, and (f) 24 ps, respectively. The pump pulse polarization is parallel to the *c*-axis of the crystal.

Figure 4.7: Side-view image of the transition-like radiation (red circles) in a $LiNbO_3$ crystal at different time delays.

Figure 4.8: (a)-(d) Background subtracted THz images in the crystal **LN1** captured at pump-probe time delays of 10 ps (a), 20 ps (b), 30 ps (c), and 40 ps (d). For comparison, images at time delays of 10 ps, 20 ps, and 30 ps are overlapped with that at a time delay of 40 ps in (d).

Figure 4.9: Background subtracted images (selected from a movie) of the THz pulse inside the **LN3** crystal captured at time delays of (a) 10 ps, (b) 20 ps, (c) 30 ps, (d) 40 ps, (e) 50 ps, (f) 60 ps. The pump polarization is parallel to the *c*-axis of the crystal and the *c*-axis is pointing out of the paper plane. The transition-like radiation that is generated at the second surface where the optical pulse gets totally internal reflected is marked by a red arrow.

Figure 4.10: Background-subtracted images of the THz pulse inside the **LN3** crystal captured at time delays of (a) 44 ps, (b) 48 ps, (c) 52 ps, (d) 56 ps, (e) 60 ps, (f) 64 ps. The pump polarization is parallel to the *c*-axis of the crystal and the *c*-axis is pointing out of the paper.

Figure 4.11: Schematic illustration of the imaging distortion when we image the transition-like radiation. The velocity of the transition-like radiation measured from the obtained images is higher than the actual value.

Figure 4.12: Illustration of the THz Cherenkov wave image and the corresponding real wavefront of the THz pulse. The black dashed lines mark the imaged THz wavefront, and the pulse propagation direction is illustrated by the black arrow. The corresponding real THz wavefront are marked by the yellow solid line and propagates along the yellow arrow.

Figure 4.13: (a) THz waveforms plotted in the AB direction in Figure 4.11. (b) The corresponding spectra of the waveforms in (a).

Figure 4.14: Illustration of the THz pulse generated by the optical pump pulse at three different locations (***O***, ***O'***, and ***O''***).

Figure 4.15: THz electric field waveforms collected at points ***B***, ***E***, and ***F*** that are marked in Figure 4.13.

Figure 4.16: Images of the THz Cherenkov wave generated by optical pump pulses as a function of the beam diameter (101.6 μm, 48.7 μm, and 27.5 μm) and the power (1.8 mW, 3.7 mW, and 7.4 mW).

Figure 4.17: Images of the THz Cherenkov wave captured at various pulse durations with the same optical pump power. 'Positive' and 'negative' mean the optical pump pulse is positively and negatively chirped, respectively.

Figure 4.18: Dependence of the THz electric field on the optical pump pulse duration. The red line (circles) is for the negatively chirped optical pump pulse, and the black line (squares) is for the positively chirped optical pump pulse.

Figure 4.19: Images of the THz Cherenkov wave inside the **LN 1** crystal captured at time delays of (a) 10 ps, (b) 20 ps, (c) 30 ps, and (d) 40 ps, respectively. The experimental parameters are the same as that of Figure 4.4 except that the optical pump pulse polarization is perpendicular to the c-axis of the crystal.

Figure 4.20: Images of the THz Cherenkov wave inside the **LN 1** crystal captured at time delays of (a) 10 ps, (b) 20 ps, (c) 30 ps, and (d) 40 ps, respectively. The experimental parameters are the same as those for Figure 4.4 except that the optical pump pulse polarization is 45 ° to the c-axis of the crystal.

Figure 4.21: Images of the THz wave inside the **LN1** crystal at time delays of (a) 10 ps, (b) 20 ps, (c) 30 ps, and (d) 40 ps. The optical pump pulse polarization is 43 ° with respect to the c-axis. The incident optical pulse travels horizontally at the left side of the air/LiNbO$_3$ interface.

Figure 4.22: Spectra of the optical pump pulse. (noLN) is the original spectrum without the LiNbO$_3$ crystal, (0deg) is transmitted through the LiNbO$_3$ crystal with the optical pump pulse polarization parallel to the c-axis; (45deg) is transmitted through the LiNbO$_3$ crystal with the angle between the optical pump pulse polarization and the c-axis 45 °; (90deg) is transmitted through the LiNbO$_3$ crystal with the optical pump pulse polarization perpendicular to the c-axis.

Figure 4.23: (a) Illustration of the top-view mode and side-view mode. The side-view probe beam

propagates along the Z direction (*c*-axis of the crystal), and the top-view probe beam is along the Y direction. (b) Experimental setup for top-view and side-view imaging. The imaging mode is determined by the crystal orientation, pump pulse polarization, and probe pulse propagation direction, as shown in (c) and (d). In the experiment, the illustration of the crystal orientation, pump pulse polarization, and probe pulse propagation direction in side-view mode (c) and top-view mode (d), respectively.

Figure 4.24: (a)-(e) Side-view images of the THz Cherenkov wave in the $LiNbO_3$ crystal captured at time delays of (a) 0 ps, (b) 6 ps, (c) 12 ps, (d) 18 ps, and (e) 24 ps, respectively. (f)-(j) Top-view images of the THz Cherenkov wave in the $LiNbO_3$ crystal at time delays of (f) 0 ps, (g) 6 ps, (h) 12 ps, (i) 18 ps, and (j) 24 ps, respectively.

Figure 4.25: Illustration of the line focused optical pump geometries. (a) The optical pump beam line is parallel to the probe pulse propagation direction. (b) The optical pump beam is perpendicular to the probe pulse propagation direction.

Figure 4.26: Images of the THz Cherenkov wave generated by the line focused pump pulse at time delays of (a) 0 ps, (b) 6 ps, (c) 12 ps, (d) 18 ps, (e) 24 ps, and (c) 30 ps, respectively. The orientation of the focused beam is parallel to the probe pulse propagation direction.

Figure 4.27: (a) Illustration of the line-focused pump geometry with the length of the focused beam line, W. (b) Illustration of the time delay (ΔL) between the two Cherenkov waves.

Figure 4.28: Images of the THz Cherenkov wave generated by the line focused pump pulse at time delays of (a) 4 ps, (b) 8 ps, (c) 12 ps, (d) 16 ps, (e) 20 ps, (f) 24 ps, (g) 28 ps, and (h) 32 ps, respectively. The orientation of the focused beam line is perpendicular to the probe pulse propagation direction and is in vertical direction.

Chapter 5

Figure 5.1: (a) Illustration of the experimental setup used to generate THz pulses with the tilted-pulse-front excitation technique and image the generated THz pulses. The optical pump beam ($\lambda_{central} = \mathbf{800\ nm}$) goes through a slit, and is then diffracted by a grating. The wave front of the optical pump pulse is tilted by the grating and is imaged onto the LiNbO$_3$ crystal with a lens. The optical probe pulse (($\lambda_{central} = \mathbf{400\ nm}$) travelling normal to the optical pump pulse images the generated THz wave and is recorded by an intensified CCD (ICCD) camera system (not shown). (b) The detailed imaging geometry (side view) in the LiNbO$_3$ crystal. The optical pump pulse polarization is parallel to the c-axis of the crystal, and the optical probe pulse polarization is parallel to the optical pump beam.

Figure 5.2: Images of the THz wave generated in the LiNbO$_3$ crystal with the optical pump beam width in the optical probe pulse propagation direction at (a) 0.25 mm, (b) 0.43 mm, (c) 0.83 mm, and (d) about 1 mm (full Gaussian beam, without slit), respectively.

Figure 5.3: Images of the THz wave generated in the LiNbO$_3$ crystal at time delays of (a) 12 ps, (b) 24 ps, (c) 28 ps, and (d) 36 ps, respectively. The size of the optical pump beam along the optical probe pulse propagation direction (out of the page) is 0.25 mm, and the optical pump beam size that is perpendicular to the probe pulse direction is 1 mm. The tilt angle of the optical pump pulse wave front is 67 °. The measured and the calibrated THz Cherenkov angles are 60 °and 64 °, respectively.

Figure 5.4: Optical setup for separating the THz pulse from the optical pump pulse. An optical pump beam is transmitted through a LiNbO$_3$ prism to generate THz pulses. A cubic LiNbO$_3$ crystal is attached to the LiNbO$_3$ prism to separate the THz pulse (marked in blue color) from the optical pump pulse (marked in red color).

Figure 5.5: Images of optical pulse and THz pulse separation process at time delays of (a) 27.2 ps, (b) 30.4

ps, (c) 33.6 ps, (d) 36.8 ps, (e) 43.2 ps, and (f) 46.4 ps. Schematic illustrations to show the THz pulse and optical pulse before (g) and after (h) they get separated by the air gap. (i) The plot of the THz signal strength along the THz pulse wave front.

Figure 5.6: The combined images of the THz wave inside the LiNbO$_3$ crystal at three different time delays (18 ps, 30 ps, and 42 ps) at optical pump pulse tilt angles of   (a) 68 °, (b) 64 °, (c) 61 °, and (d) 56 °.

Figure 5.7: The relationship between the THz pulse electric field amplitude and the tilt angle of the optical pump pulse.

Figure 5.8: Images of the THz pulse that is generated by pumping the tip of the crystal at time delays of (a) 0 ps, (b) 8 ps, (c) 16 ps, (d) 24 ps, and (e) 32 ps.   Images of the THz pulse that is generated by pumping the middle part of the crystal at time delays of (f) 0 ps, (g) 8 ps, (h) 16 ps, (i) 24 ps, and (j) 32 ps.

Figure 5.9: (a) Optics setup for collecting and detecting the output THz pulse. (b) The relationship between the THz output energy and the square of THz image signal strength. (c) The relationship between the THz image signal strength and the optical pump power.

Figure 5.10: Images of the THz wave that is generated by the optical pump pulse with the optical pump pulse polarization (a) parallel to the *c*-axis of the crystal, (b) at 45 ° with respect to the *c*-axis of the crystal, (c) perpendicular to the *c*-axis of the crystal.

Figure 5.11: (a) Illustration of the 3D THz pulse imaging setup. The 800 nm optical pump beam goes through a slit and then is diffracted by a grating. The optical pump pulse with the tilted pulse front is imaged on the LiNbO$_3$ crystal by a lens. A 400 nm optical probe pulse travelling normally to the optical pump pulse images the generated THz wave and finally is recorded by an intensified CCD (ICCD) camera system (not shown). (b) The detailed side-view imaging geometry inside the LiNbO$_3$ crystal. The pump

pulse polarization is parallel to the c-axis of the crystal, and the probe pulse polarization is in the plane defined by the probe pulse propagation direction and the c-axis of the crystal. The optical pump beam is scanned in the horizontal direction (along c-axis in (b)).

Figure 5.12: Illustration of the THz pulses that are generated by optical pump pulses that go through the slit at two positions, **A** and **B**.

Figure 5.13: Images of the THz pulse that is generated by optical pump pulses with slit positions at (a) 7.5 mm, (b) 8.0 mm, (c) 8.5 mm, (d) 9.0 mm, (e) 9.5 mm, and (f) 10.0 mm.

Figure 5.14: Images of the THz pulse (at a fixed slit position) at time delays of (a) 7 ps, (b) 13 ps, (c)19 ps, (d) 25 ps, (e) 31 ps, and   (f) 37 ps.

Figure 5.15: Relationships between the THz image position on the ICCD camera and the slit position (a), as well as the time delay (b), respectively.

Figure 5.16: Images of the THz pulse with the optical pump beam shift Δd inside the LiNbO$_3$ crystal of (a) 0.000 mm, (b) 0.215 mm, (c) 0.430 mm, (d) 0.645 mm, (e) 0.860 mm, (f) 1.075 mm, (g) 1.290 mm, (h) 1.506 mm, (i) 1.720 mm, and (j) 1.935 mm. The relative pump-probe time delay has been corrected.

Figure 5.17: (a)-(d) 3D visualization of the THz wave generated by a full beam optical pump pulse with the optical pump pulse front tilted.

Figure 5.18: Images of the THz pulse generated by the optical pump beam with the position shift Δd of (a) 0.0 mm, (b) 0.5 mm, (c) 1.0 mm, (d) 1.5 mm, (e) 2.0 mm, and (f) 2.5 mm. The relative pump-probe time delay has been corrected.

Figure 5.19: (a)-(d) 3D visualization of the THz wave pumped by a full beam optical pump pulse with the optical pump pulse front not tilted.

Chapter 6

Figure 6.1: Illustration of THz pulse reflection at (a) the crystal-air boundary and the crystal-Au boundary, and (b) the crystal-air boundary and the crystal-Au grating boundary.

Figure 6.2: Images of THz pulse reflection captured at time delays of (a) 40.0 ps, (b) 44.0 ps, (c) 48.0 ps, (d) 52.0 ps, (e) 56.0 ps, (f) 60.0 ps, (g) 64.0 ps, and (h) 68.0 ps. The Au film thickness is 250 nm.

Figure 6.3: Images of the THz pulse reflection captured at time delays of (a) 6 ps, (b) 12 ps, (c) 18 ps, (d) 24 ps, (e) 30 ps, (f) 36 ps, (g) 42 ps, and (h)48 ps. The width of the Au line and the gap are 0.1 mm and 0.2 mm, respectively.

Figure 6.4: Images of the THz pulse reflection captured at time delays of (a) 6 ps, (b) 12 ps, (c) 18 ps, (d) 24 ps, (e) 30 ps, (f) 36 ps, (g) 42 ps, and (h) 48 ps. The width of the Au line and the gap are 0.1 mm and 0.5 mm, respectively.

Figure 6.5: Illustration of the experimental setup for imaging the reflected and transmitted THz pulses in two $LiNbO_3$ crystals. The width of the Au line and the gap are 0.1 mm and 0.2 mm, respectively.

Figure 6.6: Images of the reflected and transmitted THz pulses in two $LiNbO_3$ crystals at time delays of (a) 40 ps, (b) 48 ps, (c) 56 ps, (d) 64 ps, (e) 72 ps, (f) 80 ps, (g) 88 ps, and (h) 96 ps. The width of the Au line and the gap are 0.1 mm and 0.2 mm, respectively.

Figure 6.7: Illustration of the THz total internal reflection at the $LiNbO_3$ crystal-air boundary.

Figure 6.8: Images of THz total internal reflection captured at time delays of (a) 20 ps, (b) 40 ps, (c) 60 ps, and (d) 80 ps. The THz incident angle at crystal-boundary is 53 °.

Figure 6.9: Illustration of THz tunnelling through the air gap two $LiNbO_3$ crystals. Two glass slides are inserted between the two crystals to control the gap width *d*.

Figure 6.10: Images of frustrated total internal reflection of THz pulses at an air gap of width (a) 0 μm, (b) 75 μm, and (c) 150 μm.

Figure 6.11: Theoretical calculation of the THz pulse (s-polarized) transmission at different air gap widths. The central THz frequency is 0.22 THz (λ=0.38 mm in $LiNbO_3$), the refractive index of LiNbO3 crystal is 5.1, and the incident angle is 53 °.

Figure 6.12: (a)-(c) Images of the THz reflection at time delays of 40 ps, 70 ps, and 82 ps. (d) The magnified inset of (b). For a high contrast ratio, images are treated with PHOTOSHOP.

Figure 6.13: (a) Illustration of the destructive interference between the reflected THz pulse and the backward-propagating transition-like radiation in the crystal. The forward-propagating transition-like radiation in shown as well. (b) Design of new $LiNbO_3$ THz sources using $LiNbO_3$ slides.

Chapter 7

Figure 7.1: (a) Experimental setup for imaging THz generation and propagation in a PPLN crystal. An

optical pump pulse (800 nm) is point focused onto the PPLN crystal to generate THz pulses, and the probe pulse (400 nm) is transmitted through the crystal to image the THz generation and propagation processes. (b) and (c) Are images captured with and without (background) optical pump pulse excitation, respectively. (d) The background-subtracted image of the THz pulse.

Figure 7.2: Images of the THz pulse in the PPLN crystal at time delays of (a) 0 ps, (b) 6 ps, (c) 12 ps, (d) 18 ps, (e) 24 ps, (f) 30 ps, (g) 36 ps, and (h) 42 ps.

Figure 7.3: Illustration of the experimental setup to generate and image the air plasma.

Figure 7.4: Images of the air plasma captured at time delays of (a) 40 ps, (b) 47 ps, (c) 53 ps, (d) 60 ps, (e) 67 ps, (f) 133 ps, (g) 200 ps, and (h) 267 ps.

Figure 7.5: (a) Illustration of the experimental setup to image the Kerr effect induced by femtosecond optical pulses in CS_2 (contained in a quartz cuvette). The optical pulse (800nm) is focused by a lens (not shown) in CS_2. The angle between the optical pump pulse polarization and the vertical direction is θ. The probe pulse is sent through the sample and finally is sampled by a crossed polarizer, and the probe pulse polarization is 45 ° with respect to the vertical direction. (b) The refractive index ellipsoid induced by the Kerr effect. The birefringence experienced by the probe pulse is shown in the green plane.

Figure 7.6: Images of Kerr signals in CS_2 at time delays of (a) 4 ps, (b) 8 ps, (c) 12 ps, (d) 16 ps, (e) 20 ps, and (f) 24 ps.

Figure 7.7: Images of the Kerr signal induced by the optical pump pulse polarized at (a) 0 °, (b) 30 °, (c) 60 °, and (d) 90 °.

Figure 7.8: Image of the femtosecond optical pulses tranveling in quartz, water, methnol, THF, and CS_2 at

a time delay of 0 ps.

Figure 7.9: Image of the femtosecond optical pulses tranveling in quartz, water, methnol, THF, and CS_2 at a time delay of 0.38 ps.

Figure 7.10: Image of the femtosecond optical pulses tranveling in quartz, water, methnol, THF, and CS_2 at a time delay of 0.78 ps.

Figure 7.11: Image of the femtosecond optical pulses tranveling in quartz, water, methnol, THF, and CS_2 at a time delay of 1.18 ps.

Figure 7.12: Image of the femtosecond optical pulses tranveling in quartz, water, methnol, THF, and CS_2 at a time delay of 1.58 ps.

Figure 7.13: Image of the femtosecond optical pulses tranveling in quartz, water, methnol, THF, and CS_2 at a time delay of 1.98 ps.

Figure 7.14: Image of the femtosecond optical pulses tranveling in quartz, water, methnol, THF, and CS_2 at a time delay of 2.28 ps.

Figure 7.15: Experimental setup to image the femtosecond optical pump pulse's reflection and refraction at water/glass interface. The quartz corvette is filled with water, and a piece of 1 mm thickness glass slide with cut angle ~ 7.4 ° is submergered in the water. The pump pulse (800 nm, polarized in the vertical direction) is incident on the water/glass interface at an incident angle of 82.65 °. The proble pulse (400 nm, polarized 45 ° with respect to the vertical direction) propagates through the corvette and is sampled by a crossed polarizer.

Chapter 8

power ratio between the noise signal and THz signal in the frequency domain.

Figure 8.5: (a) THz wave from collected as reference signal when the sample is taken away, 90 degree means the orientation of the grid is perpendicular to the THz polarization, 0 degree means the THz pulse collected with the grid orientation parallel to the THz polarization. (b) The corresponding Fourier transform result of the THz waveform in (a). (c) Power transmission of the THz polarizer. (d) Extinction ratio of the THz polarizer. (e) Degree of the polarization.

Figure 8.6: (a) The THz reference waveform (without CNT polarizer) and the transmitted waveforms at different CNTA orientations with respect to the THz polarization. (b) THz transmission through the CNTA sheet at different CNTA orientation angles.

List of Symbols

2D	Two dimensions
3D	Three dimensions
Au	Gold
BBO	β barium borate
c-axis	Optics axis
CCVD	Catalytic chemical vapor deposition
CNT	Carbon nanotube
CNTA	Carbon nanotube array
CS_2	Carbon disulfide
DDG	Digital delay generator
EO	Electro-optic
FESEM	Field emission scanning electron microscope
GaAs	Gallium arsenide
ICCD	Intensified CCD
$LiNbO_3$	Lithium niobate
$LiTaO_3$	Lithium tantalate
n_{eo}	Extraordinary refractive index
NLWC	Nonlinear wave conversion
n_o	Ordinary refractive index
ω	Angular frequency
OR	Optical rectification
PPLN	Periodically poled lithium niobate
SNR	Signal to noise ratio
THF	Tetrahydrofuran
THz	Terahertz

THz-TDS	THz time-domain spectroscopy
V_{op}	Optical velocity
V_{THz}	THz velocity
ZnTe	Zinc telluride
θ_c	Cherenkov angle
$\lambda/4$ plate	Quarter wave plate
σ_{dc}	Dc conductivity
τ	Scattering time

Chapter 1

Introduction

The first fast imaging technique was developed almost 160 years ago by William Henry Fox Talbot, who in 1851 took a photograph of a rapidly spinning wheel in the light of an electric spark [1]. Since then it has been realized that the short pulse duration of the light source is key for capturing instantaneous images of fast moving objects. Lots of flash photography work has been demonstrated, with one of the most famous being Eadward Muybridge's race horse imaging in 1878 [1].

Recent developments in ultrashort pulse generation technique have driven down attainable pulse widths from microseconds to picoseconds and femtoseconds, and even to pulse widths as short as a few tens of attoseconds [2, 3]. These advances led to the development of the novel ultrafast imaging techniques for studying various ultrafast phenomena.

The same advances in ultrafast optical pulse techniques have also revolutionized the field of terahertz (THz) science and technology, resulting in many novel applications such as coherent THz pulse generation and detection, THz spectroscopy, and THz optics [4-9].

In this thesis, we apply ultrafast imaging techniques to THz detection and single-shot THz spectroscopy. We also image the generation and propagation of THz pulses inside $LiNbO_3$ crystals.

The traditional method to sample THz waveforms for THz time-domain spectroscopy is to use a series of femtosecond (fs) optical pulses to map the temporal profile of the THz waveform point-by-point by scanning the optical pulse-THz pulse delay [4]. Although this method provides excellent signal to noise ratio (SNR), such point-by-point acquisition is time consuming, and limits exploration of irreversible phenomena such as material damage and chaotic dynamics.

In the past 15 years, single-shot acquisition of the entire THz waveform has been demonstrated using several ultrafast imaging methods [10-22]. The first

approach uses spectral-encoding, where the temporal profile of the THz pulse is transcribed onto the frequency spectrum of a linearly-chirped optical probe pulse [10-13]. A second scheme suggested by Shan *et al.* [14] encodes the THz waveform onto the transverse spatial profile of the optical probe beam that propagates noncollinearly with the THz pulse [14, 15]. Other methods include encoding the THz waveform on a tilted [16-18] or incrementally delayed [19] wavefront of a fs optical pulse which propagates collinearly with the THz pulse, as well as cross-correlation techniques [20, 21].

For all these methods, the spectral coding is the most developed and has been successfully applied to single-shot THz pulse diagnostics. On the other hand, the noncollinear imaging method is much easier to perform, but has never been tried for THz spectroscopy. In Chapter 3 of this thesis, we demonstrate the single-shot THz spectroscopy with the noncollinear imaging method.

Due to the low THz pulse intensity, sampling the THz electric field waveform with a reasonable SNR ratio is still challenging. Therefore, development of intense THz pulses sources is essential for single-shot THz spectroscopy.

Generation of intense THz pulses in $LiNbO_3$ crystals with the tilted-pulse-front excitation technique has been developed over the past few years [6, 9, 23-33]. Since the advent of this technique, the record for the highest THz pulse energy in $LiNbO_3$ was increased steadily [26, 28, 29, 32], with the highest pulse energy to date being 125 μJ [32]. Furthermore, a maximum THz electric field of 1.2 MV/cm has been recently realized [33]. These high energy THz pulses open exciting prospects for applications in nonlinear terahertz spectroscopy [34], spin coherent control [35], THz-pulse-induced phase transitions in strong correlation system [36], and high SNR single-shot THz spectroscopy.

One drawback of the $LiNbO_3$ THz source is the relative complexity of the optical setup. Because the electromagnetic wave can be coupled with phonons efficiently in the THz frequency range in $LiNbO_3$, THz phonon-polaritons are formed and thus make the refractive index of $LiNbO_3$ in the THz frequency much higher than that in the optical frequency range [37]. A THz Cherenkov wave is generated and the traditional collinear phase-matching condition cannot be

satisfied [6, 9, 23-33]. In order to achieve the phase matching, the wavefront of the optical pump pulse must be tilted so as to match the generated THz pulse wavefront. What's more, the generated THz pulse propagates in a different direction from that of the optical pump pulse. A detailed understanding of THz generation and propagation processes in $LiNbO_3$ is therefore very important for developing more efficient $LiNbO_3$ THz sources.

The first experiment aimed at investigating the dynamics of the THz Cherenkov wave was carried out in a $LiTaO_3$ crystal (similar to the $LiNbO_3$) in 1984 by Auston *et al.* [38]. In that experiment, two parallel optical pulses were focused in a $LiTaO_3$ crystal. One of the pulses excited the THz Cherenkov wave, while the other one sampled the THz electric field via the Pockels effect. The Cherenkov angle was calculated by changing the lateral spacing between the two pulses and recording the corresponding time delay between them. Another group also mapped the whole Cherenkov radiation structure by fine step raster scanning [39].

Instead of raster scanning, which can be time-consuming, Koehl *et al.* [40] demonstrated the full field imaging by replacing the focused probe beam with a broad beam that is large enough to cover the whole region of interest. The phase-shift image imprinted on the probe beam by the THz pulse can be converted into an amplitude image for detection by a CCD camera with various imaging configurations, such as the Talbot effect or phase-contrast microscopy [40-44].

Because of their full field imaging capability, many fascinating experiments have been done to explore THz generation and propagation inside bulk and thin waveguide ferroelectric crystals such as $LiNbO_3$ and $LiTaO_3$ [26, 40, 42, 44-49]. The evolution of a THz pulse excited by different pump configurations (e.g. point focused, cylindrically line focused and so on) has been observed and studied in bulk ferroelectric crystals [40, 45-47]. Furthermore, the reflection, refraction, and interference behavior of a THz pulse on a patterned wave guide has been demonstrated [30, 45, 49, 50], and the THz waveform generated by a bulk $LiNbO_3$ crystal and coupled through the free space into a $LiNbO_3$ waveguide has been imaged inside the waveguide [26].

In contrast to a THz wave inside a waveguide, which is two-dimensional and can be completely read out by a single image along one direction, the THz pulse in a bulk crystal is three dimensional and requires more than one view mode to extract the full spatial structure. Until now, the imaging work on bulk crystals has been done exclusively with a collinear imaging geometry, in which the probe pulse propagates collinearly or near-collinearly with the pump pulse. In this case, the imaging of the THz Cherenkov wave presents itself in a circle pattern in the point-focused optical pump geometry [40, 46, 51]. To reveal the full structure of the THz Cherenkov wave, information from other view modes is desired to complement the collinear imaging mode.

In this thesis, the side-view and top-view image of the THz wave in $LiNbO_3$ and $LiTaO_3$ are carried out with two types of transverse imaging geometries, in which the probe beam propagates perpendicular (transverse) to the optical pump beam. The THz wave that is generated in various optical excitation configurations including point focused, line focused, and tilted wavefront, is imaged experimentally for the first time. Based on these techniques, we explore the parameters of the THz Cherenkov wave such as refractive indices of the optical and THz pulses, Cherenkov angle, transition-like radiation, signal amplitude, and their dependence on various pump parameters such as pump polarization, duration, intensity. The image distortion of the THz Cherenkov wave due to the transverse imaging geometry is also discussed and calibrated.

Finally, potential applications of the transverse imaging technique in ultrafast imaging of the interaction between intense femtosecond laser pulses and various materials including periodically poled lithium niobate (PPLN), water, methanol, air, CS_2, THF, and quartz are also explored.

In Chapter 2, the fundamental knowledge related to the thesis is introduced. The principle of THz generation and detection in ZnTe and $LiNbO_3$ crystals is described theoretically. Noncollinear imaging geometry for the single-shot THz waveform sampling and the transverse imaging geometry for THz Cherenkov wave imaging are introduced.

Chapter 3 focuses on single-shot THz spectroscopy using a noncollinear imaging technique. Samplings of the THz electric field waveform in E-mode with multiple shots and the square of the THz electric field waveform in E^2-mode with single shot are demonstrated. The THz spectroscopy applications of E-mode and E^2-mode are explored with photoexcited GaAs as an example.

Chapter 4 discusses the ultrafast imaging of THz Cherenkov waves in the transverse imaging geometry. The generation and propagation of the THz Cherenkov wave and transition-like radiation in $LiNbO_3$ crystals are studied in side-view mode and top-view mode. For comparison, some experiments are also carried out in $LiTaO_3$ crystals. The image distortion due to the transverse imaging geometry is simulated and calibrated.

Chapter 5 demonstrates the imaging of the THz Cherenkov wave generated with the tilted-pulse-front excitation technique in real time. For the first time, the detection of the output THz pulse and the imaging of the THz pulse inside the $LiNbO_3$ crystal are realized at the same time. 3D imaging of the THz Cherenkov wave pumped by a full beam optical pump pulse is demonstrated as well.

In Chapter 6, THz reflection, transmission, and tunnelling are imaged. Chapter 7 explores the potential application of the transverse imaging technique in other fields and shows some preliminary results.

In addition to the ultrafast imaging experiments, a novel carbon nanotube THz polarizer is also developed and shown in Chapter 8.

The ICCD camera operation and calibration are introduced in Appendix A. The optical setup for tilting the wavefront of the optical pulse is described in Appendix B. Calculation of the ac complex conductively based on the THz electric field waveforms and the Drude mode fitting are discussed in Appendix C. Matlab codes for image processing are included in Appendix D. Calculation of the THz electric field distribution on the THz Cherenkov cone is described in Appendix E. The THz absorption spectroscopy analysis in E^2-mode is introduced in Appendix F. The study of the transition-like radiation and measurement of THz index in $LiNbO_3$ using time-domain spectroscopy method is discussed in Appendix G. Finally, a brief discussion about the possible relationship between

Lorentz contraction and the imaging distortion in the transverse imaging geometry is given in Appendix H.

References:

1. M. R. Freeman, "What to do when it's too fast to see: freeze-frame imaging, from racehorses to atoms," PIC, 148-157 (1998).

2. C. Rulliere, *Femtosecond Laser Pulses: Principles and Experiments* (Springer, 2005).

3. F. Frank, C. Arrell, T. Witting, W. A. Okell, J. McKenna, J. S. Robinson, C. A. Haworth, D. Austin, H. Teng, I. A. Walmsley, J. P. Marangos, and J. W. G. Tisch, "Invited review article: technology for attosecond science," Rev. Sci. Instrum. **83**, 071101 (2012).

4. B. Ferguson, and X.-C. Zhang, "Materials for terahertz science and technology," Nat. Mater. **1**, 26-33 (2002).

5. M. Tonouchi, "Cutting-edge terahertz technology," Nat. Photonics **1**, 97-105 (2007).

6. M. C. Hoffmann, and J. A. Fulop, "Intense ultrashort terahertz pulses: generation and applications," J. Phys. D: Appl. Phys. **44**, 083001 (2011).

7. P. U. Jepsen, D. G. Cooke, and M. Koch, "Terahertz spectroscopy and imaging - Modern techniques and applications," *Laser* Photonics Rev. **5**, 124-166 (2011).

8. P. C. M. Planken, H. K. Nienhuys, H. J. Bakker, and T. Wenckebach, "Measurement and calculation of the orientation dependence of terahertz pulse detection in ZnTe," J. Opt. Soc. Am. B **18**, 313-317 (2001).

9. F. Blanchard, G. Sharma, L. Razzari, X. Ropagnol, H. C. Bandulet, F. Vidal, R. Morandotti, J. C. Kieffer, T. Ozaki, H. Tiedje, H. Haugen, M. Reid, and F. Hegmann, "Generation of intense terahertz radiation via optical methods," IEEE J. Sel. Top. Quant. Electron. **17**, 5-16 (2011).

10. Z. P. Jiang, and X.-C. Zhang, "Electro-optic measurement of THz field pulses with a chirped optical beam," Appl. Phys. Lett. **72**, 1945-1947 (1998).

11. Z. P. Jiang, and X.-C. Zhang, "Single-shot spatiotemporal terahertz field imaging," Opt. Lett. **23**, 1114-1116 (1998).

12. K. Y. Kim, B. Yellampalle, J. H. Glownia, A. J. Taylor, and G. Rodriguez, "Measurements of terahertz electrical conductivity of intense laser-heated dense aluminum plasmas," Phys. Rev. Lett. **100**, 135002 (2008).

13. X.-Y. Peng, R. Jung, T. Toncian, O. Willi, and J.-H. Teng, "Distortion of the intense terahertz signal measured by spectral-encoding technique," Appl. Phys. Lett. **94**, 221107 (2009).

14. J. Shan, A. S. Weling, E. Knoesel, L. Bartels, M. Bonn, A. Nahata, G. A. Reider, and T. F. Heinz, "Single-shot measurement of terahertz electromagnetic pulses by use of electro-optic sampling," Opt. Lett. **25**, 426-428 (2000).

15. T. Yasui, K.-I. Sawanaka, A. Ihara, E. Abraham, M. Hashimoto, and T. Araki, "Real-time terahertz color scanner for moving objects," Opt. Express **16**, 1208-1221 (2008).

16. Y. Kawada, T. Yasuda, H. Takahashi, and S.-I. Aoshima, "Real-time measurement of temporal waveforms of a terahertz pulse using a probe pulse with a tilted pulse front," Opt. Lett. **33**, 180-182 (2008).

17. Y. Kawada, T. Yasuda, A. Nakanishi, H. Takahashi, and S.-I. Aoshima, "Single-shot measurement of terahertz temporal waveform using pulse-front tilting by a direct vision dispersion prism," Rev. Sci. Instrum. **80**, 113703 (2009).

18. Y. Kawada, T. Yasuda, A. Nakanishi, K. Akiyama, and H. Takahashi, "Single-shot terahertz spectroscopy using pulse-front tilting of an ultra-short probe pulse," Opt. Express **19**, 11228-11235 (2011).

19. K. Y. Kim, B. Yellampalle, A. J. Taylor, G. Rodriguez, and J. H. Glownia, "Single-shot terahertz pulse characterization via two-dimensional electro-optic imaging with dual echelons," Opt. Lett. **32**, 1968-1970 (2007).

20. S. P. Jamison, J. L. Shen, A. M. MacLeod, W. A. Gillespie, and D. A. Jaroszynski, "High-temporal-resolution, single-shot characterization of terahertz pulses," Opt. Lett. **28**, 1710-1712 (2003).

21. J. V. Tilborg, C. B. Schroeder, C. Toth, C. G. R. Geddes, E. Esarey, and W. P. Leemans, "Single-shot spatiotemporal measurements of high-field terahertz pulses," Opt. Lett. **32**, 313-315 (2007).

22. B. Ferguson, S. Wang, D. Gray, D. Abbott, and X.-C. Zhang, "Identification of biological tissue using chirped probe THz imaging," Microelectron. J. **33**, 1043-1051 (2002).

23. J. Hebling, K.-L. Yeh, M. C. Hoffmann, B. Bartal, and K. A. Nelson, "Generation of high-power terahertz pulses by tilted-pulse-front excitation and their application possibilities," J. Opt. Soc. Am. B **25**, B6-B19 (2008).

24. J. Hebling, G. Almasi, I. Z. Kozma, and J. Kuhl, "Velocity matching by pulse front tilting for large-area THz-pulse generation," Opt. Express **10**, 1161-1166 (2002).

25. A. G. Stepanov, J. Hebling, and J. Kuhl, "Efficient generation of subpicosecond terahertz radiation by phase-matched optical rectification using ultrashort laser pulses with tilted pulse fronts," Appl. Phys. Lett. **83**, 3000-3002 (2003).

26. K. L.-Yeh, M. C. Hoffmann, J. Hebling, and K. A. Nelson, "Generation of 10 μJ ultrashort terahertz pulses by optical rectification," Appl. Phys. Lett. **90**, 171121 (2007).

27. M. C. Hoffmann, K.-L. Yeh, J. Hebling, and K. A. Nelson, "Efficient terahertz generation by optical rectification at 1035 nm," Opt. Express **15**, 11706-11713 (2007).

28. A. G. Stepanov, L. Bonacina, S. V. Chekalin, and J.-P. Wolf, "Generation of 30 mu J single-cycle terahertz pulses at 100 Hz repetition rate by optical rectification," Opt. Lett. **33**, 2497-2499 (2008).

29. A. G. Stepanov, S. Henin, Y. Petit, L. Bonacina, J. Kasparian, and J. P. Wolf, "Mobile source of high-energy single-cycle terahertz pulses," Appl. Phys. B **101**, 11-14 (2010).

30. K.-H. Lin, C. A. Werley, and K. A. Nelson, "Generation of multicycle terahertz phonon-polariton waves in a planar waveguide by tilted optical pulse fronts," Appl. Phys. Lett. **95**, 103304 (2009).

31. J. A. Fulop, L. Palfalvi, G. Almasi, and J. Hebling, "Design of high-energy terahertz sources based on optical rectification," Opt. Express **18**, 12311-12327 (2010).

32. J. A. Fulop, L. Palfalvi, S. Klingebiel, G. Almasi, F. Krausz, S. Karsch, and J. Hebling, "Generation of sub-mJ terahertz pulses by optical rectification," Opt. Lett. **37**, 557-559 (2012).

33. H. Hirori, A. Doi, F. Blanchard, and K. Tanaka, "Single-cycle terahertz pulses with amplitudes exceeding 1 MV/cm generated by optical rectification in $LiNbO_3$," Appl. Phys. Lett. **98**, 091106 (2011).

34. F. Blanchard, D. Golde, F. H. Su, L. Razzari, G. Sharma, R. Morandotti, T. Ozaki, M. Reid, M. Kira, S. W. Koch, and F. A. Hegmann, "Effective mass anisotropy of hot electrons in nonparabolic conduction bands of n-doped InGaAs films using ultrafast terahertz pump-probe techniques," Phys. Rev. Lett. **107**, 107401 (2011).

35. T. Kampfrath, A. Sell, G. Klatt, A. Pashkin, S. Maehrlein, T. Dekorsy, M. Wolf, M. Fiebig, A. Leitenstorfer, and R. Huber, "Coherent terahertz control of antiferromagnetic spin waves," Nat. Photonics **5**, 31-34 (2011).

36. M. Liu, H. Y. Hwang, H. Tao, A. C. Strikwerda, K. Fan, G. R. Keiser, A. J. Sternbach, K. G. West, S. Kittiwatanakul, J. Lu, S. A. Wolf, F. G. Omenetto, X. Zhang, K. A. Nelson, and R. D. Averitt, "Terahertz-field-induced insulator-to-metal transition in vanadium dioxide metamaterial," Nature **487**, 11231 (2012).

37. D. W. Ward, "Polaritonics: an intermediate regime between electronics and photonics," in *Department of Chemistry*(Massachusetts Institute of Technology, 2005).

38. D. H. Auston, K. P. Cheung, J. A. Valdmanis, and D. A. Kleinman, "Cherenkov radiation from femtosecond optical pulses in electro-optic media," Phys. Rev. Lett. **53**, 1555-1558 (1984).

39. J. K. Wahlstrand, and R. Merlin, "Cherenkov radiation emitted by ultrafast laser pulses and the generation of coherent polaritons," Phys. Rev. B **68**, 054301 (2003).

40. R. M. Koehl, S. Adachi, and K. A. Nelson, "Real-space polariton wave packet imaging," J. Chem. Phys. **110**, 1317-1320 (1999).

41. P. Peier, S. Pilz, F. Mueller, K. A. Nelson, and T. Feurer, "Analysis of phase contrast imaging of terahertz phonon-polaritons," J. Opt. Soc. Am. B **25**, B70-B75 (2008).

42. Q. Wu, C. A. Werley, K.-H. Lin, A. Dorn, M. G. Bawendi, and K. A. Nelson, "Quantitative phase contrast imaging of THz electric fields in a dielectric waveguide," Opt. Express **17**, 9219-9225 (2009).

43. C. A. Werley, Q. Wu, K.-H. Lin, C. R. Tait, A. Dorn, and K. A. Nelson, "Comparison of phase-sensitive imaging techniques for studying terahertz waves in structured $LiNbO_3$," J. Opt. Soc. Am. B **27**, 2350-2359 (2010).

44. C. A. Werley, K. A. Nelson, and C. R. Tait, "Direct visualization of terahertz electromagnetic waves in classic experimental geometries," Am. J. Phys. **80**, 72-81 (2012).

45. T. Feurer, N. S. Stoyanov, D. W. Ward, J. C. Vaughan, E. R. Statz, and K. A. Nelson, "Terahertz polaritonics," Annu. Rev. Mater. Res. **37**, 317-350 (2007).

46. R. M. Koehl, S. Adachi, and K. A. Nelson, "Direct visualization of collective wavepacket dynamics," J. Phys. Chem. A **103**, 10260-10267 (1999).

47. N. S. Stoyanov, D. W. Ward, T. Feurer, and K. A. Nelson, "Direct visualization of phonon-polariton focusing and amplitude enhancement," J. Chem. Phys. **117**, 2897-2901 (2002).

48. N. S. Stoyanov, D. W. Ward, T. Feurer, and K. A. Nelson, "Terahertz polariton propagation in patterned materials," Nat. Mater. **1**, 95-98 (2002).

49. N. S. Stoyanov, T. Feurer, D. W. Ward, E. R. Statz, and K. A. Nelson, "Direct visualization of a polariton resonator in the THz regime," Opt. Express **12**, 2387-2396 (2004).

50. T. Feurer, J. C. Vaughan, and K. A. Nelson, "Spatiotemporal coherent control of lattice vibrational waves," Science **299**, 374-377 (2003).

51. Z. Chen, "Modeling phonon-polariton generation and control in ferroelectronic crystals," in *Department of Physics* (Massachusetts Institute of Technology, 2009).

Chapter 2

Fundamentals of terahertz pulse generation and imaging

This chapter provides the necessary theoretical background on experimental techniques used for (1) THz pulse generation in ZnTe and $LiNbO_3$ crystals, (2) time domain THz waveform sampling in ZnTe and $LiNbO_3$ crystals, (3) Talbot imaging, and (4) imaging of THz pulse generation and propagation in $LiNbO_3$ crystals.

2.1 THz pulses generation

In the past two decades, various techniques for generating broadband coherent terahertz (THz) radiation by excitation of various media with optical femtosecond (fs) laser pulses have been developed [1-8]. Broadband THz pulses can be generated by transient photocarriers in photoconductive antennas [5], by optical rectification of optical femtosecond pulses in nonlinear optical crystals [6], or by laser-induced gas plasma [8]. In this thesis, we mainly focus on THz pulses that are generated in ZnTe and $LiNbO_3$ crystals by optical rectification, as discussed in the following section.

2.1.1 Optical rectification

Optical rectification (OR) is a second-order nonlinear optical effect in which a quasi-DC polarization is generated in a nonlinear optical medium by intense light.

It was first demonstrated in 1962 in KDP crystals with 100 ns ruby laser pulses by Bass *et al* [9]. Far-infrared radiation was first generated by OR of 5 ps mode-locked Nd:glass laser pulses in LiNbO$_3$ crystals in 1971 [10]. Generation of THz pulses with bandwidths of 1 THz by OR of 50 fs colliding-pulse mode-locked dye laser pulses in LiTaO$_3$ crystals was demonstrated in 1990 [6].

The quasi-DC polarization due to the OR effect can be described as [11]

$$P^{(2)}(\Delta\omega) = \chi^{(2)}E(\omega + \Delta\omega) * E(\omega) \qquad (2.1)$$

where $P^{(2)}(\Delta\omega)$ is the quasi-DC polarization component, $\chi^{(2)}$ is the second-order electric susceptibility of the medium, $E(\omega + \Delta\omega)$ and $E(\omega)$ are the electric fields of different optical frequency components. According to Equation 2.1, the quasi-DC polarization is determined by the second-order electric susceptibility and the pump beam intensity. For broadband THz pulse generation, the OR of femtosecond laser pulses [6, 12-14][6, 12-14]in various nonlinear crystals such as ZnTe, LiNbO$_3$, LiTaO$_3$, and GaAs is used [6, 12, 13, 15].

2.1.2 THz pulses generation in ZnTe crystals

Because the phase-matching condition is satisfied when pumped by 800 nm femtosecond pulses [13], ZnTe crystal is one of the most popular nonlinear crystals used for coherent THz pulse generation. It has cubic crystal structure and a band gap of 2.25 eV. Its second-order electric susceptibility tensor is [16]

$$2\varepsilon_0 \begin{pmatrix} 0 & 0 & 0 & d_{14} & 0 & 0 \\ 0 & 0 & 0 & 0 & d_{14} & 0 \\ 0 & 0 & 0 & 0 & 0 & d_{14} \end{pmatrix} \qquad (2.2)$$

where ε_0 is the permittivity of free space. The second-order polarization induced

by the optical pump pulse is given by [16]

$$
\begin{pmatrix} P_x^{(2)} \\ P_y^{(2)} \\ P_z^{(2)} \end{pmatrix} = 2\varepsilon_0 d_{14} \begin{pmatrix} 0 & 0 & 0 & 1 & 0 & 0 \\ 0 & 0 & 0 & 0 & 1 & 0 \\ 0 & 0 & 0 & 0 & 0 & 1 \end{pmatrix} \begin{pmatrix} E_x^2 \\ E_y^2 \\ E_z^2 \\ 2E_y E_z \\ 2E_z E_x \\ 2E_x E_y \end{pmatrix} \qquad (2.3)
$$

where $P_x^{(2)}, P_y^{(2)}, P_z^{(2)}$ are the components of the second-order polarization along the x, y, and z directions in the crystal, and E_x, E_y, and E_z are the electric field components of the optical pump pulse.
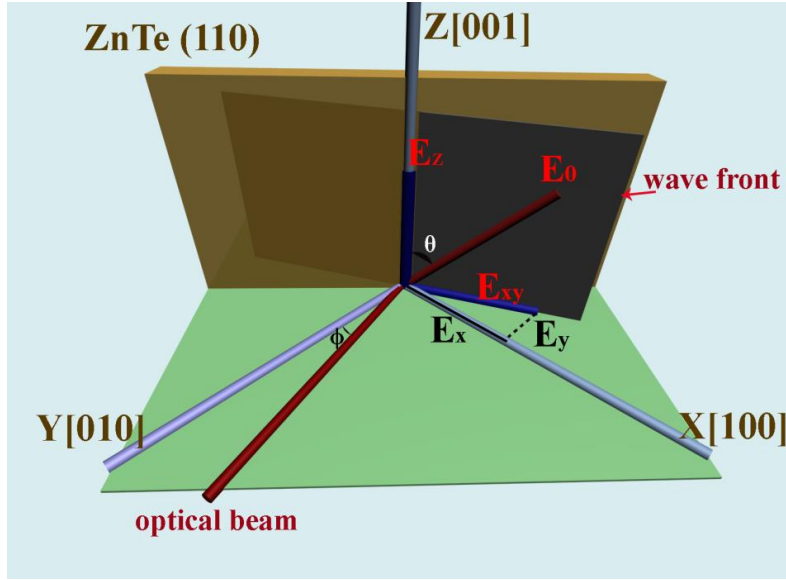
Figure 2.1: Illustration of the THz pulse generation in ZnTe (110) crystals. The optical pump pulse propagation direction is perpendicular to the z axis ([001]) of the crystal, the azimuthal angle relative to the y axis ([010]) is ϕ, and the angle between the optical pump polarization and the z axis is θ.

As illustrated in Figure 2.1, the optical pump pulse propagates perpendicularly

to the z axis of the ZnTe (001) crystal. The angle between the y axis and the optical pump pulse propagation direction is ϕ, and the angle between the optical pump pulse polarization and the z axis is θ.

The x, y, and z electric field components of the optical pump pulse are

$$E_x = E_{xy}cos\phi = E_0 sin\theta cos\phi$$
$$E_y = -E_{xy}sin\phi = -E_0 sin\theta cos\phi \quad (2.4)$$
$$E_z = E_0 cos\theta$$

From Equations 2.3 and 2.4, the second-order polarization is

$$\begin{pmatrix} P_x^{(2)} \\ P_y^{(2)} \\ P_z^{(2)} \end{pmatrix} = 4\varepsilon_0 d_{14} E_0^2 \sin\theta \begin{pmatrix} -\sin\phi\cos\theta \\ \cos\phi\cos\theta \\ -\sin\theta\sin\phi\cos\phi \end{pmatrix} . \quad (2.5)$$

The intensity of the generated THz radiation can be expressed as [16]

$$I_{THz} \propto |P^{(2)}|^2 = 4\varepsilon_0^2 d^2_{14} E_0^4 \sin^2\theta(4\cos^2\theta + \sin^2\theta\sin^2(2\phi)) \quad (2.6)$$

Based on Equation 2.6, the THz pulse is generated more efficiently if the optical pump beam is incident normally with respect to the crystal ($\phi = 45°$). In this case, Equation 2.6 becomes

$$I_{THz} \propto |P^2| = 4\varepsilon_0^2 d_{14}^2 E_0^4 sin^2\theta(4cos^2\theta + sin^2\theta) = 4\varepsilon_0^2 d_{14}^2 E_0^4 sin^2\theta(3 - sin^2\theta)$$
$$(2.7)$$

The dependence of the THz radiation intensity on the angle θ is plotted in Figure

2.2. It shows that the maximum THz generation efficiency is achieved when the angle θ is 54.7 °or 125.3 °.
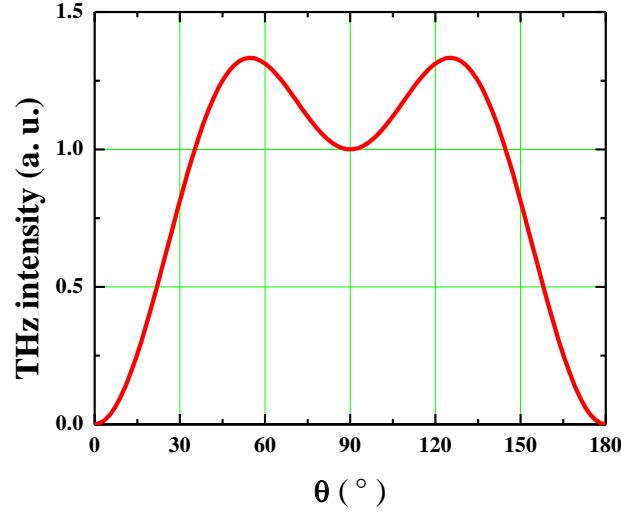
Figure 2.2: The dependence of the THz pulse intensity on θ, the angle between the optical pump polarization direction and the z axis in the ZnTe crystal.

Furthermore, for efficient THz generation, the phase-matching condition must be satisfied. The phase matching condition for the THz wave generation via difference frequency mixing is described by the following formula [3]:

$$k(\omega_{opt} + \Omega) - k(\omega_{opt}) = k(\Omega) \qquad (2.8)$$

where k is the wave vector, ω_{opt} is the angular frequency of the optical pump beam, and Ω is one particular frequency of the generated THz wave. Equation 2.8 can be written as [3]:

$$\frac{k(\Omega)}{\Omega} = \left[\frac{\partial k}{\partial \omega}\right]_{opt} \qquad (2.9)$$

which states that if the phase velocity ($\frac{\Omega}{k(\Omega)}$) of the THz wave is equal to the group velocity ($\left[\frac{\partial \omega}{\partial k}\right]_{opt}$) of the optical pump pulse, a perfect phase matching condition is satisfied, and the generated THz wave can be built up over long path lengths. On the other hand, if the THz phase velocity and optical pump pulse group velocities don't match, the coherence length, within which the THz can be built up, is described by [13, 17]

$$l_c = \frac{c}{2f\left|n_{THz} - n_g\right|} \tag{2.10}$$

where c is the speed of the light in vacuum medium, f is the frequency of the generated THz pulse, n_{THz} is the refractive index of the THz pulse in the crystal, and n_g is the optical beam group refractive index. For ZnTe crystals, the coherence length of the generated THz pulse is the longest when the central wavelength of the optical pump pulse is 800 nm [13].

2.1.3 THz pulses generation in LiNbO₃ crystals

Due to its many unique nonlinear optical, ferroelectric, piezoelectric, photoelastic and other properties, LiNbO₃ is widely used as an electro-optic material. LiNbO₃ has trigonal crystal structure, and its second-order susceptibility is given by [16]

$$2\varepsilon_0 \begin{pmatrix} 0 & 0 & 0 & 0 & d_{15} & -d_{22} \\ -d_{22} & d_{22} & 0 & d_{15} & 0 & 0 \\ d_{15} & d_{15} & d_{33} & 0 & 0 & 0 \end{pmatrix} \tag{2.11}$$

The second-order polarization induced by the optical pump pulse is then expressed as

$$
\begin{pmatrix} P_x^{(2)} \\ P_y^{(2)} \\ P_z^{(2)} \end{pmatrix} = 2\varepsilon_0 \begin{pmatrix} 0 & 0 & 0 & 0 & d_{15} & -d_{22} \\ -d_{22} & d_{22} & 0 & d_{15} & 0 & 0 \\ d_{15} & d_{15} & d_{33} & 0 & 0 & 0 \end{pmatrix} \begin{pmatrix} E_x^2 \\ E_y^2 \\ E_z^2 \\ 2E_y E_z \\ 2E_z E_x \\ 2E_x E_y \end{pmatrix} \qquad (2.12)
$$

where $P_x^{(2)}$, $P_y^{(2)}$, $P_z^{(2)}$ are the polarization components in the x, y, and z directions, and E_x, E_y, and E_z are the three electric field components of the optical pump pulse. If the optical pump beam is incident parallel to the x axis, the electric field of the optical pump pulse is

$$
\vec{E} = E(0, sin\theta, cos\theta) \qquad (2.13)
$$

where θ is the angle between the optical pump pulse polarization and the optic axis (z axis, also called c-axis) of the crystal, E is the electric field amplitude of the optical pump pulse. From Equations 2.12 and 2.13, the second-order nonlinear polarization becomes

$$
\vec{P}^{(2)} = \begin{pmatrix} P_x^{(2)} \\ P_y^{(2)} \\ P_z^{(2)} \end{pmatrix} = 2\varepsilon_0 E^2 \begin{pmatrix} 0 \\ d_{22} \sin^2\theta + 2d_{15} \sin\theta\cos\theta \\ d_{15} \sin^2\theta + d_{33} \cos^2\theta \end{pmatrix} \qquad (2.14)
$$

.

According to Ref. [18], $d_{15} = -4.7\,pm/V$, $d_{33} = -27\,pm/V$, $d_{22} = 3.2\,pm/V$. The second-order polarization is the highest when the optical pump polarization is parallel to the z axis (c-axis) ($\theta=0$ °). When the optical pump pulse

polarization is perpendicular to the z axis, the THz polarization is the smallest but non-zero.
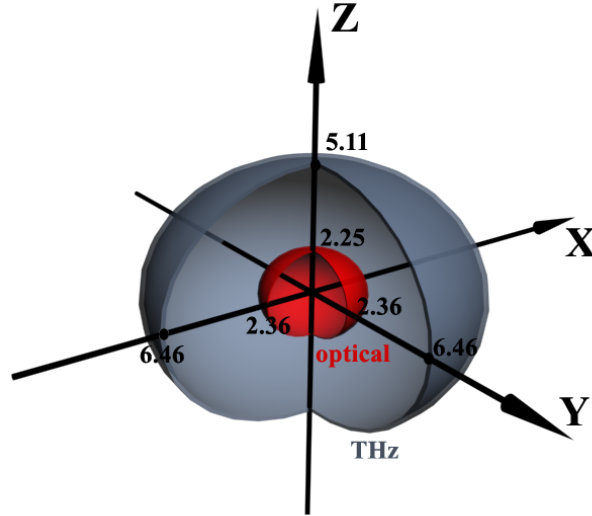
Figure 2.3: Index ellipsoid of the optical pulse (800 nm) and THz pulses (0.5 THz) in a LiNbO$_3$ crystal. The optics axis (c-axis) is along the z axis.

As shown in Figure 2.3, compared to the 800 nm optical pump pulse (n_{opt} = 2.25, for pulse polarization parallel to the z axis), the generated THz pulse experiences a much higher refractive index (n_{THz} = 5.11, for THz pulse polarization parallel to the z axis) [19]. Because the optical pump pulse propagates much faster than the THz pulse, as illustrated in Figure 2.4(a), if the pump beam size is smaller than the center wavelength of the rectified THz radiation, a THz Cherenkov cone is formed [19, 20]. The 3D structure of the THz Cherenkov cone is illustrated in Figure 2.4(b). Due to the lack of the phase matching, a large pump beam generates very low THz radiation in LiNbO$_3$. Interest about the THz generation efficiency on the pump beams size in nonlinear optical crystals is directed to Ref. [21, 22].

The polarization of the THz electric field depends on the optical pump polarization. When the polarization of the optical pump pulse is parallel to the

c-axis, the induced second-order polarization has only a *z* component.

The distribution of the THz electric field on the Cherenkov cone surface is shown in Figure 2.5, where the electric field is the strongest at the cone tip. Figure 2.5(c) and (d) illustrate two special cases: in Figure 2.5(c), the THz pulse propagation vector is in the XY plane, the THz electric field is parallel to the *c*-axis, and refractive index at 0.5 THz is 5.11; in Figure 2.5(d), the THz pulse propagates in the XZ plane, but the THz electric field is parallel to the THz wavefront, and the refractive index is in this case 6.22. Detailed calculation of the THz electric field on the Cherenkov cone is described in Appendix E.
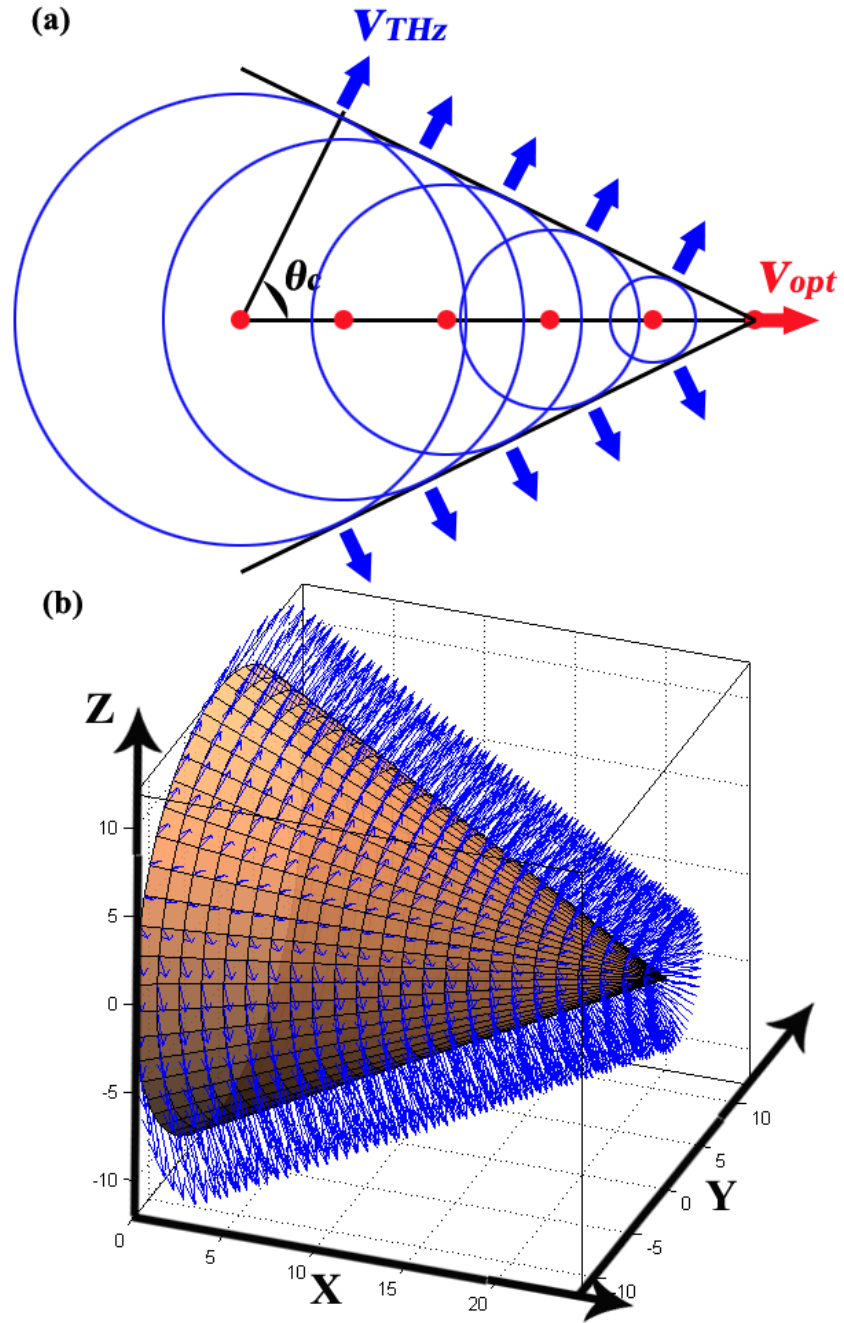
Figure 2.4: Illustration of the THz Cherenkov cone in 2D (a) and in 3D (b). The THz propagation direction is marked with blue arrows.

(a) THz radiation cone

(b) THz radiation cone
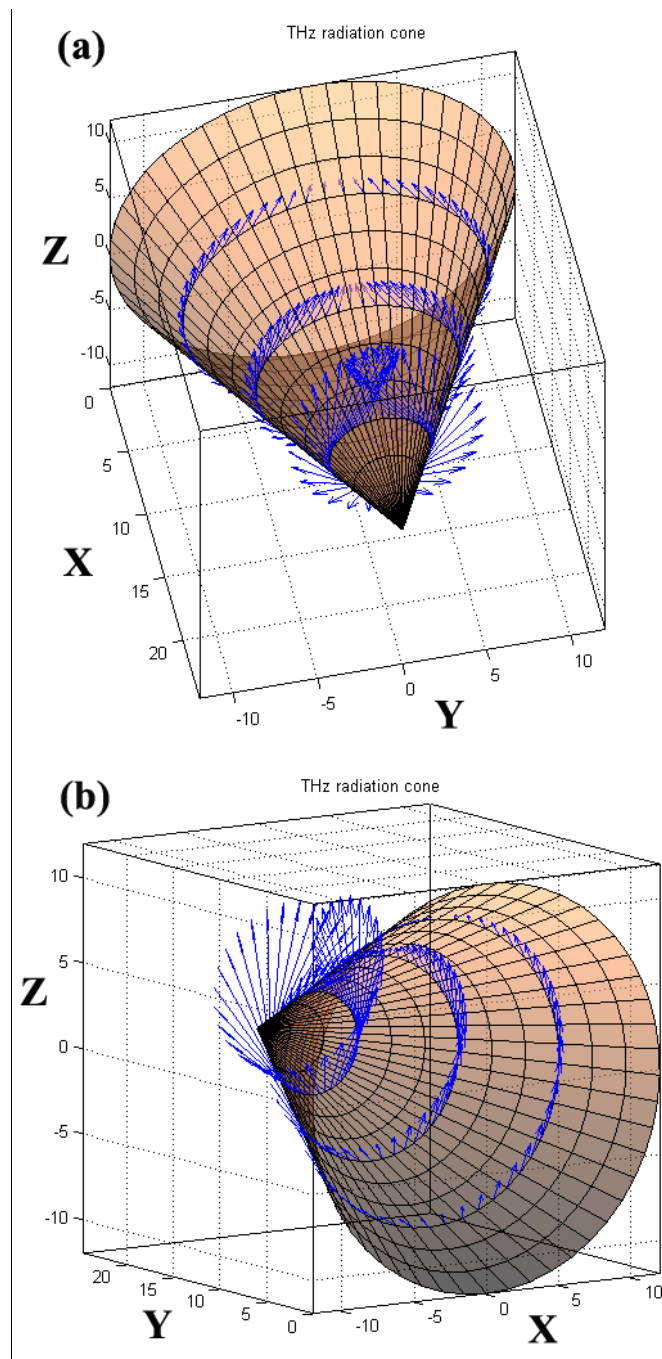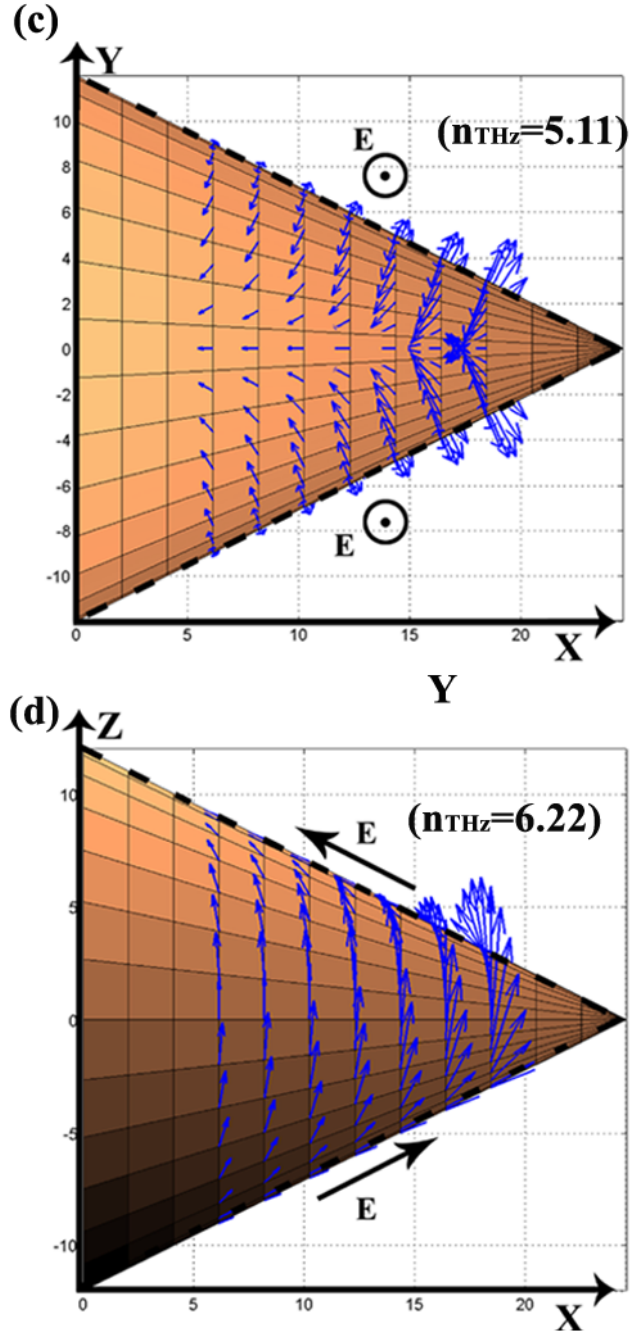
Figure 2.5: (a) and (b), Distribution of the THz electric field on the THz Cherenkov cone in different view angle. (c), (d) Illustration of the THz pulse propagating in the XY plane with polarization in *z* axis (*c*-axis) direction (c) and in the XZ plane with polarization parallel to the THz pulse wavefront (d).

Due to the large difference between the refractive indices experienced by the THz and optical pulses, the collinear phase-matching condition cannot be satisfied, and efficient THz generation in collinear pump geometry cannot be achieved. However, as illustrated in Figure 2.6, the introduction of the tilted-pulse-front excitation technique circumvents this problem and makes $LiNbO_3$ a popular THz source material [15, 23].
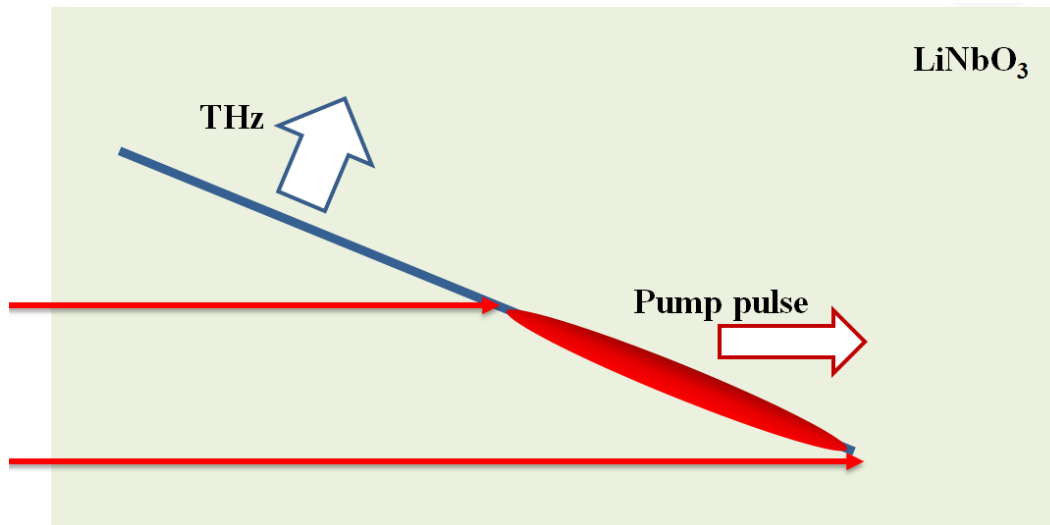
Figure 2.6: Illustration of the THz pulse generated with the tilted-pulse-front excitation technique. The wavefront of the optical pump pulse is tilted so as to be parallel to the THz wavefront.

2.2 THz pulses detection

THz pulse detection techniques can be classified into two categories: (1) detection of the THz intensity, and (2) coherent detection of the THz electric field in the time domain. THz intensity can be detected using various detectors such as bolometers, pyroelectric detectors, and even single photon detectors [24]. For coherent detection of THz pulses, ultrafast laser pulses are employed to sample the THz electric field. The photo-conductive sampling technique and the electro-optic technique are the two main methods to sample the time-domain waveform of the THz pulse. In this thesis, the electro-optic sampling technique is used and is briefly introduced in the following sections.

2.2.1 Pockels effect

The electro-optic sampling technique is based on the Pockels effect in electro-optic (EO) crystals such as ZnTe, $LiNbO_3$, $LiTaO_3$, in which the slowly changing THz electric field modulates the refractive index ellipsoid [11, 16, 17, 20, 25-27]. The refractive index ellipsoid is given by [11]

$$\left(\frac{1}{n^2}\right)_1 x^2 + \left(\frac{1}{n^2}\right)_2 y^2 + \left(\frac{1}{n^2}\right)_3 z^2 + 2\left(\frac{1}{n^2}\right)_4 yz + 2\left(\frac{1}{n^2}\right)_5 xz + 2\left(\frac{1}{n^2}\right)_6 xy = 1 \quad (2.15)$$

In the principal coordinate system, the terms $\left(\frac{1}{n^2}\right)_4$, $\left(\frac{1}{n^2}\right)_5$ and $\left(\frac{1}{n^2}\right)_6$ are zero. $\left(\frac{1}{n^2}\right)_i$ may change in response to an external electric field. For the Pockels effect,

the change $\Delta\left(\dfrac{1}{n^2}\right)_i$ can be described as [11]

$$
\begin{bmatrix}
\Delta\left(\dfrac{1}{n^2}\right)_1 \\[2mm]
\Delta\left(\dfrac{1}{n^2}\right)_2 \\[2mm]
\Delta\left(\dfrac{1}{n^2}\right)_3 \\[2mm]
\Delta\left(\dfrac{1}{n^2}\right)_4 \\[2mm]
\Delta\left(\dfrac{1}{n^2}\right)_5 \\[2mm]
\Delta\left(\dfrac{1}{n^2}\right)_6
\end{bmatrix}
=
\begin{bmatrix}
r_{11} & r_{12} & r_{13} \\
r_{21} & r_{22} & r_{23} \\
r_{31} & r_{32} & r_{33} \\
r_{41} & r_{42} & r_{43} \\
r_{51} & r_{52} & r_{53} \\
r_{61} & r_{62} & r_{63}
\end{bmatrix}
\begin{bmatrix}
E_x \\
E_y \\
E_z
\end{bmatrix}
\qquad (2.16)
$$

where r_{ij} is the electro-optic tensor, E_x, E_y and E_z are the electric field components in the x, y and z direction, respectively. According to Equation 2.16, the external electric field can change both of the refractive index ellipsoid radius and orientation.

(a) Index modulation in ZnTe

For ZnTe crystals, the electric-optic tensor is [16]

$$
\begin{bmatrix}
0 & 0 & 0 \\
0 & 0 & 0 \\
0 & 0 & 0 \\
r_{41} & 0 & 0 \\
0 & r_{41} & 0 \\
0 & 0 & r_{41}
\end{bmatrix}
\qquad (2.17)
$$

and the refractive index ellipsoid is given by [16, 25]

$$\frac{x^2}{n^2} + \frac{y^2}{n^2} + \frac{z^2}{n^2} + 2E_x r_{41} yz + 2E_y r_{41} xz + 2E_z r_{41} xy = 1 \qquad (2.18)$$

Figure 2.7 shows 3 cases of the refractive index ellipsoid in ZnTe (110) crystal. In the absence of an external electric field, the refractive index is the same in the x, y, and z directions, and the index ellipsoid is a sphere (see Figure 2.7(a)). When the electric field is along [001] direction, the refractive index is described by an ellipsoid which orientates in $[1\bar{1}0]$ direction (see Figure 2.7(b)), and when the electric field is applied in $[1\bar{1}0]$, the orientation of the index ellipsoid is 45 °with respect to $[1\bar{1}0]$ direction (Figure 2.7 (c)).
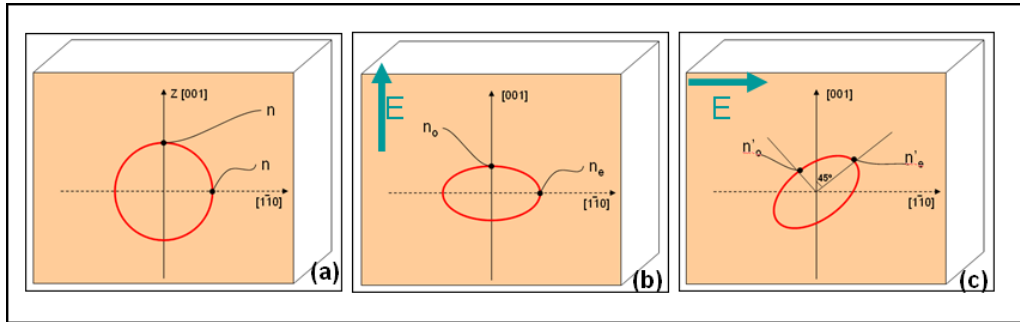
Figure 2.7: Refractive index ellipsoid of a ZnTe (110) crystal with and without an external electric field E. (a) In the absence of an electric field E, the refractive index is isotropic and the index ellipsoid is a sphere. (b) If the electric field is parallel to [001] direction, the index ellipsoid is oriented parallel to $[1\bar{1}0]$. (c) If the electric field is parallel to $[1\bar{1}0]$, the index ellipsoid is tilted by 45 °relative to [110] direction.

The electric field of the THz pulse induces a birefringence in the ZnTe crystal that modulates the optical femtosecond probe pulse. As illustrated in Figure 2.8,

the electric field of the probe pulse can be expressed as a sum of two components, along the fast and slow axis. The phase shift between the two components is

$$\Delta\phi = \phi_1 - \phi_2 = \Delta k L = (k_{y'} - k_{x'})L = 2\pi\frac{L}{\lambda}(n_{y'} - n_{x'}) = 2\pi\Delta n\frac{L}{\lambda} \quad (2.19)$$

where $\Delta n = n_{y'} - n_{x'}$ is the birefringence induced by an external electric field, λ is the wavelength of the optical probe pulse in free space, and L is the thickness of the crystal. According to Equation 2.19, the phase shift is proportional to the THz electric field E.
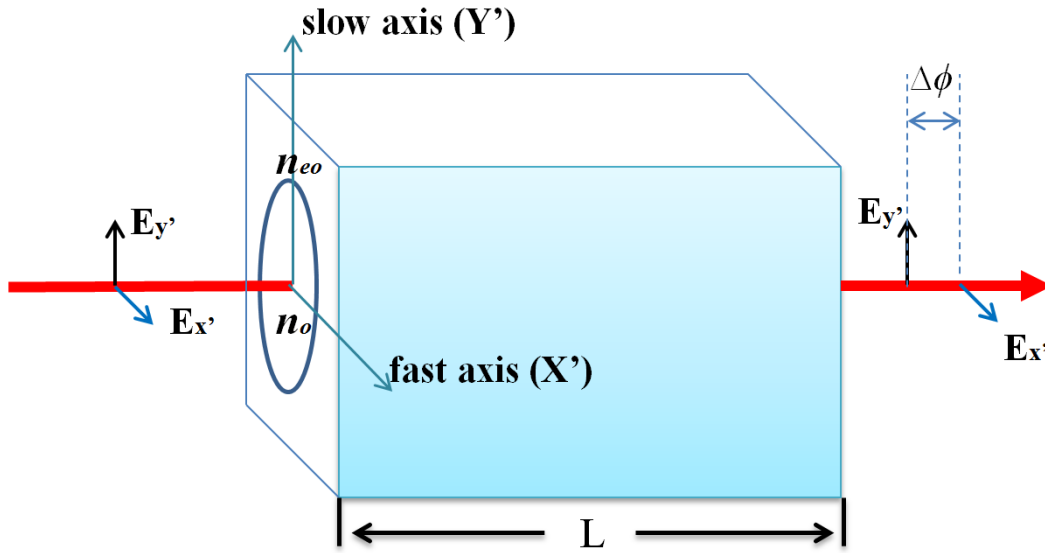
Figure 2.8: Illustration of the phase shift induced by the birefringence. The electric field components in the fast axis and the slow axis propagate at different speeds

(b) Index modulation in LiNbO₃

The electric-optic tensor of LiNbO₃ is [28]

$$
\begin{bmatrix}
0 & -r_{22} & r_{13} \\
0 & r_{22} & r_{13} \\
0 & 0 & r_{33} \\
0 & r_{51} & 0 \\
r_{51} & 0 & 0 \\
-r_{22} & 0 & 0
\end{bmatrix}
, \qquad (2.20)
$$

In the absence of an external electric field the corresponding refractive index ellipsoid is

$$
\frac{x^2}{n_o^{\,2}} + \frac{y^2}{n_o^{\,2}} + \frac{z^2}{n_e^{\,2}} = 1 \qquad (2.21)
$$

As shown in Figure 2.9, if the THz electric field is parallel to the c-axis (z axis), the equation of the index ellipsoid becomes [28]

$$
\left(\frac{1}{n_o^{\,2}} + r_{13}E\right)(x^2 + y^2) + \left(\frac{1}{n_e^{\,2}} + r_{33}E\right)z^2 = 1 \quad (2.22)
$$

Compared to $\dfrac{1}{n_o^{\,2}}$ and $\dfrac{1}{n_e^{\,2}}$, $r_{13}E$ and $r_{33}E$ are small. By using the approximation $(1 + x)^{-1/2} \approx 1 - (1/2)x$, we can write Equation 2.22 as [28]

$$
\frac{x^2 + y^2}{(n_o - \frac{1}{2}n_o^3 r_{13}E)^2} + \frac{z^2}{(n_e - \frac{1}{2}n_e^3 r_{33}E)^2} = 1 \qquad (2.23)
$$

Figure 2.9 also illustrates the index ellipsoid with and without an external THz electric field. The orientation of the ellipsoid doesn't change when the applied THz electric field is parallel to the z axis, and the change of the refractive index is proportional to the THz electric field. If the THz electric field is parallel to the y axis, the index ellipsoid becomes very complex, as both indices (ordinary and extraordinary), as well as the ellipsoid orientation become dependent on the THz electric field.
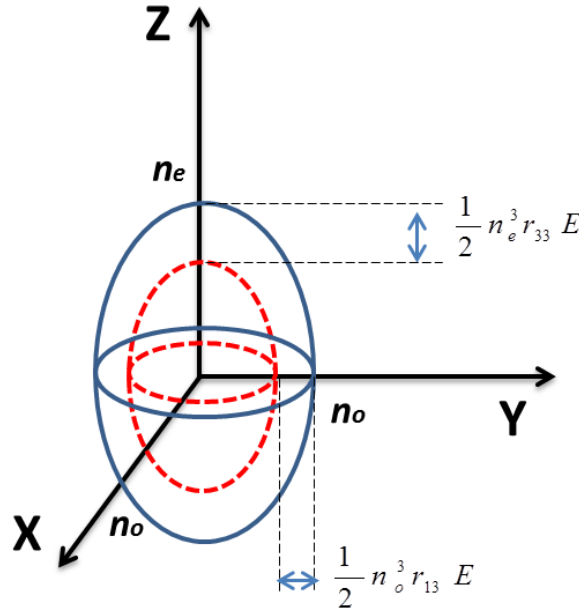
Figure 2.9: The refractive index ellipsoid of LiNbO$_3$ crystals without an electric field (solid line) and with a THz electric field that is parallel to the c-axis (z axis) (dashed line).

In an ultrafast imaging experiment, when a probe beam with large beam cross-section propagates through the crystal, depending on the electric field of the propagating THz pulse they encounter, different parts of the beam experience different phase shifts. These phase shift differences can be used to image the propagating THz pulse by various phase-sensitive imaging techniques such as

phase contrast imaging and Talbot imaging [27, 29]. For example, if the probe pulse polarization is perpendicular to the *c*-axis of the crystal, the difference in phase shift with and without electric field is

$$\Delta\phi = \phi - \phi' = \Delta kL = (k - k')L = 2\pi \frac{L}{\lambda}(n_0 - n_0') \quad (2.24)$$

where n_o and n_o' are the refractive indices with and without an THz electric field, respectively. This phase shift is proportional to the THz electric field and can be converted into the amplitude object, and finally imaged by a CCD camera.

2.2.2 Phase shift sampling techniques

As discussed in section 2.2.1, there are two situations in which the sampling beam experiences the THz electric field-induced phase shift. In the first case, the phase shift is introduced between the two polarization components of the probe beam that are polarized along the fast and the slow axis of the crystal. It can be detected by analyzing the changes in the sampling beam polarization. Depending on the initial polarization of the sampling beam, either the electric field or the square of the electric field of the THz pulse can be detected, and three different detection schemes are possible, as described in the following section (a), (b), and (c). In the second scenario, the wide cross-section sampling beam experiences refractive index that is spatially modulated by the electric field of the propagating THz pulse. The resulting spatially varying phase shift modulation can be converted into intensity object by phase contrast microscopy or Talbot effect, as discussed in Section (d).

(a) Sampling the THz electric field in E^2-mode

As illustrated in Figure 2.10, the THz pulse induced phase modulation of the probe pulse is analyzed by a crossed polarizer. The probe beam intensity after the analyzer is [26, 30].

$$I_{signal} = I_0 \left[\mu + \sin^2 \left(\frac{\phi_0 + \Delta\phi}{2} \right) \right]$$
$$= I_{scattering} + I_0 \sin^2 \left(\frac{\phi_0 + \Delta\phi}{2} \right) \qquad (2.25)$$

where I_0 is the intensity of the optical probe pulse before the polarizer, μ is the scattering coefficient and $I_{scattering} = I_0 \mu$ is the intensity of scattered light from the crystal, $\Delta\phi$ is the phase shift induced by the THz electric field, and ϕ_0 is the bias phase shift induced by the static birefringence of the EO crystal.
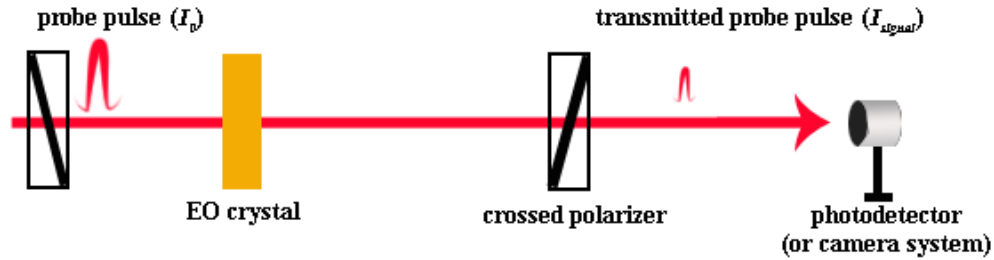
Figure 2.10: Experimental setup for THz waveforms sampling in E^2-mode.

If the initial phase shift ϕ_0 and the static birefringence of ZnTe are zero, and the phase shift due to the THz pulse electric field $\Delta\phi$ is small, Equation 2.25 can be written as

$$I_{signal} = I_{scattering} + I_0 \left(\frac{\Delta\phi}{2} \right)^2 \qquad (2.26)$$

According to Equation 2.26, the difference in the signal with and without a THz electric field is proportional to the square of the THz electric field E. This detection mode is thus called E^2-*mode*.

The advantage of this method is that the low background signal and high signal to noise ratio (SNR) makes the single-shot sampling of the THz pulse possible. On the other hand, however, because only the square of electric field is sampled, part of the THz pulse phase information is lost.

(b) Sampling the THz electric field with a *90°* bias phase shift in *E*-mode

probe pulse (I_p)   quarter wave plate   transmitted probe pulse (I_{signal})

EO crystal   crossed polarizer   photodetector (or camera system)
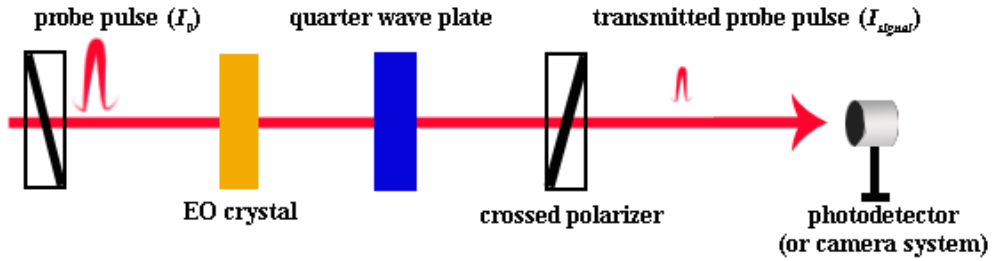
Figure 2.11: Experimental setup for THz waveforms sampling in *E-mode*.

As shown in Figure 2.11, a quarter-wave plate between an EO crystal and a crossed polarizer introduces a phase shift $\phi_0 = 90°$, and Equation 2.25 becomes

$$I_{signal} = I_{scattering} + \frac{I_0}{2}[1 + sin\Delta\phi] \qquad (2.27)$$

Because the THz induced phase shift is small, we can assume $sin\Delta\phi \cong \Delta\phi$, and Equation 2.27 can then be written as

$$I_{signal} = (I_{scattering} + \frac{I_0}{2}) + \frac{I_0}{2}\Delta\phi = I_{background} + \frac{I_0}{2}\Delta\phi \qquad (2.28)$$

where $I_{background}=I_0/2+I_{scattering}$ is the signal collected without the THz modulation. Based on Equation 2.28, the measured THz signal $I_{THzsignal} = I_{signal} - I_{background} = \frac{I_0}{2}\Delta\phi$ is proportional to the THz electric field. This detection mode is thus termed as *E-mode*.

The advantage of the *E-mode* is that it is able to directly obtain the THz electric field waveform without losing the phase information. However, the strong background signal results in a low SNR.

(c) Sampling the THz electric field with a small bias phase shift

In order to sample the THz electric field waveforms with a reasonable SNR, a small initial phase shift ϕ_0 is introduced such that $\sin\phi_0\approx\phi_0$ but $\phi_0>>\Delta\phi$. Equation 2.25 then becomes

$$
\begin{aligned}
I_{signal} &= I_0[\mu+\sin^2(\frac{\phi_0+\Delta\phi}{2})] \\
&\approx I_{scattering} + I_0(\frac{\phi_0+\Delta\phi}{2})^2 \\
&= I_{scattering} + \frac{I_0}{4}(\phi_0^2 + \Delta\phi^2 + 2\phi_0\Delta\phi) \\
&\approx (I_{scattering} + \frac{I_0}{4}\phi_0^2) + \frac{I_0}{2}\phi_0\Delta\phi
\end{aligned}
\tag{2.29}
$$

With the background subtracted, signal is proportional to the phase shift $\Delta\phi$.

With this method, the electric field of the THz pulse can be obtained with a good SNR due to the low background signal. However, care must be taken to ensure that the $1>\phi_0>>\Delta\phi$ is satisfied.

(d) Sampling the phase shift with the Talbot effect

The Talbot effect is named after Henry Fox Talbot, who discovered that a periodic

phase structure can be converted into an amplitude structure at certain distances from the image plane [27, 29, 31, 32].
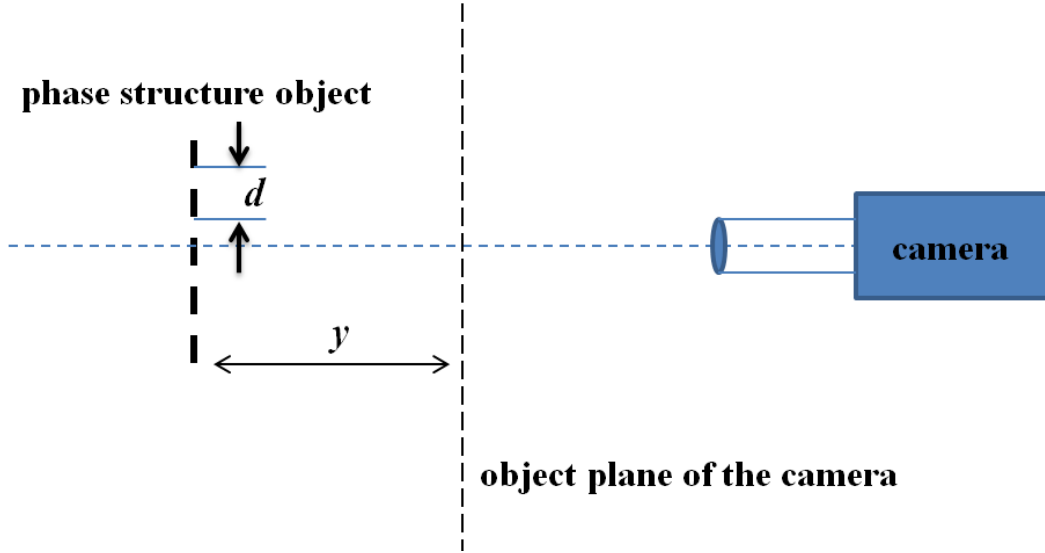
Figure 2.12: Schematic diagram of the Talbot imaging setup. The period of the phase structure object is d, the distance between the phase structure object and the object plane of the camera is y.

As illustrated in Figure 2.12, if the object plane of the camera has a particular displacement y from the phase object, only the periodic phase structure whose wave vector ($k = 2\pi/d$) satisfies [29]

$$k = 2\pi\sqrt{n/2\lambda y} \qquad (2.30)$$

can be converted into an amplitude structure completely, where d is period of the phase structure, λ is the probe beam wavelength in free space, and n is a positive odd integer [27, 29].

For example, the central frequency of the THz pulse generated in LiNbO$_3$ is 0.5 THz [33], which corresponds to a wavelength of 0.12 mm in the crystal. In order to image the THz pulse efficiently in the first order (n=1) with a 400 nm imaging beam, based on Equation 2.30, the displacement of the camera object

plane camera from the THz phase structure should be 18 mm.

In our ultrafast imaging experiments, the nonperiodic phase structure induced by the THz pulse in an EO crystal contains many wave vector components, and each of them is imaged efficiently at specific distance from the camera object plane. Since only the corresponding k component can be imaged effectively, the Talbot imaging technique is not suitable for sampling the whole THz electric field waveform quantitatively [27, 29, 32].

Talbot imaging, which is quite straightforward to set up, is used for ultrafast imaging of the THz Cherenkov wave in $LiNbO_3$ and $LiTaO_3$ crystals.

2.3 Pump-probe imaging geometry
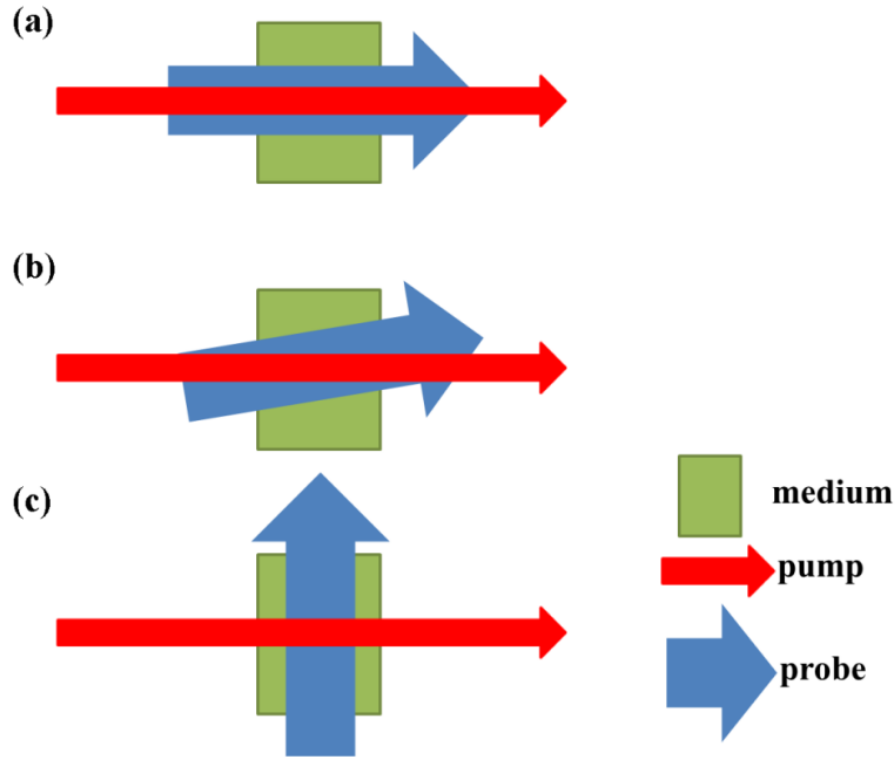
Figure 2.13: Schematic illustration of (a) collinear, (b) near-collinear, (c) transverse imaging geometries.

In this thesis, all of the ultrafast images were acquired using the pump-probe method, in which the pump beam induces the refractive index modulation inside the medium, and an optical probe pulse is sent through the crystal to sample this modulation. By varying the pump-probe time delay, the ultrafast non-linear optical processes induced by the optical pump pulse can be studied.

Depending on the propagation direction of the probe beam relative to the pump beam, imaging can be performed in collinear (Figure 2.13(a)), near-collinear (Figure 2.13(b)), and transverse imaging (Figure 2.13(c)) geometries. In this thesis, the two latter methods are used. The near-collinear

imaging is used for single-shot THz waveform sampling, and is introduced in Chapter 3, and the transverse geometry is used for imaging THz Cherenkov waves in $LiNbO_3$ and $LiTaO_3$, and Kerr signals in various media, respectively.

As shown in Figure 2.13(c), in the transverse imaging geometry the probe pulse propagates perpendicularly to the pump pulse. Unlike the collinear imaging geometry which provides the collinear view of the propagating pump pulse, side or top views are obtained in transverse imaging. As shown in Figure 2.14, this mode, however, suffers from imaging distortions, as discussed in Chapter 4.
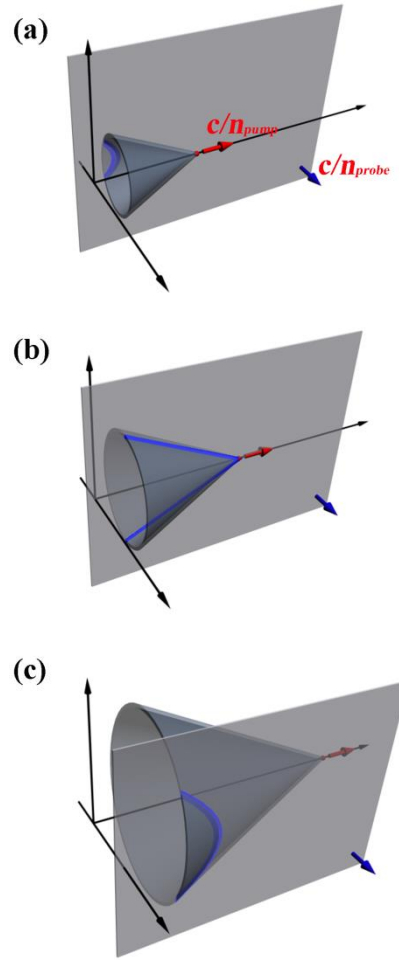
Figure 2.14: Illustration of the transverse imaging of a THz Cherenkov cone. (a), (b), and (c) simulate the imaging process.

References:

1. B. Ferguson, and X.-C. Zhang, "Materials for terahertz science and technology," Nat. Mater. **1**, 26-33 (2002).

2. M. C. Hoffmann, and J. A. Fulop, "Intense ultrashort terahertz pulses: generation and applications," J. Phys. D: Appl. Phys. **44**, 17 (2011).

3. F. Blanchard, G. Sharma, L. Razzari, X. Ropagnol, H. C. Bandulet, F. Vidal, R. Morandotti, J. C. Kieffer, T. Ozaki, H. Tiedje, H. Haugen, M. Reid, and F. Hegmann, "Generation of intense terahertz radiation via optical methods," IEEE J. Sel. Top. Quant. Electron. **17**, 5-16 (2011).

4. M. Tonouchi, "Cutting-edge terahertz technology," Nat. Photonics **1**, 97-105 (2007).

5. D. H. Auston, and P. R. Smith, "Generation and detection of millimeter waves by picosecond photoconductivity," Appl. Phys. Lett. **43**, 631-633 (1983).

6. B. B. Hu, X.-C. Zhang, D. H. Auston, and P. R. Smith, "Free-space radiation from electrooptic crystals," Appl. Phys. Lett. **56**, 506-508 (1990).

7. R. Kohler, A. Tredicucci, F. Beltram, H. E. Beere, E. H. Linfield, A. G. Davies, D. A. Ritchie, R. C. Iotti, and F. Rossi, "Terahertz semiconductor-heterostructure laser," Nature **417**, 156-159 (2002).

8. B. Clough, J. M. Dai, and X.-C. Zhang, "Laser air photonics: beyond the terahertz gap," Mater. Today **15**, 50-58 (2012).

9. M. Bass, J. F. Ward, G. Weinreich, and P. A. Franken, "Optical rectification," Phys. Rev. Lett. **9**, 446 (1962).

10. K. H. Yang, P. L. Richards, and Y. R. Shen, "Generation of far-infrared radiation by picosecond light pulses in LiNbO$_3$," Appl. Phys. Lett. **19**, 320 (1971).

11. R. Boyd, *Nonlinear Optics* (Elsevier, 2008).

12. F. Blanchard, L. Razzari, H. C. Bandulet, G. Sharma, R. Morandotti, J. C. Kieffer, T. Ozaki, M. Reid, H. F. Tiedje, H. K. Haugen, and F. A. Hegmann, "Generation of 1.5 mu J single-cycle terahertz pulses by optical rectification from a large aperture ZnTe crystal," Opt. Express **15**, 13212-13220 (2007).

13. M. Nagai, K. Tanaka, H. Ohtake, T. Bessho, T. Sugiura, T. Hirosumi, and M. Yoshida, "Generation and detection of terahertz radiation by electro-optical process in GaAs using 1.56 mu m fiber laser pulses," Appl. Phys. Lett. **85**, 3974-3976 (2004).

14. G. Chang, C. J. Divin, C.-H. Liu, S. L. Williamson, A. Galvanauskas, and T. B. Norris, "Power scalable compact THz system based on an ultrafast Yb-doped fiber amplifier," Opt. Express **14**, 7909-7913 (2006).

15. J. Hebling, G. Almasi, I. Z. Kozma, and J. Kuhl, "Velocity matching by pulse front tilting for large-area THz-pulse generation," Opt. Express **10**, 1161-1166 (2002).

16. Y.-S. Lee, *Principles of Terahertz Science and Technology* (Springer, 2009).

17. A. Nahata, A. S. Weling, and T. F. Heinz, "A wideband coherent terahertz spectroscopy system using optical rectification and electro-optic sampling," Appl. Phys. Lett. **69**, 2321-2323 (1996).

18. A. Yariv, and P. Yeh, *Optical Waves in Crystals: Propagation and Control of Laser Radiation* (Wiley-Interscience, 2002).

19. T. Feurer, N. S. Stoyanov, D. W. Ward, J. C. Vaughan, E. R. Statz, and K. A. Nelson, "Terahertz polaritonics," Ann. Rev. Mater. Res. **37**, 317-350 (2007).

20. D. H. Auston, K. P. Cheung, J. A. Valdmanis, and D. A. Kleinman, "Cherenkov radiation from femtosecond optical pulses in electro-optic media," Phy. Rev. Lett. **53**, 1555-1558 (1984).

21. J. Z. Xu, and X.-C. Zhang, "Optical rectification in an area with a diameter comparable to or smaller than the center wavelength of terahertz radiation," Opt. Lett. **27**, 1067-1069 (2002).

22. G. L. Dakovski, B. Kubera, S. Lan, and J. Shan, "Finite pump-beam-size effects in optical pump-terahertz probe spectroscopy," J. Opt. Soc. Am. B **23**, 139-141 (2006).

23. J. Hebling, K.-L. Yeh, M. C. Hoffmann, B. Bartal, and K. A. Nelson, "Generation of high-power terahertz pulses by tilted-pulse-front excitation and their application possibilities," J. Opt. Soc. Am. B **25**, B6-B19 (2008).

24. S. Komiyama, O. Astafiev, V. Antonov, T. Kutsuwa, and H. Hirai, "A single-photon detector in the far-infrared range," Nature **403**, 405-407 (2000).

25. P. C. M. Planken, H. K. Nienhuys, H. J. Bakker, and T. Wenckebach, "Measurement and

calculation of the orientation dependence of terahertz pulse detection in ZnTe," J. Opt. Soc. Am. B **18**, 313-317 (2001).

26. Z. P. Jiang, F. G. Sun, Q. Chen, and X.-C. Zhang, "Electro-optic sampling near zero optical transmission point," Appl. Phys. Lett. **74**, 1191-1193 (1999).

27. P. Peier, S. Pilz, F. Mueller, K. A. Nelson, and T. Feurer, "Analysis of phase contrast imaging of terahertz phonon-polaritons," J. Opt. Soc. Am. B **25**, B70-B75 (2008).

28. B. E. A. Saleh, and M. C. Teich, *Fundamentals of Photonics* (Wiley-Interscience, 2007).

29. C. A. Werley, Q. Wu, K.-H. Lin, C. R. Tait, A. Dorn, and K. A. Nelson, "Comparison of phase-sensitive imaging techniques for studying terahertz waves in structured LiNbO$_3$," J. Opt. Soc. Am. B **27**, 2350-2359 (2010).

30. A. D. Slepkov, "Third-order nonlinearities of novel iso-polydiacetylenes studied by a differential optical kerr effect detection technique," in *Department of Physics* (University of Alberta, 2002).

31. F. Talbot, "Fact relating to optical science no. IV," Philos. Mag. **9**, 401-407 (1836).

32. Q. Wu, C. A. Werley, K.-H. Lin, A. Dorn, M. G. Bawendi, and K. A. Nelson, "Quantitative phase contrast imaging of THz electric fields in a dielectric waveguide," Opt. Express **17**, 9219-9225 (2009).

33. K. L. Yeh, M. C. Hoffmann, J. Hebling, and K. A. Nelson, "Generation of 10 μJ ultrashort terahertz pulses by optical rectification," Appl. Phys. Lett. **90**, 171121 (2007).

Chapter 3

Single-shot terahertz time domain spectroscopy with noncollinear imaging technique

We demonstrate single-shot time-resolved terahertz (THz) spectroscopy of photoexcited GaAs using noncollinear electro-optic imaging of THz pulses. Imaging modes with THz waveform signals proportional to the amplitude (E-mode) and to the square (E^2-mode) of the THz electric field are explored. We find that E-mode THz pulse imaging requires multi-shot averaging, but provides real and imaginary components of the transient THz conductivity in photoexcited GaAs that agrees well with the Drude model. Conversely, E^2-mode imaging allows true single-shot transmitted THz power spectra to be obtained that are consistent with the Drude response observed in the multi-shot E-mode measurements.

3.1 Terahertz pulse waveform sampling in single shot

3.1.1 Development of the terahertz pulse waveform single-shot sampling technique

Potential applications for terahertz (THz) radiation have attracted much interest due to its unique capabilities [1]. Traditional detection methods use a series of femtosecond (fs) optical pulses to map the temporal profile of the THz waveform point-by-point by scanning the optical pulse-THz pulse delay [1, 2]. Coupled with balanced detection through a lock-in amplifier, this technique is widely used for THz spectroscopy of materials. However, this method is generally time consuming, and repetitive sampling severely limits exploration of irreversible phenomena such as material damage and chaotic dynamics. It is therefore necessary to develop single-shot THz techniques.

Several methods for measuring a complete THz waveform in a single shot have been proposed in the past 15 years [3-15]. The first approach uses spectral-encoding, where the temporal profile of the THz pulse is transcribed onto the frequency spectrum of a linearly-chirped optical probe pulse [3-6]. A second scheme suggested by Shan *et al.* [7] encodes the THz waveform onto the transverse spatial profile of the optical probe beam that propagates noncollinearly with the THz pulse [7, 8]. Other methods include encoding the THz waveform on a tilted [9-11] or incrementally delayed [12] wavefront of a fs optical pulse which propagates collinearly with the THz pulse, as well as cross-correlation techniques [13, 14] .

For all the methods mentioned above, the spectral coding single-shot imaging technique is the most developed and has been used to do some single-shot THz diagnostics. For example, the demonstration of single-shot THz electric field waveform acquisition has been done using the spectral-encoding technique but with averaging so as to have a reasonable signal to noise ratio (SNR) [15]. Kim *et al.* [5] used this method to measure single-shot THz pulse reflectivity of

laser-generated plasmas from aluminum targets, but averaging over 20 shots was required to show the Drude-like response of the plasma. More recently, the tilted wavefront optical pulse technique was also used to demonstrate single-shot THz spectroscopy [11].

Compared with the spectra-encoding scheme and the tilted wavefront optical pulse technique, noncollinear imaging method is much easier to realize, and can also provide spatiotemporal information [8]. But no one has used such a method to perform true THz single-shot spectroscopy analysis.

In this chapter, our main goal is to prove that the noncollinear imaging technique can be used to get the true single-shot, square of the THz electric field waveforms and that the obtained single-shot waveforms are useful for THz spectroscopic analysis. Photoexcited GaAs is chosen as a sample to test true single-shot THz spectroscopic approach.

3.1.2 Sampling THz pulses with noncollinear imaging

Figure 3.1 shows how the temporal information of the THz pulse waveform in the ZnTe detection crystal is encoded onto the transverse spatial profile of the optical imaging beam [7]. Since the intersection between the optical pulse and THz pulse occurs within the electro-optic (EO) detection crystal ZnTe, different points across the transverse profile of the optical imaging beam experience the THz electric field at different instances in time.

 Because of the THz electric field induced birefringence inside the ZnTe crystal, if the probe pulse goes through the crystal with the linear polarization 45 ° with respect to the fast axis, the polarization state of the probe pulse will be changed, and the phase shift can be recorded on the optical probe pulse wavefront. Because the phase modulation is proportional to the THz electric field, we can sample the THz time domain electric field waveform by measuring the phase modulation of the probe pulse. Using various methods such as *E-mode*, or *E²-mode*, the THz time domain waveform can be finally sampled.
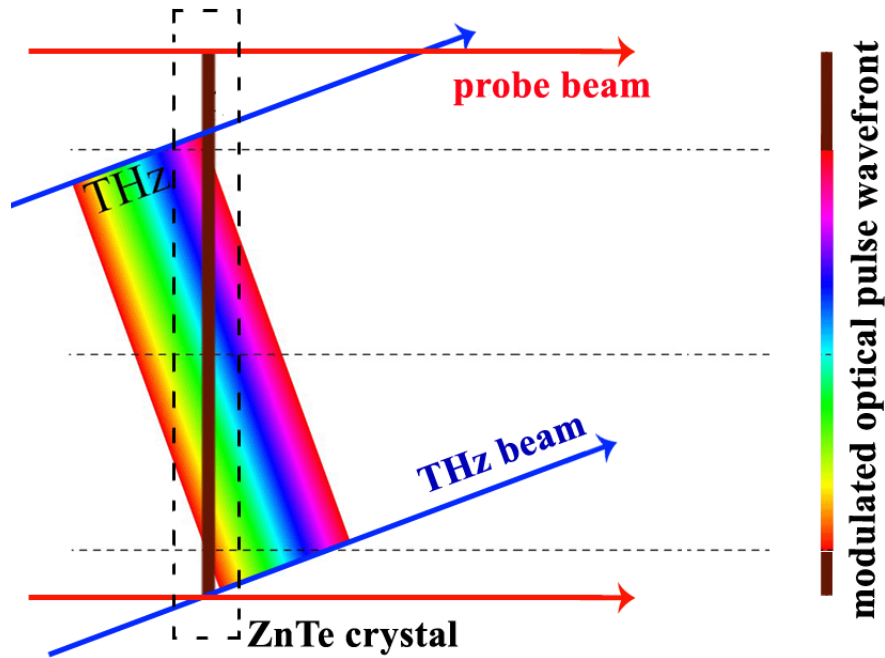
Figure 3.1: Illustration of sampling THz pulses with the noncollinear imaging technique. The optical probe pulse and THz pulse propagate noncollinearly through a ZnTe crystal.

3.2 Experiment

3.2.1 Experimental setup

Figure 3.2: Schematic of the experimental setup. 1: low power imaging beam; 2: medium power optical pump beam; 3: high power beam for THz pulse generation; 4: THz beam; ZnTe: zinc telluride crystal; BP: black polyethylene; PM: parabolic mirror; L: lens; GaAs: gallium arsenide sample; P1: polarizer; P2: analyzer; λ/4: quarter-wave plate (inserted for E-mode, removed for E^2-mode); DDG: Digital delay generator (Stanford Research System, DG 645); ICCD: intensified CCD camera with relay lens for imaging the THz waveform in the ZnTe detection crystal. For multi-shot, the gate of the ICCD camera system is trigged directly by a laser trigger and opens when every optical probe pulse comes in. While for single shot, A DDG is connected between the laser trigger and the ICCD gate. It is used to open the ICCD camera gate just one time, and the CCD only integrates one optical probe pulse. The inset shows the THz detection principle.

Figure 3.2 shows a schematic of the experimental setup. An amplified Ti: sapphire laser source that provides 800 nm, 100 fs, 0.9 mJ pulses at a 1 kHz repetition rate was divided into three beams: (1) a low power beam for imaging the THz pulse waveform by free-space EO sampling in a 0.5 mm-thick (110) ZnTe detection crystal (Nikko Materials), (2) a medium power beam for

photoexciting a 0.5 mm-thick SI GaAs sample, and (3) a high power beam for generating THz pulses by optical rectification in a 2 mm-thick [110] ZnTe crystal. The THz pulse was focused by an off axis parabolic mirror through the GaAs wafer to a spot size diameter of about 3 mm on the ZnTe detection crystal. The optical pump fluence at the GaAs was 4.4 $\mu J/cm^2$ (the photoexited GaAs is detected by THz pulses after 5 ps photoexcitation), and the spot diameters on the GaAs for the optical pump beam and THz probe beam were 17 and 5 mm, respectively. After passing through a polarizer, the low power optical beam passes through the ZnTe EO detection crystal at normal incidence, while the THz pulse enters the crystal noncollinearly at an incident angle of 20°. The optical beam then goes through a crossed analyzer, and the THz waveform in the ZnTe detection crystal is imaged through a relay lens by an intensified CCD camera system (PicoStar HR ICCD, see Appendix A) with a 500 ps gate width. The gate of the ICCD camera system is triggered by the laser trigger, which is delayed by the ICCD camera system so that the gate opens only when the probe pulse reaches the gate. For the multi-shot imaging, the exposure time is set to 400 ms and every frame is exposed to 400 optical pulses. On the other hand, for single-shot imaging, an additional digital delay generator (DDG) is connected between the laser trigger and the ICCD camera system. The single-shot function of the DDG enables the ICCD camera gate to open only one time (gate width 500 ps) no matter how many laser trigger signals the DDG receives.

We adopt two imaging modes referred to here as "E-mode" and "E^2-mode" THz imaging. As discussed in Section 2.2.2, in E-mode THz imaging, a quarter-wave ($\lambda/4$) plate with the fast axis at 45° to P1 is inserted just after the ZnTe detection crystal (between the crossed polarizers P1 and P2). (We note that the static birefringence in our ZnTe EO detection crystal is extremely low. The estimated ratio between the static birefringence and the birefringence induced by the THz electric field is lower than 2%.) Removing the $\lambda/4$ plate enables us to measure the THz intensity waveform in E^2-mode.

3.2.2 Sample imaging of THz waveforms

(a) Imaging THz waveforms in *E-mode*
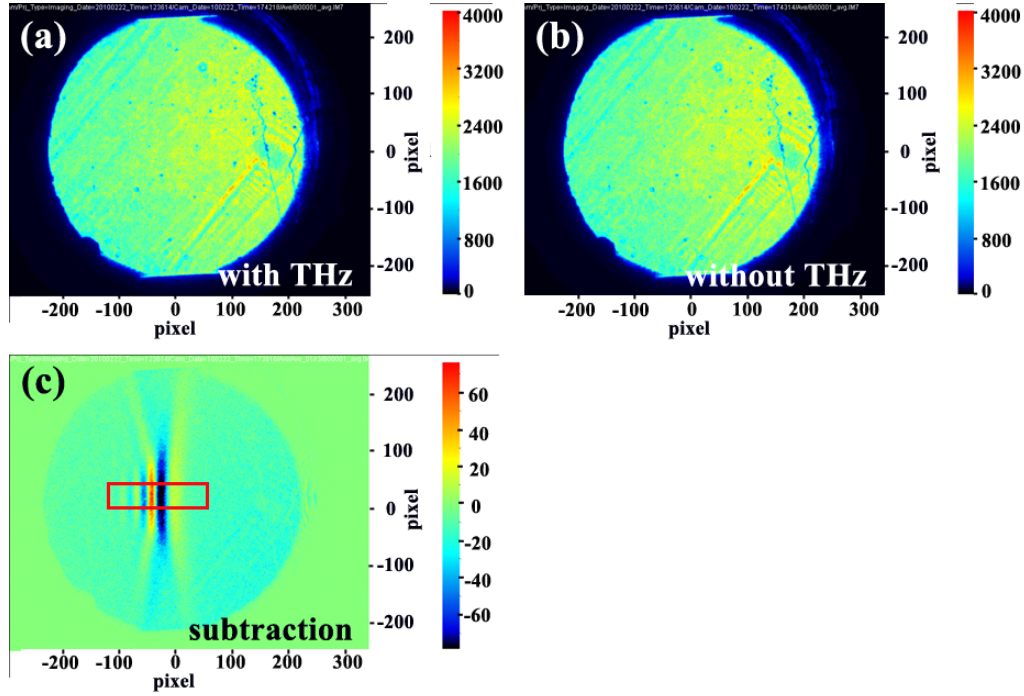
Figure 3.3: Sample imaging of the THz electric field waveform in *E-mode* in multi-shot. (a) Signal image captured with a THz modulation. (b) Background image taken without a THz modulation. (c) Background-subtracted image. The solid red rectangle defines the area for the THz waveform sampling.

For *E-mode*, a λ/4 plate is inserted between the ZnTe crystal and the crossed polarizer P2 and the sample images are shown in Figure 3.3. Figure 3.3(a) is the image taken at the presence of the THz pulse, and Figure 3.3(b) is the background image taken in the absence of the THz pulse. In order to remove the high level of noise associated with the strong background intensity, the image in Figure 3.3(a) and (b) are averaged over 100 frames (40,000 shots in total). We note that we also tried 50 frames and 400 frames, and found that 100 frames provided an adequate SNR with a reasonable data collection time (40 s). Figure 3.3(c) shows the

subtraction result between Figure 3.3(a) and (b). The temporal profiles of the THz waveforms are extracted from Figure 3.3(c) by binning over 50 pixels (~ 1 mm) in the vertical direction, as defined in the red rectangle in Figure 3.3(c).

(b) Imaging THz waveforms in E^2-mode
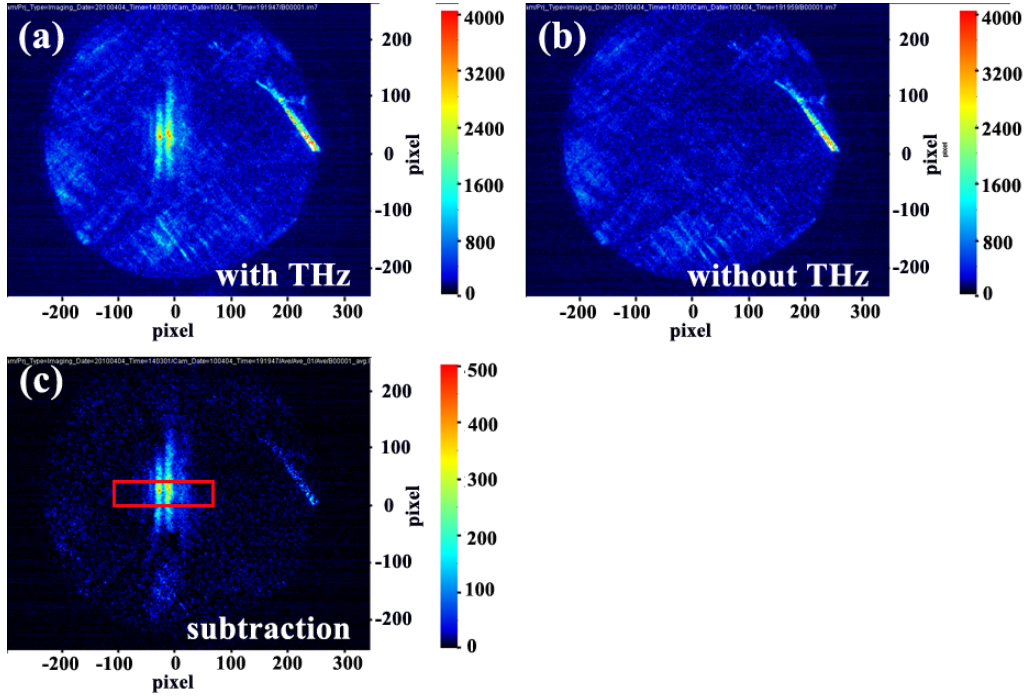
Figure 3.4: Sample imaging of the square of the THz electric field waveform in E^2-mode in single shot. (a) Imaging with a THz modulation. (b) Imaging without a THz modulation. (c) Background-subtracted image. The solid red rectangle defines the window used for THz waveform sampling. The scale bar is in the unit of counts.

Sample imaging in E^2-mode is shown in Figure 3.4. Because there is no $\lambda/4$ plate in E^2-mode, the transmitted optical pulse intensity through the crossed polarizer is very low. Figure 3.4(a) and (b) show the result obtained in single shot with and without a THz pulse modulation, respectively. Figure 3.4(b) shows a background image which has a low intensity. The THz waveform is easy to recognize against the low background light. Figure 3.4(c) is the subtraction between Figure 3.4(a) and (b).

In order to compare the SNR between *E-mode* and E^2*-mode*, we obtained THz waveforms in both modes. Figure 3.5(a) shows the THz waveforms obtained in *E-mode*. The bold line (red line) is the waveform obtained with multi-shot (40,000), and the thin line (black line) is the waveform obtained in single-shot. We find that the SNR=2 in single shot is too low to be used for THz spectroscopy. Figure 3.5(b) shows the square of the THz electric field waveforms taken in E^2-*mode* with single shot and the SNR=41 appears to be very good. We note that the SNR is calculated by dividing the signal peak with the standard deviation.
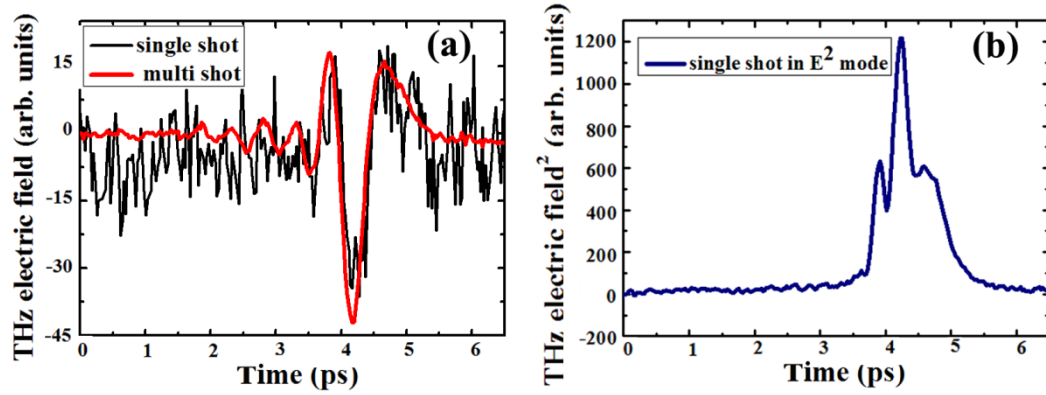
Figure 3.5: (a) THz electric field waveforms taken in *E-mode* with single shot and multi-shot (400,000). (b) Waveform of the square of the THz electric field in E^2-*mode* in single shot.

(c) Time scale calibration

The time scale of the image is calibrated by changing the time delay between the THz pulse and optical imaging pulse. For instance, Figure 3.6 shows the images taken in E^2-*mode*, and we find that the peak of the THz waveform shifts when the time delay is changed. We note that 0.15 mm delay stage displacement results in a 1 ps time delay. By plotting the THz pulse peak position with the optical delay stage position (Figure 3.7), the time scale can be found.
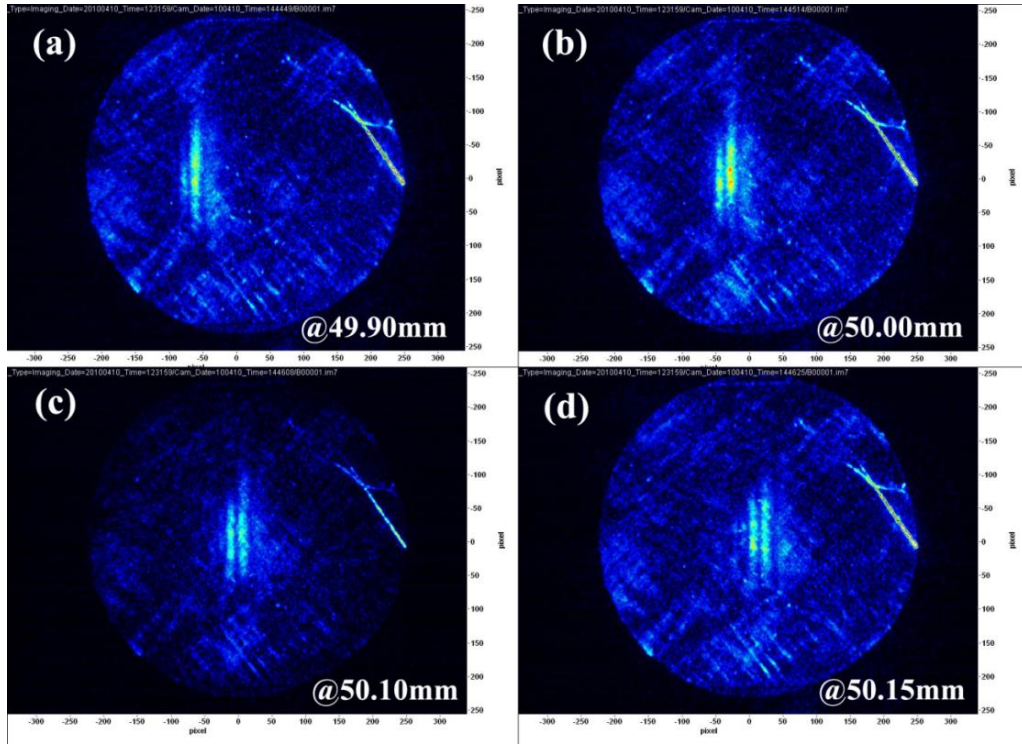
Figure 3.6: Images of the THz waveform at different time delays. The images are taken at delay stage positions of (a) 49.90 mm, (b) 50.00 mm, (c) 50.10 mm, and (d) 50.15 mm.

10
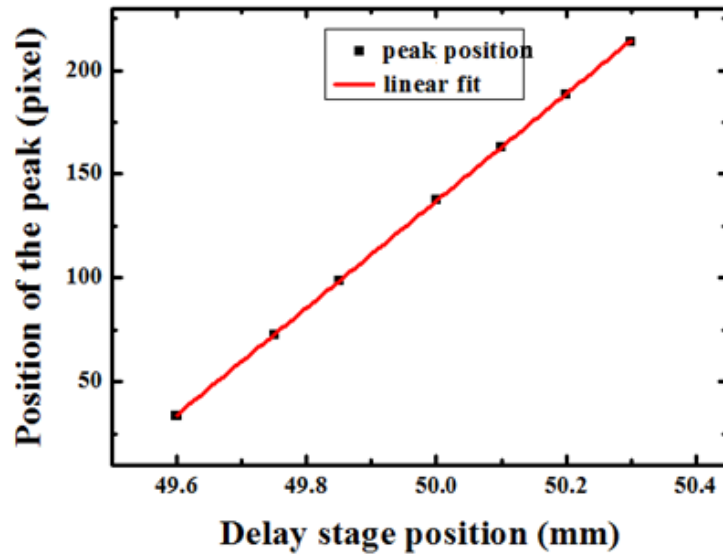
Figure 3.7: The change of the peak position with the delay stage position.

3.3 Experimental results and discussions

3.3.1 THz spectroscopy based on THz electric field waveforms in *E-mode* (multi-shot)

Figure 3.8: Background-subtracted multi-shot-averaged images of the electric field waveforms of the THz pulses that are transmitted through (a) the unexcited (reference) and (b) excited (pumped) GaAs sample in the *E*-mode configuration. The time scale is 45 pixels/ps and the arrows denote the direction of motion of the THz pulses. The solid red rectangles define the binning windows used for obtaining the THz waveforms. (c) THz reference and pumped waveforms obtained in images (a) and (b). (d) The real (black symbols) and imaginary (red symbols) components of the THz conductivity measured in the photoexcited GaAs sample. A Drude model fit to the data (blue lines) is also shown.

Figures 3.8(a) and (b) show background-subtracted *E*-mode images of the THz electric field waveforms transmitted through the unexcited and excited GaAs sample, respectively. Each image is the average of 100 frames taken at an

exposure time of 400 ms, corresponding to an overall average of 40,000 THz pulse waveforms. As shown in Figure 3.8(c), the temporal profiles of the THz waveforms are extracted from these images by binning over 50 pixels (~ 1 mm) in the vertical direction.

The frequency-dependent complex conductivity, $\sigma(\omega)$, of the photoexcited GaAs sample can be calculated from Ref. [16] and Appendix C,

$$E_{pump}(\omega)/E_{ref}(\omega) = (N+1)/(N+1+Z_0 d\sigma(\omega)) \qquad (3.1)$$

where $E_{pump}(\omega)$ and $E_{ref}(\omega)$ are the Fourier transforms of the THz electric field waveforms transmitted through the excited (pumped) and unexcited (reference) GaAs, respectively, $Z_0 = 377\ \Omega$ is the impedence of free space, $N = 3.6$ is the refractive index of GaAs at THz frequencies, and $d = 900$ nm is the optical penetration depth of 800 nm light in GaAs [16]. Figure 3.8(d) shows the complex THz conductivity extracted from the THz waveforms in Figure 3.8(c), which fits very well to the Drude model with a dc conductivity of 126 Ω^{-1}cm^{-1} and a relaxation time of 211 fs, consistent with other time-resolved THz conductivity measurements of photoexcited GaAs [16, 17]. The detailed information about the THz conductivity calculation and Drude model fit is introduced in Appendix C.

The excellent fit to the Drude model implies that the THz electric field waveforms captured with the noncollinear imaging technique can be used for time-resolved THz spectroscopy of materials. However, the low SNR in single shot renders that the *E*-mode THz imaging unsuitable for true single-shot THz measurements so far.

3.3.2 THz spectroscopy based on THz waveforms in E^2-mode (single-shot)
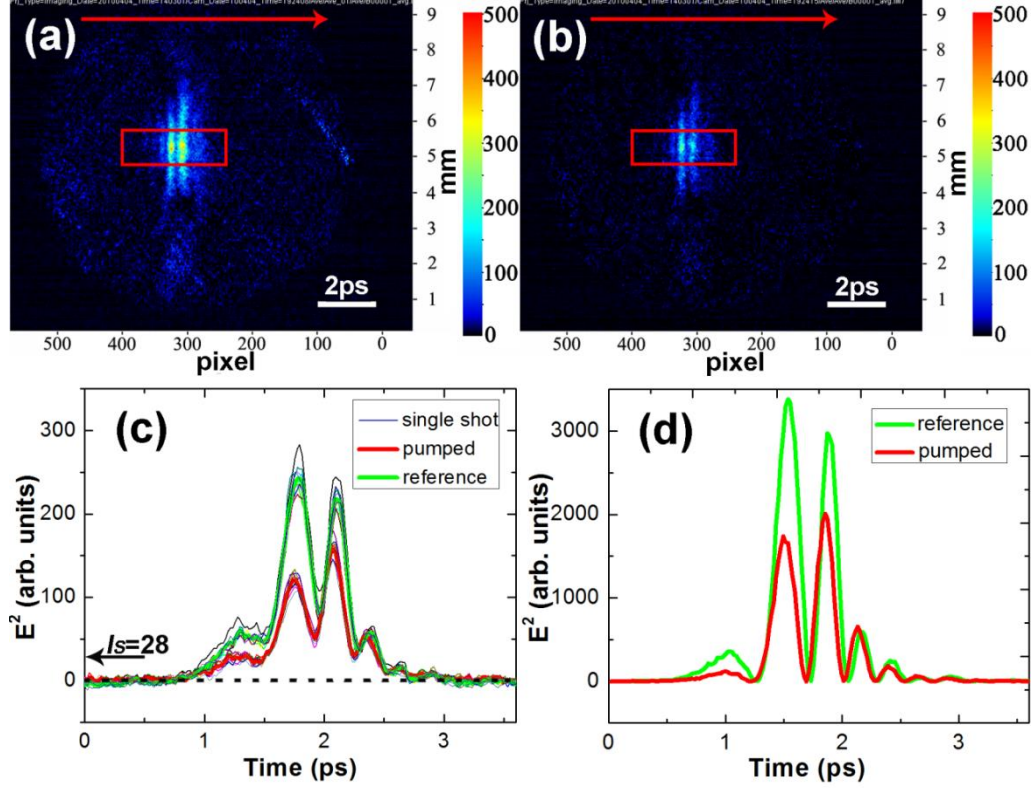
Figure 3.9: Single-shot images of a transmitted THz pulse through (a) the unexcited GaAs sample, (b) the excited GaAs sample. (c) Extracted THz single-shot waveforms for the unexcited and excited GaAs. Thick lines depict the average of 10 single-shot THz waveforms. The arrow indicates the relative level of the background light that was subtracted from the original images. (d) The square of the THz waveforms in Figure 3.8(c).

In order to achieve single-shot THz spectroscopy of the photoexcited GaAs sample, E^2-mode THz imaging is used. Figure 3.9(a) shows a single-shot image (reference) of a THz pulse that is transmitted through an unexcited GaAs. We note that the background around the THz pulse is mainly due to scattering. Figure 3.9(b) shows the single-shot image of the THz pulse that is transmitted through a photoexcited GaAs. The temporal profiles of the corresponding background-subtracted single-shot THz waveforms are plotted in Figure 3.9(c) along with

examples of 10 other single-shot waveforms, showing good repeatability between shots. The square of the THz electric fields from the E-mode waveforms in Figure 3.8(c) are plotted in Figure 3.9(d), closely matching the E^2-mode waveforms in Figure 3.9(c). The difference between Figure 3.9(c) and (d) is due to the convolution effect of the optical probe pulse.
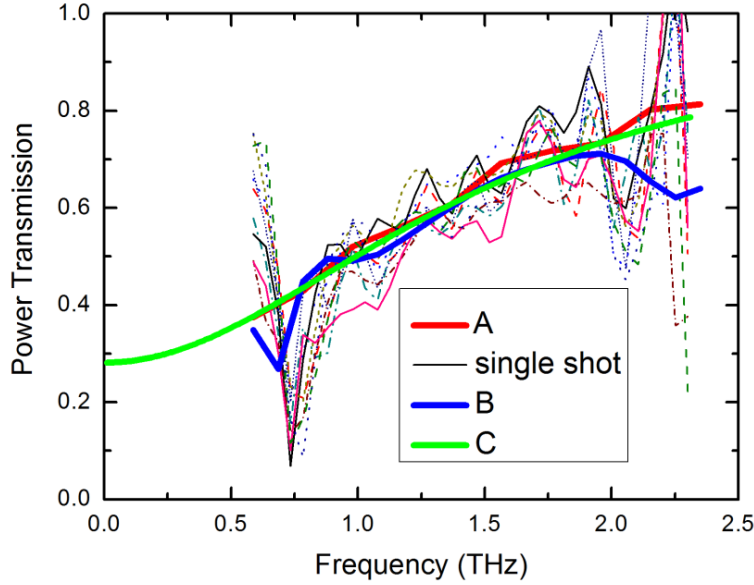
Figure 3.10: Single-shot and multi-shot THz power transmission spectra through photoexcited GaAs. The thin lines represent single-shot power transmission spectra obtained from the single-shot E^2-mode THz waveforms in Figure 3.9(c). Line A (thick red line) is obtained from the power spectra of the E-mode THz waveforms in Figure 3.8(c). Line B (thick blue line) is obtained from the amplitude spectra of the E^2-mode 10-shot-averaged reference and pumped THz waveforms in Figure 3.9(c). Line C (thick green line) is the calculated power transmission spectrum based on the Drude fit in Figure 3.8(d).

The relative THz power transmission spectra through the photoexcited GaAs are shown in Figure 3.10. Line A represents the relative power transmission derived from the power spectra of the multi-shot E-mode waveforms in Figure 3.8(c), which agrees well with the relative power transmission (Line C) predicted by the Drude model fit to the E-mode data in Figure 3.8(d) using Equation 3.1.

As introduced in Appendix F, the E^2-mode THz imaging method already gives a waveform proportional to the power of the THz pulse, and so the power

spectrum is obtained by taking the amplitude Fourier transform of the E^2-mode waveforms and dividing the frequency by a factor of 2 to account for the frequency doubling that occurs in the signal going from E-mode to E^2-mode. The thin lines in Figure 3.10 represent THz power transmission derived from single-shot THz intensity waveforms with single shot. In order to check whether the single-shot 10 separate results are consistent with each other, the result from the average of these 10 single shot is shown in Line B, which is consistent with the single-shot results. Furthermore, both of the thin lines and average line B agree with Line A from the E-mode data and Line C from the Drude fit, confirming that the E^2-mode THz imaging method can be used for reproducible true single-shot time-resolved THz spectroscopy.

3. 4 Conclusions

We have used noncollinear electro-optic THz imaging to demonstrate for the first time true single-shot and multi-shot time-resolved THz spectroscopy of transiently photoexcited GaAs. The E-mode THz pulse imaging technique allows extraction of the complex THz conductivity, but requires multi-shot acquisition with waveform averaging. On the other hand, E^2-mode THz pulse imaging with its low background level enables single-shot THz spectroscopy of the transmitted THz power spectra.

Reference:

1. B. Ferguson, and X.-C. Zhang, "Materials for terahertz science and technology," Nat. Mater. **1**, 26-33 (2002).

2. P. C. M. Planken, H. K. Nienhuys, H. J. Bakker, and T. Wenckebach, "Measurement and calculation of the orientation dependence of terahertz pulse detection in ZnTe," J. Opt. Soc. Am. B **18**, 313-317 (2001).

3. Z. P. Jiang, and X.-C. Zhang, "Electro-optic measurement of THz field pulses with a chirped optical beam," Appl. Phys. Lett. **72**, 1945-1947 (1998).

4. Z. P. Jiang, and X.-C. Zhang, "Single-shot spatiotemporal terahertz field imaging," Opt. Lett. **23**, 1114-1116 (1998).

5. K. Y. Kim, B. Yellampalle, J. H. Glownia, A. J. Taylor, and G. Rodriguez, "Measurements of terahertz electrical conductivity of intense laser-heated dense aluminum plasmas," Phys. Rev. Lett. **100**, 135002 (2008).

6. X.-Y. Peng, R. Jung, T. Toncian, O. Willi, and J.-H. Teng, "Distortion of the intense terahertz signal measured by spectral-encoding technique," Appl. Phys. Lett. **94**, 221107 (2009).

7. J. Shan, A. S. Weling, E. Knoesel, L. Bartels, M. Bonn, A. Nahata, G. A. Reider, and T. F. Heinz, "Single-shot measurement of terahertz electromagnetic pulses by use of electro-optic sampling," Opt. Lett. **25**, 426-428 (2000).

8. T. Yasui, K.-I. Sawanaka, A. Ihara, E. Abraham, M. Hashimoto, and T. Araki, "Real-time terahertz color scanner for moving objects," Opt. Express **16**, 1208-1221 (2008).

9. Y. Kawada, T. Yasuda, H. Takahashi, and S.-I. Aoshima, "Real-time measurement of temporal waveforms of a terahertz pulse using a probe pulse with a tilted pulse front," Opt. Lett. **33**, 180-182 (2008).

10. Y. Kawada, T. Yasuda, A. Nakanishi, H. Takahashi, and S.-I. Aoshima, "Single-shot measurement of terahertz temporal waveform using pulse-front tilting by a direct vision dispersion prism," Rev. Sci. Instrum. **80,** 113703 (2009).

11. Y. Kawada, T. Yasuda, A. Nakanishi, K. Akiyama, and H. Takahashi, "Single-shot terahertz spectroscopy using pulse-front tilting of an ultra-short probe pulse," Opt. Express **19**, 11228-11235 (2011).

12. K. Y. Kim, B. Yellampalle, A. J. Taylor, G. Rodriguez, and J. H. Glownia, "Single-shot terahertz pulse characterization via two-dimensional electro-optic imaging with dual echelons," Opt. Lett. **32**, 1968-1970 (2007).

13. S. P. Jamison, J. L. Shen, A. M. MacLeod, W. A. Gillespie, and D. A. Jaroszynski, "High-temporal-resolution, single-shot characterization of terahertz pulses," Opt. Lett. **28**, 1710-1712 (2003).

14. J. van Tilborg, C. B. Schroeder, C. Toth, C. G. R. Geddes, E. Esarey, and W. P. Leemans, "Single-shot spatiotemporal measurements of high-field terahertz pulses," Opt. Lett. **32**, 313-315 (2007).

15. B. Ferguson, S. Wang, D. Gray, D. Abbott, and X.-C. Zhang, "Identification of biological tissue using chirped probe THz imaging," Microelectron. J. **33**, 1043-1051 (2002).

16. D. G. Cooke, F. A. Hegmann, E. C. Young, and T. Tiedje, "Electron mobility in dilute GaAs bismide and nitride alloys measured by time-resolved terahertz spectroscopy," Appl. Phys. Lett. **89**, 122103 (2006).

17. M. C. Beard, G. M. Turner, and C. A. Schmuttenmaer, "Transient photoconductivity in GaAs as measured by time-resolved terahertz spectroscopy," Phys. Rev. B **62**, 15764-15777 (2000).

Chapter 4

Ultrafast imaging of terahertz Cherenkov waves in the LiNbO$_3$ and LiTaO$_3$ crystals

This chapter demonstrates the ultrafast imaging of terahertz (THz) Cherenkov waves in the transverse imaging geometry (side view and top view) in LiNbO$_3$ and LiTaO$_3$ crystals for the first time. The image distortion due to the transverse imaging geometry is simulated and corrected. Various Cherenkov wave parameters such as the Cherenkov angle, the THz pulse velocity and the optical pulse group velocity are measured. The propagation of the optical pump pulse as well as the THz generation and propagation are imaged directly in real time. Furthermore, the transition-like radiation generated at the LiNbO$_3$ surface is also imaged for the first time. The dependence of THz Cherenkov wave on the optical pump configuration, including the point focused and the line focused optical pump pulses, the optical pump pulse polarization, the optical pump pulse power, and the optical pump pulse duration is also explored.

4.1 Introduction to THz Cherenkov waves

A THz Cherenkov wave is a nonlinear optics phenomenon in which the optical pump pulse propagates faster than the generated THz pulse [1-3]. Ferroelectric crystals, including $LiNbO_3$ and its counterpart $LiTaO_3$, have been used to demonstrate this phenomenon when pumped by an 800 nm femtosecond (fs) laser pulse [1, 3-5]. As shown in Figure 4.1(a), a THz Cherenkov wave is generated, and the Cherenkov angle is determined by the velocity of the optical pump pulse and the generated THz pulse. Recently, due to the high second-order nonlinear efficiency, $LiNbO_3$ crystals have been employed to generate intense THz pulses with the tilted-pulse-front excitation technique [6-13]. However, the complex optics setup makes the optimization of $LiNbO_3$ sources very challenging. So understanding THz generation and propagation inside the crystal is very important.
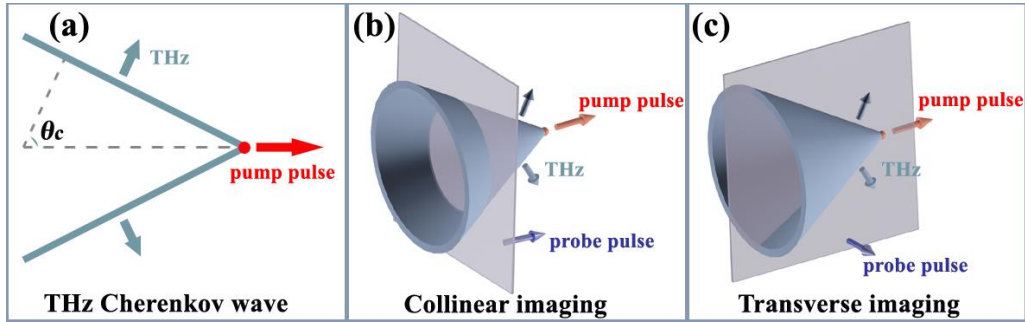
Figure 4.1: (a) Illustration of the THz Cherenkov wave. The Cherenkov angle θ_c is determined by the velocities of the optical pump pulse and the THz pulse. (b) Imaging the THz Cherenkov wave using the collinear imaging method, in which a probe pulse propagates collinearly with the pump pulse. (c) Imaging the THz Cherenkov wave using the transverse imaging method, in which a probe pulse propagates perpendicularly to the pump pulse.

Various techniques were developed to study THz pulse generation and evolution processes inside $LiNbO_3$ and $LiTaO_3$ crystals [1, 3-5, 14-30]. The first experiment aimed at investigating the dynamics of THz waves inside $LiTaO_3$ crystal was carried out in 1984 by Auston *et al.* [1]. In these experiments, two optical pulses propagated parallel to each other, and were focused into a $LiTaO_3$

crystal. One of the pulses was employed to excite the THz Cherenkov wave and another one was used to sample the THz electric field via the Pockels effect [31]. By changing the lateral spacing between the pump and probe beams and measuring the corresponding time delay at which the probe pulse gets modulated by the THz electric field, the THz Cherenkov wave could be mapped in two dimensional (2D). The decay behaviour of the THz wave inside the crystal was also studied in later work [16]. Mapping the whole three dimensional (3D) radiation structure by raster scanning the probe beam with fine steps was recently carried out to investigate the THz Cherenkov wave [17], but such data collection is time consuming.

As illustrated in Figure 4.1(b), instead of the raster scanning method, Koehl *et al.* [4] demonstrated full field imaging by replacing the focused probe beam with a broad beam that is large enough to cover the whole region of interest. The phase modulation imprinted on the probe pulse wavefront by the THz wave can be converted into an amplitude image in various imaging configurations, such as the Talbot effect or phase-contrast microscopy [4, 20, 21].

Based on the full field imaging method, a wealth of fascinating work has been done to explore THz generation and propagation behaviour inside bulk and thin waveguide ferroelectric crystals [3, 4, 18, 21-24, 32]. The evolution of the THz waves excited by different pump configurations (e.g. point focused, line focused and so on) has been observed and studied in bulk $LiNbO_3$ and $LiTaO_3$ crystals [3, 4, 18, 22]. Furthermore, the reflection, refraction, and interference behaviours of a THz wave in a patterned wave guide have been demonstrated [3, 19, 24, 33].

In contrast to THz waves inside a waveguide, which is in 2D and can be visualized completely by a single imaging direction, the THz Cherenkov cone in a bulk crystal is 3D in character and requires more than one view mode to extract the full spatial form. However, imaging work on bulk crystals has been done exclusively in the collinear imaging mode, where the probe pulse propagates collinearly or near-collinearly with the pump pulse. The captured image of the THz Cherenkov wave presents itself in a circle pattern [4, 15, 18]. To reveal the

full structure of THz generation within ferroelectric crystals, information from other view modes is desired to complement that gathered in the collinear mode.

In this chapter, as shown in Figure 4.1(c), a transverse imaging geometry, for the first time, is used to investigate THz Cherenkov waves in $LiNbO_3$. The shock wave pattern, which was only realized in simulation works or by raster scanning methods before [3, 5, 14, 15, 17, 25], is imaged experimentally. As illustrated in Figure 4.2(a) and (b), the THz Cherenkov cone is imaged in the **side-view mode** when the probe pulse propagates parallel to the optics axis (*c*-axis) of the crystal. On the other hand, Figure 4.2(c) and (d) show that if the probe beam is perpendicular to the *c*-axis of the crystal, images of the THz Cherenkov wave can be captured in the **top-view mode**.
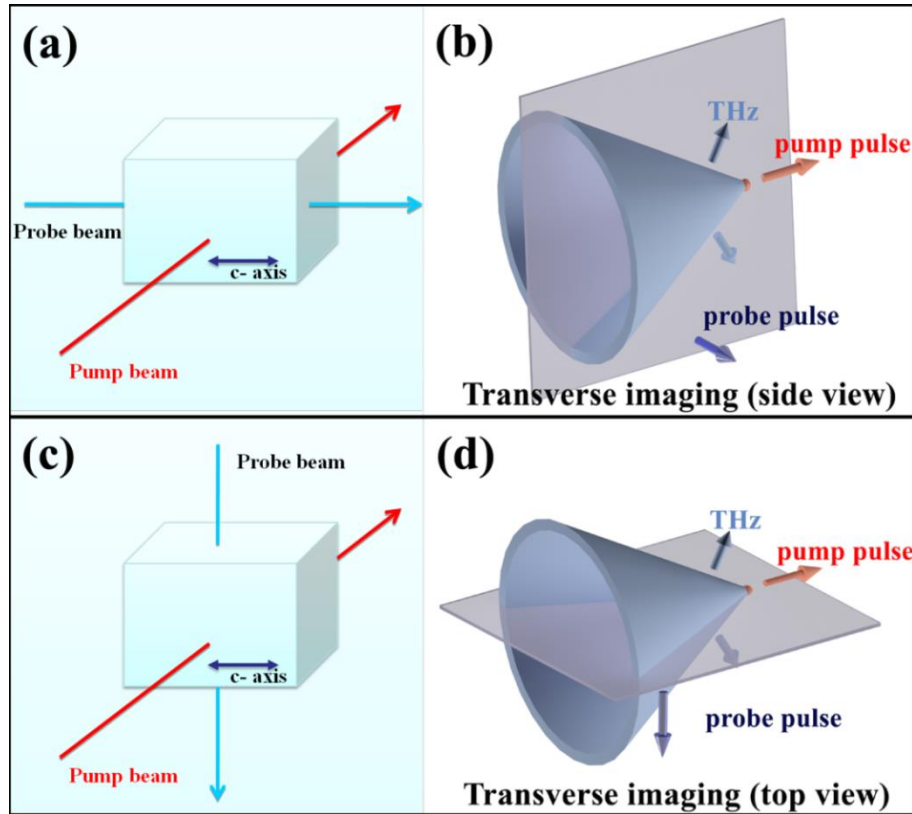
Figure 4.2: Illustration of the transverse imaging setup. (a) and (b), The side-view imaging of the THz Cherenkov wave, the probe pulse propagates parallel to the *c*-axis of the crystal. (c) and (d), Top-view imaging of the THz Cherenkov wave, the probe pulse propagates perpendicular to the *c*-axis of the crystal.

In section 4.2, imaging the THz Cherenkov wave in side-view mode in LiNbO$_3$ crystals is used as an example to demonstrate how to measure THz wave velocity, optical pulse group velocity and the corresponding Cherenkov angle. At the same time, transition-like radiation is imaged and discussed [5, 14, 15, 25-30]. The THz Cherenkov wave dependence on the optical pump pulse polarization, pulse duration, and pulse power is also explored.

In section 4.3, top-view imaging of the THz Cherenkov wave is explored. Together with the side-view images obtained in section 4.2, the 3D structure of the THz Cherenkov wave is constructed.

In section 4.4, THz Cherenkov waves that are generated in LiNbO$_3$ crystals by a line focused optical pump pulse are explored and discussed.

4.2 Imaging THz Cherenkov waves in $LiNbO_3$ and $LiTaO_3$ in side-view mode

4.2.1 Experimental setup

As illustrated in Figure 4.3(a) and (b), an amplified Ti:sapphire laser system (pulse energy = 0.9 mJ, pulse duration = 100 fs, central wavelength = 800 nm, repetition rate = 1 kHz) was employed to generate and image the THz Cherenkov waves in $LiNbO_3$ crystals. Three different $LiNbO_3$ prisms (**LN1**, **LN2**, and **LN3**), one $LiNbO_3$ rectangular block (**LN4**), and one $LiTaO_3$ rectangular block are employed in the experiment and the relevant parameters are listed in Table 4.1. Unless specified otherwise, the data shown in this chapter are from crystal **LN1**. The pump beam is focused by a lens (f = 500 mm) onto the crystal. The spot size $(1/e^2)$ of the focused beam on the crystal is 170 μm (measured with the knife-edge method) and is assumed to be constant throughout the whole crystal (6.5 mm in depth). The polarization of the pump pulse is controlled by a half-wave plate. A computer controlled optical delay stage is used to change the optical path of the pump pulse. The second 800 nm optical beam is frequency doubled by a β-Barium borate (BBO) crystal and used as a probe beam (remaining fundamental optical pulse is removed by a filter). After being cleaned by a spatial filter, the generated 400 nm probe beam is expanded so as to be broad enough to cover the whole crystal. As specified in Figure 4.3(b), the 400 nm probe beam propagates perpendicularly to the 800 nm pump beam and images the optically induced THz Cherenkov wave in side-view mode. Because the polarization of the probe beam doesn't affect the phase modulation in this mode (as shown in Figure 4.3(c), also tested experimentally), it is set at an arbitrary orientation. The phase-modulated probe beam is then transmitted through a filter which is used to block the scattered light from the 800 nm pump pulse. The Talbot effect (imaging the phase shift by moving the object plane of an camera out of the object), described and applied in many references [4, 18, 20, 21] and Section 2.2.2(b), is employed to

convert the phase object into an amplitude object. The object plane of the ICCD camera is put about 14 mm away from the phase object, which makes it sensitive to phase structure period 0.12 mm (corresponds to about 0.5 THz pulse in LiNbO$_3$). Finally, the converted amplitude image is recorded by an intensified CCD camera system (PicoStar HR ICCD). The ICCD camera system consists of an intensifier and a CCD head, where the intensifier functions as a signal amplifier and a shutter. The shutter, working at a gate width of 500 picosecond (ps), is triggered by an external electronic trigger and opens only when the probe pulse arrives. The effective pixel size of the ICCD camera system is 13.74 μm. The CCD is thermoelectrically cooled and has a dynamic range of 12 bits (4096 counts). Detailed information about the ICCD camera system and its operation are given in Appendix A.

The ICCD camera scale calibration was performed by counting how many pixels the location of the image changes when the ICCD camera was moved vertically using a micrometer translation stage (discussed further in Appendix A4 and A5). For the imaging collection, 200 frames at an exposure time of 400 ms were collected and averaged prior to recording the THz signal. The averaged image was used as the ICCD background and subtracted automatically by the computer from the THz image, which was captured with 200 counts offset using the same exposure time. Although the THz signal can be seen in one frame of the background subtracted image, 50 frames are collected and averaged for better signal to noise ratio (SNR) and images shown in this thesis are all obtained in the same way. The movie is made of frames collected at different time delays with a movie maker software (Windows Live Movie Maker). Considering a better printed copy for readers, some THz images shown in this thesis are further treated with PHOTOSHOP to enhance the image contrast and no information is found lost or distorted. An original image is shown in Figure 4.3(d).

Table 4.1: The shape, size, cutting angle, MgO: doping level and growth type of the three $LiNbO_3$ and $LiTaO_3$

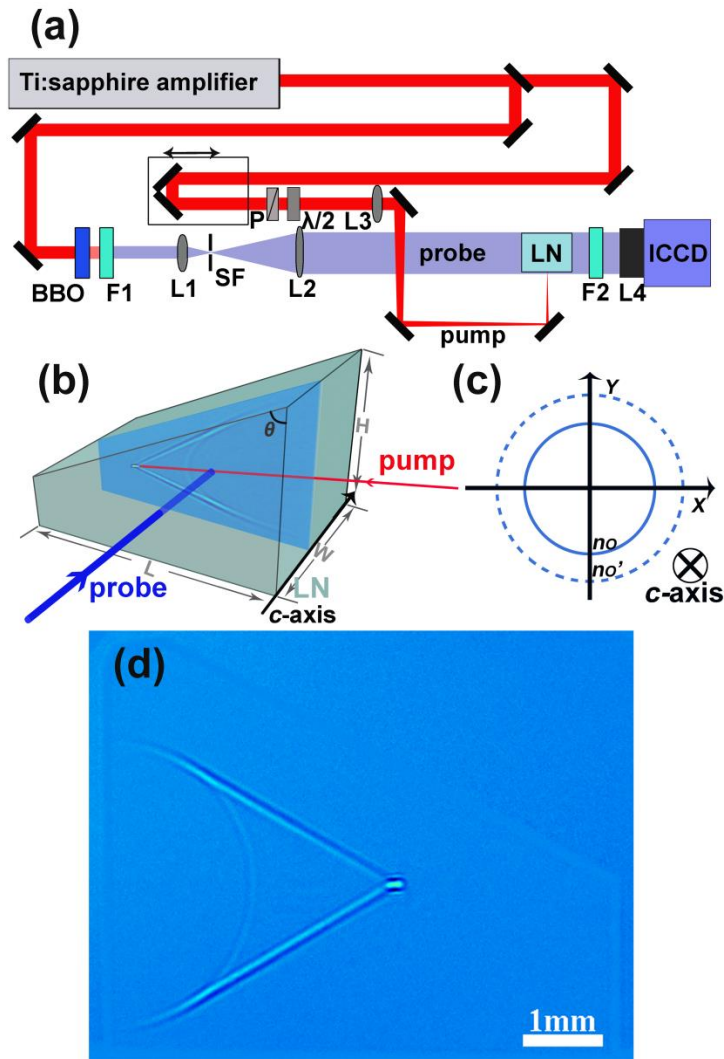| crystal	shape	L (mm)	W (mm)	H (mm)	θ (°)	MgO: doping (mol)	growth type
LN1	prism	6.5	6	6.4	62	1.3%	stoichiometric
LN2	prism	6.5	6	6.4	63	0.6%	stoichiometric
LN3	prism	6.5	6	6.4	64	5%	congruent
LN4	rectangular	7	6	6	/	0.6%	congruent
$LiTaO_3$	rectangular	7	6	6	/	/	/

Figure 4.3: (a) Experimental setup in side-view mode. An amplified Ti:sapphire laser pulse (100 fs, 800 nm, 0.9 mJ, 1 kHz) is split into two parts. The pump pulse (7.4 µJ) is focused by a lens

(focal length 500 mm) onto the LiNbO$_3$ crystal (or LiTaO$_3$) to generate a THz wave. The probe pulse is frequency doubled through a BBO crystal and further spatially filtered and expanded to obtain a clean and uniform 400 nm probe beam. The expanded 400 nm probe pulse is transmitted through the crystal from the side (parallel to the c-axis). A filter after the crystal is used to remove the scattering from the 800 nm optical pump pulse. L1, L2, and L3 are optical lenses, L4 is the imaging microscope of the camera. F1 and F2 are bandpass coloured glass filters, BBO is β-Barium borate crystal, SF is the spatial filter, P is the polarizer, $\lambda/2$ is the half-wave plate, LN is the sample crystal (LiNbO$_3$ or LiTaO$_3$), and ICCD means Intensified CCD camera. (b) Detailed geometry of the optical pump and probe beams in the crystal. The pump polarization is controlled by a half-wave plate. The probe polarization is 54 ° relative to the pump-probe intersection plane (actually, the measurement is independent on the probe polarization). L, H, and W are the size of the crystal, θ is the cutting angle. (c) Diagram of the index ellipsoid of the LiNbO$_3$ and LiTaO$_3$ crystal in the presence of the THz electric field which is parallel to the c-axis. The refractive index n$_o$ is isotropic in the plane that is perpendicular to the c-axis and the change of the refractive index "n$_o$'-n$_o$" is proportional to the THz electric field [34]. (d) Background-subtracted image of the THz Cherenkov wave obtained from the ICCD.

4.2.2 Measurement of the optical pulse group velocity, the THz wave velocity, and the THz Cherenkov angle

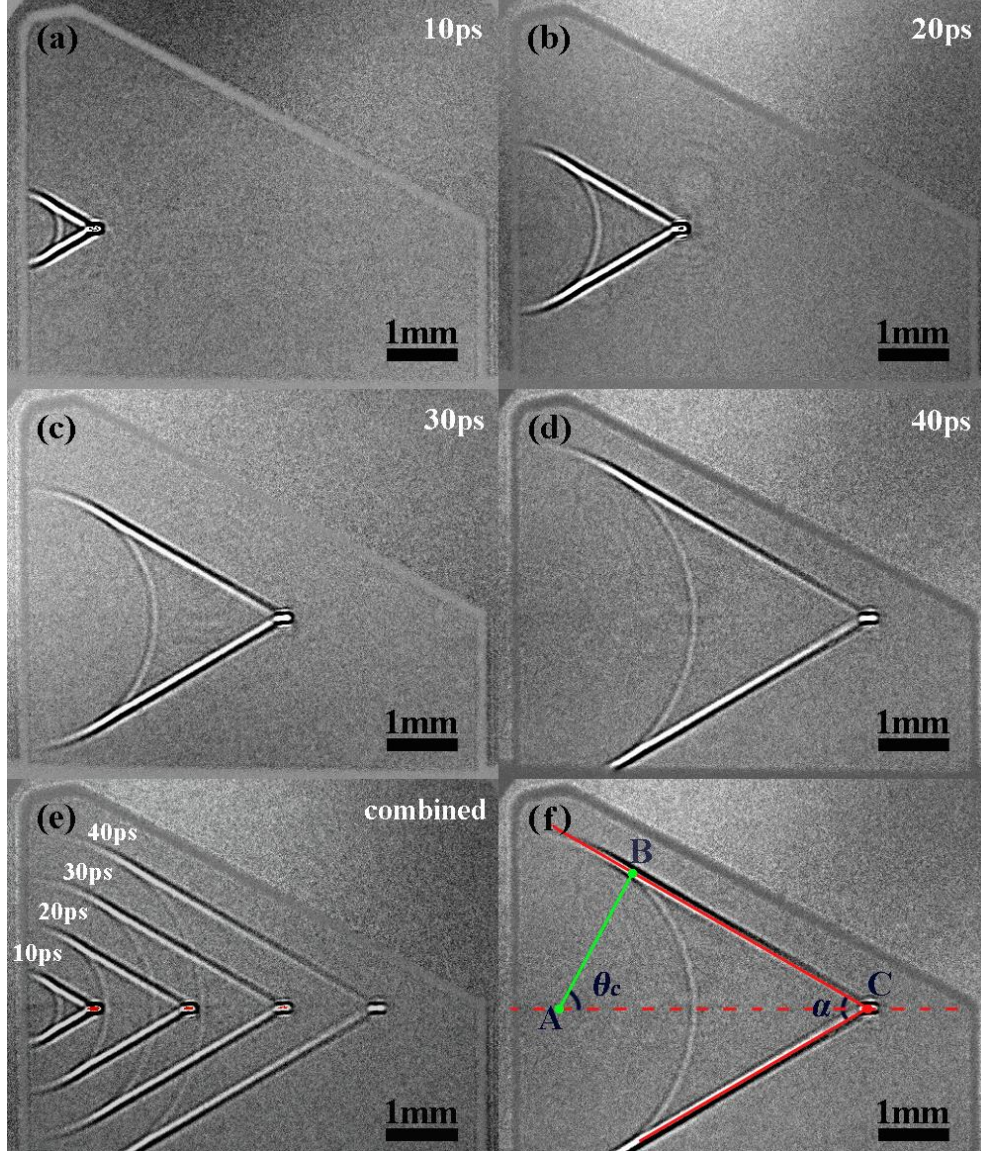**Figure 4.4:** Background-subtracted images of the THz pulse inside the **LN1** crystal captured at time delays of (a) 10 ps, (b) 20 ps, (c) 30 ps, and (d) 40 ps, respectively. (e) Overlay image of (a), (b), (c), and (d). (f) An illustration of the THz Cherenkov wave and the THz Cherenkov angle. The optical pump polarization is parallel to the c-axis of the crystal and the c-axis is pointing out of the paper plane.

An optical pump pulse with its polarization parallel to the c-axis of the LiNbO$_3$ crystal is focused onto the crystal by a lens (f = 500 mm). The generated THz wave is imaged by a 400 nm optical probe beam which propagates perpendicularly to the pump beam. By changing the relative time delay between the optical pump pulse and the probe pulse, the generation and propagation processes of the THz pulse are imaged. Figure 4.4(a), (b), (c), and (d) show images of the propagating THz pulse inside the crystal **LN1** at four different time delays.

Due to the nature of the Talbot effect, the ICCD is away from the image plane, and as a consequence, the image of the object becomes blurred. However, we have confirmed that the angle and distance information of the image are still reliable by performing preliminary imaging of a grid calibration plate (as shown in Appendix A5).

In order to measure the velocities of the optical pump pulse and the THz pulse, we combine all the images together to form an overlay image (as shown in Figure 4.4(e)) and then measure the displacement of the signal at a certain time delay in the optical pulse propagation and the THz pulse propagation direction, respectively. Based on the measured optical group velocity and the THz wave velocities, the Cherenkov angle θ_c (illustrated in Figure 4.4(f)) can be calculated by [10],

$$\theta_c = cos^{-1}(v_{THz}/v_{op}) \qquad (4.1)$$

where v_{op} and v_{THz} are the optical pulse group velocity and the THz wave velocity, respectively. Meanwhile, the Cherenkov angle can also be measured using,

$$\theta_c = 90° - \alpha/2 \qquad (4.2)$$

where α is the cone angle (illustrated in Figure 4.4(f)) and can be imaged directly.

As shown in Table 4.2, the extraordinary group velocity and indices of the optical pump pulse and THz pulse and the corresponding calculated and measured Cherenkov angles in three different LiNbO$_3$ crystals **LN1**, **LN2**, and **LN3** are

listed. We find that the calculated Cherenkov angles are consistent with their corresponding measured values for all of these three crystals. The extraordinary optical group indices look almost the same for all three crystals and are close to the literature value of 2.25 [3]. However, there is a large difference between our THz wave index (4.41-4.55) and the literature data (around 5.1 at central frequency of 0.5 THz) [3]. This is also the reason why our Cherenkov angles (around 60) is smaller than the estimated value (64) reported in the literature [3, 7, 35]. We note that, as described in Appendix G, the actual THz wave index in LiNbO$_3$ slab is also measured experimentally (5.1 at 1 THz, 4.998 at 0.5 THz) using terahertz time-domain spectroscopy (THz-TDS).

Table 4.2: The measured and calculated velocity, refractive index, Cherenkov angle for three different LiNbO$_3$ crystals. The calculated Cherenkov angle is based on the velocities obtained from the images.

	Measured optical pulse velocity (v_{opt}) (10^8 m/s)	Measured THz pulse velocity (v_{THz}) (10^8 m/s)	Calculated optical group index (n_{opt})	Calculated THz index (n_{THz})	Calculated Cherenkov angle (θ_c Equation 4.1)	Measured Cherenkov angle (θ_c Equation 4.2)
LN1	1.347±0.008	0.680±0.005	2.23±0.01	4.41±0.03	59.7±0.4 °	60.4±0.3 °
LN2	1.348±0.007	0.679±0.004	2.23±0.01	4.42±0.03	59.7±0.4 °	60.0±0.2 °
LN3	1.340±0.008	0.659±0.006	2.24±0.01	4.55±0.04	60.5±0.5 °	60.8±0.2 °

The Cherenkov angle difference between the actual angle and the measured angle from the image is due to a smearing effect in the transverse imaging geometry, as mentioned in Chapter 2.

Figure 4.5(a), (b), (c) illustrate the process about how the probe pulse wavefront gets modulated by the THz electric field when the optical pump pulse and probe pulse propagate perpendicularly to each other. Figure 4.5(e) shows the simulated result, and we find that when the true Cherenkov angle is 64 °(as shown in Figure 4.5(d)), the Cherenkov angle from the image is 60.2 ° (as shown in Figure 4.5(e)), which is the same as our experimental result (as shown in Figure 4.5(f)).
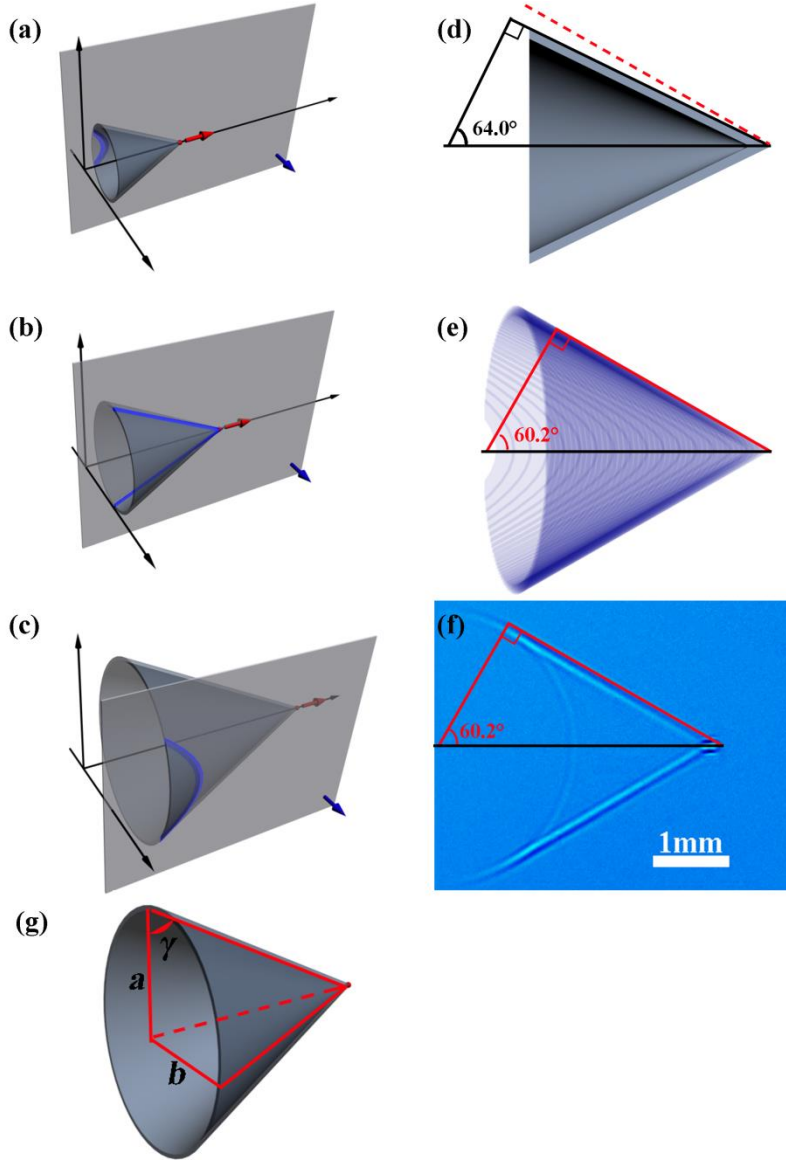
Figure 4.5: (a)-(c) Schematic illustration of how the probe pulse wavefront (grey square plane) gets modulated by the THz Cherenkov cone when the optical pump pulse and the probe pulse propagate perpendicular to each other. (d) The THz cone and its Cherenkov angle in the probe image plane is 64 °, the cone is squeezed due to different refractive indices at different propagation directions. The red dashed line shows the observed cone edge in the image. (e) Simulation results of the image using 3ds Max. (f) Experimental image with an observed Cherenkov angle of 60.2 °. (g) Schematic diagram of the Cherenkov cone. The cone is squeezed with major radius *a* and minor radius *b*

Based on our simulation results, we also find that the angle difference is determined by the true Cherenkov angle, the relative velocity ratio between the optical pump pulse and the probe pulse, as well as the ratio between the major radius *a* and minor radius *b* of the cone (as illustrated in Figure 4.5(g)). The actual Cherenkov angle and the corresponding angles obtained from simulation and experiment for various imaging conditions are given in Table 4.3.

Table 4.3: Actual THz Cherenkov angle (γ), and corresponding simulated and observed Cherenkov angles (γ'), for various imaging schemes for both LiNbO$_3$ and LiTaO$_3$ crystals.

crystal	imaging scheme		a/b	actrual Cherenkov angle (γ)	Cherenkov angle from simulation (γ')	Cherenkov angle from experiment (γ')
LiNbO$_3$	side view	probe (o ray)	1.22	**64°**	**60.2°**	**60.2°**
	top view	probe (o ray)	0.82	**68.8°**	**62.8°**	**62.7°**
		probe (eo ray)	0.82	**68.8°**	**63.8°**	**63.9°**
LiTaO$_3$	side view	probe (o ray)	1.05	**68.7°**	**66.3°**	**67.0°**
	top view	probe (o ray)	0.96	**69.7°**	**67.2°**	**67.3°**
		probe (eo ray)	0.96	**69.7°**	**67.2°**	**67.3°**

For comparison, side-view images of the THz Cherenkov wave in the LiTaO$_3$ crystal are also captured under the same experimental conditions. Figure 4.6 shows images of THz Cherenkov waves in the LiNbO$_3$ and LiTaO$_3$ crystals side by side. In contrast to the images of the THz Cherenkov wave in the LiNbO$_3$ crystal (shown in Figure 4.6(a)-(c)), the measured Cherenkov angle in the LiTaO$_3$ crystal is 67.0 ° with a calibrated (through simulation) Cherenkov angle of 68.8 ° (shown in Figure 4.6(d)-(f)), which is consistent with the value (68.7 °) in Ref. [3].
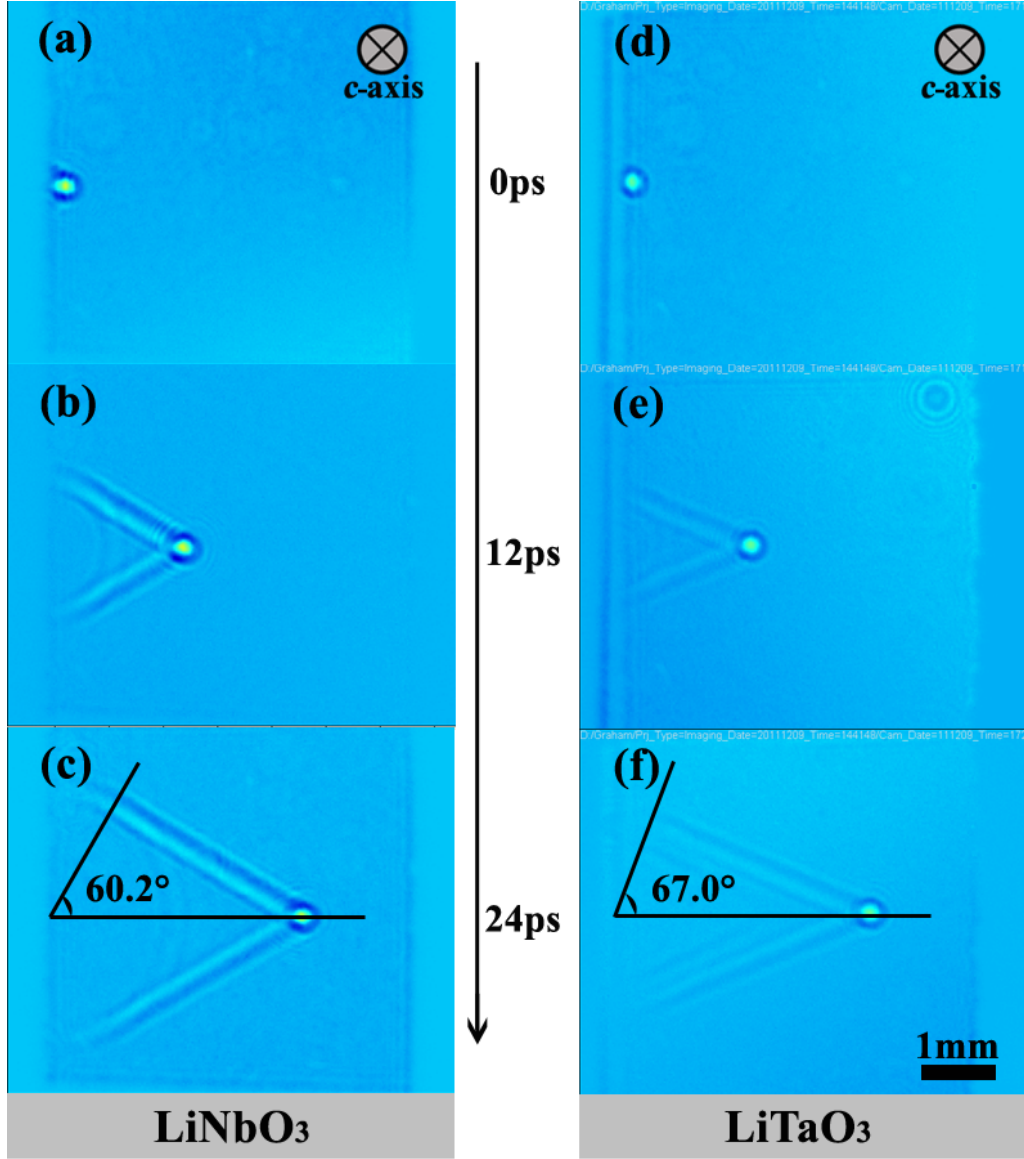
Figure 4.6: (a)-(c) Side-view images of the THz Cherenkov wave in the LiNbO$_3$ crystal captured at time delays of (a) 0 ps, (b) 12 ps, and (c) 24 ps, respectively. (d)-(f) Side-view images of the THz Cherenkov wave in the LiTaO$_3$ crystal captured at time delays of (d) 0 ps, (e) 12 ps, and (f) 24 ps, respectively. The pump pulse polarization is parallel to the *c*-axis of the crystal. The ring pattern around the tip (dot) is due to the diffraction.
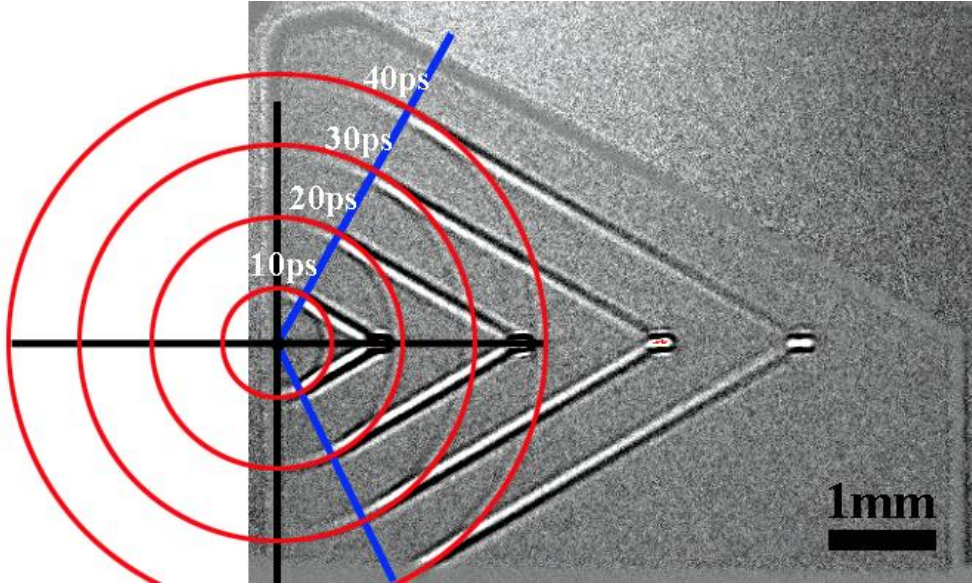
4.2.3 Observation of the transition-like radiation

Figure 4.7: Side-view image of the transition-like radiation (red circles) in a LiNbO$_3$ crystal at different time delays.

As shown in Figure 4.4 and Figure 4.6, we observed not only the THz Cherenkov wave, but also the transition-like radiation, which is in circular profile. The transition-like radiation (also called transition radiation in some papers [28, 36]) generated on the crystal surface by a laser pulse was first suggested theoretically in 1962 [36], and was first reported experimentally in 1992 [26], in which twin THz pulses were measured. Since then, in order to understand the generation mechanism of such radiation, some theoretical and experimental work has been done and two models were proposed [5, 25-30, 36]. The first theory is the nonlinear wave conversion model (NLWC), which is based on the nonlinear wave equation and suggests that the transition-like radiation is the constructive interference of the inhomogeneous wave and the homogeneous wave over the coherence length [25]. The coherence length is calculated by [12, 37],

$$l_c = \frac{\pi c}{\omega_{THz} \left| n_{opt} - \lambda_{opt} \left. \frac{dn_{opt}}{d\lambda} \right|_{\lambda_{opt}} - n_{THz} \right|} \qquad (4.3)$$

where c is the speed of light, n_{THz} is the refractive index at THz frequencies, n_{opt} is the refractive index of the optical pump pulse, and λ_{opt} is the wavelength of the optical pump pulse. The coherence length l_c is 140 μm for $\lambda_{opt} = 800\ nm$ and a THz wave frequency at 0.5 THz in LiNbO$_3$ crystals. On the other hand, the generation of such radiation on the surface of nonlinear media is interpreted by analogy with transition radiation, in which a charge moving through two different media emits electromagnetic radiation due to the acceleration or deceleration of charge [27, 28, 36]. However, it's still difficult to tell which model is correct so far, and more experimental work is needed to fully understand this process.
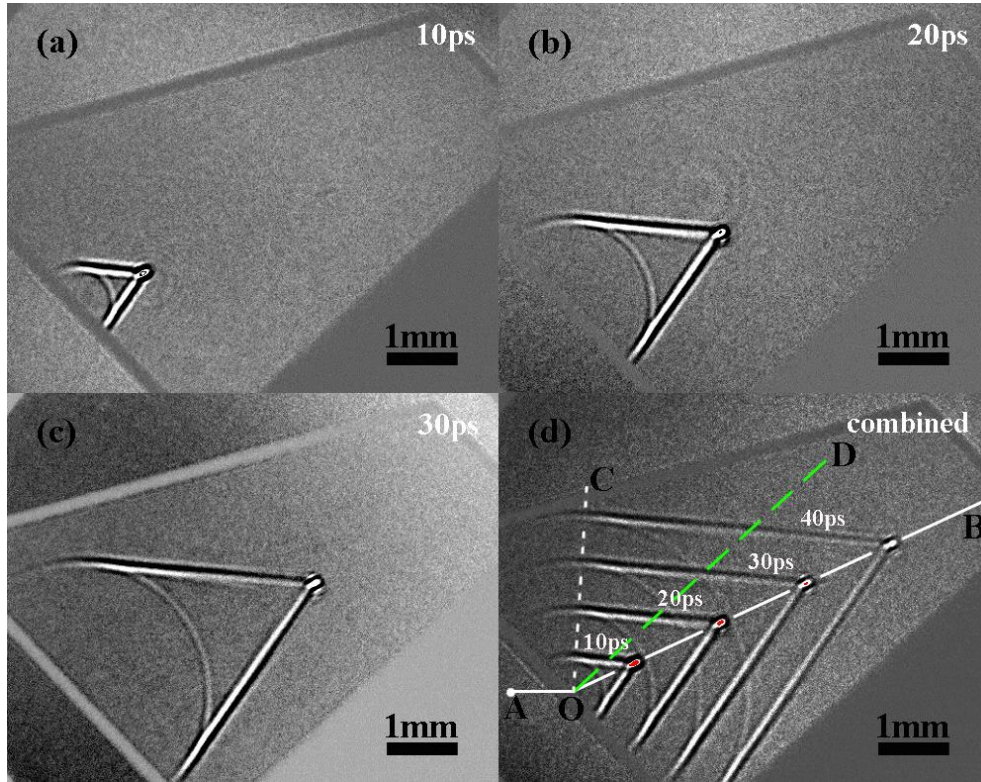

Figure 4.8: (a)-(d) Background subtracted THz images in the crystal **LN1** captured at pump-probe time delays of 10 ps (a), 20 ps (b), 30 ps (c), and 40 ps (d). For comparison, images at time delays of 10 ps, 20 ps, and 30 ps are overlapped with that at a time delay of 40 ps in (d). The red color in (d) means a saturated signal

Different from the measurement of transition-like radiation that has been transmitted out of the crystal [26-28], the transverse imaging geometry allows us

to image such radiation inside the crystal and offers extra information. In Figure 4.4, which is strikingly similar to the simulations described in Ref. [15], a ring like radiation is found to originate from the front surface of the $LiNbO_3$ crystal and propagates with a semicircle wavefront (as specified in Figure 4.7).
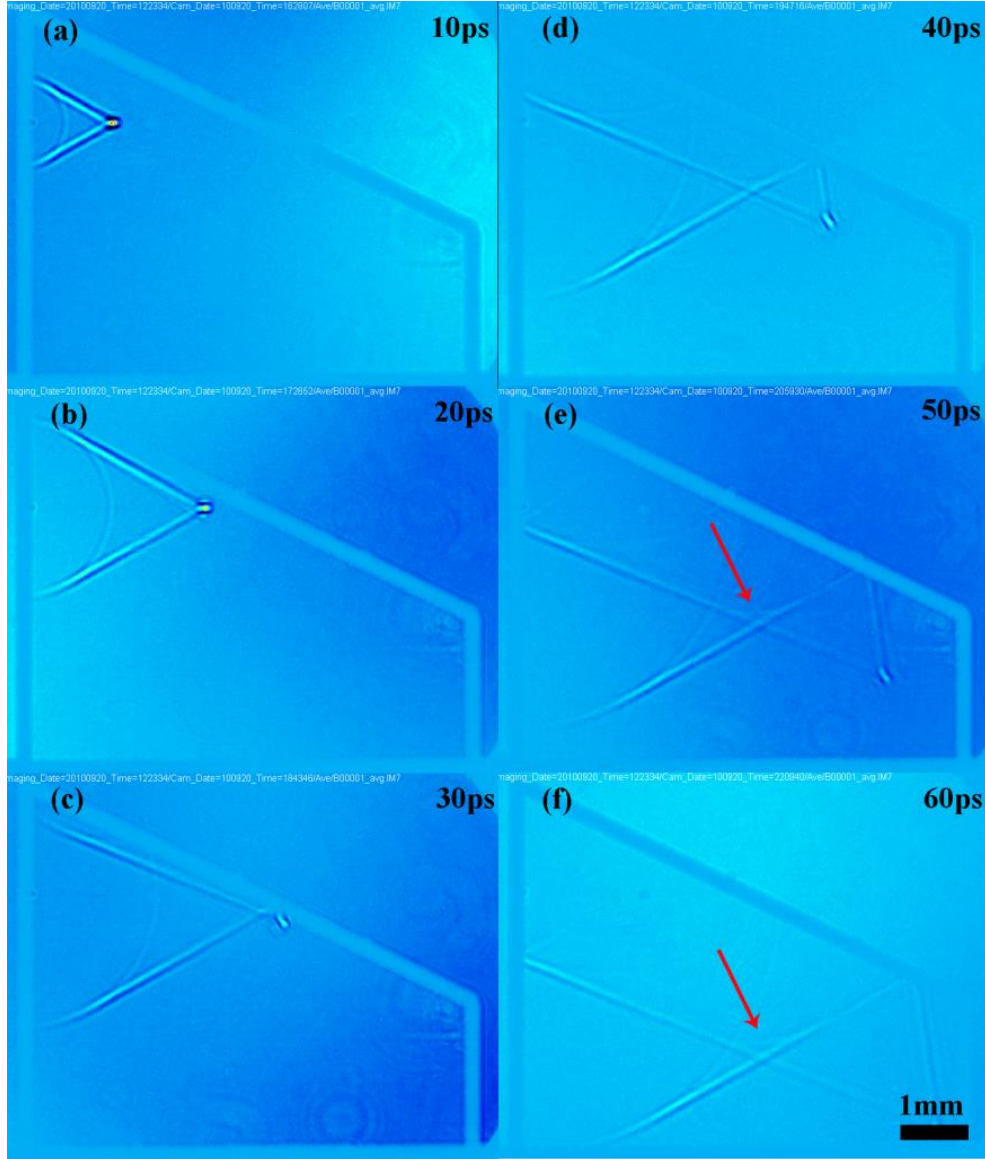

Figure 4.9: Background subtracted images (selected from a movie) of the THz pulse inside the **LN3** crystal captured at time delays of (a) 10 ps, (b) 20 ps, (c) 30 ps, (d) 40 ps, (e) 50 ps, (f) 60 ps. The pump polarization is parallel to the c-axis of the crystal and the c-axis is pointing out of the paper plane. The transition-like radiation that is generated at the second surface where the optical pulse gets totally internal reflected is marked by a red arrow.

Within the limits of our time resolution, the ring shaped transition-like radiation is excited at the same time as the optical pump pulse hits the crystal surface. As shown in Section 2.1.3, the reason that the wavefront of the transition-like radiation is in a circle profile is because the polarization of the transition-like radiation is parallel to the *c*-axis. The transition-like radiation propagating in any direction in this plane (XY plane) experiences the same refractive index. We also find that the propagation velocity of the ring shaped radiation is the same as that of the THz Cherenkov wave and the circular wavefront is always tangent to the shock wave.

In order to study the dependence of the main emission direction of the transition-like radiation on the pump pulse's propagation direction, we repeated the experiment with the crystal rotated 43 °around its *c*-axis, as shown in Figure 4.8. As shown in Figure 4.8(d), **AO** is the incident direction of the optical pump pulse, while **OB** and **OC** are the propagation directions of the optical pump pulse and the THz pulse inside the crystal, respectively. Because the optical pulse is no longer normally incident on the crystal, the central axis of the shock wave is not perpendicular to the crystal surface. In contrast, the central axis of the circular radiation (**OD**) remains normal to the surface despite the crystal rotation. The independence of this symmetry relative to the incident optical pump angle proves that the circular wavefront is generated at the crystal surface. We also note that the measured optical refractive index, the THz refractive index, and the Cherenkov angle in Figure 4.8(a)-(d) are the same as those in Figure 4.4.

In fact, the transition-like radiation not only happens at the first surface of the crystal, but also appears at the second surface. Figure 4.9 shows a series of images when the optical pump pulse experiences a total internal reflection inside the crystal **LN3**. As indicated by the arrow, the transition-like radiation ring generated on the reflection surface can be seen. On the other hand, Figure 4.10 shows the **LN3** where the optical pump pulse propagates normally through the crystal. Furthermore, as illustrated in Figure 4.11, there is also an imaging distortion issue when we image the transition-like radiation in the transverse imaging geometry, and the measured velocity is higher than the actual value.

As shown in Appendix G, the transition-like radiation generated on the front and back surfaces of a LiNbO$_3$ slab are sampled with THz-TDS.
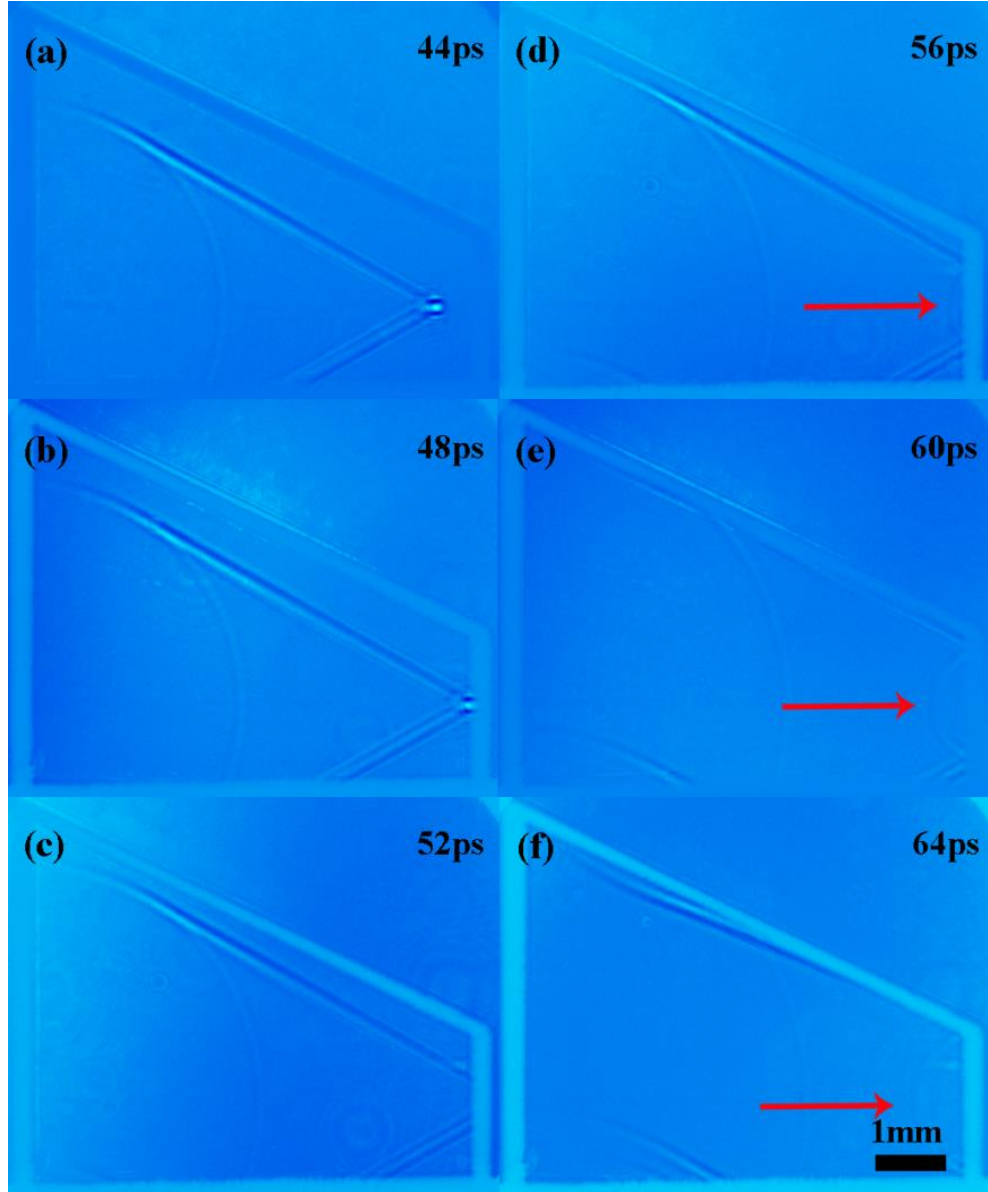

Figure 4.10: Background-subtracted images of the THz pulse inside the **LN3** crystal captured at time delays of (a) 44 ps, (b) 48 ps, (c) 52 ps, (d) 56 ps, (e) 60 ps, (f) 64 ps. The pump polarization is parallel to the c-axis of the crystal and the c-axis is pointing out of the paper.
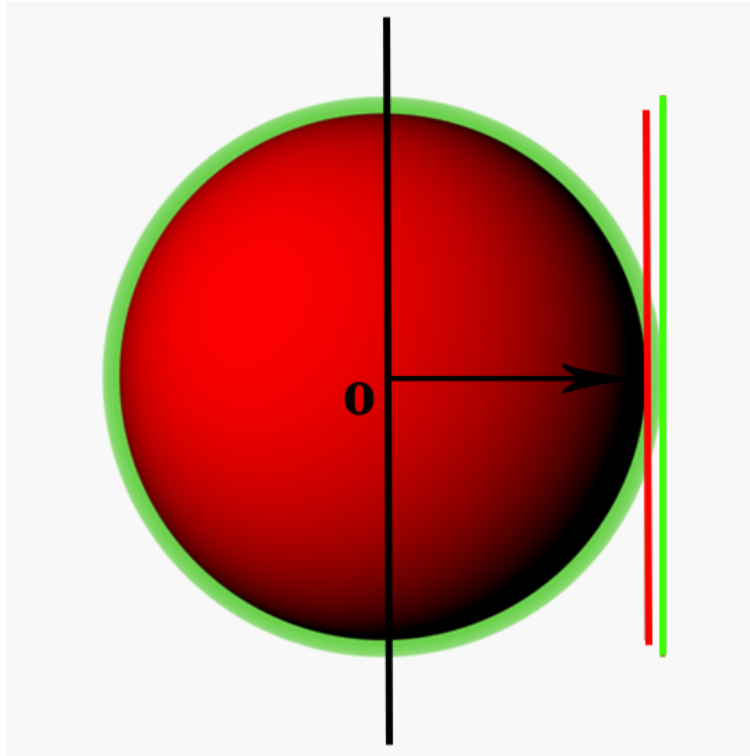
Figure 4.11: Schematic illustration of the imaging distortion when we image the transition-like radiation. The velocity of the transition-like radiation measured from the obtained images is higher than the actual value.

4.2.4 Temporal evolution of the THz Cherenkov wave in the LiNbO$_3$ crystal
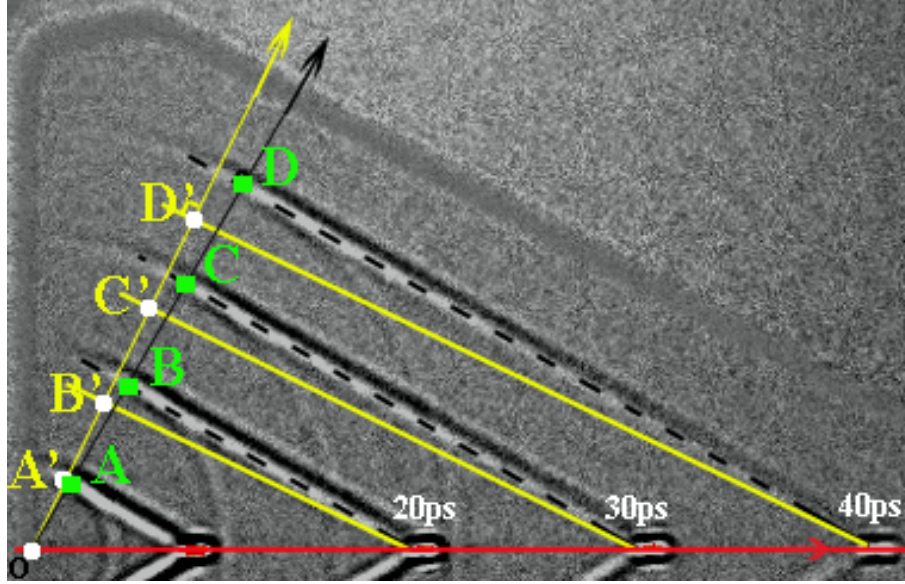

Figure 4.12: Illustration of the THz Cherenkov wave image and the corresponding real wavefront of the THz pulse. The black dashed lines mark the imaged THz wavefront, and the pulse propagation direction is illustrated by the black arrow. The corresponding real THz wavefront are marked by the yellow solid line and propagates along the yellow arrow.

In contrast to the collinear imaging geometry, the transverse imaging geometry can be used to not only calculate the optical and THz wave refractive indices, but also provide insight into the THz generation and propagation processes. As shown in Figures 4.4 and 4.12, the shock wave tip becomes longer in size and weaker in strength as the optical pulse propagates through the crystal, likely caused by the dispersion and energy loss of the optical pump pulse.

As illustrated in Figure 4.12, once the THz pulse is generated from point O, it will propagate away from point O along line AB. However, due to the image distortion caused by the transverse imaging geometry, instead of the black dashed lines, the real THz pulse wavefront at different time delays is marked with the yellow solid lines. Because we can sample the THz wave forms at point A, B, C, and D in the image, the THz wave forms at real positions A', B', C', and D' can

be sampled. Figure 4.13(a) shows the THz wave form at time delays of 10 ps (A), 20 ps (B), 30 ps (C), and 40 ps (D). Figure 4.13(b) shows the corresponding spectra, which are similar to the THz pulse spectra generated by tilted-pulse-front excitation scheme in Ref. [32]. The decay of the THz electric field is due to the THz Cherenkov cone expanding and the THz absorption in the $LiNbO_3$ crystal.
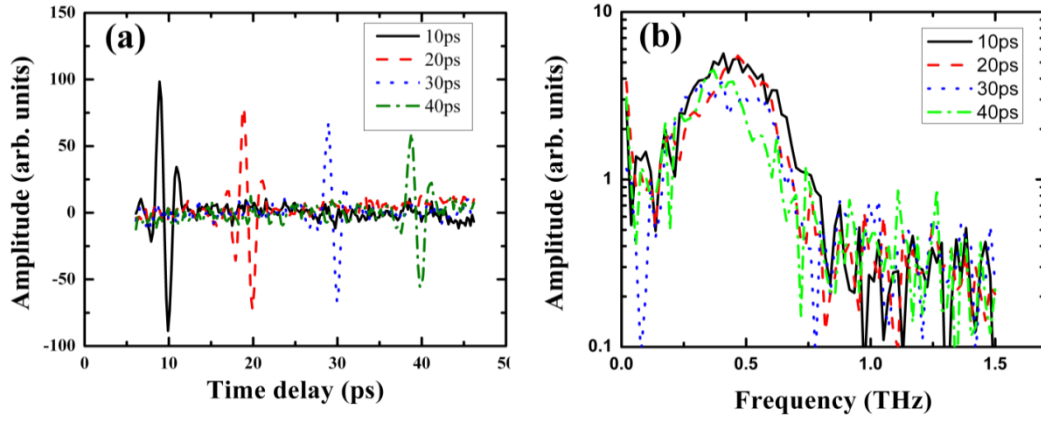

Figure 4.13:   (a) THz waveforms plotted in the AB direction in Figure 4.12. (b) The corresponding spectra of the waveforms in (a).
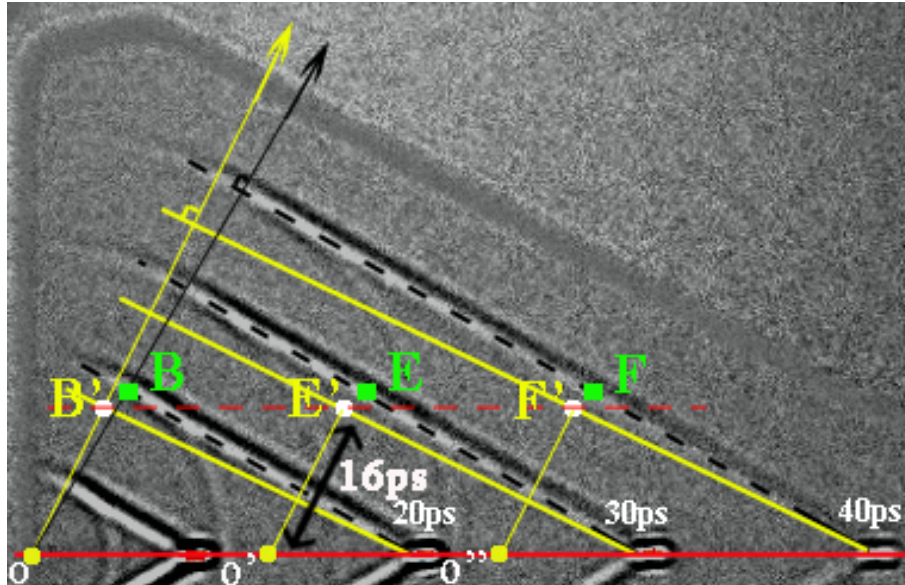

Figure 4.14: Illustration of the THz pulse generated by the optical pump pulse at three different locations (*O*, *O'*, and *O''*).
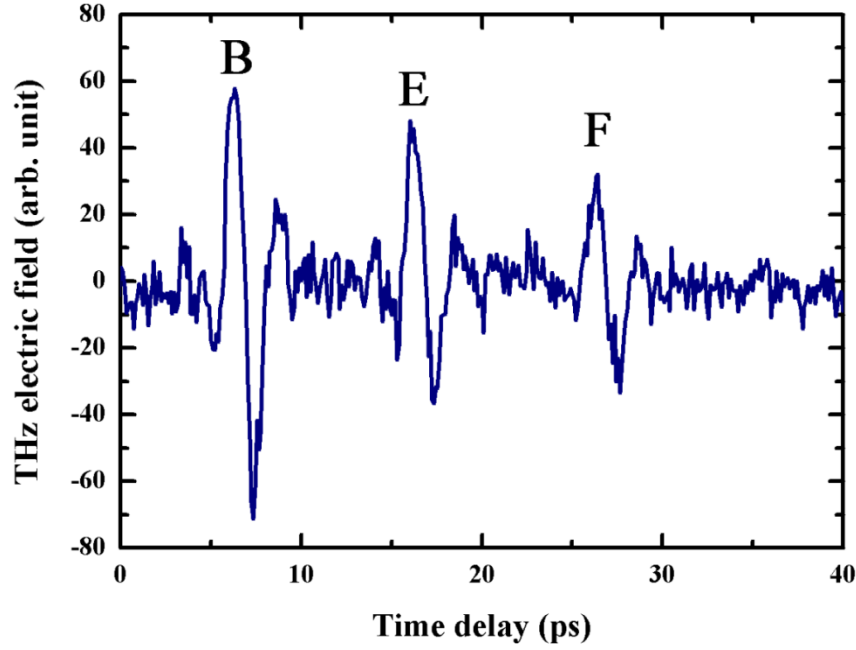
Figure 4.15: THz electric field waveforms collected at points **B**, **E**, and **F** that are marked in Figure 4.14.

As shown in Figure 4.14, the THz pulses that are generated at different points **O**, **O'**, and **O''** by the optical pump pulse can be mapped and studied. For example, it takes 16 ps for the THz pulses to propagate from points **O**, **O'**, and **O''** to **B'**, **E'**, and **F'**, respectively. As we know, because of the image distortion, points **B'**, **E'**, and **F'** correspond to points **B**, **E**, and **F** in the image, respectively. Figure 4.15 shows the THz wave forms that origin from points **O**, **O'**, and **O''**. We find that when the optical pump pulse propagates through the crystal, the generated THz pulse becomes weaker.

4.2.5 The dependence of THz Cherenkov angle on the optical pump pulse beam size and pulse energy

In order to check if there are other nonlinear optical effects when the crystal is pumped by a high energy THz pulse, and if the optical pump beam size influences the THz pulse generation [38, 39], we tried three different beam sizes of 101.6 μm, 48.7 μm, and 27.5 μm, with three different pulse powers at each beam size. Figure 4.16 shows images of the THz Cherenkov wave generated by various beam sizes and pump powers at a time delay of 30 ps. The THz Cherenkov angles measured at various beam sizes, pulse energy, and time delays are summarized in Table 4.4. The Cherenkov angles are the same (approximately 60°, which corresponds to an actual angle of 64°).
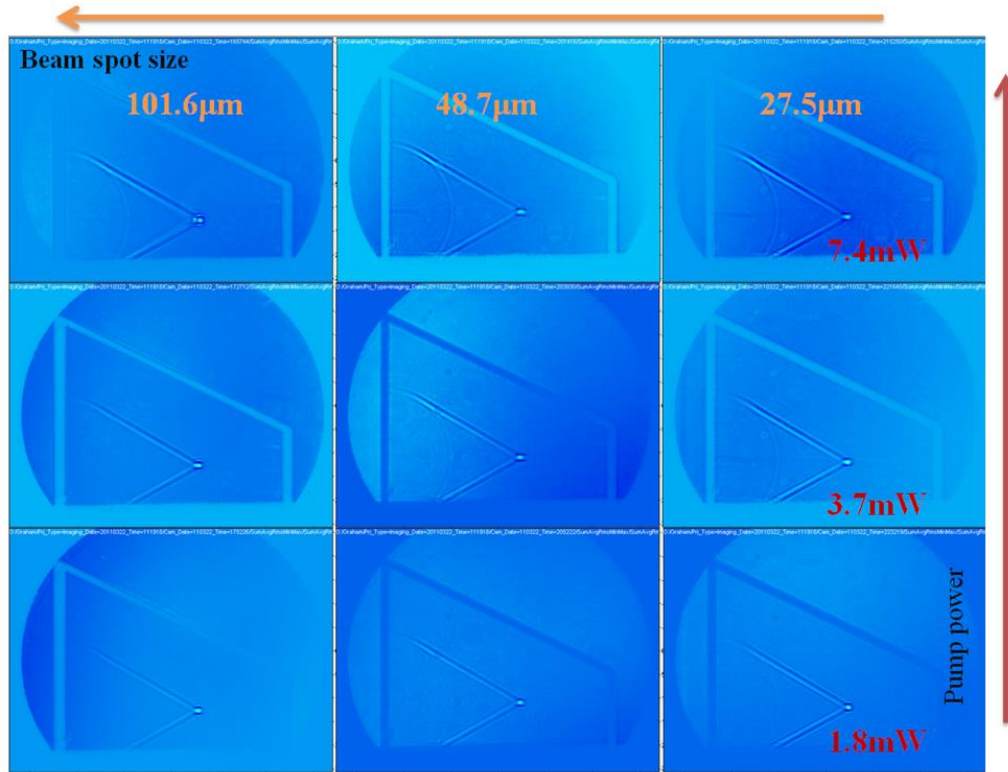

Figure 4.16: Images of the THz Cherenkov wave generated by optical pump pulses as a function of the beam diameter (101.6 μm, 48.7 μm, and 27.5 μm) and the power (1.8 mW, 3.7 mW, and 7.4 mW).

Table 4.4: Cherenkov angles of the THz Cherenkov wave generated by various optical pump beam spot sizes, pulse energy, and time delays.

		Spot size: 101.6μm		Spot size: 48.7μm		Spot size: 27.5μm	
		cone angle	Cherenkov angle	cone angle	Cherenkov angle	cone angle	Cherenkov angle
7.4mW	10ps	58	61	57.7	61.15	60.3	59.85
	20ps	60.4	59.8	58.5	60.75	58.7	60.65
	30ps	58.3	60.85	60.1	59.95	59.2	60.4
	40ps	58.5	60.75	60.1	59.95	59.4	60.3
	Average	58.8±0.8	60.6±0.4	59.1±1	60.45±0.5	59.4±0.45	60.3±0.225
3.7mW	10ps	60.4	59.8	60.3	59.85	58.7	60.65
	20ps	59.2	60.4	58.5	60.75	58.9	60.55
	30ps	58.8	60.6	60	60	59.3	60.35
	40ps	58.6	60.7	59.7	60.15	60.3	59.85
	Average	59.25±0.55	60.375±0.275	59.63±0.55	60.188±0.275	59.3±0.5	60.35±0.25
1.8mW	10ps	60.2	59.9	58.4	60.8	60.1	59.95
	20ps	61.2	59.4	58.6	60.7	58.7	60.65
	30ps	60.6	59.7	59.1	60.45	59	60.5
	40ps	59.8	60.1	59.9	60.05	59.1	60.45
	Average	60.45±0.45	59.775±0.225	59±0.5	60.5±0.25	59.225±0.44	60.39±0.22

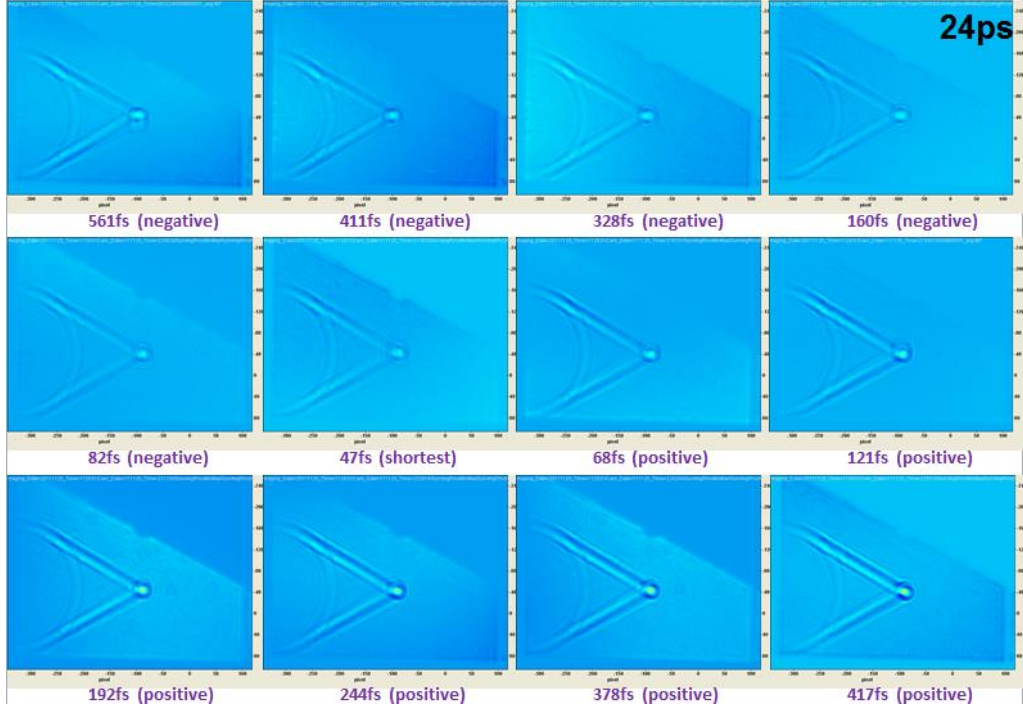## 4.2.6 THz Cherenkov wave dependence on optical pump pulse duration

Figure 4.17: Images of the THz Cherenkov wave captured at various pulse durations with the same optical pump power. 'Positive' and 'negative' mean the optical pump pulse is positively and negatively chirped, respectively.

The generated THz Cherenkov wave on optical pump pulse duration is investigated by imaging THz Cherenkov waves at various optical pump pulse durations. As shown in Figure 4.17, THz Cherenkov angles are the same at various optical pump pulse durations. However, the THz electric field depends on the optical pump pulse duration. Figure 4.18 shows the relationship between the signal strength of the THz wave and the optical pulse duration for positive or negative chirping. We find that the THz generation efficiency is the lowest at the shortest optical pump pulse duration. For the longer pulse with negative chirping, the THz electric field is the same as the THz pulse that is generated by the shortest optical pulse. For longer optical pump pulses with positive chirping, the

THz electric field becomes higher. At around 450 fs, the highest THz pulse amplitude is achieved. We note that, from literature [9], in the tilted-pulse-front excitation geometry, the highest THz generation efficiency exits for negatively chirped optical pump pulses, which is totally different from our results. We are not sure why this is the case. One possible reason for this could be the experimental deviation due to the limitation of the Talbot imaging effect. Since all the experiments were carried out with the same imaging distance between the ICCD camera and the crystal, only one particular THz wave frequency component can be imaged efficiently, so the THz pulse generated by a negatively chirp pump pulse might have a different central frequency and cannot be imaged efficiently.
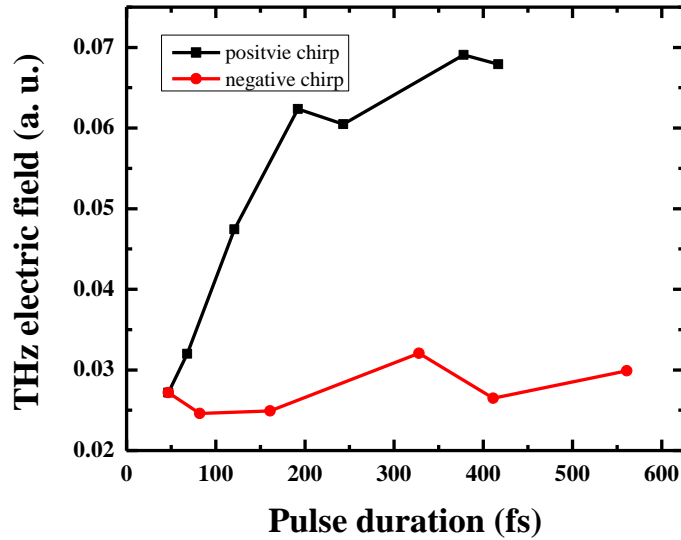

Figure 4.18: Dependence of the THz electric field on the optical pump pulse duration. The red line (circles) is for the negatively chirped optical pump pulse, and the black line (squares) is for the positively chirped optical pump pulse.

4.2.7 THz Cherenkov wave dependence on optical pump pulse polarization

As discussed earlier in Chapter 2, the second-order nonlinear polarization in LiNbO$_3$ follows,

$$\vec{P}^{(2)} = \begin{pmatrix} P_x^{(2)} \\ P_y^{(2)} \\ P_z^{(2)} \end{pmatrix} = 2\varepsilon_0 E^2 \begin{pmatrix} 0 \\ d_{22}\sin^2\theta + 2d_{15}\sin\theta\cos\theta \\ d_{15}\sin^2\theta + d_{33}\cos^2\theta \end{pmatrix}$$

$$= 2\varepsilon_0 E^2 \begin{pmatrix} 0 \\ 0 \\ d_{33} \end{pmatrix} (for\,\theta = 0°) \tag{4.4}$$

$$= 2\varepsilon_0 E^2 \begin{pmatrix} 0 \\ d_{22} \\ d_{15} \end{pmatrix} (for\,\theta = 90°)$$

where θ is the angle between the optical pump pulse polarization and the c-axis of the crystal. According to Ref. [40], $d_{15} = -4.7\,pm/V$, $d_{33} = -27\,pm/V$, $d_{22} = 3.2\,pm/V$, the second-order polarization is the largest when the optical pump pulse polarization is parallel to the c-axis, while for the case that the optical pump pulse polarization is perpendicular to the c-axis, the second-order polarization is small but non zero.
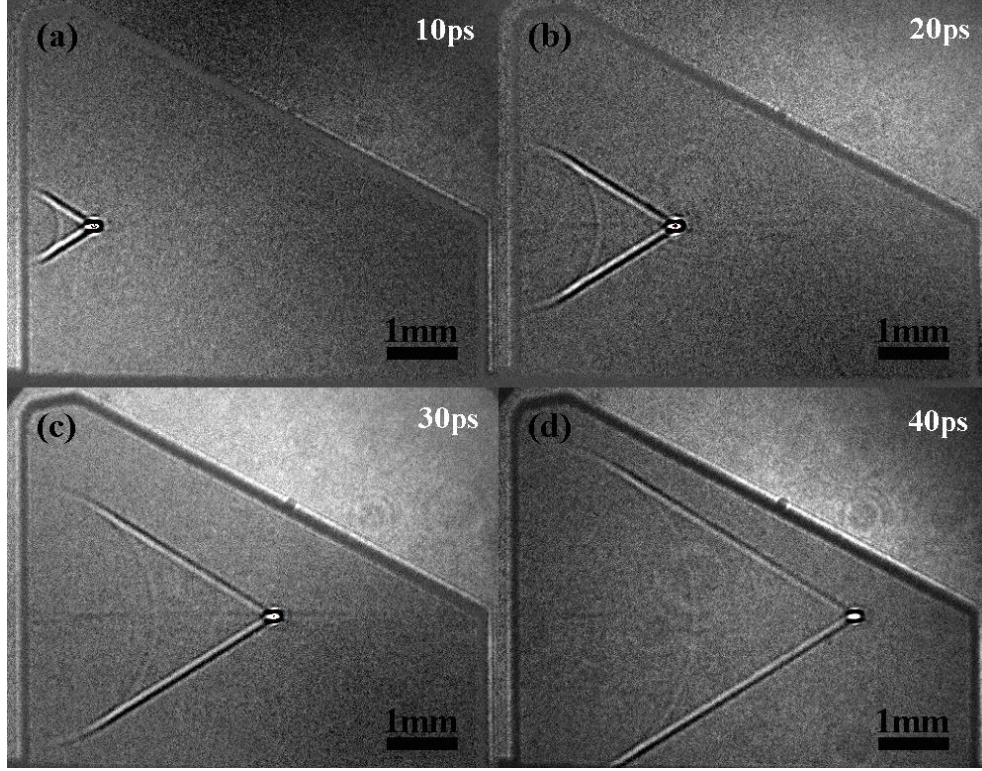
Figure 4.19: Images of the THz Cherenkov wave inside the **LN 1** crystal captured at time delays of (a) 10 ps, (b) 20 ps, (c) 30 ps, and (d) 40 ps, respectively. The experimental parameters are the same as that of Figure 4.4 except that the optical pump pulse polarization is perpendicular to the c-axis of the crystal.

Figure 4.19 shows images of the THz Cherenkov wave with the same experimental conditions as in Figure 4.4, except that the optical pump pulse polarization is perpendicular to the c-axis. We find that both the THz Cherenkov wave and the transition-like radiation become weaker. Furthermore, the velocity of the THz Cherenkov wave and the transition-like radiation are the same as those obtained in Figure 4.4. However, the velocity of the optical pump pulse becomes smaller and the optical index changes from 2.23 ± 0.01 to 2.36 ± 0.01. The measured Cherenkov angle also decreases from 59.7 ± 0.3 °to 57.8 ± 0.3 °. This is because the optical pulse experiences the ordinary refractive index when its polarization is perpendicular to the c-axis of the LiNbO$_3$ crystal. We note that the measured ordinary optical refractive index (2.36 ± 0.01) also matches the value (2.358) in the literature [3]. Because both ordinary and extraordinary optical pump

88

rays can generate THz waves but propagate at different speeds, it's interesting to explore what happens when both rays are present in the crystal.
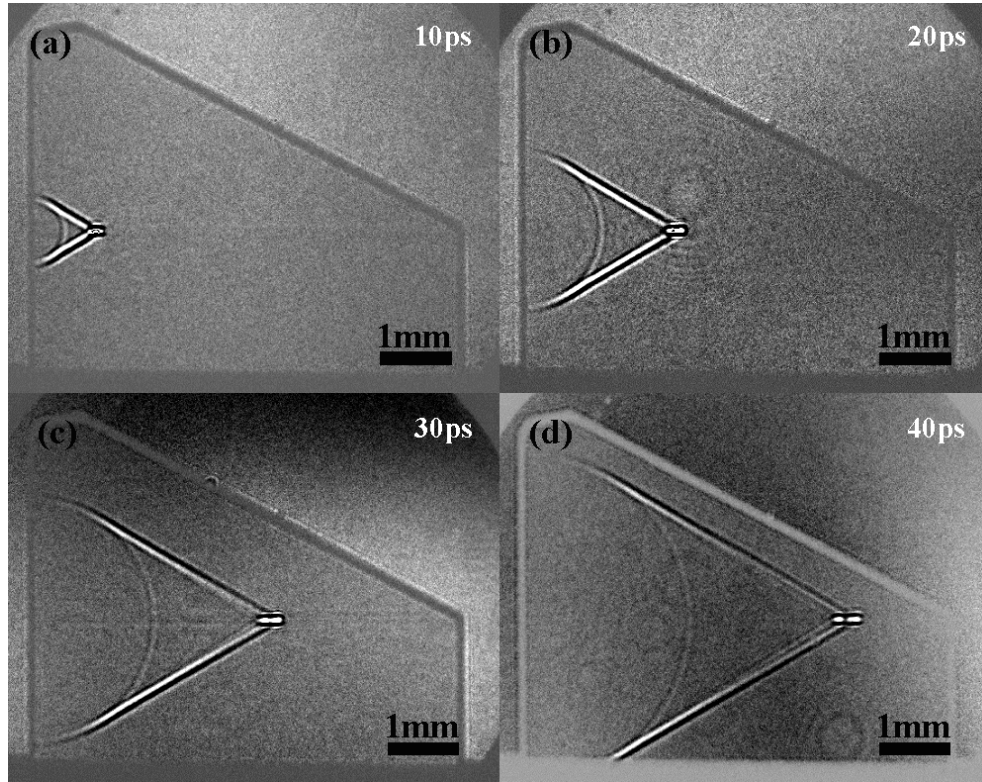

Figure 4.20: Images of the THz Cherenkov wave inside the **LN 1** crystal captured at time delays of (a) 10 ps, (b) 20 ps, (c) 30 ps, and (d) 40 ps, respectively. The experimental parameters are the same as those for Figure 4.4 except that the optical pump pulse polarization is 45 °to the *c*-axis of the crystal.
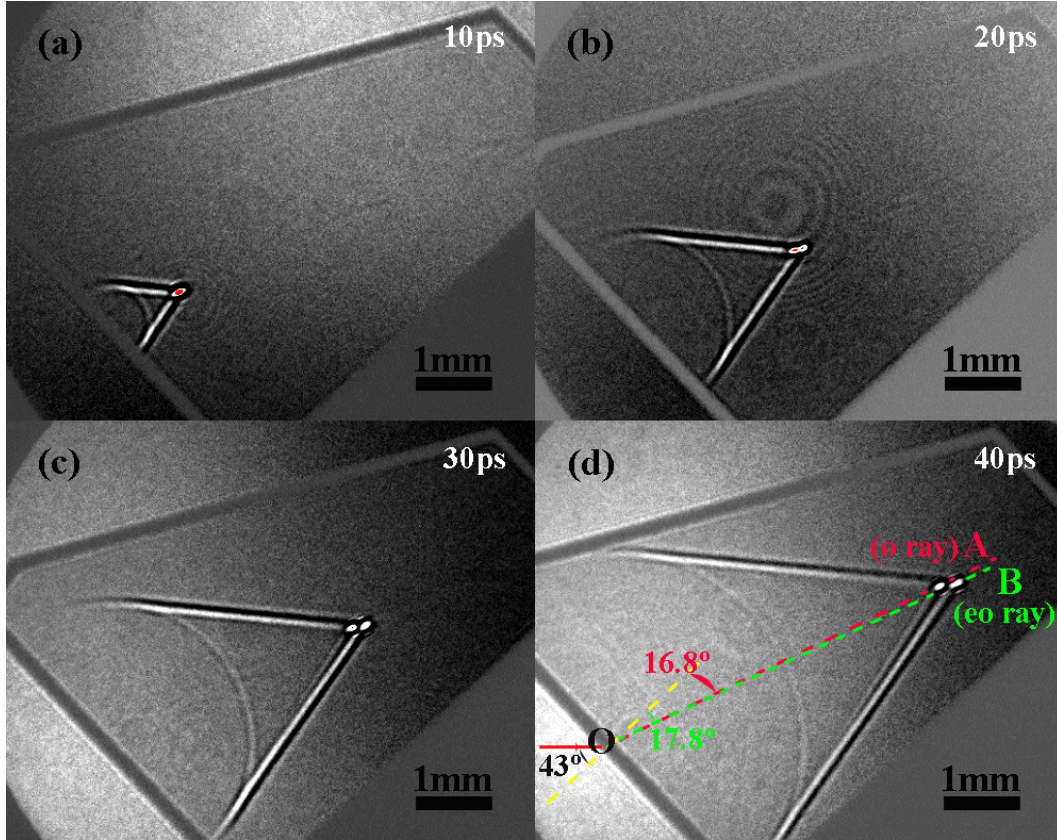
Figure 4.21: Images of the THz wave inside the **LN1** crystal at time delays of (a) 10 ps, (b) 20 ps, (c) 30 ps, and (d) 40 ps. The optical pump pulse polarization is 43 ° with respect to the *c*-axis. The incident optical pulse travels horizontally at the left side of the air/LiNbO$_3$ interface.

The imaging experiment was carried out with the optical pump pulse polarization 43 ° relative to the *c*-axis of the crystal. This splits the pump beam into two rays, the ordinary ray (with index n_o) and the extraordinary ray (with index n_{eo}). As shown in Figure 4.20, the two rays are separated from each other as they propagate through the LiNbO$_3$ crystal. Moreover, if the crystal is tilted, as shown in Figure 4.21, the propagation directions of the two rays are different due to different refraction angles. Lastly, from Figure 4.20 and Figure 4.21, we find that the THz Cherenkov wave is generated more efficiently by the extraordinary ray, which is consistent with the predicted second-order polarization. Because the transition-like radiation is generated on the surface of the crystal by the two rays at the same time and has the same polarization along the *c*-axis, no separation

happens. On the other hand, since the two rays are separated further and further in the process of propagation, the THz Cherenkov wave generated by the two rays are also separated and the interference pattern can be clearly seen in Figure 4.20(d) and Figure 4.21(d).

According to the Snell's law,

$$\frac{sin\theta_1}{sin\theta_2} = \frac{n_2}{n_1} \tag{4.5}$$

where θ_1 and θ_2 are the incident angle and refractive angle, respectively, and n_1 and n_2 are the refractive indices of the first and the second medium, respectively, we can calculate the refractive indices of the o ray and eo ray from Figure 4.21(d). We find that $n_o = \frac{sin43°}{sin16.8°} = 2.36$, and $n_{eo} = \frac{sin43°}{sin17.8°} = 2.23$, which are consistent with both experiment results that are calculated from group velocities measurement ($n_o = 2.36 \pm 0.01$, $n_{eo} = 2.23 \pm 0.01$) and group indices in the literature ($n_o = 2.358$, $n_{eo} = 2.250$) [3].

Finally, as done in Ref. [32], we also measured the spectra of the transmitted optical pump pulse at different optical pump pulse polarizations. As shown in Figure 4.22, we find that the redshifting is enhanced (i.e. wavelength region from 830-860 nm) when we decrease the angle between the optical pump pulse polarization and the *c*-axis of the crystal, which is consistent with the observation made in Ref. [32].
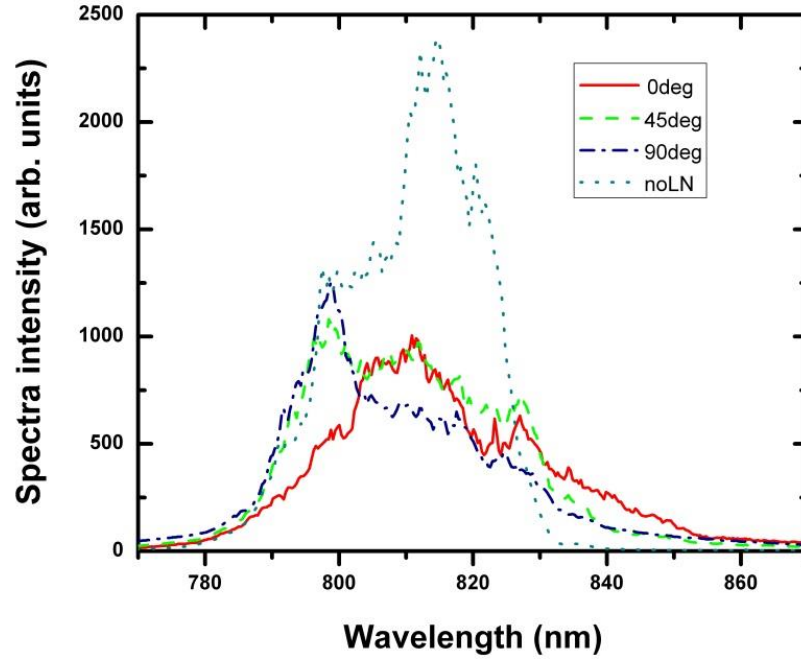
Figure 4.22: Spectra of the optical pump pulse. (noLN) is the original spectrum without the LiNbO$_3$ crystal, (0deg) is transmitted through the LiNbO$_3$ crystal with the optical pump pulse polarization parallel to the c-axis; (45deg) is transmitted through the LiNbO$_3$ crystal with the angle between the optical pump pulse polarization and the c-axis 45°; (90deg) is transmitted through the LiNbO$_3$ crystal with the optical pump pulse polarization perpendicular to the c-axis.

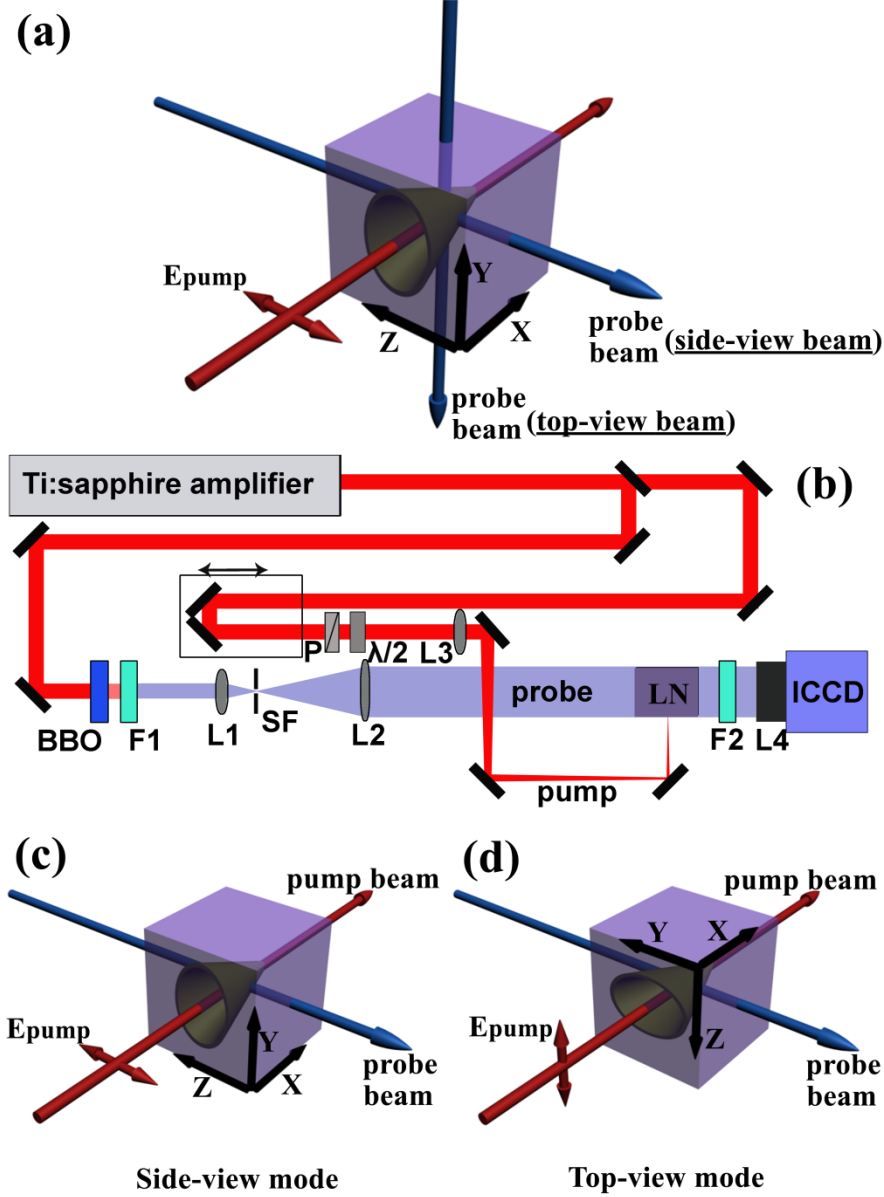# 4.3 Imaging THz Cherenkov waves in LiNbO$_3$ in top-view mode

Figure 4.23: (a) Illustration of the top-view mode and side-view mode. The side-view probe beam propagates along the Z direction (*c*-axis of the crystal), and the top-view probe beam is along the Y direction. (b) Experimental setup for top-view and side-view imaging. The imaging mode is determined by the crystal orientation, pump pulse polarization, and probe pulse propagation direction, as shown in (c) and (d). In the experiment, the illustration of the crystal orientation, pump pulse polarization, and probe pulse propagation direction in side-view mode (c) and top-view mode (d), respectively.

As illustrated in Figure 4.2 (in Section 4.1) and Figure 4.23(a), depending on the relative relationship between the crystal orientation, pump pulse polarization, and probe beam propagation direction, THz Cherenkov waves can be imaged in side-view, and top-view modes. In Section 4.2, images of the THz Cherenkov wave are captured in side-view mode, in which the probe pulse propagates parallel to the Z direction (c-axis of the crystal, as illustrated in Figures 4.2(a) and (b), and Figure 4.23(c)). In this section, as shown in Figure 4.2(c) and (d) and Figure 4.23(d), we make the probe pulse propagate perpendicular to the c-axis of the crystal (Y direction) and try to image THz Cherenkov waves in top-view mode.

Instead of the $LiNbO_3$ prism that is used in Section 4.2, a rectangular $LiNbO_3$ crystal is employed for top-view imaging here. As illustrated in Figure 4.23(b), in order to make the experimental performed easily, the probe and pump propagation directions are kept the same for both side-view mode and top-view mode. Instead, as shown in Figures 4.23(c) and (d), the crystal orientation and pump beam polarization are rotated around the propagation direction of the pump pulse (X direction). For side-view mode, the pump pulse polarization and the c-axis of the crystal are parallel to the probe beam, while for top-view mode, they are perpendicular to the probe beam.

Figures 4.24(a)-(e) show the side-view images at different time delays, and Figures 4.24(f)-(j) show the top-view images at different time delays. For both imaging modes, the optical pump pulse propagates along the x-axis with optical pump pulse polarization parallel to the c-axis of the $LiNbO_3$ crystal. The measured optical pulse group index at 800 nm is 2.25, which is the same as observed in Section 4.2 and the literature value [3]. Different from the Cherenkov angle (60.2 °) measured in the side-view images, the Cherenkov angle measured in top-view mode is 63.9 °, corresponding to an actual value of 69 ° and a simulated value of 68.8 ° (as shown in Table 4.3). As shown in Figure 2.5 in Section 2.12, the reason for observing different Cherenkov angles in different imaging modes is that the THz pulse propagating in the XY plane is imaged in side-view mode and the THz electric field is parallel to the c-axis of the crystal (marked in Figure 4.24(e)), while the THz pulse propagating in the XZ plane is imaged in top-view

mode, and the THz pulse polarization is parallel to the wavefront of the THz pulse (marked in Figure 4.24(j)). THz pulses that propagate in the XY versus XZ planes experience different refractive indices and thus show different Cherenkov angles.
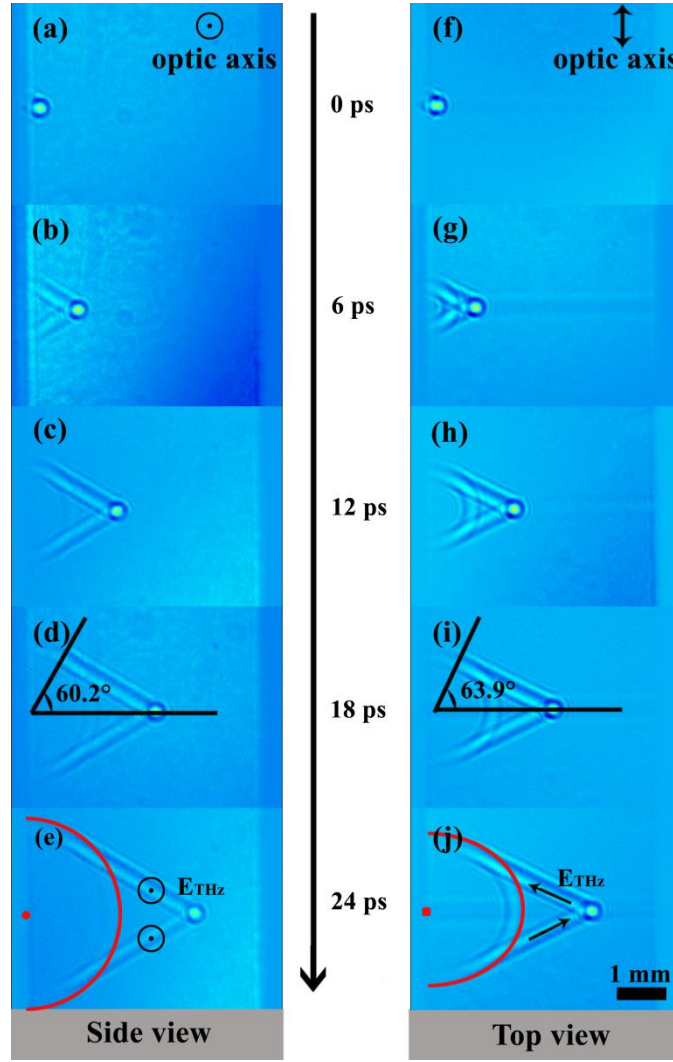

Figure 4.24: (a)-(e) Side-view images of the THz Cherenkov wave in the $LiNbO_3$ crystal captured at time delays of (a) 0 ps, (b) 6 ps, (c) 12 ps, (d) 18 ps, and (e) 24 ps, respectively. (f)-(j) Top-view images of the THz Cherenkov wave in the $LiNbO_3$ crystal at time delays of (f) 0 ps, (g) 6 ps, (h) 12 ps, (i) 18 ps, and (j) 24 ps, respectively.

Compared to the semicircle wavefront of the transition-like radiation in the side-view image, the wavefront of the transition-like radiation in top-view shows an elliptical profile. This is because the polarization of the THz wave that propagates at different directions in the XZ plane is different.

95

Based on the images of the THz Cherenkov wave in both of side-view mode and top-view mode, a 3D THz Cherenkov wave can be constructed experimentally.

4.4 Side-view imaging of the THz Cherenkov wave generated by a line-focused optical pump pulse

As illustrated in Figures 4.25(a) and (b), the optical pump pulse is focused by a cylindrical lens onto the LiNbO$_3$ crystal with its long axis oriented in two different directions, respectively. One orientation of the pump beam line is parallel to the probe pulse propagation direction (Figure 4.25(a)), and another one is perpendicular to the propagation direction (Figure 4.25(b)).
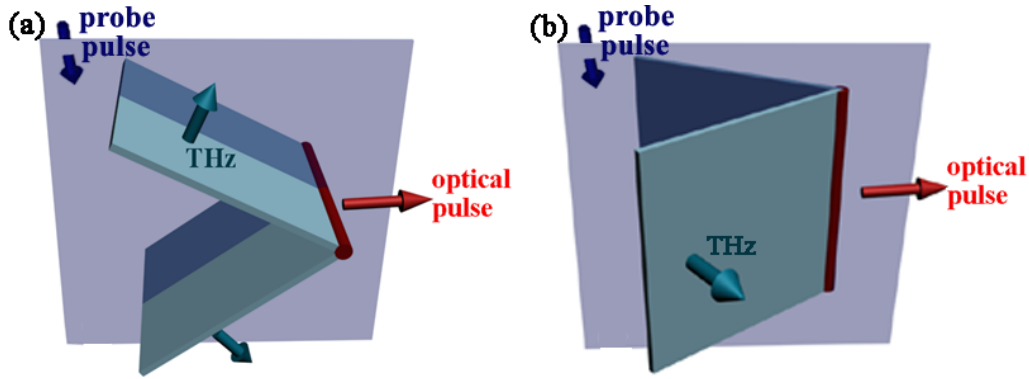

Figure 4.25: Illustration of the line focused optical pump geometries. (a) The optical pump beam line is parallel to the probe pulse propagation direction. (b) The optical pump beam is perpendicular to the probe pulse propagation direction.

Figure 4.26 shows the side-view images of the THz wave in a LiNbO$_3$ crystal generated in the pump geometry shown in Figure 4.25(a). Different from one Cherenkov cone in the point focused geometry, two Cherenkov cones are found in the image. This is because a THz pulse has both positive and negative electric field. When the probe pulse and the THz pulse propagate perpendicularly to each other, the positive phase shift modulation is neutralized by the negative phase shift modulation, and only the modulation at two ends of the line survives. As shown in Figure 4.27, the time delay (ΔL) is proportional to the length of the focused beam line (W).
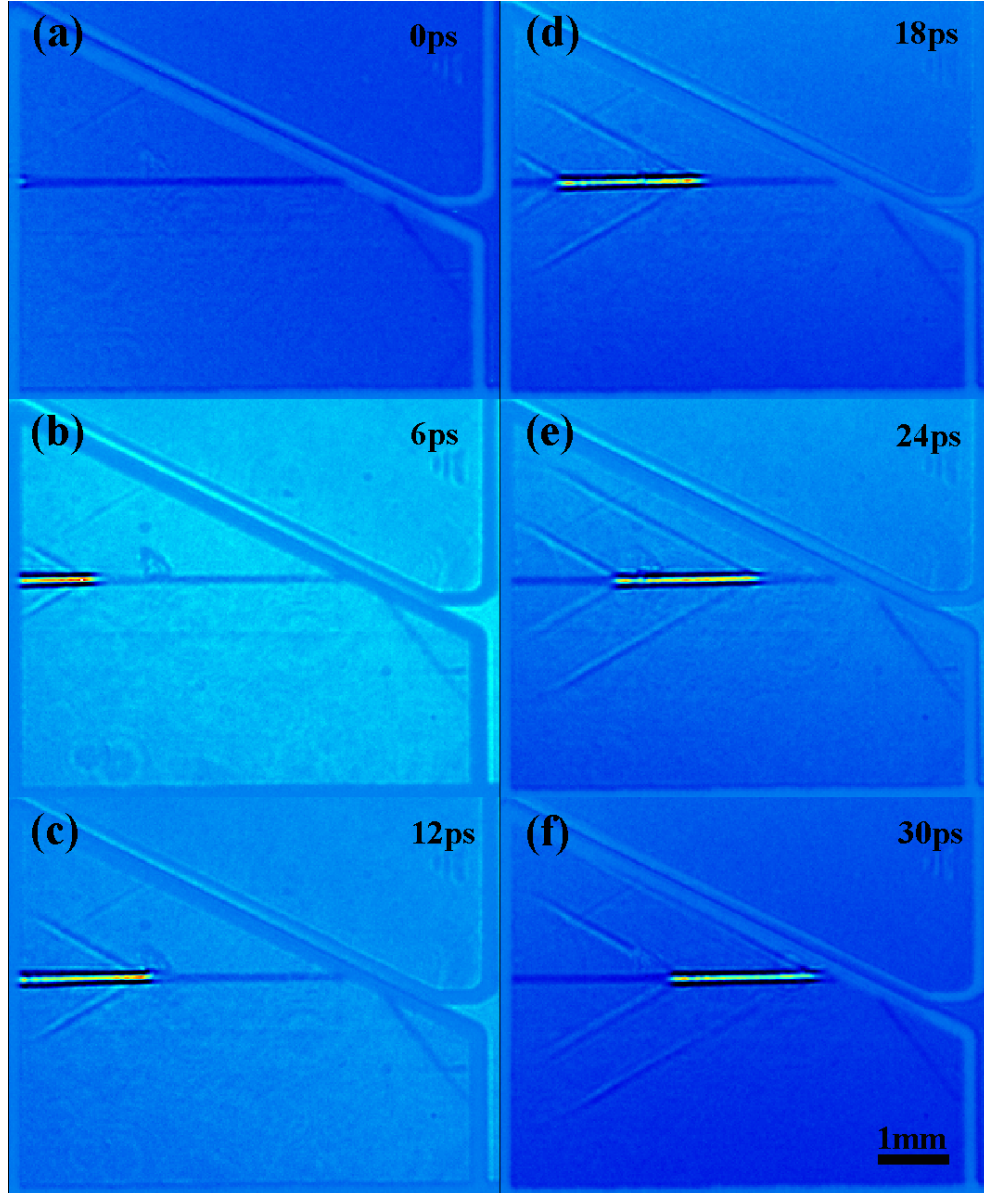
Figure 4.26: Images of the THz Cherenkov wave generated by the line focused pump pulse at time delays of (a) 0 ps, (b) 6 ps, (c) 12 ps, (d) 18 ps, (e) 24 ps, and (c) 30 ps, respectively. The orientation of the focused beam is parallel to the probe pulse propagation direction.

Figure 4.25(b) and Figure 4.28 demonstrate why a broad optical pump beam cannot generate THz pulses efficiently. As shown in Figure 4.28, we find that the THz Cherenkov wave generated from different points along the line cancelled with each other. Because the phase match condition cannot be satisfied, as marked

by the arrow in Figure 4.28, the generated THz pulse is mainly due to the transition-like radiation.
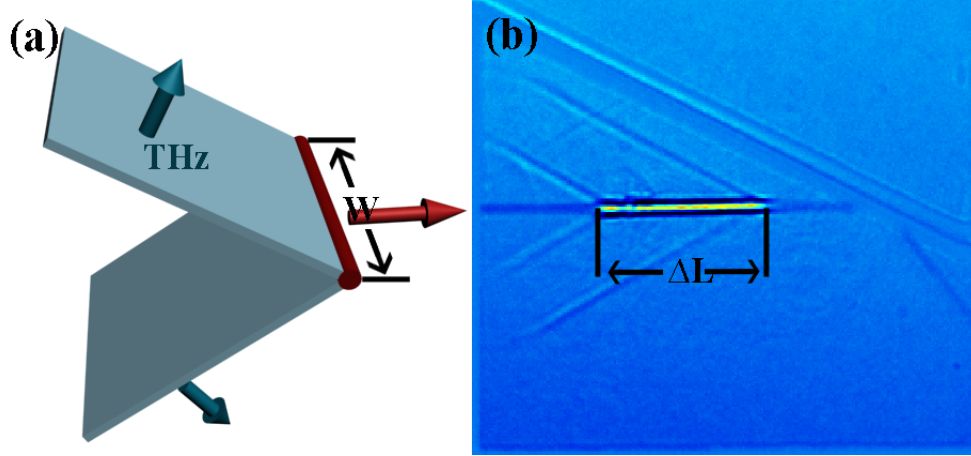

Figure 4.27: (a) Illustration of the line-focused pump geometry with the length of the focused beam line, W. (b) Illustration of the time delay (ΔL) between the two Cherenkov waves.
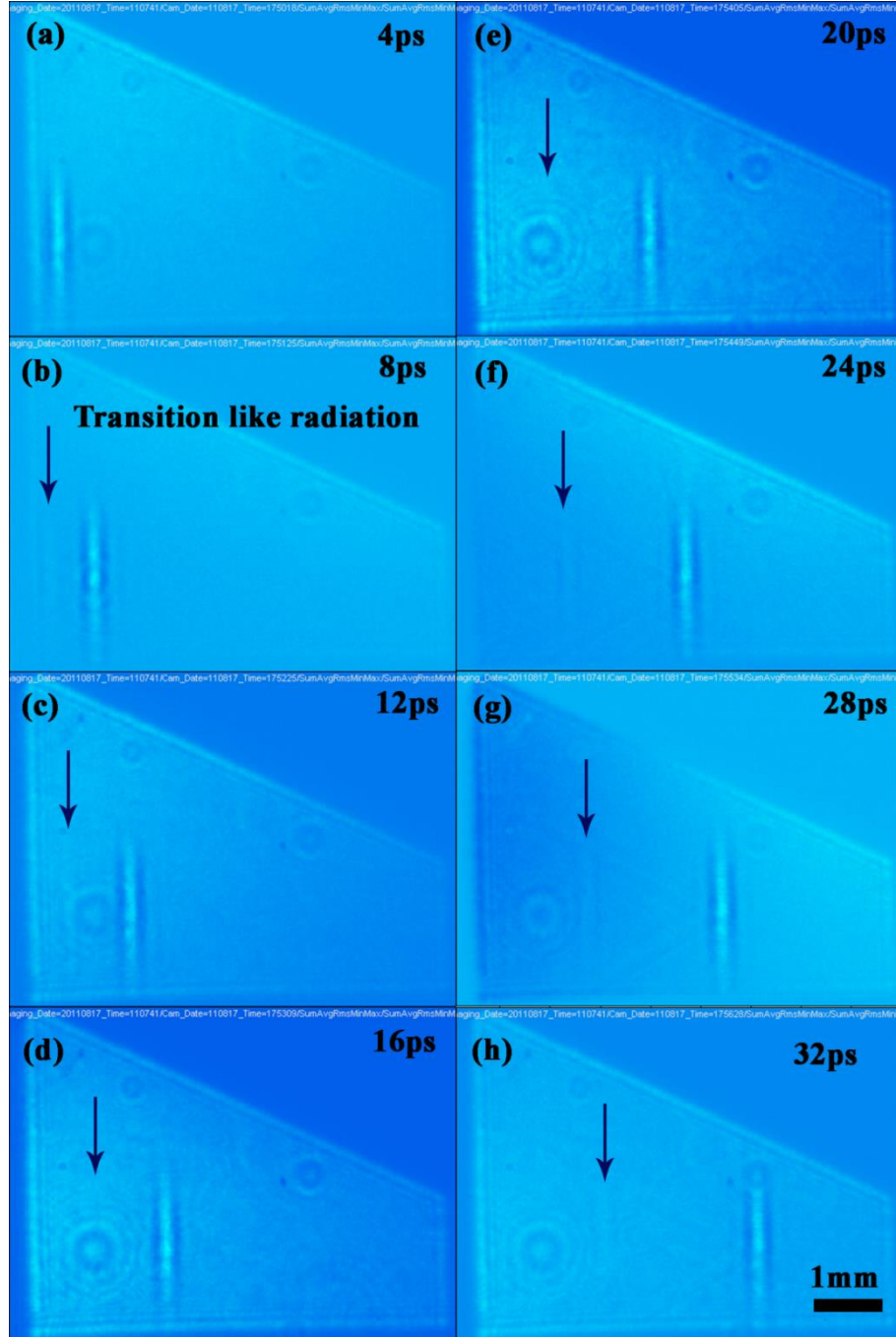
Figure 4.28: Images of the THz Cherenkov wave generated by the line focused pump pulse at time delays of (a) 4 ps, (b) 8 ps, (c) 12 ps, (d) 16 ps, (e) 20 ps, (f) 24 ps, (g) 28 ps, and (h) 32 ps, respectively. The orientation of the focused beam line is perpendicular to the probe pulse propagation direction and is in vertical direction.

4.5 Conclusions

In this Chapter, we have demonstrated how to image THz Cherenkov waves in $LiNbO_3$ and $LiTaO_3$ crystals with the transverse imaging technique. The imaging distortion caused by the transverse imaging geometry is simulated with the 3ds Max software package. Based on the transverse imaging technique, we can observe how THz waves are generated in $LiNbO_3$ crystals in both side-view mode and top-view mode. The velocities of the THz pulse and the optical pulse can be measured directly. We find that the THz Cherenkov angle is independent of the optical pump pulse energy, pulse duration, and pump beam size. The THz generation efficiency is strongly determined by the optical pump pulse duration. We also find that when the optical pump pulse is the shortest (47 fs) or negatively chirped, the generation efficiency is the lowest, and when the pump pulse duration is about 450 fs (positively chirped), the generation efficiency is the highest. Two types of the line-focused pump geometries are employed to demonstrate the imaging smearing effect due to the transverse imaging geometry, as well as reduction in THz generation efficiency.

References:

1. D. H. Auston, K. P. Cheung, J. A. Valdmanis, and D. A. Kleinman, "Cherenkov radiation from femtosecond optical pulses in electro-optic media," Phys. Rev, Lett. **53**, 1555-1558 (1984).

2. M. C. Hoffmann, K.-L. Yeh, J. Hebling, and K. A. Nelson, "Efficient terahertz generation by optical rectification at 1035 nm," Opt. Express **15**, 11706-11713 (2007).

3. T. Feurer, N. S. Stoyanov, D. W. Ward, J. C. Vaughan, E. R. Statz, and K. A. Nelson, "Terahertz polaritonics," Annu. Rev. Mater. Res. **37**, 317-350 (2007).

4. R. M. Koehl, S. Adachi, and K. A. Nelson, "Real-space polariton wave packet imaging," J. Chem. Phys. **110**, 1317-1320 (1999).

5. D. W. Ward, E. Statz, N. Stoyanov, and K. A. Nelson, "Simulation of phonon-polariton generation and propagation in ferroelectric $LiNbO_3$ crystals," (arXiv.org, 2004).

6. J. Hebling, G. Almasi, I. Z. Kozma, and J. Kuhl, "Velocity matching by pulse front tilting for large-area THz-pulse generation," Opt. Express **10**, 1161-1166 (2002).

7. J. Hebling, K.-L. Yeh, M. C. Hoffmann, B. Bartal, and K. A. Nelson, "Generation of high-power terahertz pulses by tilted-pulse-front excitation and their application possibilities," J. Opt. Soc. Am. B **25**, B6-B19 (2008).

8. J. A. Fulop, L. Palfalvi, G. Almasi, and J. Hebling, "Design of high-energy terahertz sources based on optical rectification," Opt. Express **18**, 12311-12327 (2010).

9. J. A. Fulop, L. Palfalvi, S. Klingebiel, G. Almasi, F. Krausz, S. Karsch, and J. Hebling, "Generation of sub-mJ terahertz pulses by optical rectification," Opt. lett. **37**, 557-559 (2012).

10. A. G. Stepanov, J. Hebling, and J. Kuhl, "Efficient generation of subpicosecond terahertz radiation by phase-matched optical rectification using ultrashort laser pulses with tilted pulse fronts," Appl. Phys. Lett. **83**, 3000-3002 (2003).

11. M. C. Hoffmann, and J. A. Fulop, "Intense ultrashort terahertz pulses: generation and applications," J. Phys. D: Appl. Phys. **44**, 17 (2011).

12. F. Blanchard, G. Sharma, L. Razzari, X. Ropagnol, H. C. Bandulet, F. Vidal, R. Morandotti, J. C. Kieffer, T. Ozaki, H. Tiedje, H. Haugen, M. Reid, and F. Hegmann, "Generation of Intense Terahertz Radiation via Optical Methods," IEEE J. Sel. Top. Quant. Electron. **17**, 5-16 (2011).

13. H. Hirori, A. Doi, F. Blanchard, and K. Tanaka, "Single-cycle terahertz pulses with amplitudes exceeding 1 MV/cm generated by optical rectification in LiNbO3," Appl. Phys. Lett. **98**, 091106 (2011).

14. D. W. Ward, "Polaritonics: an intermediate regime between electronics and photonics," in *Department of Chemistry* (Massachusetts Institute of Technology, 2005).

15. Z. Chen, "Modeling phonon-polariton generation and control in ferroelectronic crystals," in *Department of Physics* (Massachusetts Institute of Technology, 2009).

16. D. H. Auston, and M. C. Nuss, "Electrooptic generation and detection of femtosecond electrical transients," IEEE J. Sel. Top. Quant. Electron. **24**, 184-197 (1988).

17. J. K. Wahlstrand, and R. Merlin, "Cherenkov radiation emitted by ultrafast laser pulses and the generation of coherent polaritons," Phys. Rev. B **68**, 054301 (2003).

18. R. M. Koehl, S. Adachi, and K. A. Nelson, "Direct visualization of collective wavepacket dynamics," J. Phys. Chem. A **103**, 10260-10267 (1999).

19. T. Feurer, J. C. Vaughan, and K. A. Nelson, "Spatiotemporal coherent control of lattice vibrational waves," Science **299**, 374-377 (2003).

20. P. Peier, S. Pilz, F. Mueller, K. A. Nelson, and T. Feurer, "Analysis of phase contrast imaging of terahertz phonon-polaritons," J. Opt. Soc. Am. B **25**, B70-B75 (2008).

21. Q. Wu, C. A. Werley, K.-H. Lin, A. Dorn, M. G. Bawendi, and K. A. Nelson, "Quantitative phase contrast imaging of THz electric fields in a dielectric waveguide," Opt. Express **17**, 9219-9225 (2009).

22. N. S. Stoyanov, D. W. Ward, T. Feurer, and K. A. Nelson, "Direct visualization of phonon-polariton focusing and amplitude enhancement," J. Chem. Phys. **117**, 2897-2901 (2002).

23. N. S. Stoyanov, D. W. Ward, T. Feurer, and K. A. Nelson, "Terahertz polariton propagation in patterned materials," Nat. Mater. **1**, 95-98 (2002).

24. N. S. Stoyanov, T. Feurer, D. W. Ward, E. R. Statz, and K. A. Nelson, "Direct visualization of a polariton resonator in the THz regime," Opt. Express **12**, 2387-2396 (2004).

25. M. I. Bakunov, S. B. Bodrov, A. V. Maslov, and M. Hangyo, "Theory of terahertz generation in a slab of electro-optic material using an ultrashort laser pulse focused to a line," Phys. Rev. B **76**, 085346 (2007).

26. L. Xu, X.-C. Zhang, and D. H. Auston, "Terahertz beam generation by femtosecond optical pulses in electrooptic materials," App. Phys. Lett. **61**, 1784-1786 (1992).

27. N. N. Zinov'ev, A. S. Nikoghosyan, and J. M. Chamberlain, "Terahertz radiation from a nonlinear slab traversed by an optical pulse," Phys. Rev. Lett. **98**, 044801 (2007).

28. N. N. Zinov'ev, A. S. Nikoghosyan, R. A. Dudley, and J. M. Chamberlain, "Conversion of short optical pulses to terahertz radiation in a nonlinear medium: Experiment and theory," Phys. Rev. B **76**, 253114 (2007).

29. M. I. Bakunov, A. V. Maslov, and S. B. Bodrov, "Fresnel formulas for the forced electromagnetic pulses and their application for optical-to-terahertz conversion in nonlinear crystals," Phys. Rev. Lett. **99**, 203904 (2007).

30. A. Schneider, "Theory of terahertz pulse generation through optical rectification in a nonlinear optical material with a finite size," Phys. Rev. A **82**, 033825 (2010).

31. R. Boyd, *Nonlinear Optics* (Elsevier, 2008).

32. K. L. Yeh, M. C. Hoffmann, J. Hebling, and K. A. Nelson, "Generation of 10 μJ ultrashort terahertz pulses by optical rectification," Appl. Phys. Lett. **90**, 171121 (2007).

33. K.-H. Lin, C. A. Werley, and K. A. Nelson, "Generation of multicycle terahertz phonon-polariton waves in a planar waveguide by tilted optical pulse fronts," Appl. Phys. Lett. **95**, 103304 (2009).

34. B. E. A. Saleh, and M. C. Teich, *Fundamentals of Photonics* (Wiley-Interscience, 2007).

35. Y.-M. Sun, Z.-L. Mao, B.-H. Hou, G.-Q. Liu, and L. Wang, "Giant birefringence of lithium niobate crystals in the terahertz region," Chin. Phys. Lett. **24**, 414-417 (2007).

36. G. A. Askaryan, "Cerenkov radiation and transition radiation from electromagnetic waves," Sov. Phys. JETP **15**, 943-946 (1962).

37. A. Nahata, A. S. Weling, and T. F. Heinz, "A wideband coherent terahertz spectroscopy system using optical rectification and electro-optic sampling," Appl. Phys. Lett. **69**, 2321-2323 (1996).

38. Z. Xu, and X. C. Zhang, "Optical rectification in an area with a diameter comparable to or smaller than the center wavelength of terahertz radiation," Opt. Lett. **27**, 1067-1069 (2002).

39. G. L. Dakovski, B. Kubera, S. Lan, and J. Shan, "Finite pump-beam-size effects in optical pump-terahertz probe spectroscopy," J. Opt. Soc. Am. B **23**, 139-141 (2006).

40. A. Yariv, and P. Yeh, *Optical Waves in Crystals: Propagation and Control of Laser Radiation* (Wiley-Interscience, 2002).

Chapter 5

Ultrafast imaging of terahertz pulses generated by the tilted-pulse-front excitation technique

In this chapter, ultrafast imaging of the terahertz pulse generated by the tilted-pulse-front excitation technique is demonstrated. The Cherenkov angle, the tilt angle of the optical pump pulse wave front and the optical pump beam size are determined from the obtained images. The terahertz pulse generation efficiency is found to be the highest when the tilt angle of the optical pump pulse is between $61\,^\circ$ and $67\,^\circ$, and it can be optimized in real time using the imaging method. In addition, the 3D structure of the generated THz wave is analyzed using MATLAB.

5.1 Introduction to intense THz pulse generation in LiNbO₃ crystals

There has been much interest recently in the development and application of intense table-top terahertz (THz) pulse sources [1-9]. One of the most popular methods employs femtosecond laser pulses to pump a LiNbO₃ crystal and generate coherent THz pulses by optical rectification [1-8, 10]. As discussed in Chapter 4, since the refractive index of the generated THz wave is much larger than that of the optical pump pulse, collinear phase matching cannot be satisfied and a Cherenkov THz shock wave is formed [1, 2, 7, 8]. In order to generate THz waves in LiNbO₃ crystals more efficiently, the tilted-pulse-front excitation technique (mentioned in Chapter 2), in which the optical pump pulse wave front is tilted to match the wave front of the generated THz wave, was proposed and demonstrated in the past several years [1-8]. Based on this technique, the highest THz electric field 1.2 MV/cm was reported [4]. More recently, the sub-mJ THz pulse with the 0.25% generation efficiency was achieved [11], and more work is being done to improve the generation efficiency and increase the THz pulse energy [5].

The energy of the THz pulse generated by optical rectification depends on many parameters such as the optical pump pulse energy, the THz generation efficiency, the THz absorption in the crystal, and the THz coupling efficiency from the crystal to the air. In the case of the tilted-pulse-front excitation technique, additional parameters are introduced, such as the tilt angle of the optical pump pulse, the distortion of the optical pump pulse wave front, the optical pump pulse duration [5], and the cut angle of the LiNbO₃ prism.

The most commonly used method of optimizing the THz generation and coupling efficiency is to collect the output THz pulse with parabolic mirrors and measure the energy with a THz energy detector [4, 7]. The significant downside of this technique is its sensitivity to the alignment of the THz pulse collection setup outside the LiNbO₃ crystal, as well as to all of the parameters listed above.

In this Chapter, we demonstrate that real time imaging of THz waves generated by the tilted-pulse-front excitation technique in a LiNbO$_3$ crystal. It allows for a much more efficient optimization of THz generation by visualizing the changes in the THz generation due to changes in the tilt angle of the optical pump pulse, the wave front distortion, the THz absorption, as well as in the reflection losses at the exit face of the crystal.

5.2 Imaging THz pulses generated by the tilted-pulse-front excitation technique

5.2.1 Experimental setup

Figure 5.1: (a) Illustration of the experimental setup used to generate THz pulses with the tilted-pulse-front excitation technique and image the generated THz pulses. The optical pump beam ($\lambda_{central} = 800 \text{ nm}$) goes through a slit, and is then diffracted by a grating. The wave front of the optical pump pulse is tilted by the grating and is imaged onto the LiNbO$_3$ crystal with a lens. The optical probe pulse (($\lambda_{central} = 400 \text{ nm}$) travelling normal to the optical pump pulse images the generated THz wave and is recorded by an intensified CCD (ICCD) camera system (not shown). (b) The detailed imaging geometry (side view) in the LiNbO$_3$ crystal. The optical pump pulse polarization is parallel to the c-axis of the crystal, and the optical probe pulse polarization is parallel to the optical pump beam.

An amplified Ti:sapphire laser system (0.9 mJ, 100 fs, 800 nm, 1 kHz) was employed to generate and image the THz wave in the LiNbO$_3$ (MgO 5% doped) crystal. The laser pulse from the Ti:sapphire laser system was split into two beams:

a higher power pump beam and a lower power probe beam. The pump pulse wave front is tilted by a diffraction grating and imaged on the $LiNbO_3$ crystal (see Figure 5.1(a)). In order to prevent the smearing of the THz pulse, which will be discussed in the next section, a slit is inserted in the optical pump beam path before the grating to reduce the optical pump beam width along the optical probe pulse propagation direction. The demagnification factor of the relay imaging system is close to 2 and can be adjusted by slight adjustments in the positions of the imaging lens and the grating. The detailed description of the tilted-pulse-front excitation technique is given in Appendix B.

The probe pulse is frequency doubled in a BBO crystal. It passes through a spatial filter and through a pair of lenses which expand it before it enters the $LiNbO_3$ crystal (see Figure 5.1). The image pulse experiences a phase modulation due to the change of the refractive index induced by the THz electric field. The phase object in the crystal is then recorded by an intensified CCD (ICCD) camera system through the Talbot effect (see Section 2.2.2(d)) [12-14]. The distance between the crystal and the camera object plane is about 25 mm.

As introduced in Appendix A, the ICCD camera system consists of an intensifier and a CCD head, where the intensifier functions as a signal amplifier and a shutter. The shutter, with the gate width 500 ps, is triggered by an external electronic trigger pulse and opens only when the probe pulse arrives. The CCD is thermoelectrically cooled and has a dynamic range of 12 bits. A background image with the optical pump beam blocked is collected before the THz image acquisition, and the background subtraction is performed automatically by the ICCD system. With the frame rate of about 2 frames per second (fps), we can monitor the THz generation process and optimize the alignment in real time. For a better signal to noise ratio (SNR), all images shown in this chapter are averaged over 50 frames.
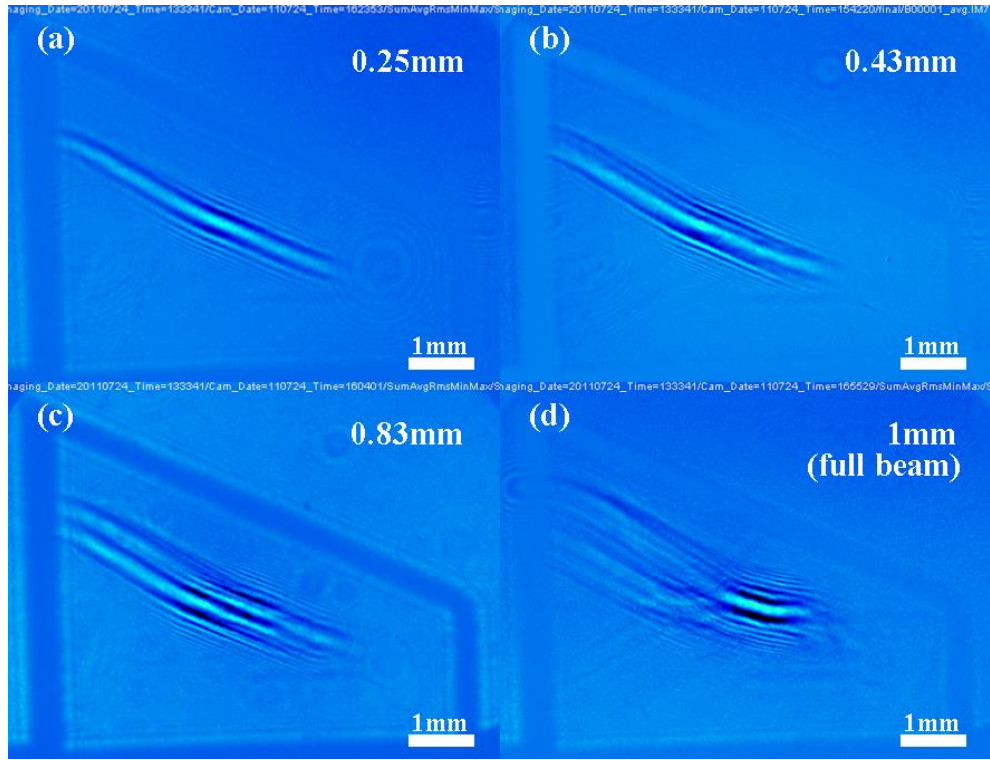
5.2.2 The smearing of the THz image

Figure 5.2: Images of the THz wave generated in the LiNbO$_3$ crystal with the optical pump beam width in the optical probe pulse propagation direction at (a) 0.25 mm, (b) 0.43 mm, (c) 0.83 mm, and (d) about 1 mm (full Gaussian beam, without slit), respectively.

Because the optical pump pulse and the optical probe pulse propagate normally to each other, the phase-matching condition cannot be satisfied. As illustrated in Figure 5.1(b), the finite width of the optical pump beam along the optical probe pulse propagation direction results in THz image blurring. This is due to the accumulation of phase modulation experienced by the probe pulse at different depths. To reduce this smearing, we placed a slit in the optical pump beam path to decrease the width of the optical pump beam in the optical probe beam direction.

Figure 5.2(a), (b), (c), (d) show the THz images collected with the optical pump beam width of 0.25 mm, 0.43 mm, 0.83 mm, and about 1 mm (full Gaussian beam, without slit inserted). In the case of the full Gaussian beam, the

THz image (see Figure 5.2(d)) is so blurred that little useful information can be extracted from it. On the other hand, when the size of the optical pump beam is reduced, the THz image becomes sharper. We also found that when the beam size is reduced beyond 0.25 mm, the sharpness of the THz image is no longer enhanced while the signal strength is reduced. We have therefore chosen the optical pump beam size of 0.25 mm for studying THz generation and propagation processes in the LiNbO$_3$ crystal.

5.2.3 THz pulse generation and propagation in LiNbO$_3$

As shown in Figures 5.3(a), (b), (c), and (d), THz images at time delays of 12 ps, 24 ps, 28 ps, and 36 ps are captured with the optical pump beam width in the probe pulse propagation direction of 0.25 mm. The THz pulse and optical pump pulse in Figure 5.3 can be recognized. The main part of the THz pulse wave front is uniform in strength and the length of the THz pulse wave front grows when the optical pump pulse propagates through the crystal. On the other hand, the optical pump pulse propagates horizontally within the optical pump beam region (see the red shaded area in Figure 5.3(d)), which is 1 mm in width.

As illustrated in Figure 5.3(d), the tilt angle of the optical pump pulse is 67 ° and the Cherenkov angle is 60 °. Because the THz wave generated in the tilted-pulse-front excitation technique has the half-cone profile, the THz Cherenkov wave image suffers from the distortion discussed earlier (Chapters 4). According to the angle calibration (see Table 4.3 in Chapter 4), the imaged THz Cherenkov angle of 60 ° in Figure 5.3(d) corresponds to a calibrated angle of 64 °.

In the area of overlap with optical pump beam, the THz pulse spatial profile is no longer Gaussian. Instead, the THz intensity increases along the optical pump pulse wave front. This phenomenon is further explored in Section 5.2.4.
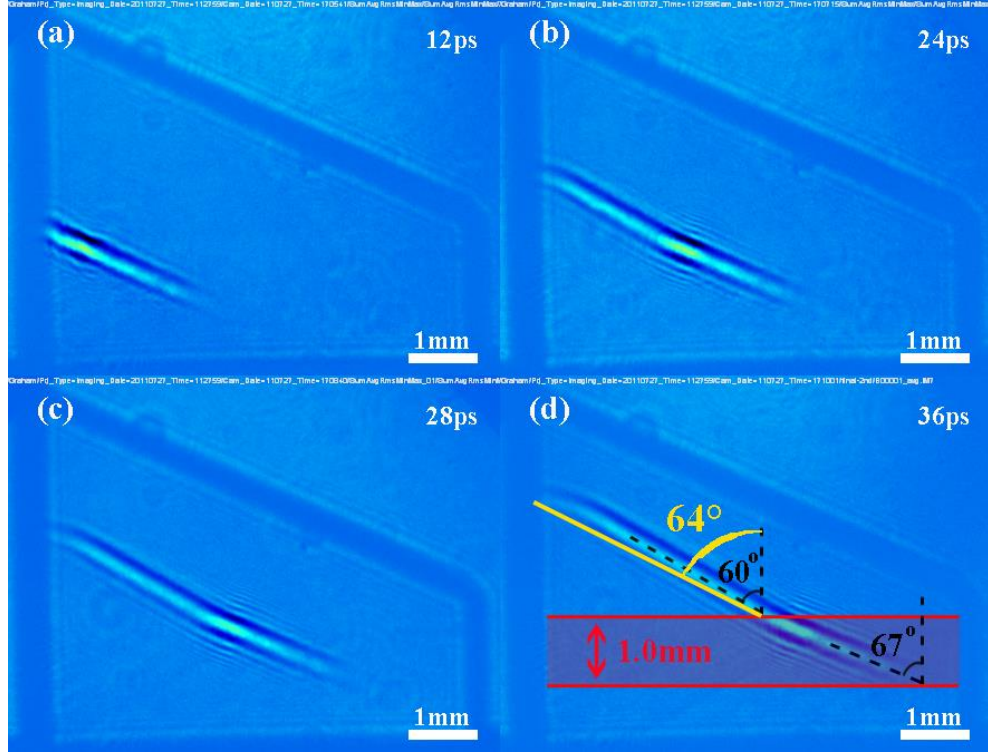
Figure 5.3: Images of the THz wave generated in the LiNbO$_3$ crystal at time delays of (a) 12 ps, (b) 24 ps, (c) 28 ps, and (d) 36 ps, respectively. The size of the optical pump beam along the optical probe pulse propagation direction (out of the page) is 0.25 mm, and the optical pump beam size that is perpendicular to the probe pulse direction is 1 mm. The tilt angle of the optical pump pulse wave front is 67°. The measured and the calibrated THz Cherenkov angles are 60° and 64°, respectively.

5.2.4 Separation of the THz pulse from the optical pump pulse
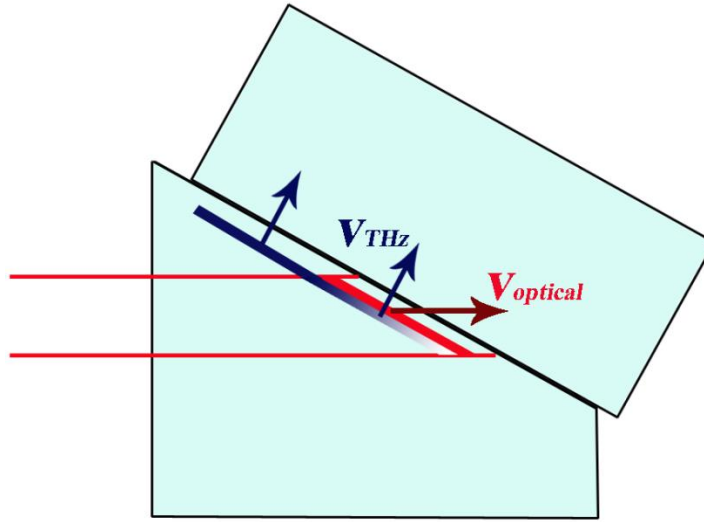
Figure 5.4: Optical setup for separating the THz pulse from the optical pump pulse. An optical pump beam is transmitted through a $LiNbO_3$ prism to generate THz pulses. A cubic $LiNbO_3$ crystal is attached to the $LiNbO_3$ prism to separate the THz pulse (marked in blue color) from the optical pump pulse (marked in red color). Because there are some dust particles with size larger than 1 micron, the gap between the two crystals is larger than the optical pulse wavelength (800nm).

As shown in Figure 5.3, the generated THz and the optical pump pulse coexist in the optical pump beam area. To demonstrate the build-up of the THz intensity along the optical pump pulse wave front within the optical pump beam region, we designed an experiment to separate the THz pulse from the optical pump pulse (as shown in Figure 5.4). To do so, we attached another $LiNbO_3$ crystal to the $LiNbO_3$ prism. Because the THz and optical pulses have different propagation directions, their incidence angles are also different. Part of the THz pulse, which is incident normally at the interface, tunnels through the air gap between the two crystals, while the optical pump pulse experiences the total internal reflection due to the high incidence angle and that the small air gap (due to the dust between the two crystals) is larger than the pump wavelength (800 nm). We note that, in the experiment, the thicknesses of the two crystals along the probe pulse propagation direction are not necessary to be equal. However, the two crystal surfaces that face to the incident probe pulse must be in the same plane.
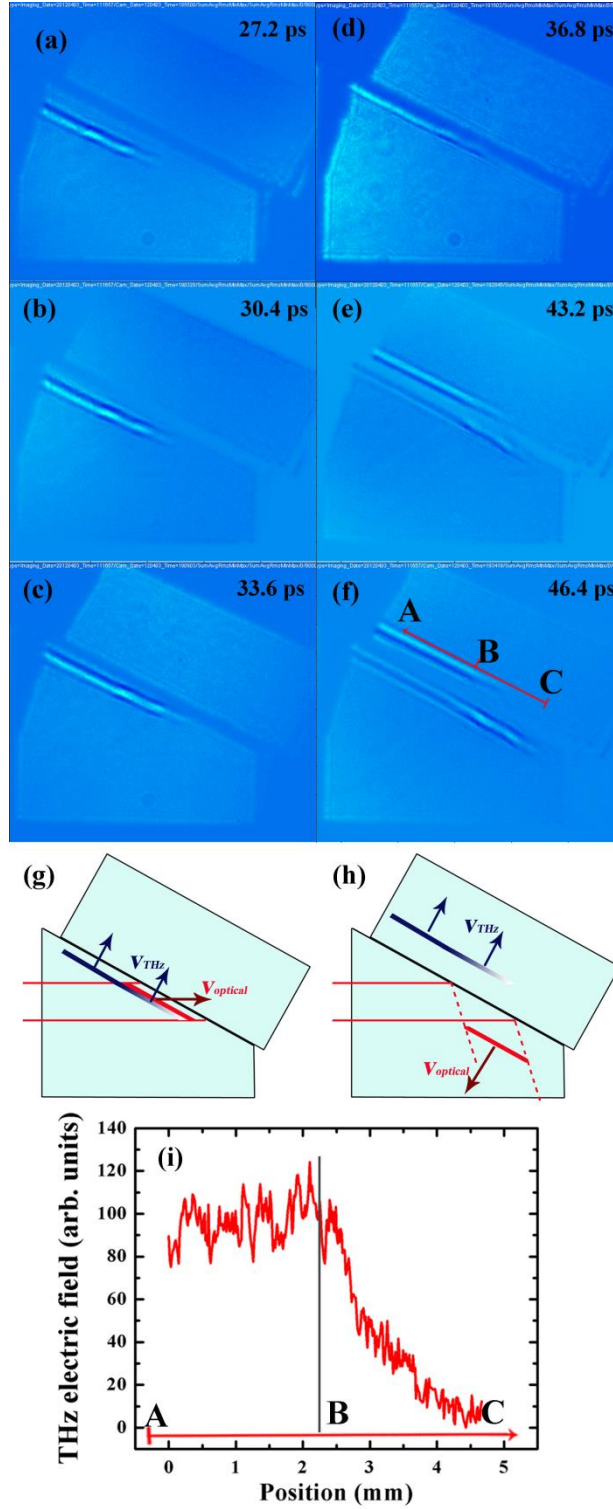
Figure 5.5: Images of optical pulse and THz pulse separation process at time delays of (a) 27.2 ps, (b) 30.4 ps, (c) 33.6 ps, (d) 36.8 ps, (e) 43.2 ps, and (f) 46.4 ps. Schematic illustrations to show the THz pulse and optical pulse before (g) and after (h) they get separated by the air gap. (i) The plot of the THz signal strength along the THz pulse wave front.

Figures 5.5(a)-(f) show images of the separation process between the optical pulse and the generated THz pulse. For clarification, Figures 5.5(g) and (h) illustrate the THz pulse and optical pulse before and after the separation, respectively. As shown in Figure 5.5(f), the THz wave that has tunnelled through the small air gap between the two crystals is imaged in the second LiNbO$_3$ crystal. The THz electric field strength along **AC** line is plot in Figure 5.5(i). We find that the THz signal strength is a constant value between the point **A** and **B**. Since the THz pulse in area AB has already been separated from the optical pump pulse before the tunnelling. On the other hand, in the **CB** direction, the THz electric field strength increases in the area of **CB**.

For the first time, based on the experiment that is illustrated in Figure 5.4, we visually demonstrate the THz pulse energy accumulation process of the tilted-pulse-front excitation scheme.

5.2.5 Optical pulse-tilt-angle dependence of the THz generation efficiency

In order to study the influence of the optical pump pulse tilt angle on the THz generation efficiency, we varied the tilt angle by changing the image demagnification through adjustments in the grating and imaging lens positions. Figure 5.6 shows the combined THz images at three different time delays with optical pump pulse tilt angles of (a) 68°, (b) 64°, (c) 61°, and (d) 56°, respectively. As shown in Figure 5.6(b), for all the tilt angles, the imaged THz Cherenkov angle is 60°, which corresponds to the true Cherenkov angle of 64°. The wave front of the optical pump pulse experiences no distortion except at a tilt angle of 56°. Variation in optical pump pulse tilt angles, as well as the wave front distortion, results in variation in the THz electric field strength. Figure 5.7 shows the THz electric field magnitude measured at ten different tilt angles. We find that the THz electric field is the highest when the pump pulse tilt angle is between 61° and 67°, and decreases rapidly for the pump pulse tilt angles smaller than 61° or

larger than 67 °. Since the THz Cherenkov angle is 64 °, which is between 61 ° and 67 °, our experiment result makes sense.
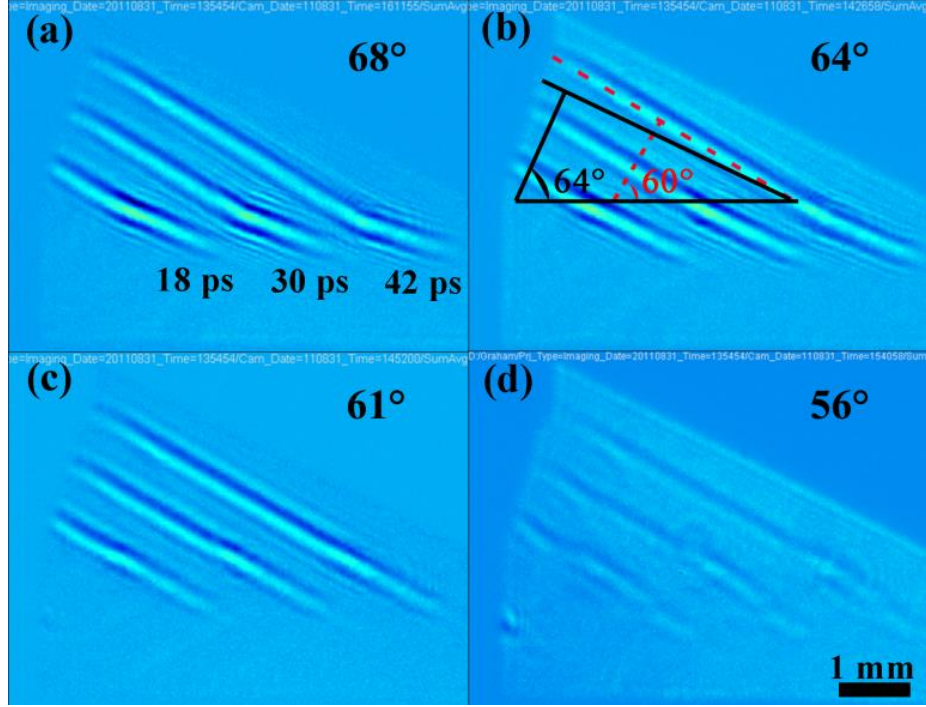

Figure 5.6: The combined images of the THz wave inside the LiNbO$_3$ crystal at three different time delays (18 ps, 30 ps, and 42 ps) at optical pump pulse tilt angles of (a) 68 °, (b) 64 °, (c) 61 °, and (d) 56 °.
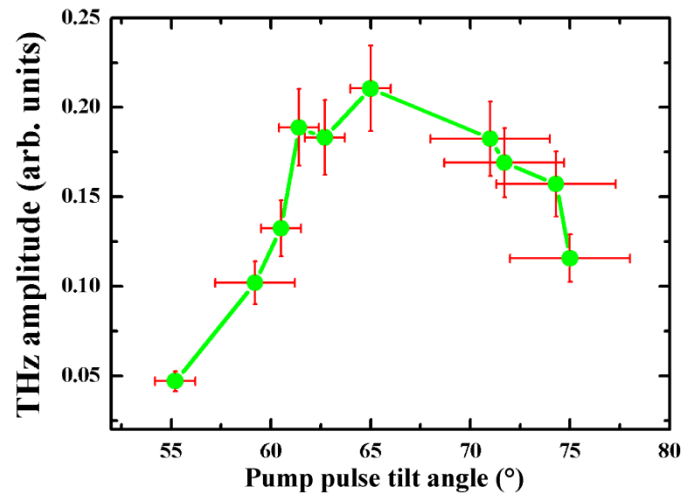

Figure 5.7: The relationship between the THz pulse electric field amplitude and the tilt angle of the optical pump pulse.

116

5.2.6 Measurement of the THz pulse output energy with a pyroelectric detector

Modifications to the THz generation and collection setup were necessary for measurement of the output THz pulse energy with a pyroelectric detector. As illustrated in Figures 5.8(a)-(e) and 5.9(a), we found that the LiNbO$_3$ crystal needed to be pumped close to its tip for efficient detection of output THz pulses with the pyroelectric detector. This geometry allows us to correlate the imaged THz intensity with the energy of the THz pulse. The corresponding images of the THz pulse taken in this (tip pumped) geometry, with the slit inserted, are shown in Figures 5.8(a)-(e).

Figure 5.9(b) shows the relationship between the measured THz pulse energy and the square of the imaged THz signal strength. The linear relationship implies that the imaged THz signal strength is proportional to the THz electric field. Therefore, we can use the THz imaging method to quantitatively study the THz generation efficiency. Furthermore, Figure 5.9(c) shows a linear relationship between the imaged THz signal strength and the optical pump pulse power, which confirms that the THz generation in LiNbO$_3$ crystals is a second-order nonlinear optics process (as discussed in Chapter 2).

In comparison to the images captured in the tip-pumped geometry, the images of the THz pulses generated by the optical pump pulse incident on the centre of the LiNbO$_3$ crystal are shown in Figures 5.8(f)-(j). In this case, the optical pump pulse travels a much longer distance before the THz pulse is emitted from the crystal which should, at the first glance, result in a more intense THz pulse. However, we cannot detect the emitted THz pulses in this geometry, suggesting that the coupling efficiency is very low. Based on these observations, it appears that the tip-pumped geometry is preferable for the generation of THz pulses in the LiNbO$_3$ crystal. This phenomenon is further explored in Section 6.3.
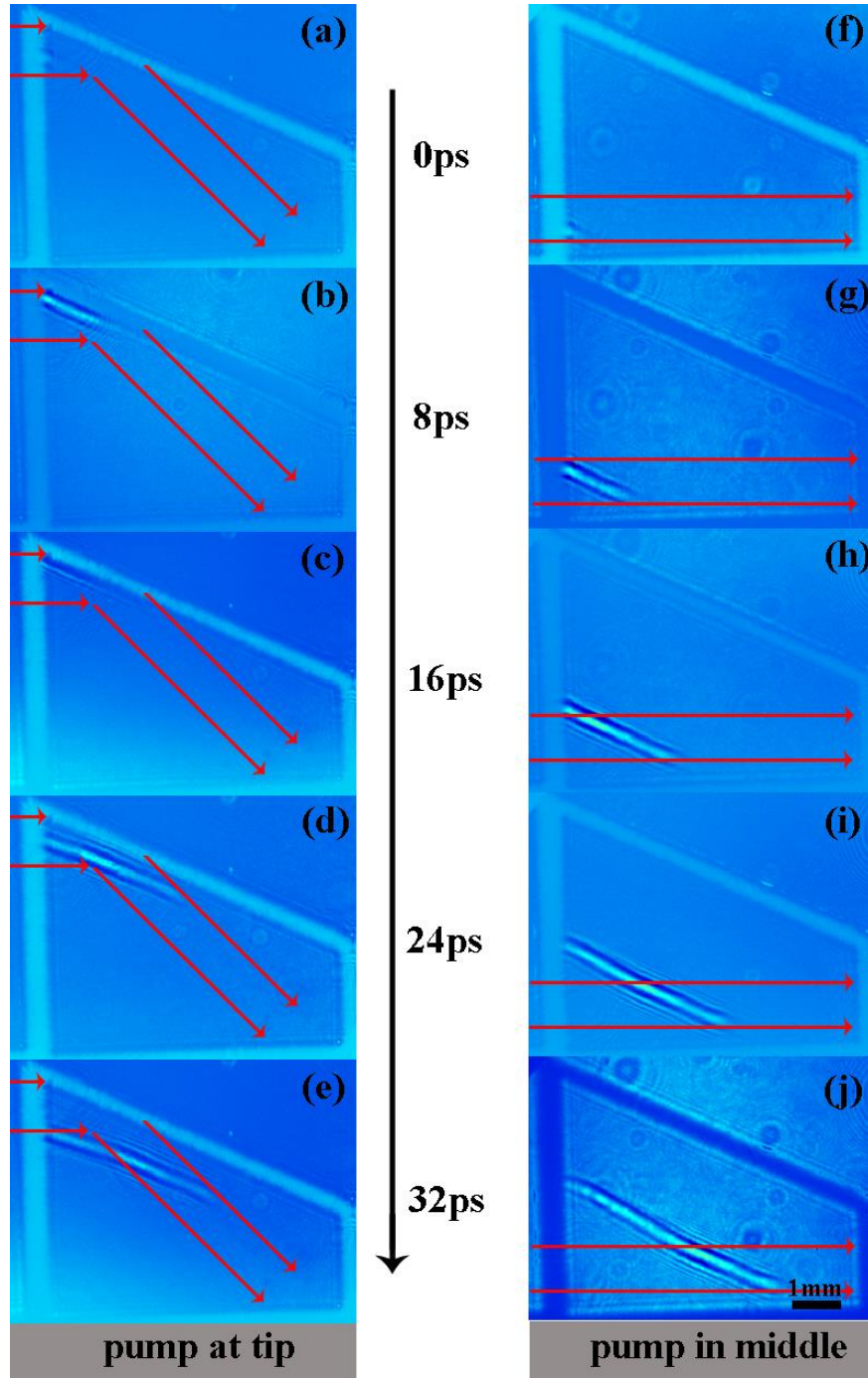
Figure 5.8: Images of the THz pulse that is generated by pumping the tip of the crystal (as illustrated in Figure 5.9 (a)) at time delays of (a) 0 ps, (b) 8 ps, (c) 16 ps, (d) 24 ps, and (e) 32 ps. Images of the THz pulse that is generated by pumping the middle part of the crystal at time delays of (f) 0 ps, (g) 8 ps, (h) 16 ps, (i) 24 ps, and (j) 32 ps.
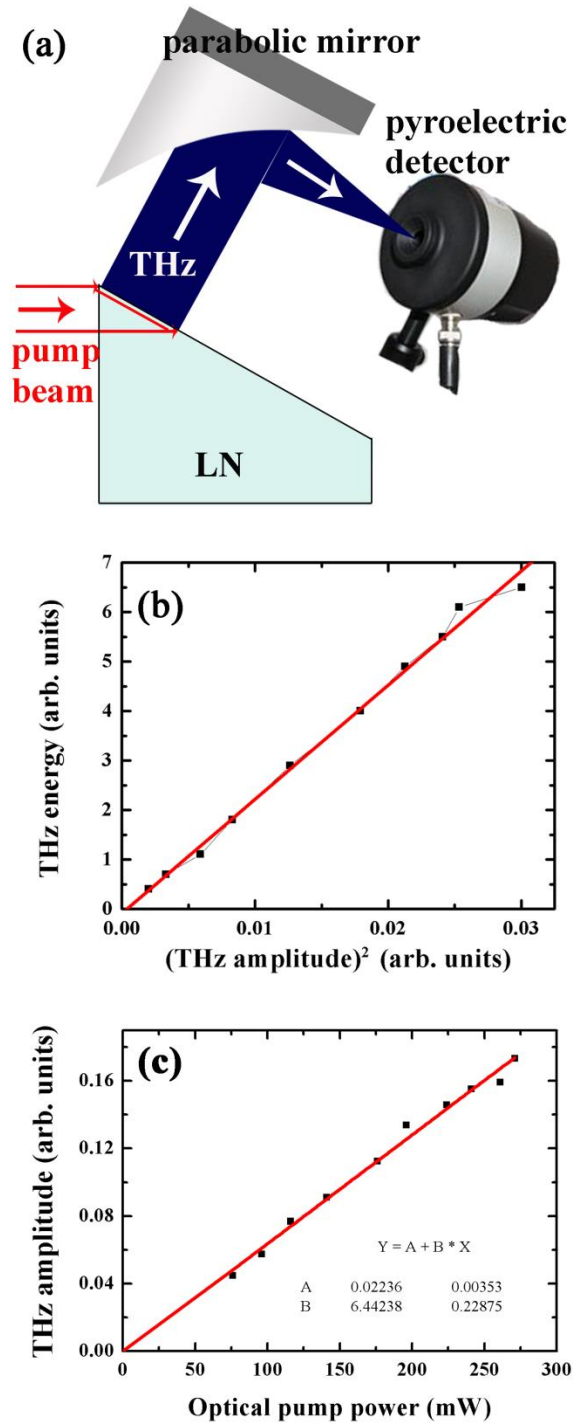
Figure 5.9: (a) Optics setup for collecting and detecting the output THz pulse, the obtained images are shown in Figure 5.8 (a)-(e). (b) The relationship between the THz output energy and the square of THz image signal strength. (c) The relationship between the THz image signal strength and the optical pump power.

5.2.7 The optical pump pulse polarization dependence of the THz Cherenkov wave
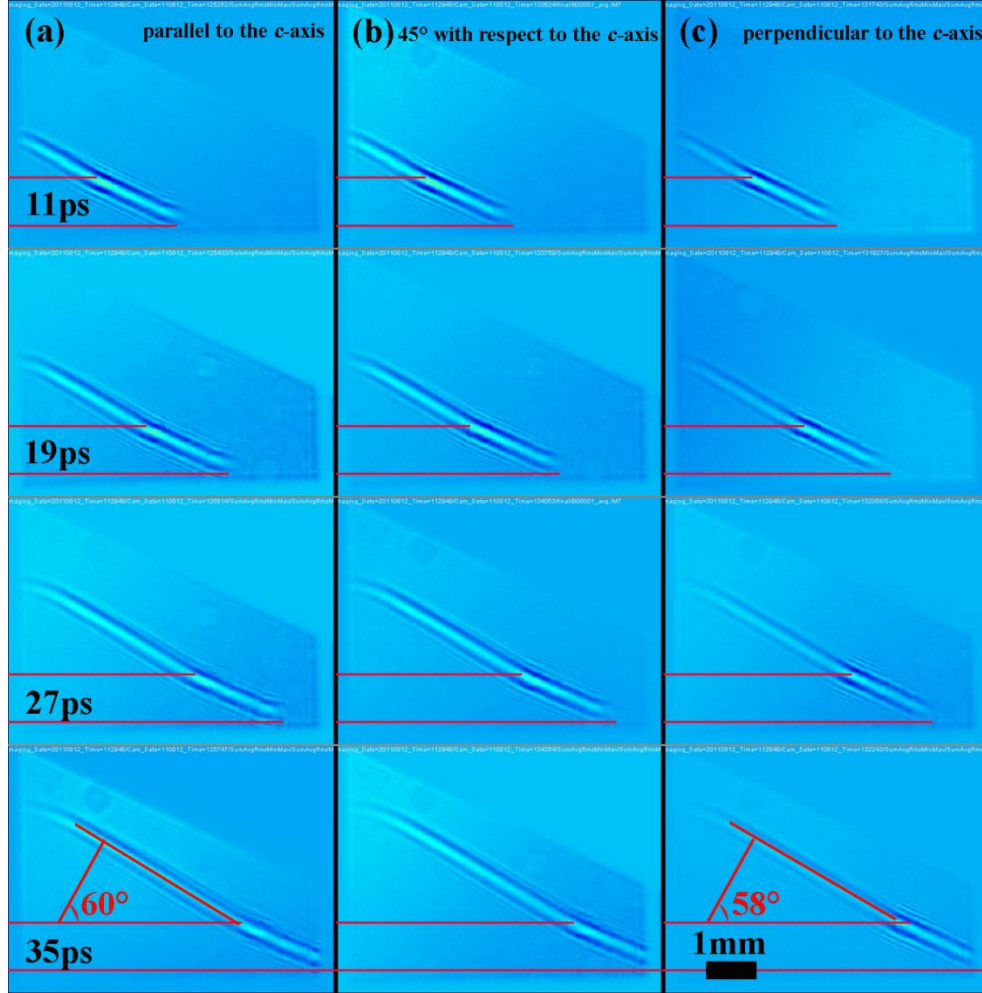
Figure 5.10: Images of the THz wave that is generated by the optical pump pulse with the optical pump pulse polarization (a) parallel to the *c*-axis of the crystal, (b) at 45 ° with respect to the *c*-axis of the crystal, (c) perpendicular to the *c*-axis of the crystal.

We have also explored the dependence of the THz Cherenkov wave on the optical pump pulse polarization. Figure 5.10 shows images of the THz wave at three different optical pump pulse polarizations. We find that the THz pulse generation is the most efficient when the optical pump pulse polarization is parallel to the *c*-

axis of the crystal, which is consistent with the point focused result discussed in Chapter 4. We also observe that the Cherenkov angle is different for THz pulses generated by optical pulses polarized parallel or perpendicularly to the *c*-axis due to the refractive index difference between ordinary ray (o ray) and extraordinary ray (eo ray) in the LiNbO$_3$. We note that the measured Cherenkov angles for o ray (58°) and eo ray (60°) are consistent with the point focused result (o ray 58.7 ± 0.3°, eo ray 59.7 ±0.3°) in Chapter 4.

For the case that the pump pulse polarization is 45° with respect to the *c*-axis of the crystal, the o ray and eo should get separated when they propagate inside the crystal due to different velocities, as what we see in the pump pulse point focused case in Figure 4.19 in Chapter 4. However, as shown in Figure 5.10(b), the separation is not observed, this is because the image of the pump pulse here is so blurred that the small separation between the two rays is hard to be recognized.

5.3 3D imaging of the THz Cherenkov wave generated by the full-size optical pump beam

5.3.1 Introduction to 3D imaging of the THz wave

As shown in Figures 5.1(a) and (b), in order to reduce the smearing of the THz wave image in the transverse imaging geometry, a slit placed before the grating is used to limit the size of the optical pump beam in the optical probe pulse propagation direction. However, the slit has to be removed to allow the full power of the optical pump beam to be used for generating intense THz pulses. In order to visualize the 3D structure of the THz pulse generated by the full optical pump beam, we scan the slit across the optical pump beam, capture THz images at different slit positions, and finally combine the acquired images using MATLAB.

5.3.2 Experimental setup

As illustrated in Figure 5.11(a), experimental condition is the same as Section 5.2.1. Instead of a slit that stays at a fixed position in Section 5.2.1, the slit here is mounted on a translation stage. As shown in Figure 5.11(b), when the slit position is scanned along the probe pulse propagation direction, the THz wave generated by a different part of the optical pump beam is imaged. Since the relative time delay between the pump pulse and the probe pulse changes when slit position changes, a calibrated time delay should be performed, which is discussed in section 5.3.3.
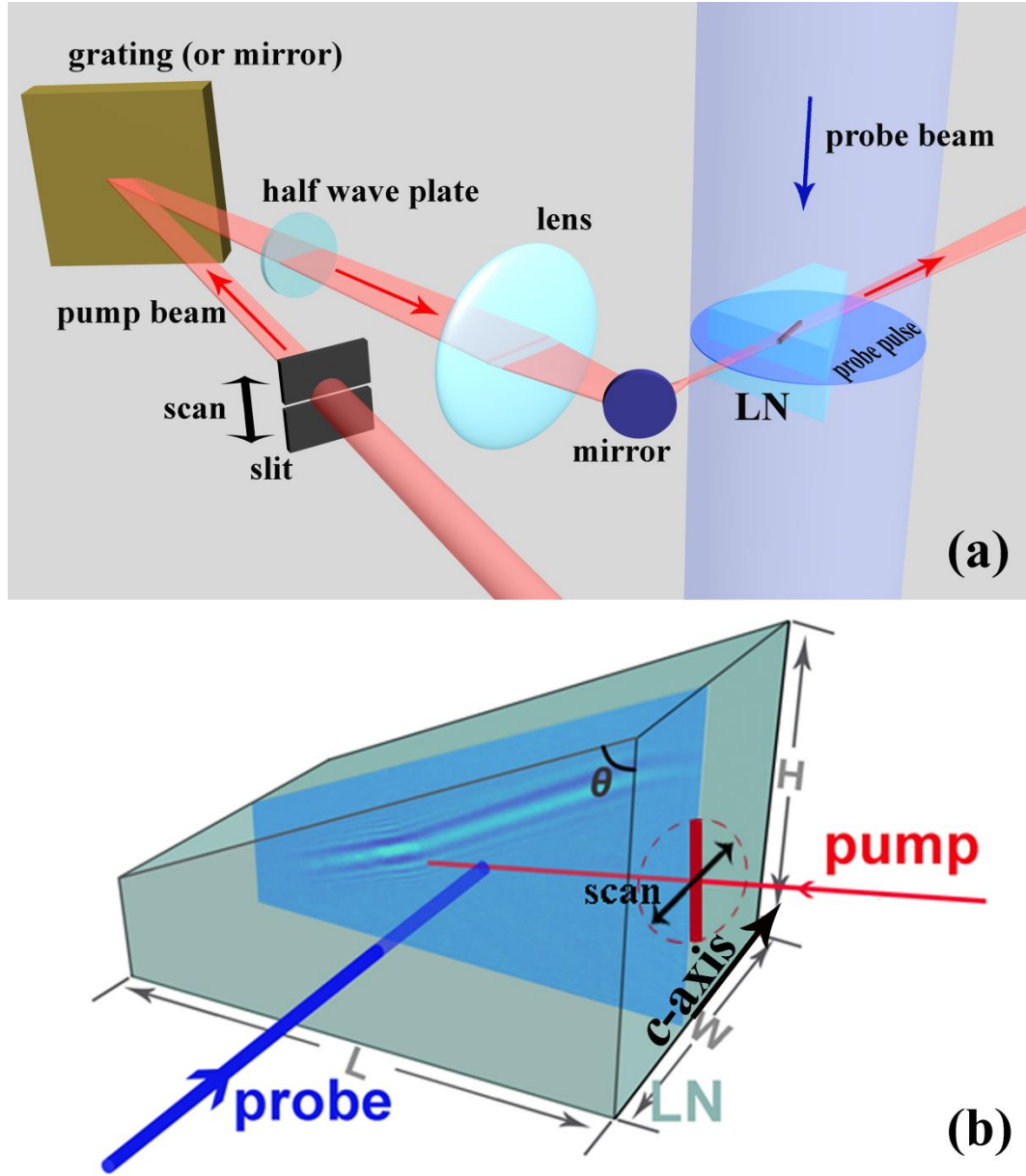
Figure 5.11: (a) Illustration of the 3D THz pulse imaging setup. The 800 nm optical pump beam goes through a slit and then is diffracted by a grating. The optical pump pulse with the tilted pulse front is imaged on the LiNbO$_3$ crystal by a lens. A 400 nm optical probe pulse travelling normally to the optical pump pulse images the generated THz wave and finally is recorded by an intensified CCD (ICCD) camera system (not shown). (b) The detailed side-view imaging geometry inside the LiNbO$_3$ crystal. The pump pulse polarization is parallel to the c-axis of the crystal, and the probe pulse polarization is in the plane defined by the probe pulse propagation direction and the c-axis of the crystal. The optical pump beam is scanned in the horizontal direction (along c-axis in (b)).

5.3.3 Calibration of the pump-probe time delay at different slit positions

In order to reconstruct the 3D structure of the THz wave from the THz images acquired by scanning the slit across the optical pump beam, the time delay between the optical pump and probe pulses at different slit positions has to be calibrated. As illustrated in Figure 5.12, moving the slit position from point **A** to **B** results in the change (Δd) in the distance the probe pulse has to travel to reach the generated THz wave. As a result, the imaged THz pulse appears to be delayed. Figure 5.13 show images of the THz pulses captured at different slit positions. By defining the THz image taken at the slit position of 7.5 mm as a reference image (Figure 5.13(a)), we plot the relationship between the slit position and the image shift in Figure 5.15(a). We find that 1 mm slit-position-change shifts the THz image by *37.3* pixels, or, alternatively, a pump-probe delay of 1 ps introduces *8.5* pixel shift into the THz image (see Figures 5.14 and 5.15(b)). Therefore, we calculate that for a 1 mm change in the slit position, the pump-probe time delay compensation should be 37.3 [pixels]/8.5[pixel/ps]=4.39 ps, close to the value of 4.42 ps obtained by the following calculation,

$$\Delta t = \frac{\Delta d}{c/n_{40_m}} = \frac{1mm/D}{c/n_{400nm}} = \frac{1(mm)/2.3}{3*10^8(\frac{m}{s})/3.05} = \boldsymbol{4.42ps}$$

where, *c* is the speed of light in free space, $\Delta \boldsymbol{d} = \boldsymbol{1mm/D}$ is the shift of the optical pump beam in the $LiNbO_3$ crystal, D = 2.3 is the lens imaging demagnification which corresponds to a tilt angle of 66.1 ° (the relationship between the demagnification D and the tilt angle is summarized in Table B.1 in Appendix B).
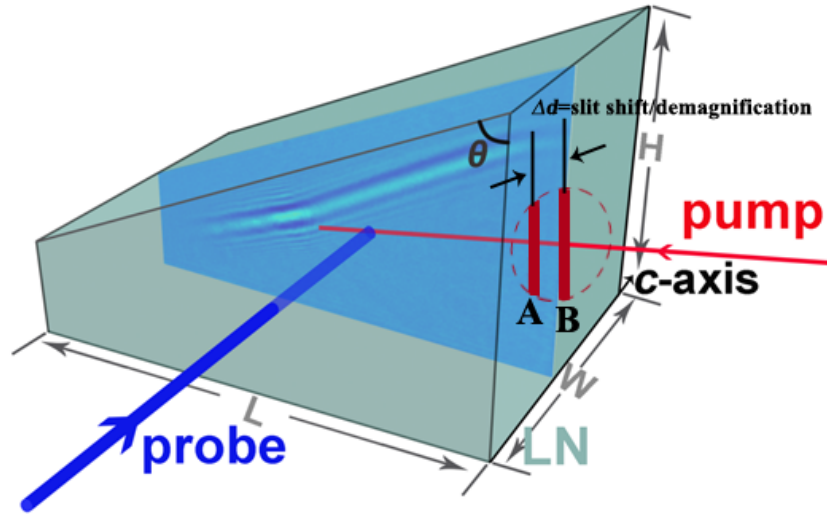
Figure 5.12: Illustration of the THz pulses that are generated by optical pump pulses that go through the slit at two positions, **A** and **B**.
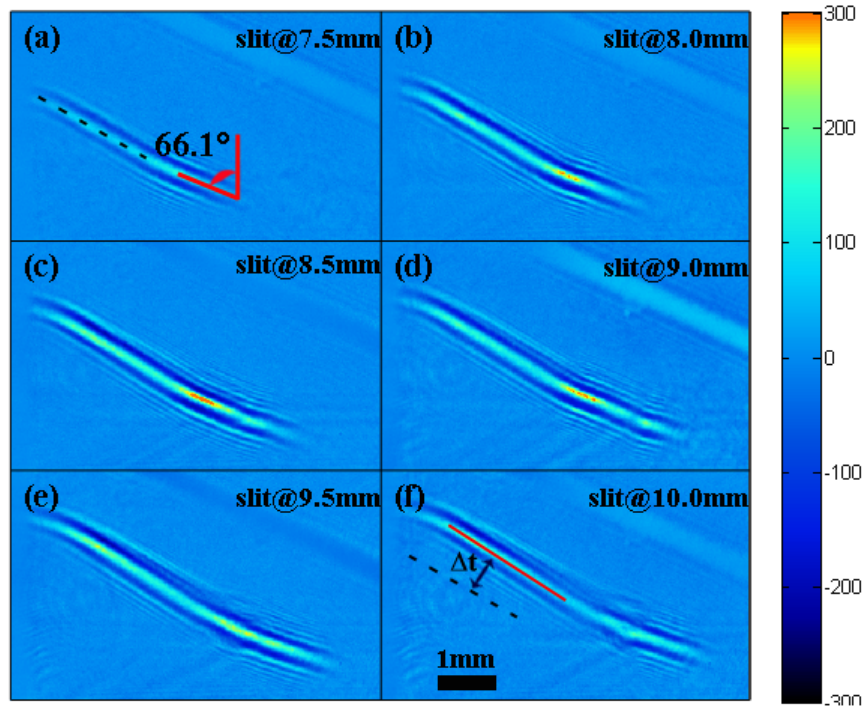

Figure 5.13: Images of the THz pulse that is generated by optical pump pulses with slit positions at (a) 7.5 mm, (b) 8.0 mm, (c) 8.5 mm, (d) 9.0 mm, (e) 9.5 mm, and (f) 10.0 mm. The red lines in (a) and (f) hi-light the angle of the wavefronts.
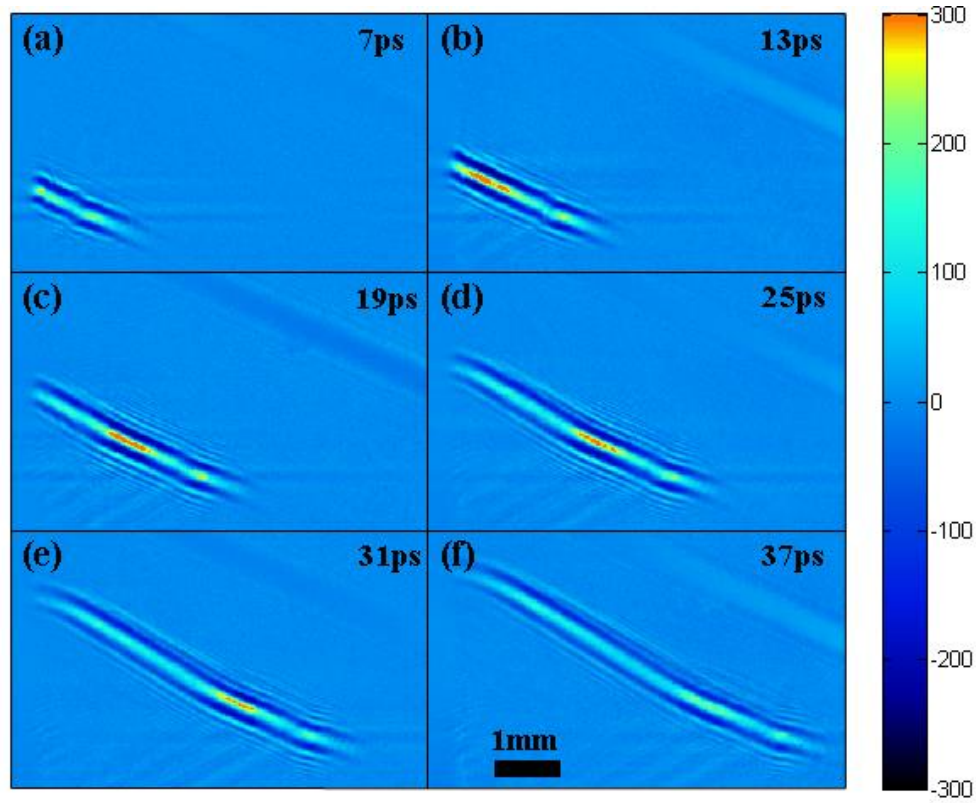
Figure 5.14: Images of the THz pulse (at a fixed slit position) at time delays of (a) 7 ps, (b) 13 ps, (c)19 ps, (d) 25 ps, (e) 31 ps, and (f) 37 ps.
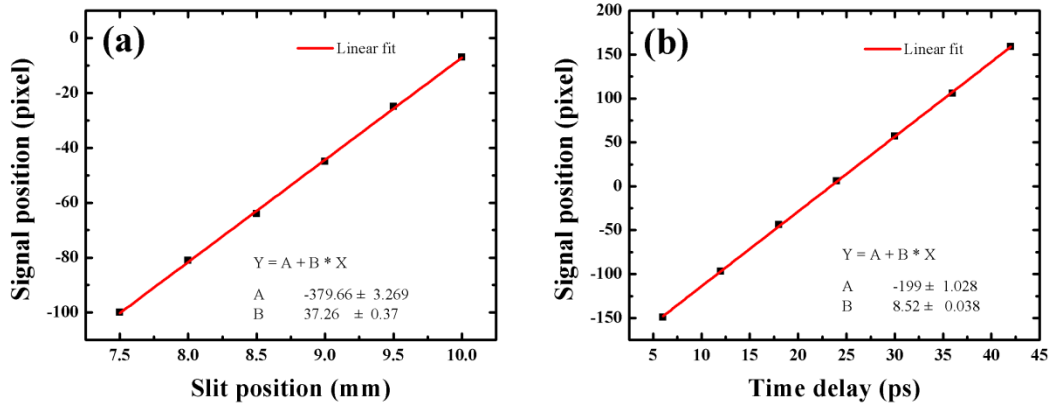
Figure 5.15: Relationships between the THz image position on the ICCD camera and the slit position (a), as well as the time delay (b), respectively.

5.3.4 3D image of the THz pulse generated by a full beam tilted-pulse-front optical pump pulse
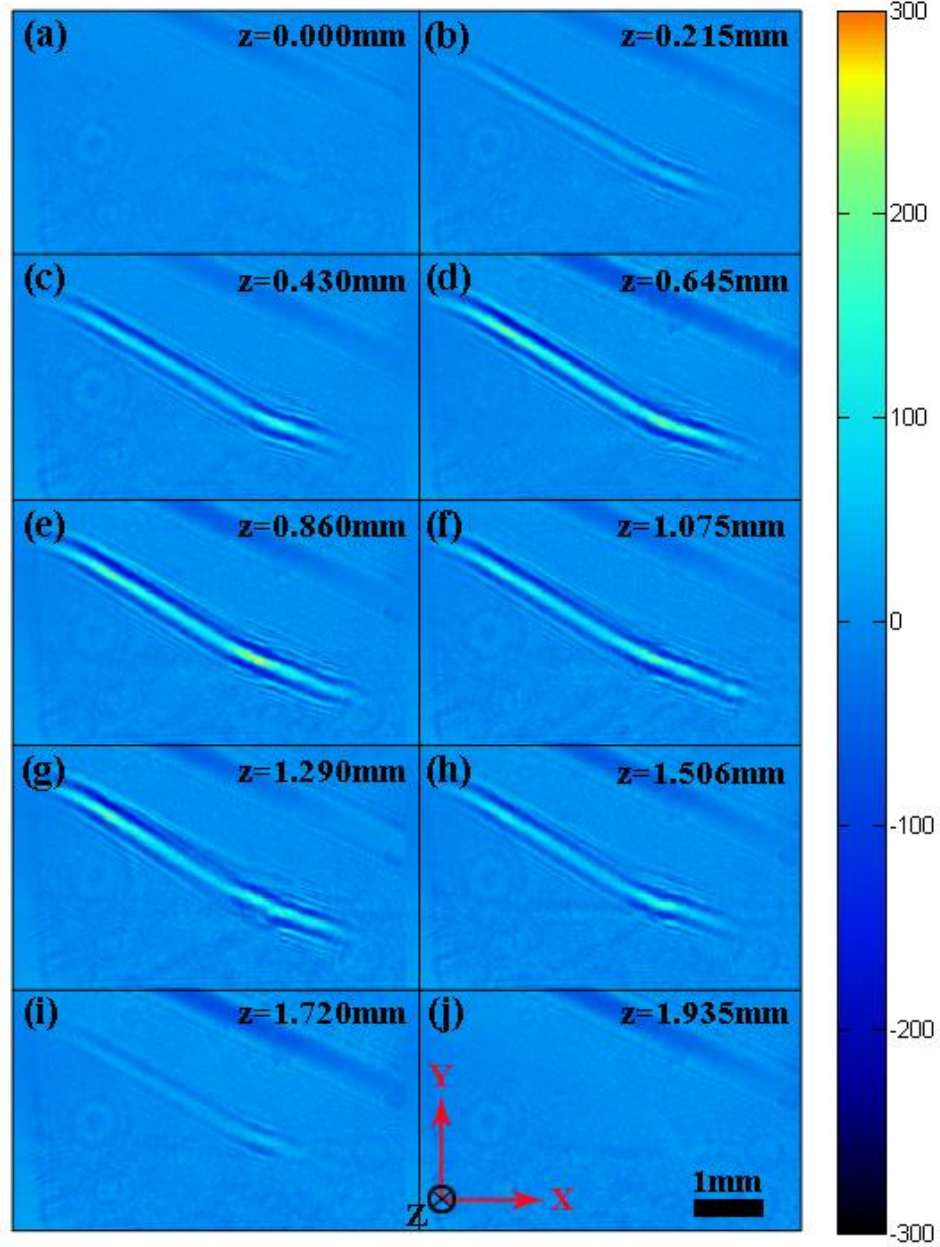
Figure 5.16: Images of the THz pulse with the optical pump beam shift Δd inside the LiNbO$_3$ crystal of (a) 0.000 mm, (b) 0.215 mm, (c) 0.430 mm, (d) 0.645 mm, (e) 0.860 mm, (f) 1.075 mm, (g) 1.290 mm, (h) 1.506 mm, (i) 1.720 mm, and (j) 1.935 mm. The relative pump-probe time delay has been corrected.

Figure 5.16 shows images of the THz pulse that is generated by the tilted-pulse-front excitation technique at various slit positions. The position value z shown in the figure is the relative position of the THz pulse in the z direction. Since the use of the slit, the images of the THz wave still has the distortion problem due to the transverse imaging geometry, as discussed in Chapter 4.

In analogy to the MRI 3D visualization method, all images shown in Figure 5.17 are processed to construct the 3D THz wave image, as shown in Figure 5.17. Based on the 3D image presented here, we can check the distortion condition of the optical pump pulse wave front, and study the THz wave generation and propagation processes in 3D. In order to show the intensity information in 3D, a better method to interpret the structure should be developed in the future. Again, we note that the THz Cherenkov angle in the 3D structure is distorted.
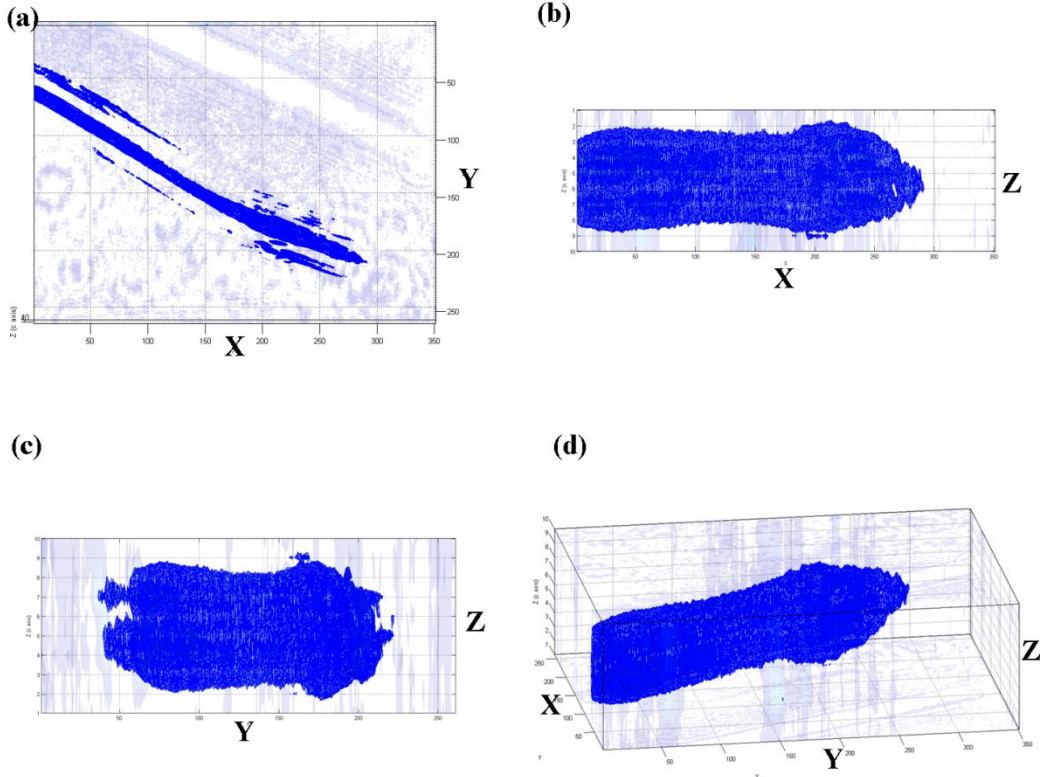
Figure 5.17: (a)-(d) 3D visualization of the THz wave generated by a full beam optical pump pulse with the optical pump pulse front tilted.

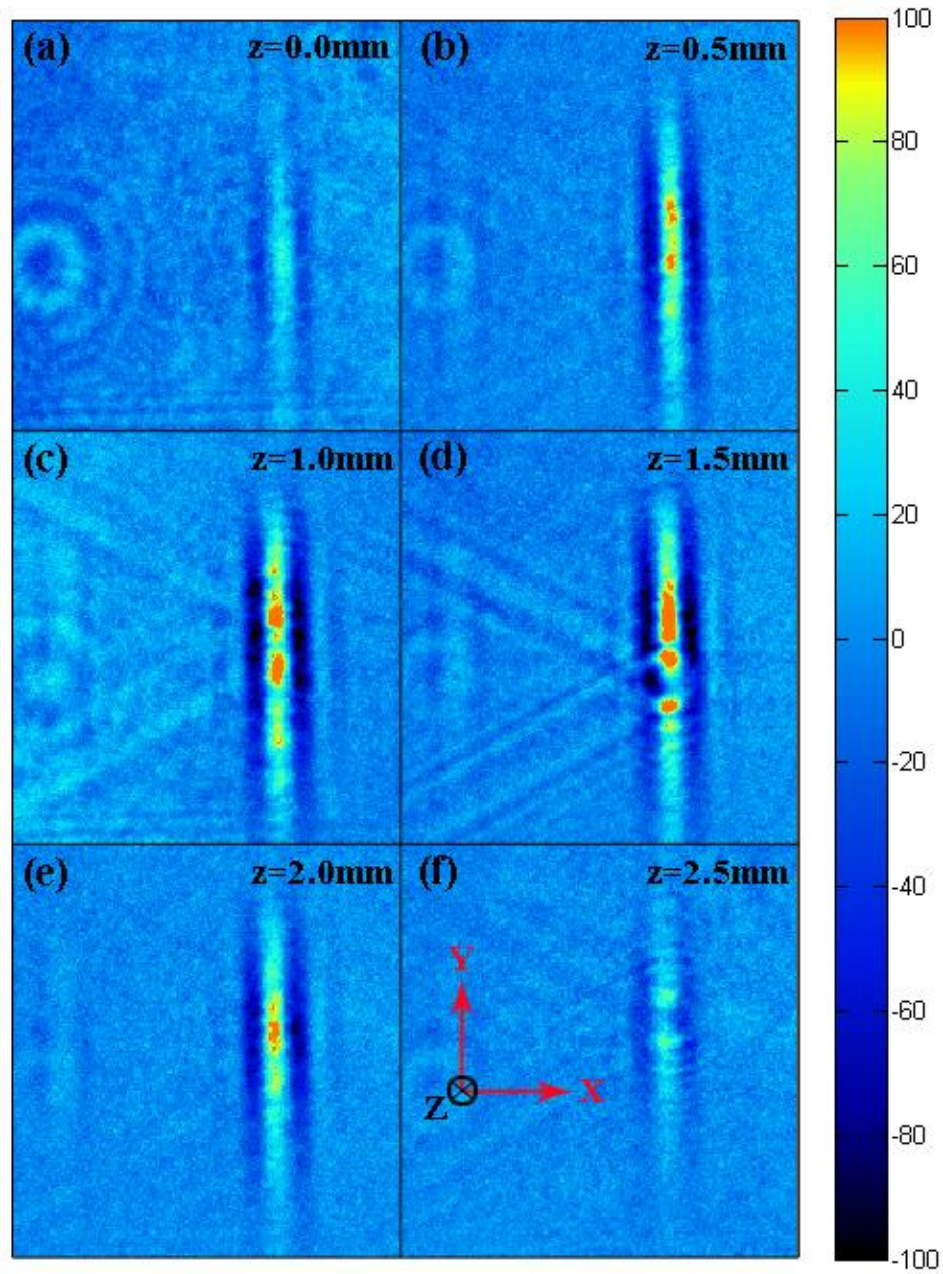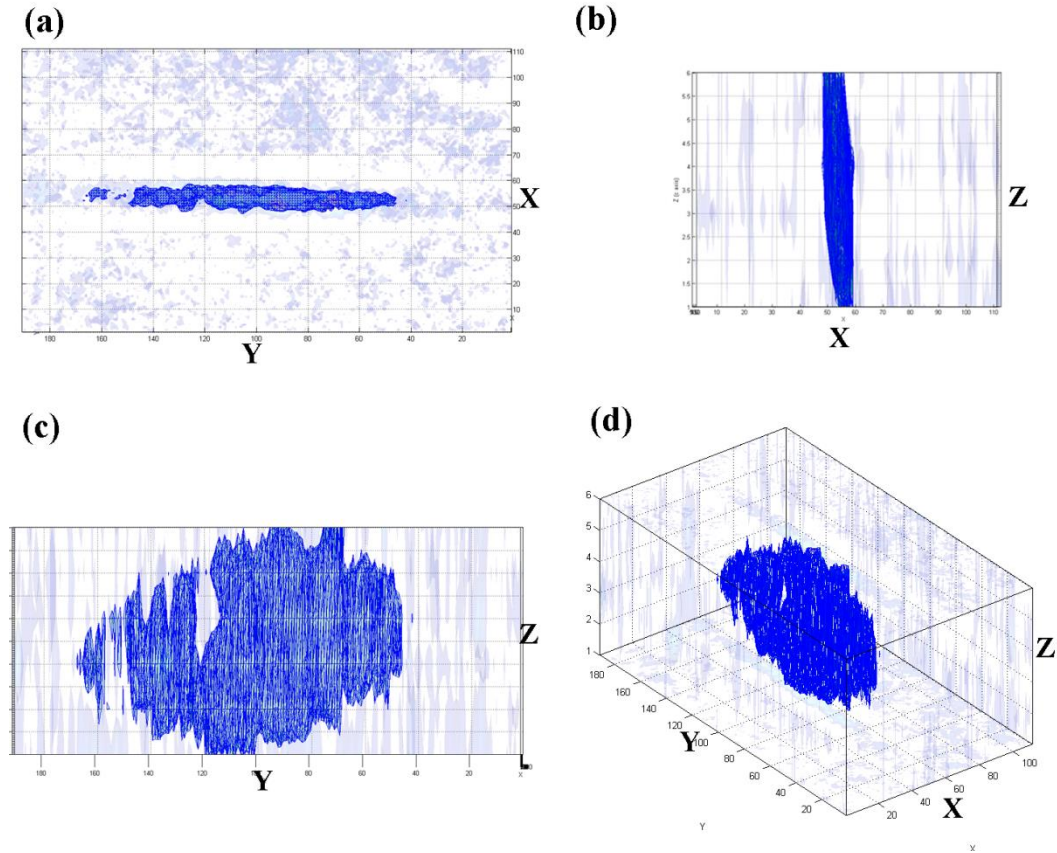## 5.3.5 3D image of the THz pulse generated by a full beam optical pump pulse with the pulse front not tilted

Figure 5.18: Images of the THz pulse generated by the optical pump beam with the position shift Δd of (a) 0.0 mm, (b) 0.5 mm, (c) 1.0 mm, (d) 1.5 mm, (e) 2.0 mm, and (f) 2.5 mm. The relative pump-probe time delay has been corrected.

In addition to imaging the 3D spatial structure of the THz wave generated in the tilted-pulse-front excitation technique (Figure 5.17), we have also imaged the THz wave generated by a full beam optical pump pulse with the pulse front not tilted. For this, the grating in Figure 5.11(a) was replaced by a mirror. Figure 5.18 shows images captured at different slit positions (with the relative pump-probe time delay corrected in the same principle as Section 5.3.3). As it can be seen in a 3D spatial profile of the resulted THz wave (Figure 5.19), no THz Cherenkov wave is generated due to the poor phase-matching condition. Since there is no THz Cherenkov wave, we don't need to worry about the angle distortion problem. Again, a better 3D interpretation method should be developed to show the intensity information.

Figure 5.19: (a)-(d) 3D visualization of the THz wave pumped by a full beam optical pump pulse with the optical pump pulse front not tilted.

5.4 Conclusions

Imaging of the THz pulse generated with the tilted-pulse-front excitation technique in the LiNbO$_3$ crystal is demonstrated. The optical pump beam size, the tilt angle of the optical pump pulse wave front, and the THz Cherenkov angle are measured directly from the image. Changes in the tilt angle of the optical pump pulse wave front do not affect the THz Cherenkov angle, which has been determined to be 64 ° (after counting on the distortion). On the other hand, the tilt angle significantly affects the THz generation efficiency. We find that the THz generation is the most efficient for the tilt angles between 61 ° and 67 °. We also find that the intensity of the THz pulses can be efficiently coupled out of the crystal into the free space only when the optical pump beam is incident close to the tip of the LiNbO$_3$ crystal. Because of this phenomenon, we have no free space to optimize THz output energy. We have used this geometry to calibrate the THz image intensity relative to the THz pulse energy measured by a pyroelectric detector. The linear relationship between the square of the THz image intensity and the THz energy confirms that the image intensity is representative of the THz electric field. The high SNR of the THz images acquired at a fast frame rate of 2 fps allowed optimization of the THz source optical alignment in real time. Finally, the 3D visualization of the THz pulse is also demonstrated, thus allows the investigation of the spatial structure of the emitted THz Cherenkov radiation.

References:

1. J. Hebling, G. Almasi, I. Z. Kozma, and J. Kuhl, "Velocity matching by pulse front tilting for large-area THz-pulse generation," Opt. Express **10**, 1161-1166 (2002).

2. M. C. Hoffmann, and J. A. Fulop, "Intense ultrashort terahertz pulses: generation and applications," J. Phys. D: Appl. Phys. **44**, 17 (2011).

3. A. G. Stepanov, S. Henin, Y. Petit, L. Bonacina, J. Kasparian, and J. P. Wolf, "Mobile source of high-energy single-cycle terahertz pulses," Appl. Phys. B: Lasers Opt. **101**, 11-14 (2010).

4. H. Hirori, A. Doi, F. Blanchard, and K. Tanaka, "Single-cycle terahertz pulses with amplitudes exceeding 1 MV/cm generated by optical rectification in $LiNbO_3$," Appl. Phys. Lett. **98**, 091106 (2011).

5. J. A. Fulop, L. Palfalvi, G. Almasi, and J. Hebling, "Design of high-energy terahertz sources based on optical rectification," Opt. Express **18**, 12311-12327 (2010).

6. F. Blanchard, G. Sharma, L. Razzari, X. Ropagnol, H. C. Bandulet, F. Vidal, R. Morandotti, J. C. Kieffer, T. Ozaki, H. Tiedje, H. Haugen, M. Reid, and F. Hegmann, "Generation of Intense Terahertz Radiation via Optical Methods," IEEE J. of Sel. Top. Quant. Electron. **17**, 5-16 (2011).

7. K. L. Yeh, M. C. Hoffmann, J. Hebling, and K. A. Nelson, "Generation of 10 μJ ultrashort terahertz pulses by optical rectification," Appl. Phys. Lett. **90**, 171121 (2007).

8. M. C. Hoffmann, K.-L. Yeh, J. Hebling, and K. A. Nelson, "Efficient terahertz generation by optical rectification at 1035 nm," Opt. Express **15**, 11706-11713 (2007).

9. F. Blanchard, L. Razzari, H. C. Bandulet, G. Sharma, R. Morandotti, J. C. Kieffer, T. Ozaki, M. Reid, H. F. Tiedje, H. K. Haugen, and F. A. Hegmann, "Generation of 1.5 mu J single-cycle terahertz pulses by optical rectification from a large aperture ZnTe crystal," Opt. Express **15**, 13212-13220 (2007).

10. D. H. Auston, K. P. Cheung, J. A. Valdmanis, and D. A. Kleinman, "Cherenkov radiation from femtosecond optical pulses in electro-optic media," Phys. Rev. Lett. **53**, 1555-1558 (1984).

11. J. A. Fulop, L. Palfalvi, S. Klingebiel, G. Almasi, F. Krausz, S. Karsch, and J. Hebling, "Generation of sub-mJ terahertz pulses by optical rectification," Opt. lett. **37**, 557-559 (2012).

12. Z. Wang, F.-H, Su, F. A. Hegmann, "Ultrafast imaging of the THz Cherenkov waves," Opt. Express (2012). (menuscript)

13. R. M. Koehl, S. Adachi, and K. A. Nelson, "Direct visualization of collective wavepacket dynamics," J. Phys. Chem. A **103**, 10260-10267 (1999).

14. P. Peier, S. Pilz, F. Mueller, K. A. Nelson, and T. Feurer, "Analysis of phase contrast imaging of terahertz phonon-polaritons," J. Opt. Soc. Am. B **25**, B70-B75 (2008).

Chapter 6

Ultrafast imaging of terahertz pulse reflection, transmission, and tunnelling at the LiNbO$_3$ crystal boundary

Ultrafast imaging of terahertz (THz) pulse refection, transmission, and tunneling at the LiNbO$_3$ crystal boundary is demonstrated with the transverse- imaging method. We find that the THz pulse has a 180° phase change when it gets reflected at a crystal-Au boundary. On the other hand, the reflected THz pulse has no phase change at the crystal-air boundary. Thanks to the 180° phase difference between the reflected THz pulse at the crystal-Au and the crystal-air boundary, a novel broad band electromagnetic wave antireflection coating is proposed and demonstrated by depositing an Au grating on the crystal surface. By attaching another piece of the LiNbO$_3$ crystal on the first one and controlling the gap between them, the gap dependence of the THz pulse transmission and tunnelling are imaged as well.

6.1 Ultrafast imaging of THz pulse reflection and the development of a broad band THz antireflection coating
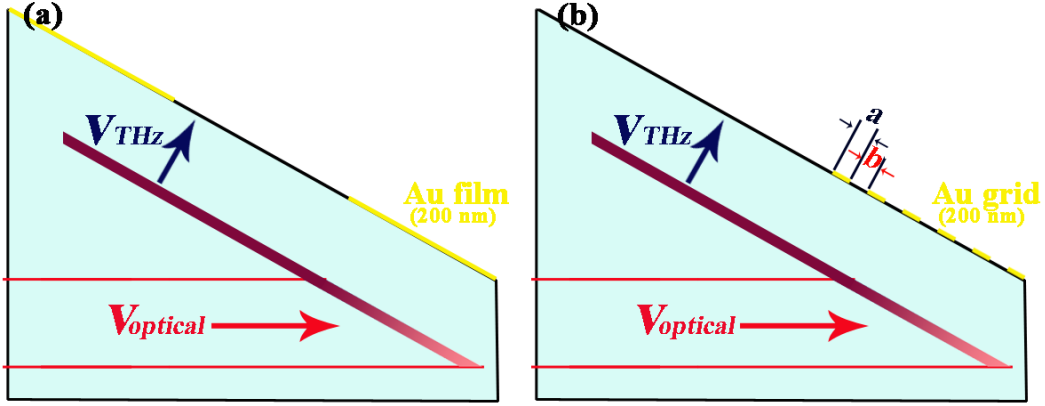
Figure 6.1: Illustration of THz pulse reflection at (a) the crystal-air boundary and the crystal-Au boundary, and (b) the crystal-air boundary and the crystal-Au grating boundary.

As illustrated in Figure 6.1(a), the THz pulse is generated in the $LiNbO_3$ crystal by an optical pump pulse with the tilted-pulse-front excitation technique (see Chapter 5) [1, 2]. The generated THz pulse propagates through the crystal and gets reflected at the crystal surface. Part of the crystal surface is deposited with a 200 nm-thick gold (Au) film (using thermal deposition method) and the rest of the surface is exposed to the air.

The whole THz pulse reflection process at the $LiNbO_3$ crystal surface is shown in Figure 6.2. We find that the THz pulse doesn't change in phase at the crystal-air boundary, but has a 180 °phase change at the crystal-Au film boundary. According to Maxwell's theory [3], if an electromagnetic wave propagates from a high refractive index medium to a low refractive index medium, the reflected wave has no phase change. On the other hand, if the electromagnetic wave is incident on a conductive film, the reflected wave has 180 °phase change.
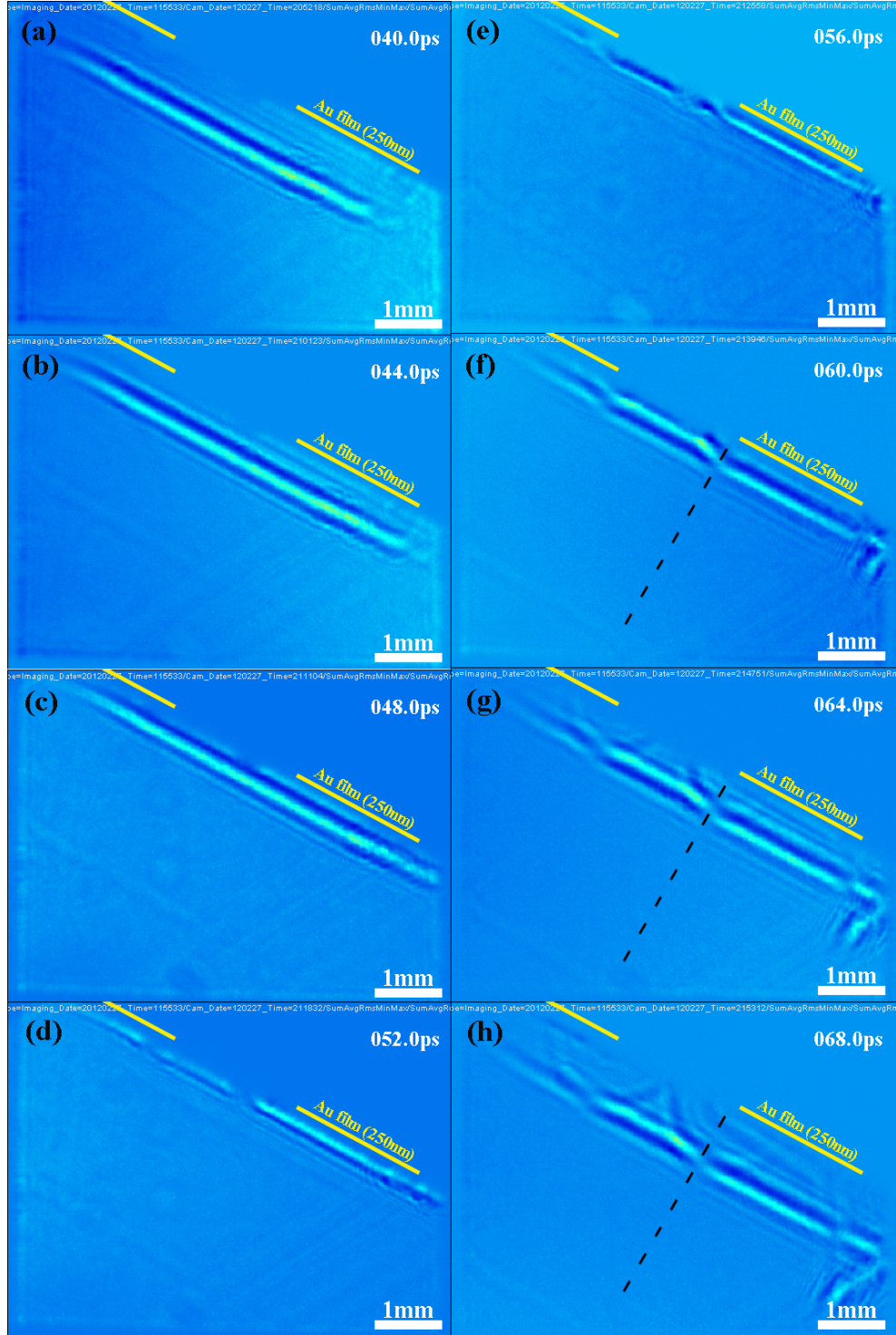
Figure 6.2: Images of THz pulse reflection captured at time delays of (a) 40.0 ps, (b) 44.0 ps, (c) 48.0 ps, (d) 52.0 ps, (e) 56.0 ps, (f) 60.0 ps, (g) 64.0 ps, and (h) 68.0 ps. The Au film thickness is 250 nm.

Besides a nice demonstration of Maxwell's theory, Figure 6.2 also enables us to observe THz destructive interference by THz pulses reflected at the crystal-air boundary and the crystal-Au boundary. As marked by the dashed line in Figure 6.2, we find that the THz electric field is almost zero at the meeting point, suggesting a new type of THz antireflection coating could be made.

In order to demonstrate this as a possible antireflection coating, the large area Au film is replaced by an Au grating (deposited using thermal deposition method with a mask), as shown in Figure 6.1(b), where the width of the Au line and gap are a and b, respectively.

Figure 6.3 shows the images of the reflected THz pulse when the width of the Au line and the gap are 0.1 mm and 0.2 mm, respectively. Compared to the reflected THz pulse shown in Figure 6.2, the main part of the reflected THz pulse still has $180°$ phase change (marked by the red and white dashed lines in Figure 6.3(h)), and the rest part of the THz pulse propagates in other directions. The $180°$ phase change implies that the THz pulse reflected at the crystal-Au line boundary is much stronger than that at the crystal-air gap boundary.

As shown in Figure 6.4, another experiment is carried out with the width of the Au line and gap 0.1 mm and 0.5 mm, respectively. We find that the reflected THz pulse doesn't have the phase change. Figure 6.3 and Figure 6.4 demonstrate that the reflected THz pulse could be eliminated completely if we can optimize the width of Au line and the gap. Compared to the quarter-wave antireflection coating, which only works at a fixed wavelength, this Au grating antireflection coating could work in a broad band width, due to the independence of the phase change ($180°$) at the crystal-Au boundary on the wavelength.

Instead of depositing Au grating structures with a mask, some groups have deposited thin metal films on various substrates to create nanostructured films (e.g. metal islands and gaps) for antireflection application [4, 5]. We also tried to deposit 5 nm Au film [6], which has a random nanoisland structure, on a $LiNbO_3$ slab and study its antireflection behaviour with THz-TDS method as well. Although no encouraging result was obtained in the preliminary experiment, it's

still worth to keep exploring in the future, especially using the transverse imaging method.

Besides imaging the reflected THz pulse, we are also able to image the transmitted THz pulse. As illustrated in Figure 6.5, a second $LiNbO_3$ crystal is attached to the first crystal. Figure 6.6 shows how the reflected and transmitted THz pulses propagate in these two crystals. At the crystal-Au grating boundary, different from the reflected THz pulse, which is distorted, the wavefront of the transmitted THz pulse is uniform (see Figure 6.6(g)).

Figure 6.3: Images of the THz pulse reflection captured at time delays of (a) 6 ps, (b) 12 ps, (c) 18 ps, (d) 24 ps, (e) 30 ps, (f) 36 ps, (g) 42 ps, and (h)48 ps. The width of the Au line and the gap are 0.1 mm and 0.2 mm, respectively.

Figure 6.4: Images of the THz pulse reflection captured at time delays of (a) 6 ps, (b) 12 ps, (c) 18 ps, (d) 24 ps, (e) 30 ps, (f) 36 ps, (g) 42 ps, and (h) 48 ps. The width of the Au line and the gap are 0.1 mm and 0.5 mm, respectively.

Figure 6.5: Illustration of the experimental setup for imaging the reflected and transmitted THz pulses in two LiNbO$_3$ crystals. The width of the Au line and the gap are 0.1 mm and 0.2 mm, respectively.

Figure 6.6: Images of the reflected and transmitted THz pulses in two LiNbO$_3$ crystals at time delays of (a) 40 ps, (b) 48 ps, (c) 56 ps, (d) 64 ps, (e) 72 ps, (f) 80 ps, (g) 88 ps, and (h) 96 ps. The width of the Au line and the gap are 0.1 mm and 0.2 mm, respectively.

6.2 Imaging of THz pulse total internal reflection, transmission and tunneling

The total internal reflection of the THz pulse is imaged with the transverse imaging technique. As illustrated in Figure 6.7, the THz pulse is generated with the tilted-pulse-front excitation technique in the LiNbO$_3$ crystal. Because the crystal is flipped, the incident angle of the THz pulse at the crystal-air boundary is much higher than the critical angle (~12 °) [7], and THz total internal reflection occurs. Images of the total internal reflection process are shown in Figure 6.8 and we find that the amplitude of the reflected THz pulse is the same as the incident THz pulse. However, we did not observe the Goos-Hänchen shift, the reason could be due to the imaging smearing (because of the Talbot imaging effect).
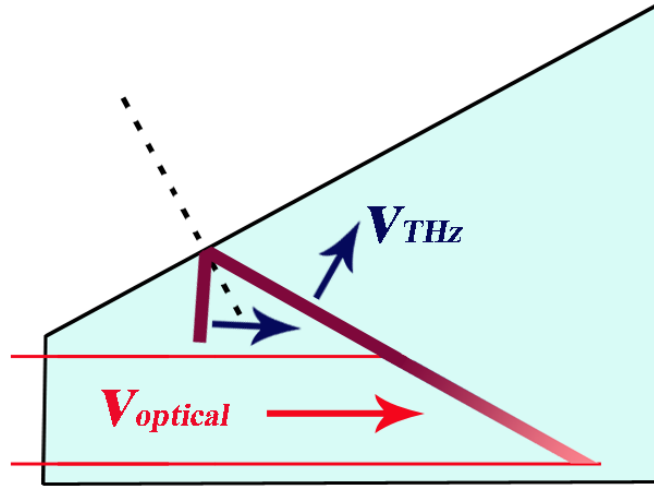
Figure 6.7: Illustration of the THz total internal reflection at the LiNbO$_3$ crystal-air boundary.

Frustrated total internal reflection of the THz pulse is illustrated in Figure 6.9. A second piece of the LiNbO$_3$ crystal is attached to the first one and the gap between the two crystals is controlled by the thickness of inserted glass slabs.

According to Chapter 2 and Chapter 5, the THz pulse has different k (wave vector) components, and every component is imaged efficiently through the Talbot effect only at certain displacement between the THz pulse object and the

camera object plane. Here, because the displacement is 25 mm, which makes the wavelength 0.38 mm (at 0.22 THz, also verified in Figure 6. 10) in LiNbO$_3$ be imaged efficiently. Since parameters including wavelength (0.38 mm), refractive index of the LiNbO$_3$, incident angle (53°) are known, theoretical tunneling transmission coefficient of the s-polarized THz pulse is calculated by equation [8],

$$t = \sqrt{1/(\alpha sinh^2(y) + 1)}$$
$$\alpha = [(n_i^2 - 1)/2n_i]^2 [1/(cos^2\theta_i [n_i^2 sin^2\theta_i - 1])] \qquad (6.1)$$
$$y = (2\pi d/\lambda)\sqrt{n_i^2 sin^2\theta_i - 1}$$

where t is the transmission of the s-polarized THz wave, $n_i = 5.1$ is the refractive index in LiNbO$_3$, $\lambda = 0.38$ mm is the THz wavelength in LiNbO$_3$, and $\theta_i = 53°$ is the incident angle. The plot is shown in Figure 6.11.

As shown in Figure 6.10, images of the tunnelled THz pulse are obtained at three different gap widths. When the gap width is zero, most of the THz pulse goes through the boundary (Figure 6.10(a)). When the gap width is 75 μm (Figure 6.10(b), part of the THz pulse gets reflected and the rest tunnels to the second crystal. If the gap becomes wider, the transmitted THz pulse becomes weaker, as shown in Figure 6.10(c), where almost all the THz pulse gets reflected when the gap is as wide as 150 μm. Compared to the theoretical plot in Figure 6.11, the transmissions at air gap widths 0 μm and 150 μm make sense. However, at 75 μm, the imaged data shows a higher transmission, which could be due to the measurement error of the air gap width. We note that, as shown in Figure 6.10(b), the THz pulse in the attached crystal has a reversed phase. This could be caused by the accidental change of crystal orientation in the experiment. On the other hand, it could also be a new physics phenomenon. Further experiments should be done to clarify this.
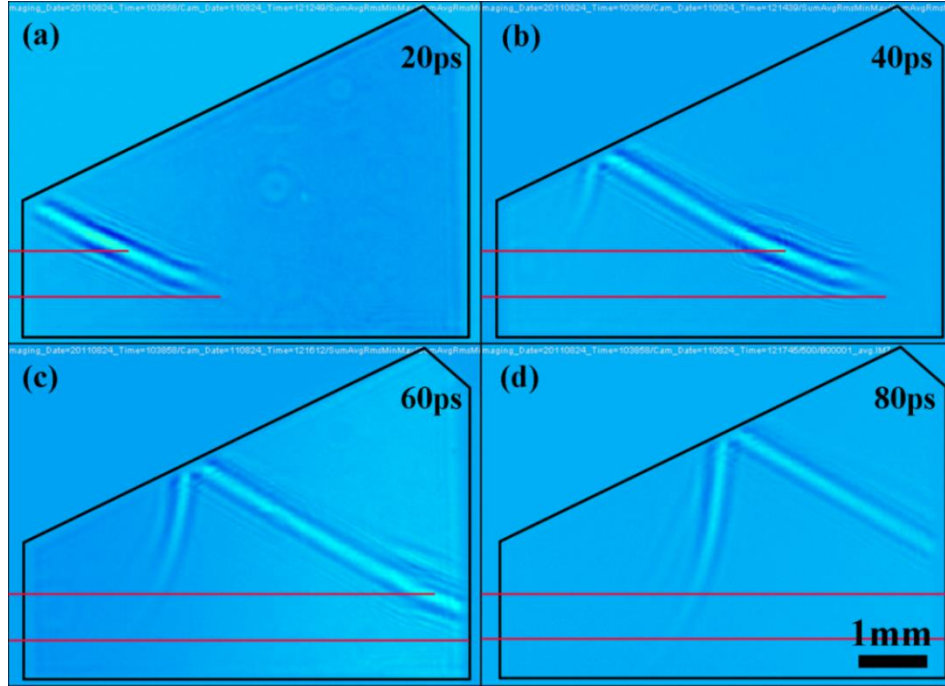
Figure 6.8: Images of THz total internal reflection captured at time delays of (a) 20 ps, (b) 40 ps, (c) 60 ps, and (d) 80 ps. The THz incident angle at crystal-boundary is 53 °.
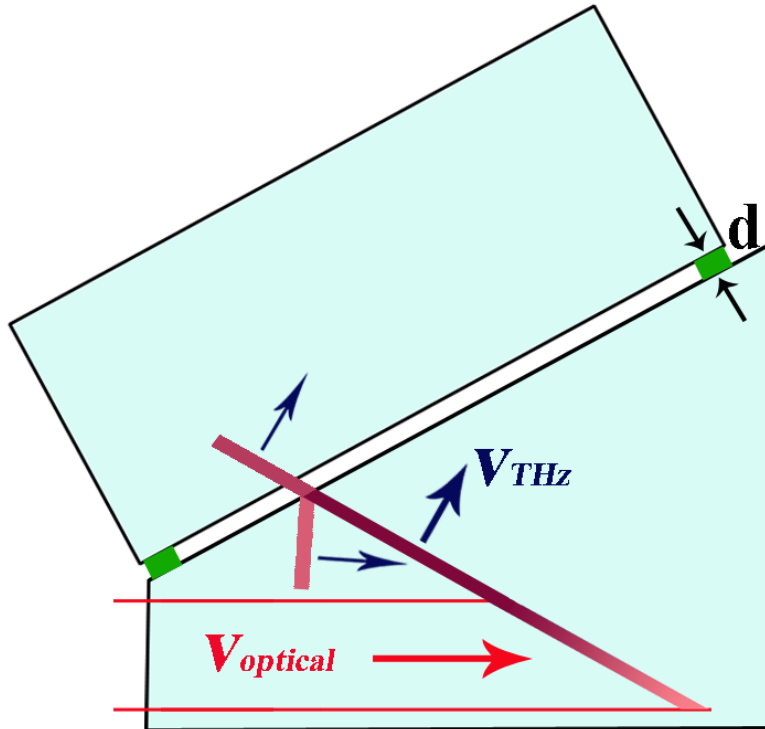

Figure 6.9: Illustration of THz tunnelling through the air gap two LiNbO$_3$ crystals. Two glass slabs are inserted between the two crystals to control the gap width **d**.
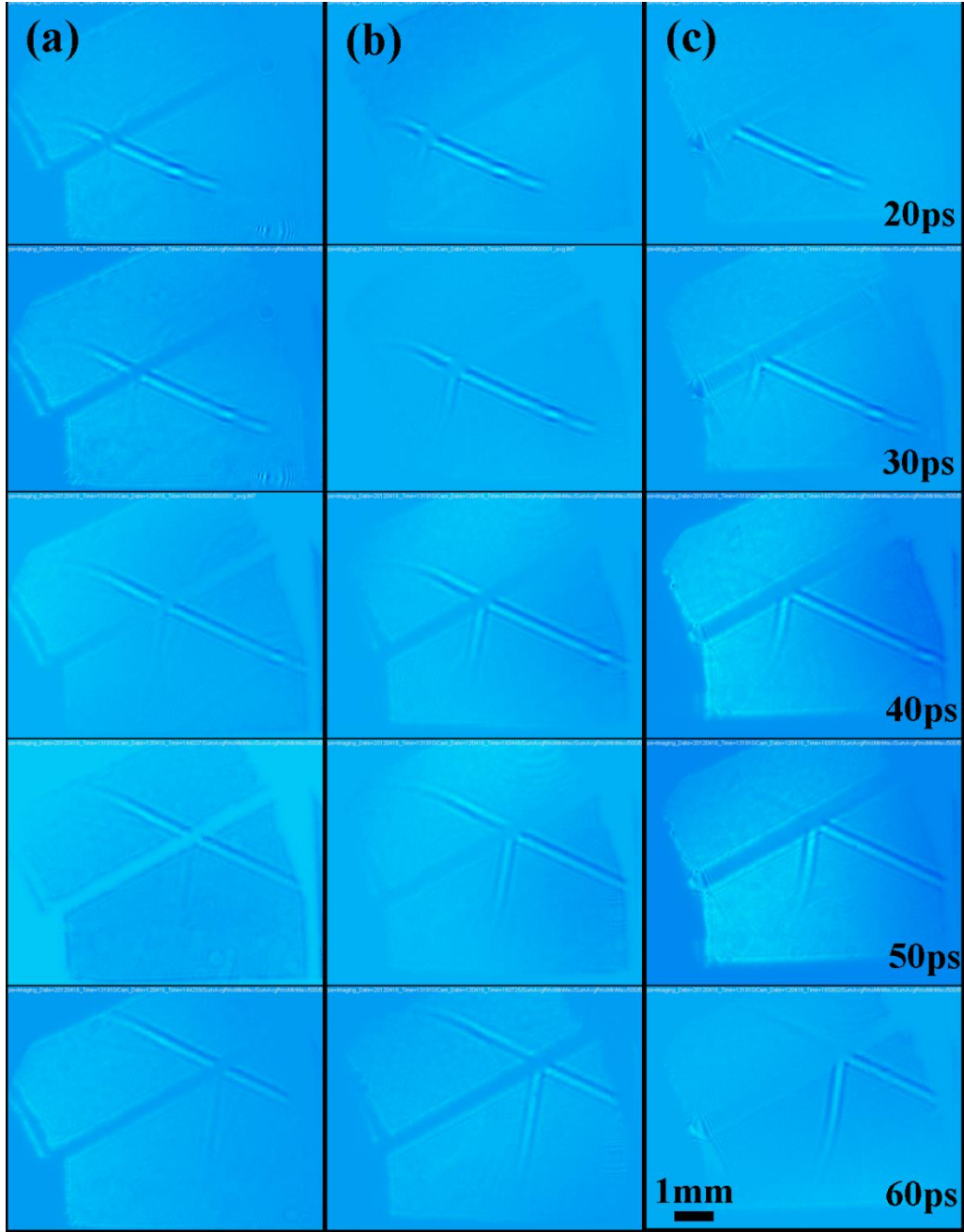
Figure 6.10: Images of frustrated total internal reflection of THz pulses at an air gap width of (a) 0 μm, (b) 75 μm, and (c) 150 μm. The phase reverse in the attached crystal shown in (b) could be due to the change of crystal orientation in the experiment by accident, further experiment should be done to figure out this issue.
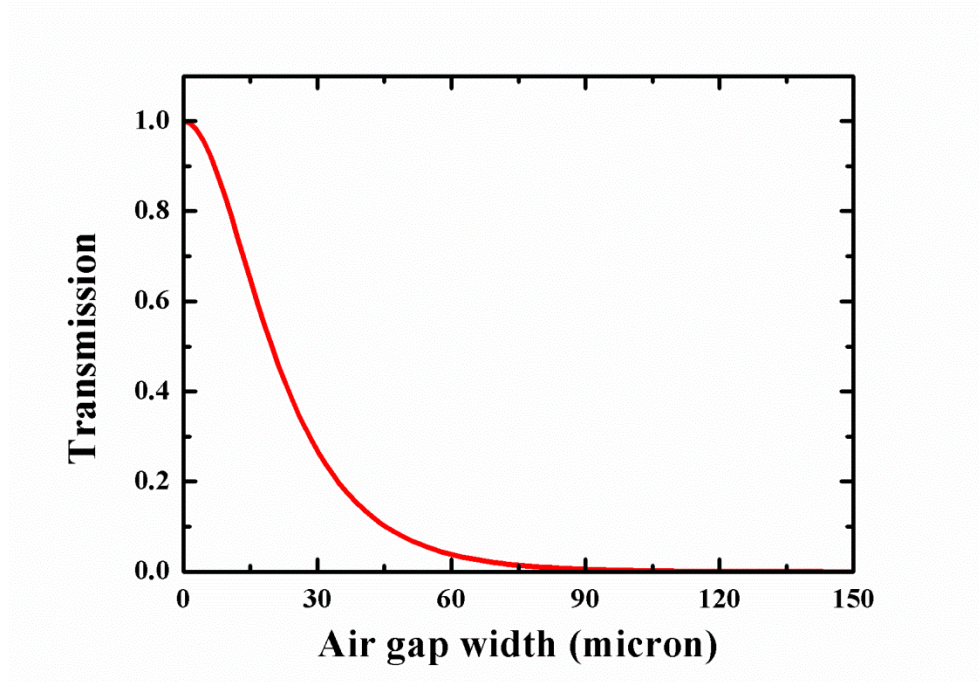
Figure 6.11: Theoretical THz pulse (s-polarized) transmission at different air gap widths. The central THz frequency is 0.22 THz (λ=0.38 mm in LiNbO$_3$), the refractive index of LiNbO$_3$ crystal is 5.1, and the incident angle is 53 °.

6.3 Anomalous THz reflection within the region of the optical pump beam
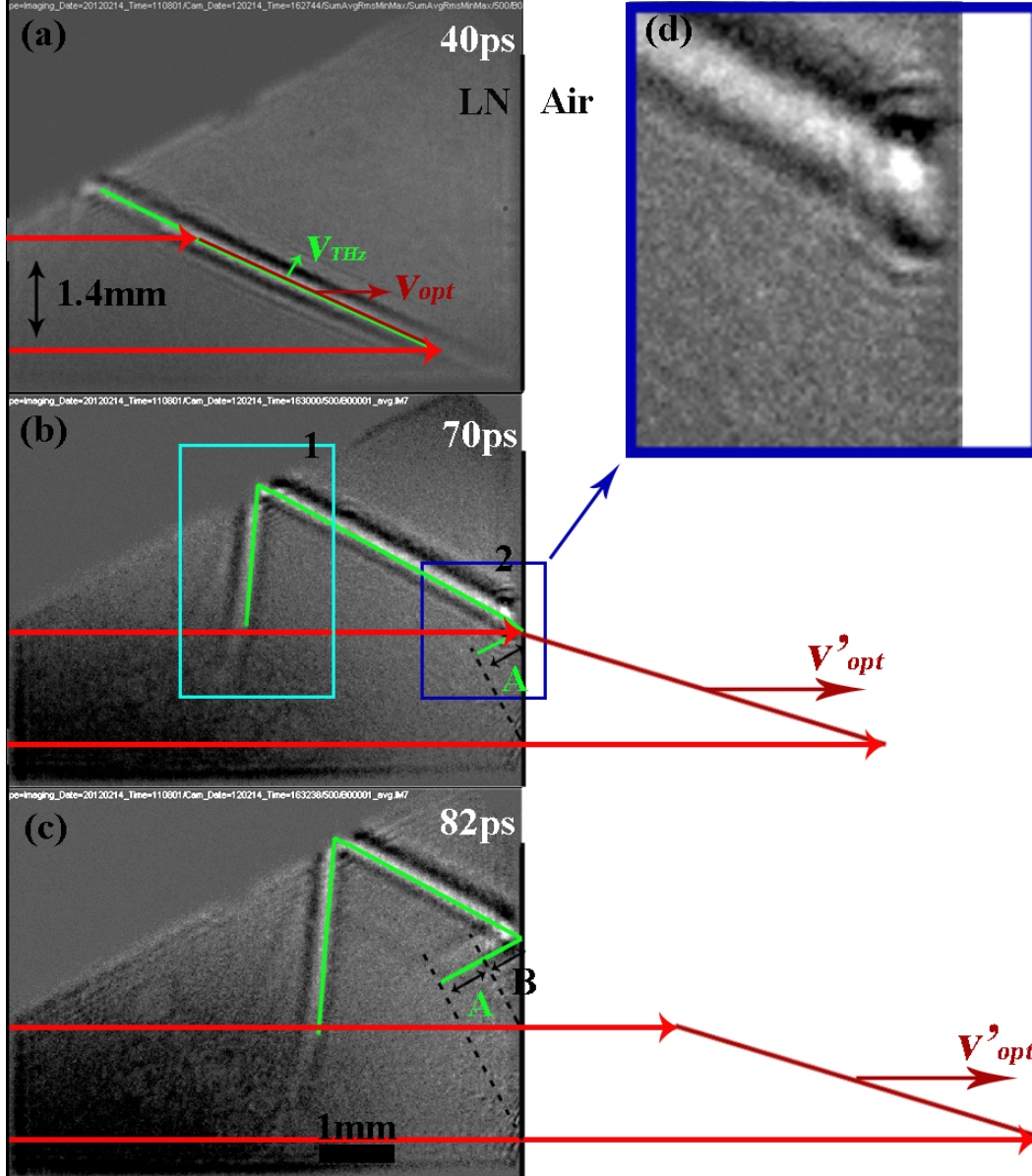
Figure 6.12: (a)-(c) Images of THz reflection at time delays of 40 ps, 70 ps, and 82 ps. (d) The magnified inset of (b). For a high contrast ratio, images are treated with PHOTOSHOP.

The purpose of this section is to figure out anomalous THz pulse reflection within the region of the optical pump beam. For comparison, illustration of THz pulses (green line) and optical pulses (red line), and actual experimental images are shown together, as shown in Figure 6.12.

Figures 6.12(a)-(c) show THz pulse reflection process at two crystal-air interfaces (the top interface is in the tilted direction, and the right interface is in the vertical direction). Optical pump pulses (1.4 mm beam width) propagate through the crystal and generate THz pulses.

Due to large THz incident angles (larger than the critical angle ~12° [7]) at the tilted interface (in square 1 shown in Figure 6.12(b)) and the vertical interface (in square 2 shown in Figure 6.12(b)), the THz pulse is supposed to get totally internal reflected at both interfaces, as illustrated by green lines in Figures 6.12(a)-(c).

As shown in Figure 6.12(b) and (c), we observed a reflected THz pulse (in square 1) at the tilted interface, which is consistent with the prediction (illustrated in green line). On the other hand, at the vertical interface (in square 2 shown in Figure 6.12(b)), no reflected THz pulse is observed in both Figure 6.12(b) and its magnified inset Figure 6.12(d), which is different from the prediction (see green line **A** in Figure 6.12(b)).

We note that, different from the THz pulse in square 1, which has already been separated from the optical pulse before the reflection, the predicted reflected THz pulse (green line **A** in square 2 shown in Figure 6.12(b)) comes from the THz pulse that is still mixed with the optical pump pulse in the region of the optical pump beam, as we discussed in Section 5.2.4. In short, pure THz pulses experiences total internal reflection, while the THz pulse that is mixed with the optical pump pulse in the region of the optical pump beam does not. In conclusion, the THz pulse in the region of the optical pump beam experiences an anomalous reflection (zero reflection).

Figure 6.12(c), which is taken at a later time delay (82 ps), further proves our assumption. We find that the reflected THz pulse (see area indicated by green line **B**) at the vertical interface appears. But this reflected THz pulse comes from the

region outside of the optical pump beam (pure THz pulse). The reflected THz pulse that is from the region of the optical pump beam (mixed THz pulse) is still not observed (see line **A**).

Now the question turns out that why the mixed THz pulse experiences an anomalous (zero) reflection. We don't have a clear answer yet. However, the transition-like radiation induced by the optical pulse at the interface could be the reason.
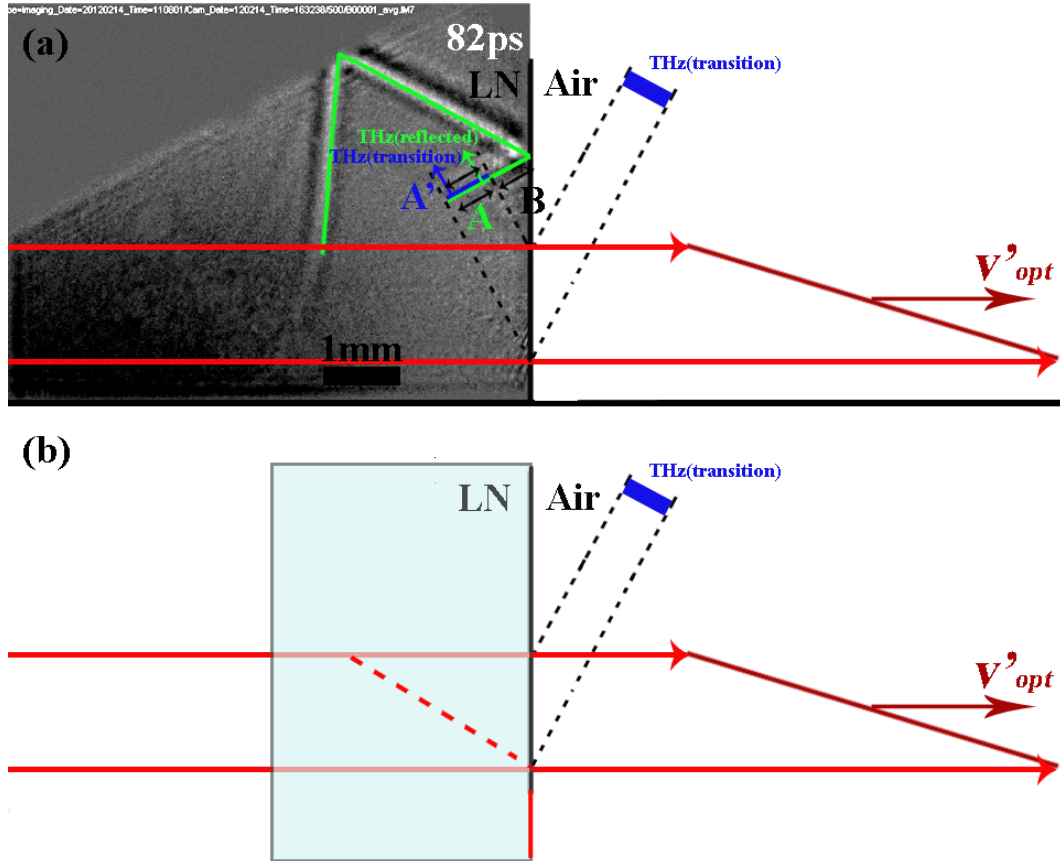

Figure 6.13: (a) Illustration of the destructive interference between the reflected THz pulse and the backward-propagating transition-like radiation in the crystal. The forward-propagating transition-like radiation in air is shown as well. (b) Design of new LiNbO$_3$ THz sources using LiNbO$_3$ slab based on the transition-like radiation.

In fact, in the discussion of Figure 6.12, we ignored the transition-like radiation that is induced by the optical pump pulse when it exits through the

vertical interface. We note that the optical pulse transmission is 100% due to the anti-reflection (AR) coating. As discussed in Ref. [9-11], the induced transition-like radiation has two components: one propagates forward into air (forward-propagating transition-like radiation), and another one propagates backward (backward-propagating transition-like radiation) into the crystal. As shown in Figure 6.13(a), the induced transition-like radiation (blue line **A'**) inside the crystal propagates in the exact same direction and velocity as the reflected THz pulse (green line **A**).

Since the transition-like radiation and the reflected THz pulse overlap with each other in region **A** (or **A'**), the two waves have an interference. According to Ref. [9, 10, 12], the backward-propagating transition-like radiation and the reflected THz pulse have a 180° phase difference, which makes the two waves cancel with each other and finally results in an anomalous (zero) reflection in the region of the optical pump beam. We note that the destructive interference should happen exactly at the interface, the illustration shown in Figure 6.13(a), in which the interference happens far from the interface, is only for an easier explanation. Yet, the equal amplitude of the two waves, which causes completed cancellation, need to be verified in the future.

The last question is where the mixed THz pulse goes after an anomalous reflection. Due to the destructive interference between the reflected THz pulse and the transient-like radiation inside the crystal, the lost THz pulse energy may be transferred to the forward-propagating transition-like radiation that propagates in air, as shown in Figure 6.13(a). In other words, the THz pulse in the region of the optical pump beam doesn't have a reflection loss. Instead, it transmits through the crystal-air interface with the electric field strength doubled (due to the addition of the forward-propagating transition-like radiation wave).

The anomalous THz reflection phenomenon in the region of the optical pump pulse may be able to explain why the output THz pulse energy is detectable (due to the maximum THz energy output) only when it is pumped at the tip of the prism (as discussed in Section 5.2.6), in which the THz and optical pulse are mixed.

Based on the observed anomalous THz reflection and tip-pumped geometry discussed in Section 5.2.6, it turns out that the THz pulse generated inside the bulk LiNbO$_3$ doesn't contribute too much to the THz output energy, and that the transition-like radiation generated in the region of the optical pump beam contributes a lot.

Here a new design of LiNbO$_3$ THz sources is proposed. As shown in Figure 6.13(b), instead of an expensive LiNbO$_3$ prism, a piece of LiNbO$_3$ slab is pumped by a tilted wave front optical pump pulse to generate the THz pulse. Compared to the geometry with optical pump pulse front not tilted, the tilted pump pulse wave front enables the transition-like radiation generated on front and back surfaces to add each other to form a THz pulse with higher pulse energy. Of course, optimization of the slab thickness and experiments need to be performed in the future.

6.4 Conclusions

THz pulse reflection, transmission, and tunnelling phenomena are imaged with the transverse imaging technique. By imaging the phase change of the reflected THz pulse at the crystal-air boundary and the crystal-Au boundary, the phase modulation predicted by Maxwell's theory is demonstrated. What's more, because the reflected THz pulse at the crystal-Au boundary has a $180\,^{\circ}$ phase change, we propose and demonstrate a possible broad band antireflection coating. By adding a second $LiNbO_3$ crystal, we also imaged the THz total internal reflection, transmission and tunnelling successfully. Furthermore, an anomalous (zero) reflection of the THz pulse in the region of the optical pump beam is observed and explained. A new design of $LiNbO_3$ THz sources is proposed as well. The successful demonstration of THz reflection, transmission, tunneling convinces us that the transverse imaging technique is a useful tool to study various optics phenomena at interfaces.

References:

1. J. Hebling, G. Almasi, I. Z. Kozma, and J. Kuhl, "Velocity matching by pulse front tilting for large-area THz-pulse generation," Opt. Express **10**, 1161-1166 (2002).

2. J. Hebling, K.-L. Yeh, M. C. Hoffmann, B. Bartal, and K. A. Nelson, "Generation of high-power terahertz pulses by tilted-pulse-front excitation and their application possibilities," J. Opt. Soc. Am. B **25**, B6-B19 (2008).

3. D. J. Griffiths, *Introduction to electrodynamics* (Addison Wesley, 1999).

4. J. Kroll, J. Darmo, and K. Unterrainer, "High-performance terahertz electro-optic detector," Electron. Lett. **40**, 763-764 (2004).

5. A. Thoman, A. Kern, H. Helm, and M. Walther, "Nanostructured gold films as broadband terahertz antireflection coatings," Phys. Rev. B **77**, 9 (2008).

6. M. Walther, D. G. Cooke, C. Sherstan, M. Hajar, M. R. Freeman, and F. A. Hegmann, " Terahertz conductivity of thin gold films at the metal-insulator percolation transition," Phys. Rev. B **76**, 9 (2007).

7. T. Feurer, N. S. Stoyanov, D. W. Ward, J. C. Vaughan, E. R. Statz, and K. A. Nelson, "Terahertz polaritonics," Ann. Rev. Mater. Res. **37**, 317-350 (2007).

8. I. N. Court, and F. K. v. Willisen, "Frustrated total internal reflection and application of Its principle to laser cavity design," Appl. Opt. **3**, 719-726 (1964).

9. M. I. Bakunov, S. B. Bodrov, A. V. Maslov, and M. Hangyo, "Theory of terahertz generation in a slab of electro-optic material using an ultrashort laser pulse focused to a line," Phys. Rev. B **76,** 085346 (2007).

10. M. I. Bakunov, A. V. Maslov, and S. B. Bodrov, "Fresnel formulas for the forced electromagnetic pulses and their application for optical-to-terahertz conversion in nonlinear crystals," Phys. Rev. Lett. **99,** 203904 (2007).

11. M. I. Bakunov, S. B. Bodrov, and E. A. Mashkovich, "aa(very good theary paper about THz fringes)Terahertz generation with tilted-front laser pulses: dynamic theory for low-absorbing crystals," J. Opt. Soc. Am. B **28**, 1724-1734 (2011).

12. L. Xu, X.-C. Zhang, and D. H. Auston, "Terahertz beam generation by femtosecond optical pulses in electrooptic materials," Appl. Phys. Lett. **61**, 1784-1786 (1992).

Chapter 7

Ultrafast imaging of femtosecond optical pulses in various media

The purpose of this chapter is to demonstrate other potential applications of the transverse imaging technique. A couple of preliminary experiments are carried out to image the interaction between femtosecond optical pump pulses and various media. Similar to the LiNbO$_3$ crystal, a periodically poled lithium niobate (PPLN) crystal is pumped by a point focused optical femtosecond pulse and the generated THz pulse is imaged. An air plasma generated by an intense optical pump pulse is imaged. Based on the Kerr effect, the refractive index modulation induced by femtosecond pulses in CS$_2$, water, methanol, THF, and quartz is imaged as well.

7.1 Ultrafast imaging of terahertz pulse generation in periodically poled lithium niobate

The periodically poled lithium niobate (PPLN) crystal is a very popular EO crystal for generating new frequencies of radiation through the second-order nonlinear optics effect [1-8]. By adjusting the poling period, the phase matching can be optimized for the specified radiation frequency.
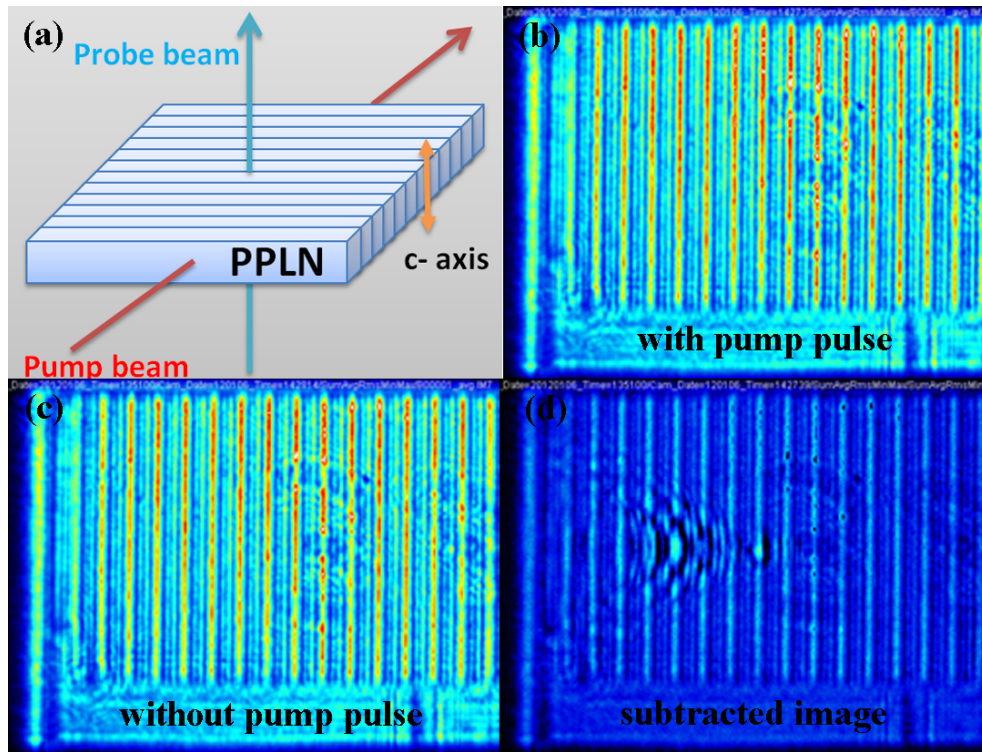
Figure 7.1: (a) Experimental setup for imaging THz generation and propagation in a PPLN crystal. An optical pump pulse (800 nm) is point focused onto the PPLN crystal to generate THz pulses, and the probe pulse (400 nm) is transmitted through the crystal to image the THz generation and propagation processes. (b) and (c) Are images captured with and without (background) optical pump pulse excitation, respectively. (d) The background-subtracted image of the THz pulse.

Here, we demonstrate the imaging of nonlinear optics phenomenon inside a PPLN crystal (provided by Prof. Rene Beigang's group). As illustrated in Figure 7.1(a), an optical pump pulse is incident on the PPLN crystal to generate terahertz

(THz) pulses, and a probe pulse is employed to image the THz pulse in the PPLN crystal by propagating perpendicular to that of the optical pump pulse. The probe pulse phase modulation by the THz electric field is finally imaged by the ICCD camera through Talbot effect [9, 10], as discussed in Chapter 2.
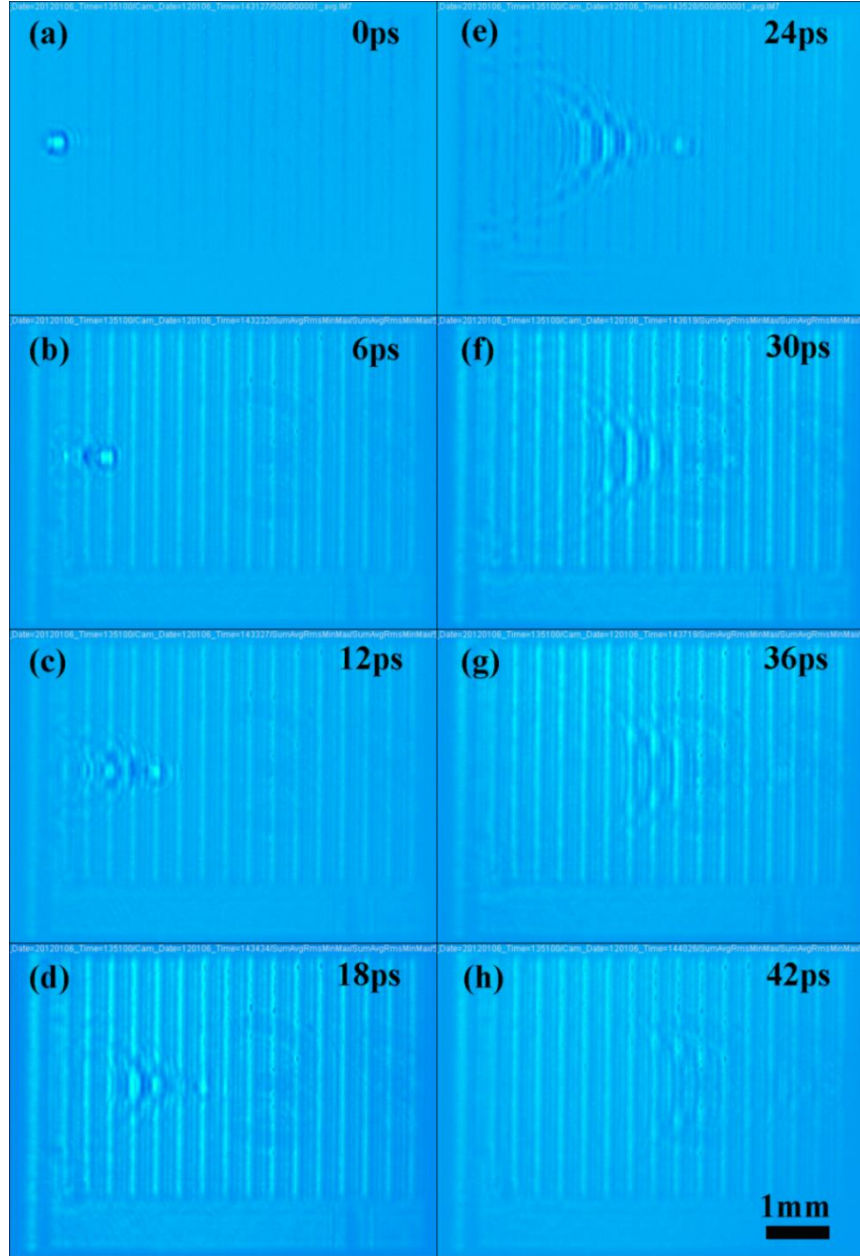
Figure 7.2: Images of the THz pulse in the PPLN crystal at time delays of (a) 0 ps, (b) 6 ps, (c) 12 ps, (d) 18 ps, (e) 24 ps, (f) 30 ps, (g) 36 ps, and (h) 42 ps.

Sample images are shown in Figures 7.1(b)-(d). Figure 0073(c) shows the image captured without the optical pump pulse excitation and is considered as the background image, Figure 7.1(b) is the image captured with the optical pump pulse excitation, and the background-subtracted image is shown in Figure 7.1(d).

As shown in Figure 7.2, images of the generated THz pulse at different time delays are captured. As what we demonstrated here and the work done by Yeh [11], since the ability to image THz pulses in PPLN and $LiNbO_3$ slides, the transverse imaging technique can be a powerful tool to study the nonlinear optics in nonlinear crystals.

7.2 Ultrafast imaging of an air plasma generated by intense optical femtosecond pulses

When the air is excited by an intense optical pulse, air molecules are ionized into positive ions and negative electrons and an air plasma is generated [12-18]. In this section, imaging of the air plasma with the transverse imaging method is demonstrated.

As illustrated in Figure 7.3, an optical pump pulse (~ 0.4 mJ, 100 fs) is focused by a lens (400 mm) in the air to generate the air plasma. At the same time, a probe pulse is sent through the pumped area to image it. By changing the time delay between the pump pulse and probe pulse, the evolution process of the generated air plasma is recorded.

The images of the air plasma are averaged over many shots and are shown in Figure 7.4. According to the diffraction pattern induced by the air plasma, the generated air plasma last 200 ps. However, because of the complex behaviour of the plasma, we are not satisfied by the measurement of plasma relaxation time. Unfortunately, the current laser system is not powerful enough to create a large area plasma. We want to image the dynamics of a large area air plasma in the future and hope this preliminary experiment can be a good beginning.
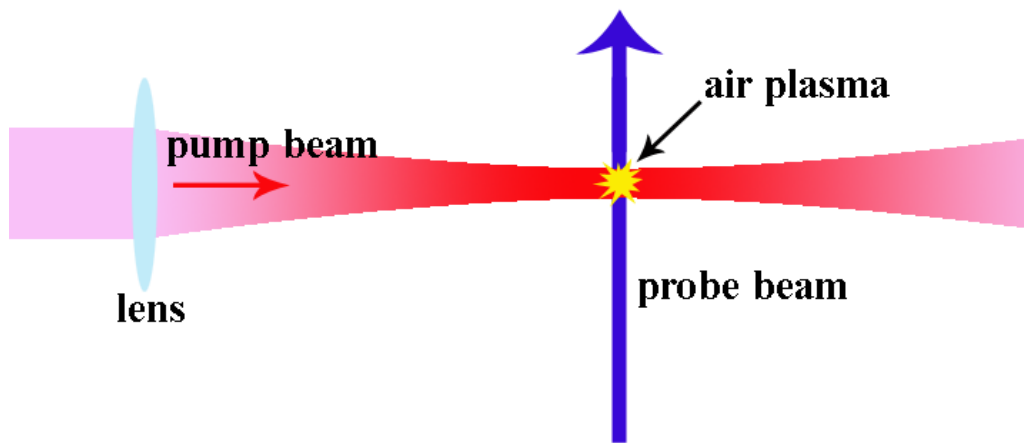
Figure 7.3: Illustration of the experimental setup to generate and image the air plasma.
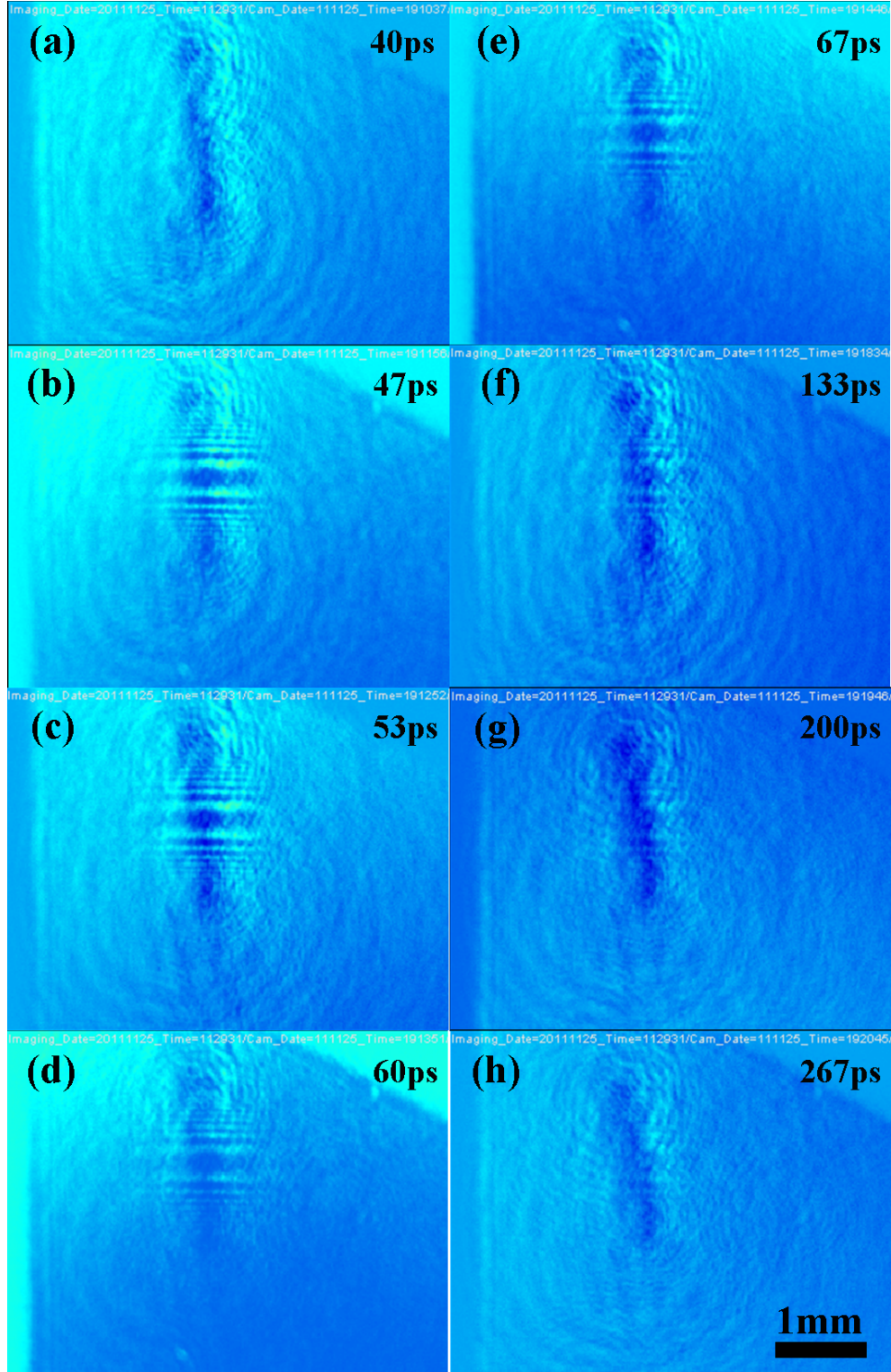
Figure 7.4: Images of the air plasma captured at time delays of (a) 40 ps, (b) 47 ps, (c) 53 ps, (d) 60 ps, (e) 67 ps, (f) 133 ps, (g) 200 ps, and (h) 267 ps. The images are taken by averaging many shots. The optical pump pulse energy is about 0.4 mJ with pulse duration 100 fs.

7.3 Ultrafast imaging of the Kerr effect induced by femtosecond optical pulses in CS$_2$
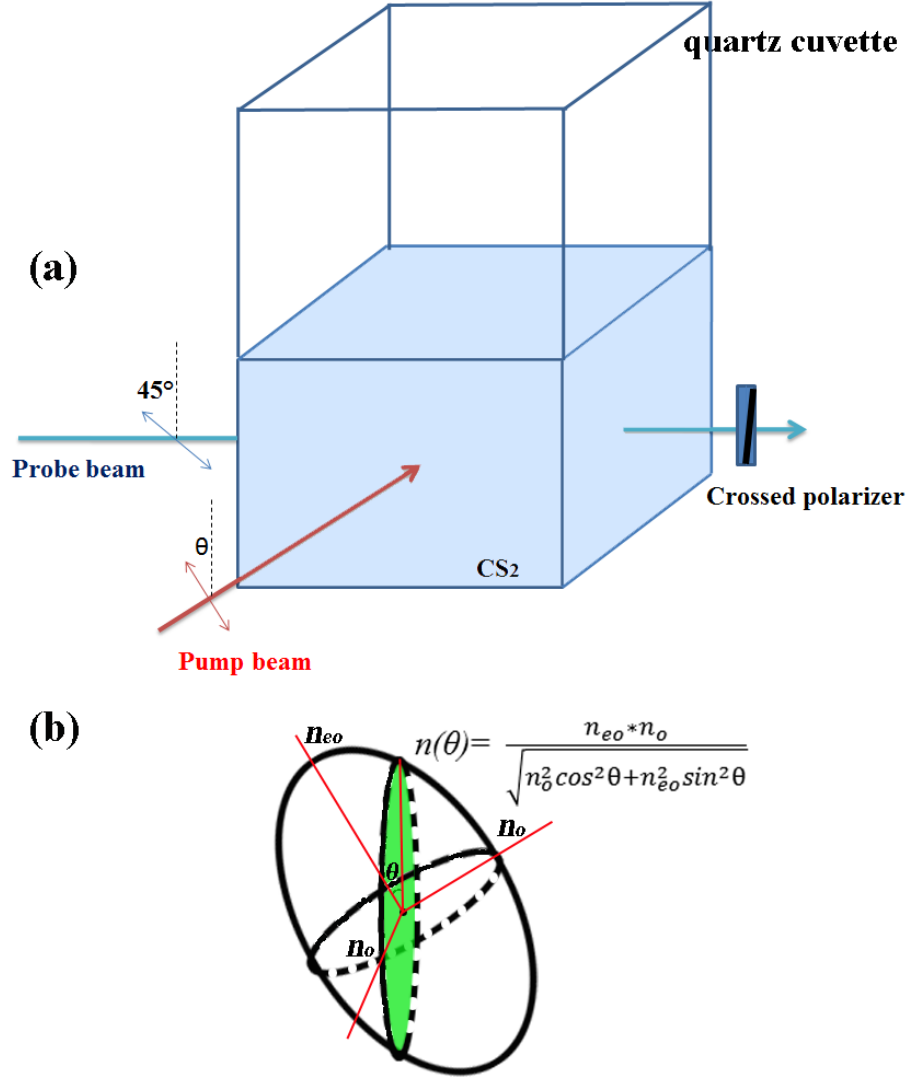

Figure 7.5: (a) Illustration of the experimental setup to image the Kerr effect induced by femtosecond optical pulses in CS$_2$ (contained in a quartz cuvette). The optical pulse (800nm) is focused by a lens (not shown) in CS$_2$. The angle between the optical pump pulse polarization and the vertical direction is θ. The probe pulse is sent through the sample and finally is sampled by a crossed polarizer, and the probe pulse polarization is 45° with respect to the vertical direction. (b) The refractive index ellipsoid induced by the Kerr effect. The birefringence experienced by the probe pulse is shown in the green plane.

CS$_2$ is commonly used for studying the Kerr effect [19-25]. Figure 7.5(a) illustrates the experimental setup for imaging the femtosecond pulse induced Kerr signal in CS$_2$. An optical pump pulse is focused on the CS$_2$ sample to induce the birefringence. The linearly polarized probe pulse is then sent through the pumped area with polarization 45 ° relative to the vertical direction. After propagating through the pumped area, the probe pulse is sampled with a crossed polarizer and finally imaged by the ICCD camera. As shown in Figure 7.5(b), the orientation of the refractive index ellipsoid is the same as the pump pulse polarization, with the refractive index along the optics axis and perpendicular to the optics axis as n_{eo} and n_o, respectively.
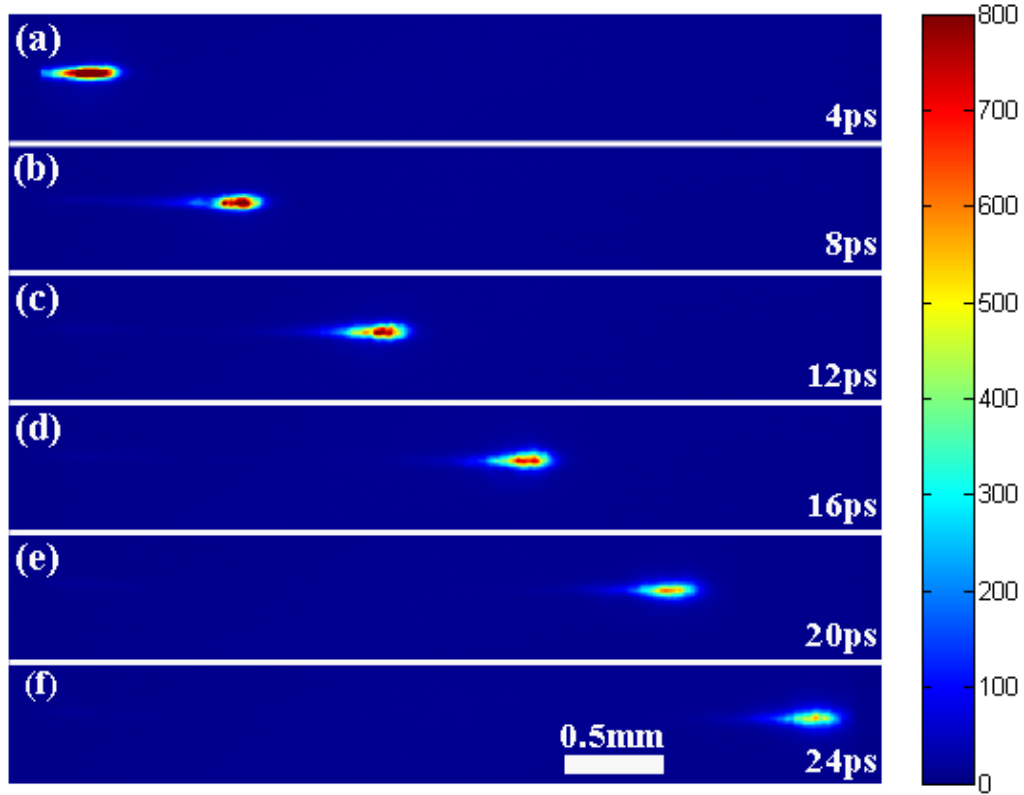
Figure 7.6: Images of Kerr signals in CS$_2$ at time delays of (a) 4 ps, (b) 8 ps, (c) 12 ps, (d) 16 ps, (e) 20 ps, and (f) 24 ps. The color scale bar is in units of counts.

Figure 7.6 shows a series of Kerr signal images with the pump pulse polarization in the vertical direction. Because CS_2 has a long relaxation time (1.75ps) [24, 25], the image of the femtosecond pulse has a long tail. This is because the aligned CS_2 molecules need time to recover back to their original homogenous state. What's more, due to the optical pulse dispersion in CS_2, the Kerr signal becomes weaker when the pump pulse propagates through the sample.
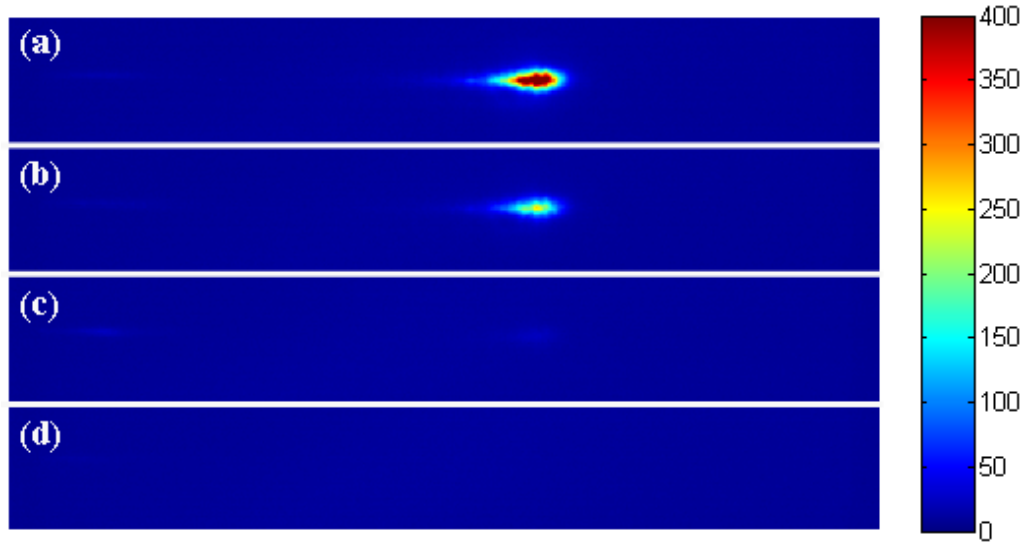

Figure 7.7: Images of the Kerr signal induced by the optical pump pulse polarized at (a) 0 °, (b) 30 °, (c) 60 °, and (d) 90 °. The color scale bar is in units of counts.

If the angle between the optical pump pulse polarization and the vertical direction is θ, the orientation of the optics axis also follows the pump polarization. As shown in Figure 7.5(b), the birefringence experienced by the probe pulse follows the equation,

$$\Delta n = n(\theta) - n_o = \frac{n_{eo}*n_o}{\sqrt{n_o^2 cos^2\theta + n_{eo}^2 sin^2\theta}} - n_o \quad (7.1)$$

where θ is the angle between the pump polarization and the vertical direction, and $n(\theta)$ and n_o are the refractive indices experienced by the two polarization components of the probe pulse. We find that when the pump polarization is

horizontal (θ =90 °), the birefringence experienced by the probe pulse is zero, and no Kerr signal should be imaged. As shown in Figure 7.7, we find that the Kerr signal becomes smaller when the angle θ changes from 0° to 90° and becomes zero at 90 °.

7.4 Movies of femtosecond optical pulses that travel in quartz, water, methanol, THF, and CS_2

As discussed in Section 7.3, the Kerr signal induced by femtosecond optical pulses in CS_2 liquid can be imaged with the transverse imaging technique. Here, using the same experimental setup as Figure 7.5(a), we made movies of femtosecond optical pulses travelling in various media including quartz, water, methanol, THF, and CS_2.

As shown in Figures 7.8-7.14, images of the femtosecond optical pulses in quartz, water, methanol, THF, and CS_2 are captured at time delays of 0 ps, 0.38 ps, 0.78 ps, 1.18 ps, 1.58 ps, 1.98 ps, and 2.28 ps, respectively. According to these images, we find that femtosecond optical pulses travel faster in both water and methanol. We also note that, different from CS_2, Kerr signals in quartz, water, methanol, and THF don't have long tails, which is due to a very short relaxation time. The measured indices in these materials (shown in Table 7.1) match the literature values very well.
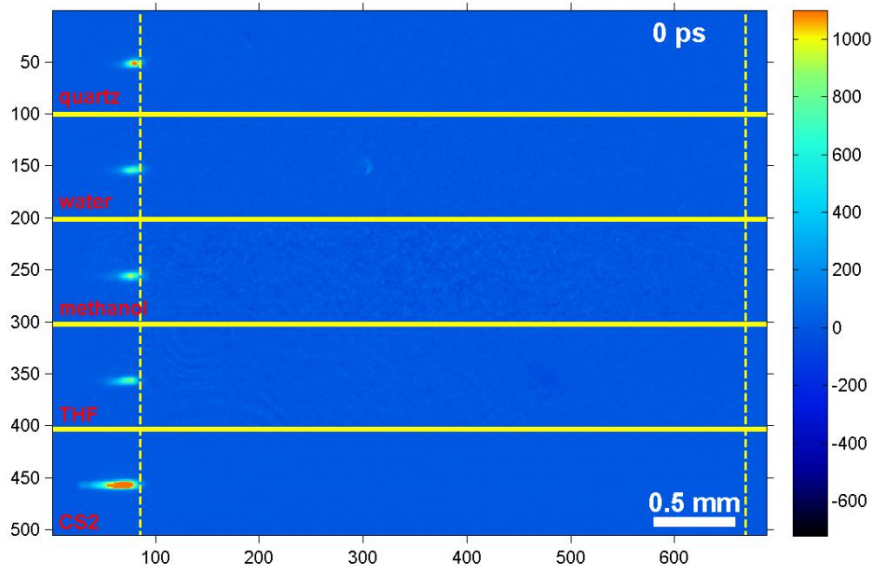
Figure 7.8: Image of the femtosecond optical pulses tranveling in quartz, water, methnol, THF, and CS_2 at a time delay of 0 ps. The color scale bar is in units of counts.
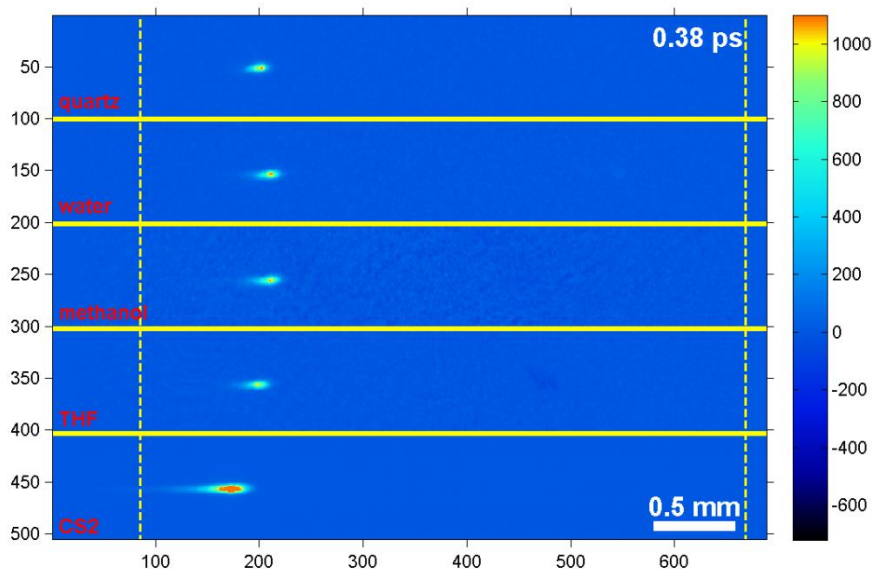
Figure 7.9: Image of the femtosecond optical pulses tranveling in quartz, water, methnol, THF, and CS_2 at a time delay of 0.38 ps. The color scale bar is in units of counts.
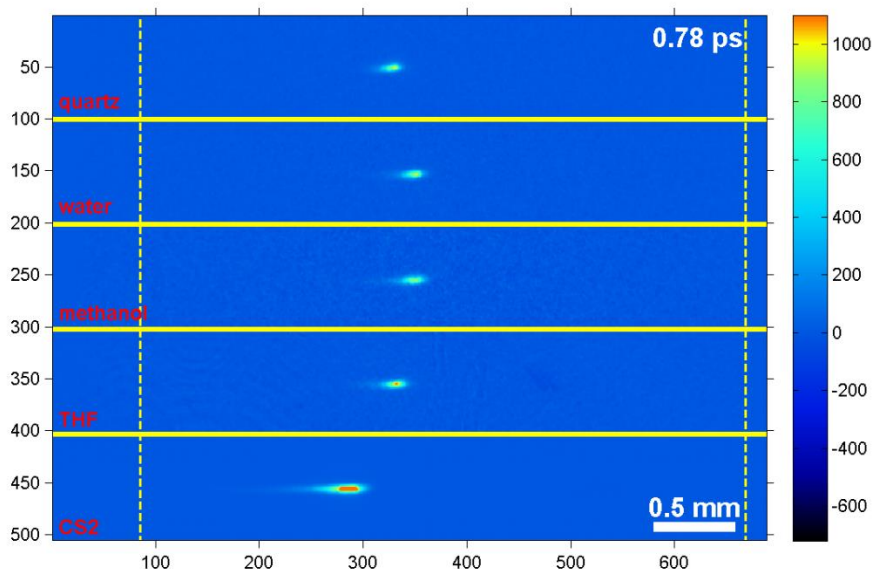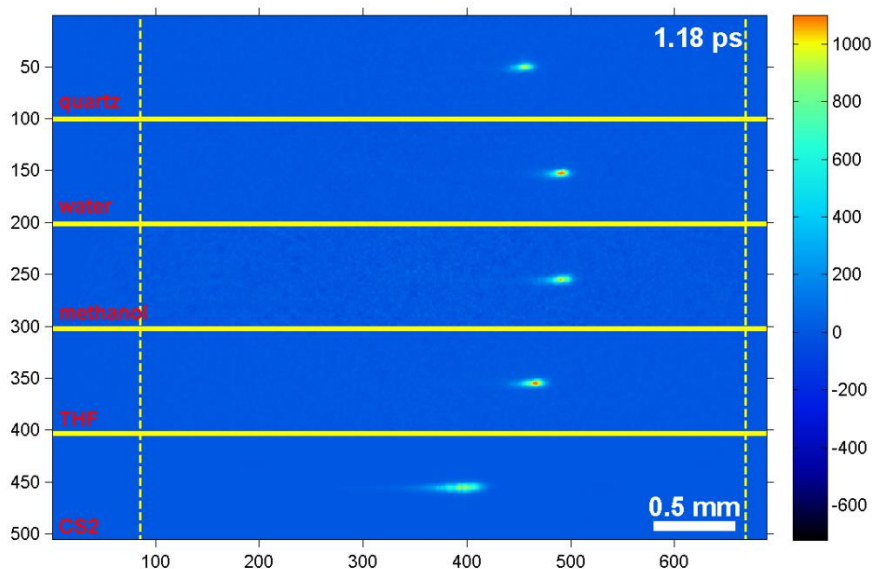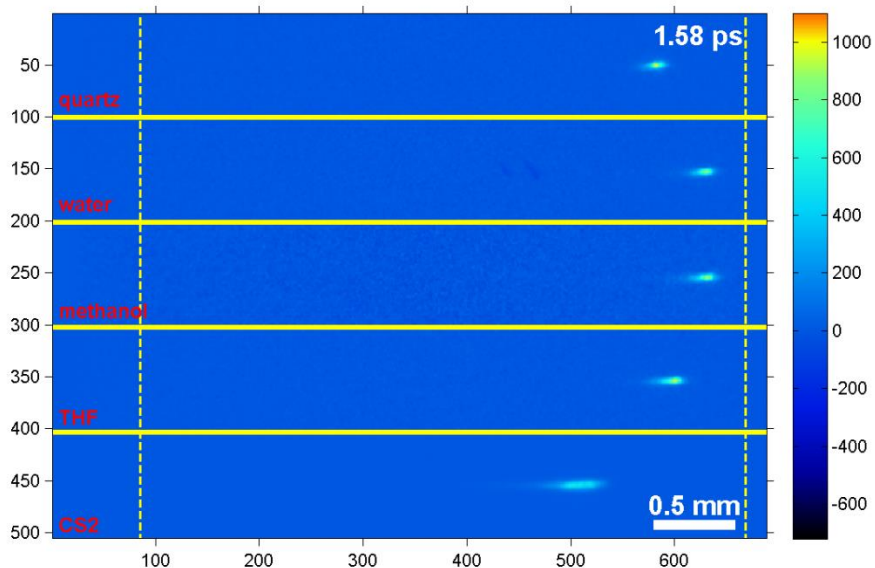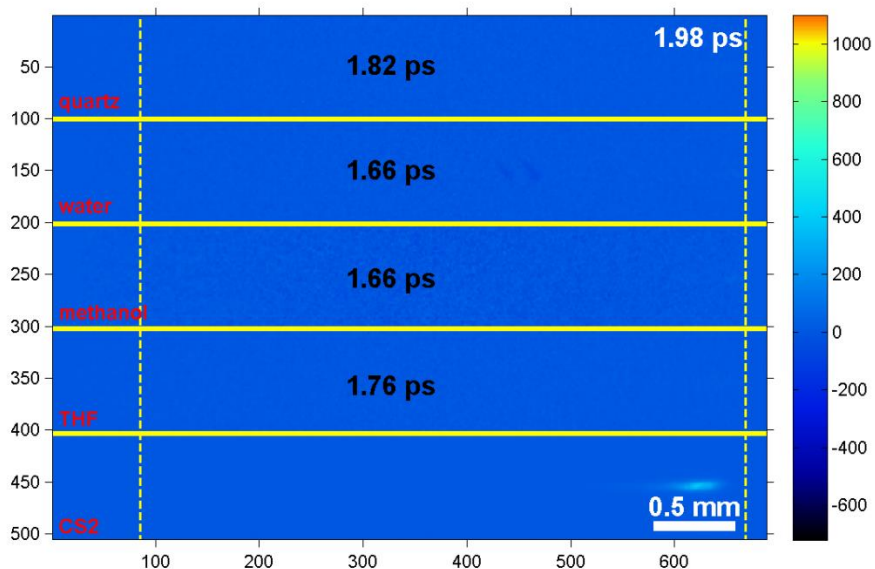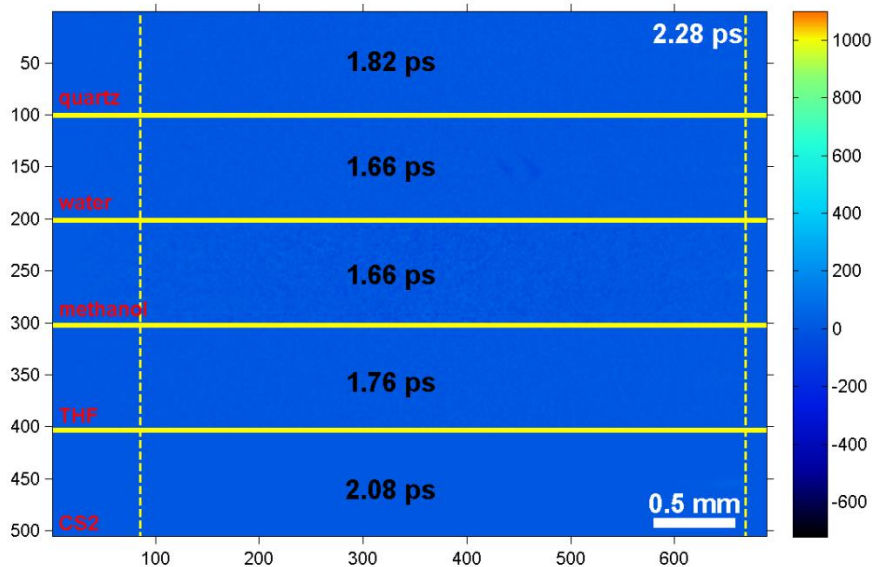

Figure 7.10: Image of the femtosecond optical pulses tranveling in quartz, water, methnol, THF, and CS_2 at a time delay of 0.78 ps. The color scale bar is in units of counts.

Figure 7.11: Image of the femtosecond optical pulses tranveling in quartz, water, methnol, THF, and CS$_2$ at a time delay of 1.18 ps. The color scale bar is in units of counts.

Figure 7.12: Image of the femtosecond optical pulses tranveling in quartz, water, methnol, THF, and CS$_2$ at a time delay of 1.58 ps. The color scale bar is in units of counts.

Figure 7.13: Image of the femtosecond optical pulses tranveling in quartz, water, methnol, THF, and CS_2 at a time delay of 1.98 ps. The color scale bar is in units of counts.

Figure 7.14: Image of the femtosecond optical pulses tranveling in quartz, water, methnol, THF, and CS_2 at a time delay of 2.28 ps. The color scale bar is in units of counts.

Table 7.1: The measured refractive indices at 800 nm in quartz, water, methonal, THF, and CS_2.

	quartz	water	methonal	THF	CS_2
Index(800nm) from imaging	1.467	1.345	1.338	1.407	1.7
Literature value	1.539[1]	1.340[2]	1.329[2]	1.407[2]	1.628[1]

[1]http://en.wikipedia.org/wiki/List_of_refractive_indices $(\lambda = 549$ nm$)$

[2]http://www.sigmaaldrich.com/chemistry/solvents/methanol-center.html $(\lambda\ unknown)$

7.5 Movie of reflection and refraction of femtosecond optical pulses at water/glass interface
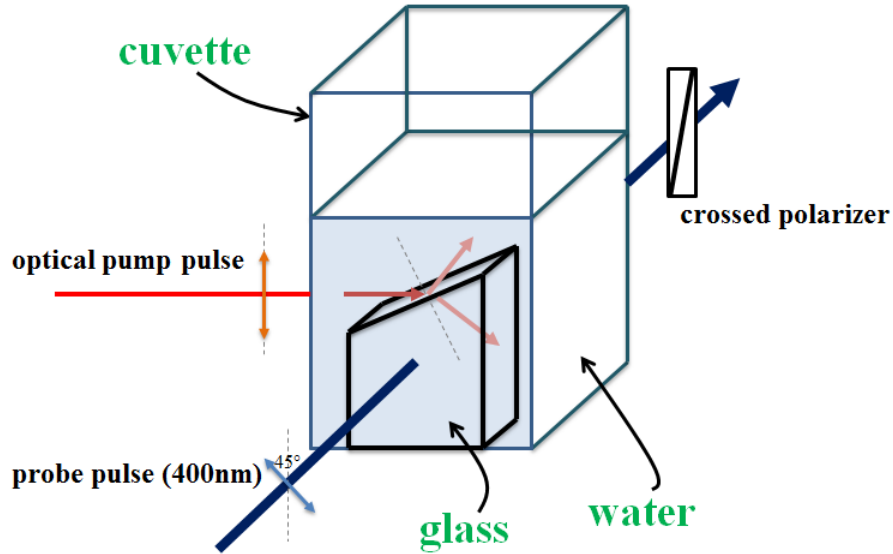
Figure 7.15: Experimental setup to image the femtosecond optical pump pulse's reflection and refraction at water/glass interface. The quartz cuvette is filled with water, and a piece of 1 mm thickness glass slide with cut angle ~ 7.4 ° is submergered in the water. The pump pulse (800 nm, polarized in the vertical direction) is incident on the water/glass interface at an incident angle of 82.65 °. The proble pulse (400 nm, polarized 45 ° with respect to the vertical direction) propagates through the cuvette and is sampled by a crossed polarizer.

As discussed in Section 7.4, the proagation of the femtosecond optical pulse was imaged in various media. Here, we demonstrate femtosecond optical pulse's reflection and refraction at the water/glass interface.

As illustated in Figure 7.15, The quartz cuvette is filled with water, and a piece of 1 mm thickness glass slide with cut angle ~ 7.4 ° is submergered in the water. The pump pulse (800 nm, polarized in the vertical direction) is incident on the water/glass interface at an incident angle of 82.65 °. The proble pulse (400 nm, polarized 45 ° with respect to the vertical direction) propagates through the cuvette and is sampled by a crossed polarizer. By changing the time delay between the pump pulse and proble pulse, a series of images were captured. Figures 7.16-7.19

show the images of femotsecond pulse at time delays of 1 ps, 4.8 ps, 10 ps, and 13.4 ps, respectively.

Actually, totally 87 images have been collected for movie with a step of 0.2 ps. Based on the relationship between the proagation distance and the time delay, the group velocities of the optical pulse in water and glass are found $v_{water} = (2.15 \pm 0.01) \times 10^8 \ m/s$, and $v_{glass} = (1.94 \pm 0.01) \times 10^8 \ m/s$, respectively. The corresponding group indices in water and glass are $n_{water} = 1.395 \pm 0.006$, and $n_{glass} = 1.546 \pm 0.008$, respectively, which are consistent with the literature [26].

The comination of 87 images at different time delays (with step 0.2 ps) is shown in Figure 7.20. According to Figure 7.20, the incident angle and refracted angle are 82.65 ° and 61.7 °, respectively. Based on the snell's law [26], the relative refractive index of the glass to water is,

$$n_{relative} = \frac{sin(incident\ angle)}{sin(refracted\ angle)} = \frac{sin(82.65°)}{sin 61.7°} = 1.1263 \qquad (7.2)$$

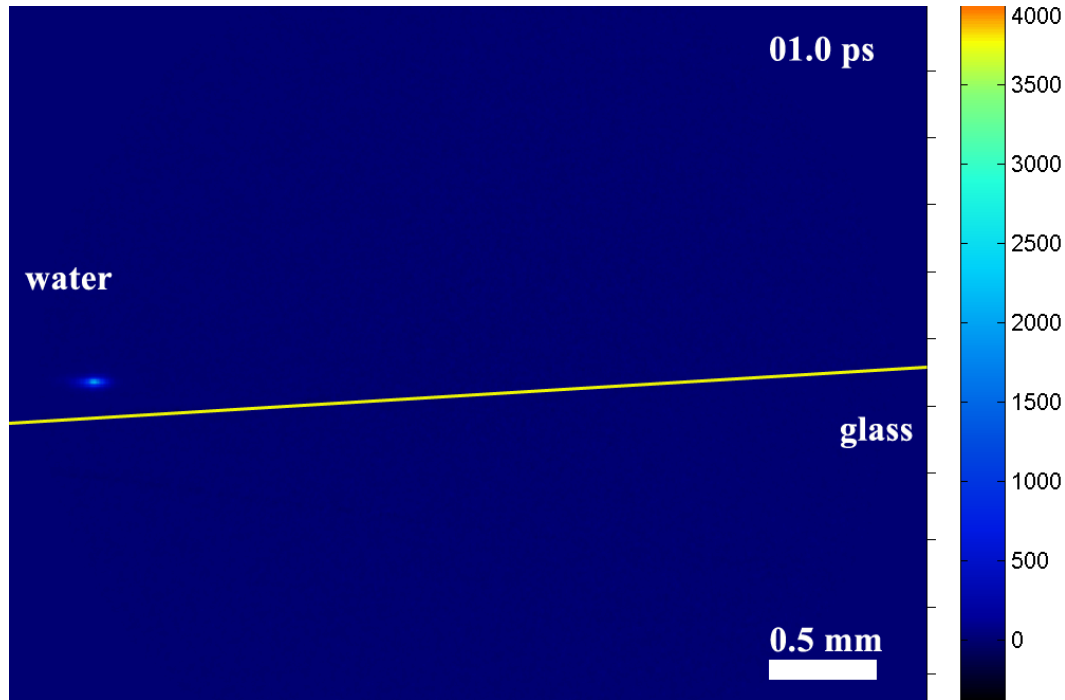which matches with $\frac{n_{glass}}{n_{water}} = 1.11 \pm 0.01$.

Figure 7.16: Image of the femtosecond optical pulse at a time delay of 1.0 ps.
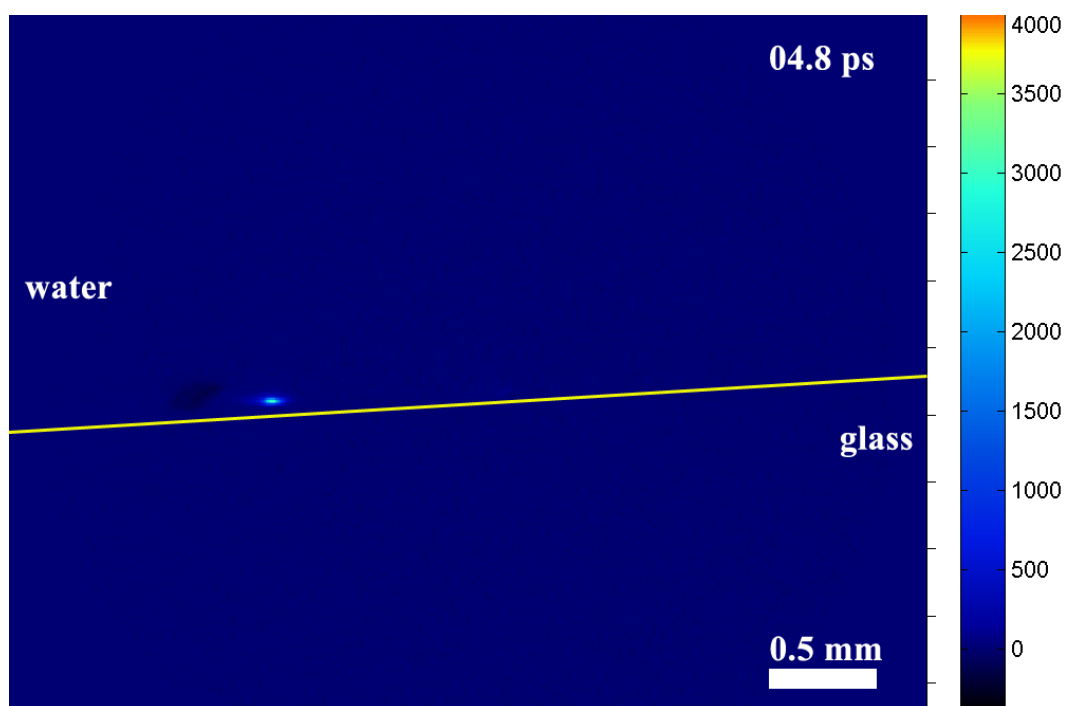
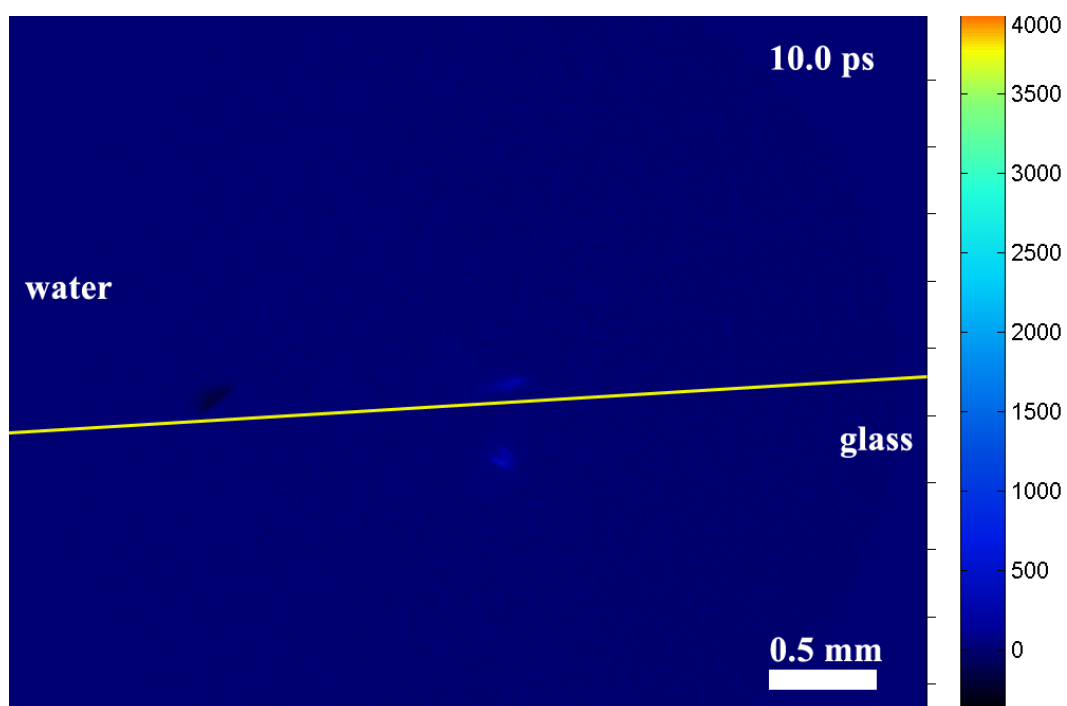**Figure 7.17:** Image of the femtosecond optical pulse at a time delay of 4.8 ps.

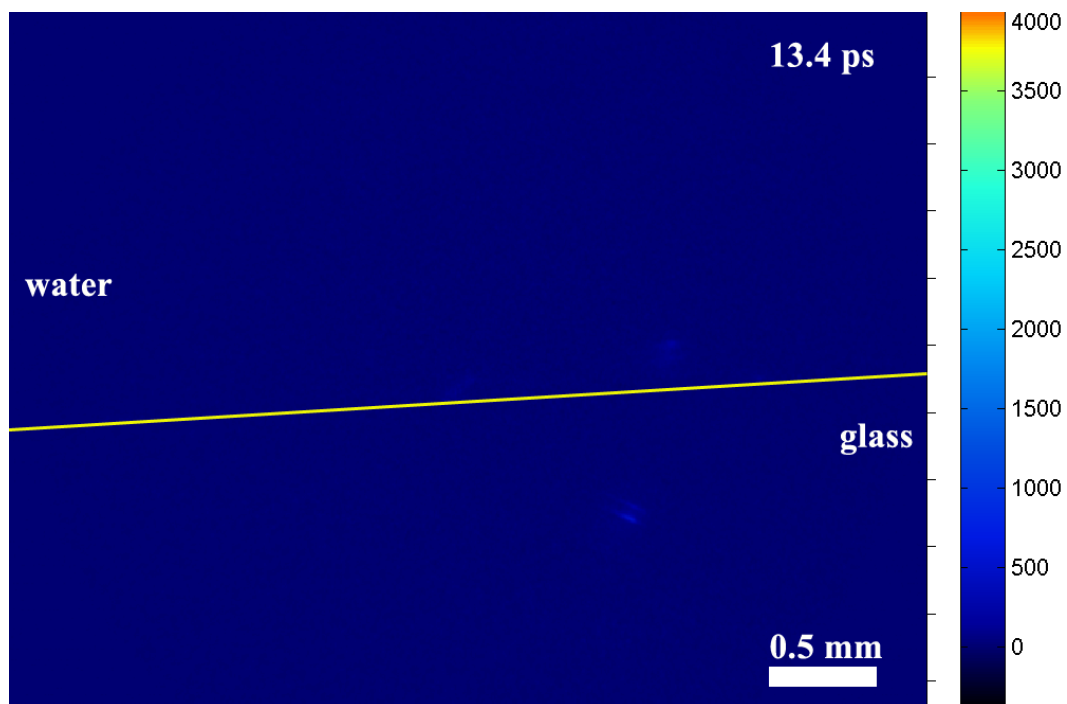**Figure 7.18:** Image of the femtosecond optical pulse at a time delay of 10.0 ps.

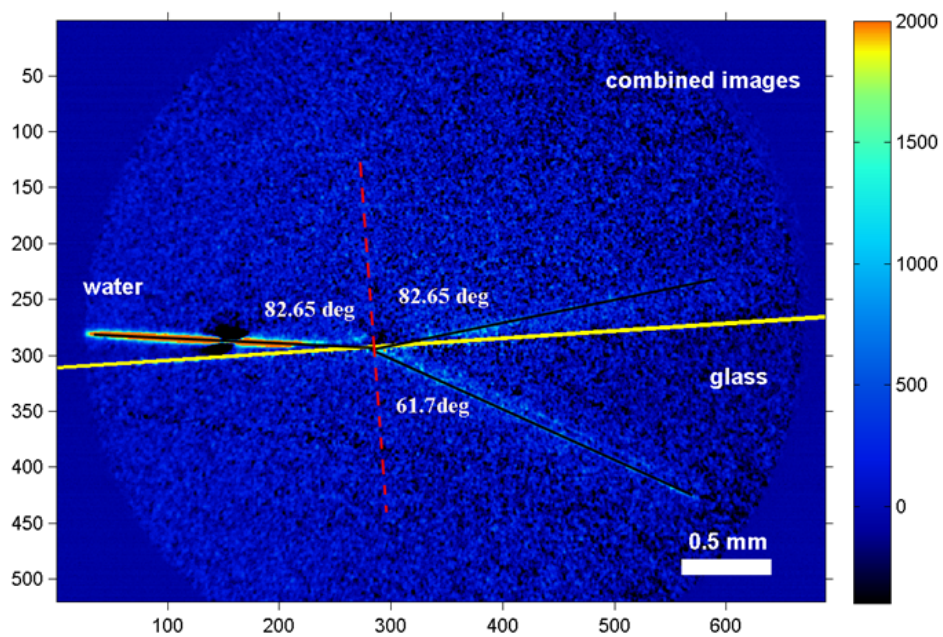**Figure 7.19:** Image of the femtosecond optical pulse at a time delay of 13.4 ps.

Figure 7.20: Combined image of 87 images with a time delay step of 0.2 ps.

7.6 Conclusions

Several preliminary experiments were carried out to develop potential applications of the transverse imaging technique. Imaging THz pulses generation in the PPLN crystal was demonstrated. An air plasma was generated and imaged with femtosecond pulses. Based on the Kerr effect induced by the femtosecond pulse, propagation of the femtosecond pulse in various materials including quartz, methanol, water, THF, and CS_2 was imaged. The femtosecond optical pulse's reflection and refraction at water/glass interface was imaged as well. The successful demonstration of the transverse imaging technique in various materials implies that the transverse imaging technique will be a very powerful tool for future science and technology development. Furthermore, by imaging classical optical phenomena such as light propagation, reflection, refraction, and tunneling, it's a very useful tool to develop movies for educational demonstration.

References:

1. M. Asobe, T. Umeki, and O. Tadanaga, "Phase sensitive amplification with noise figure below the 3 dB quantum limit using CW pumped PPLN waveguide," Opt. Express **20**, 13164-13172 (2012).

2. J. H. Chang, T. T. Wang, and Q. H. Mao, "Widely tunable difference frequency generation around 3.4 mu m using index dispersion property of PPLN," Laser Phys. **22**, 592-597 (2012).

3. K. Chen, Ai N, and J. SP, "Reasons for the high stability of nano-structured $(La,Sr)MnO_3$ infiltrated YSZ composite oxygen electrodes of solid oxide electrolysis cells.," Electrochem. Commun. **19**, 119-122 (2012).

4. F. Kienle, D. Lin, A. Shaif-ul, H. S. S. Hung, C. B. E. Gawith, H. E. Major, D. J. Richardson, and D. P. Shepherd, "Green-pumped, picosecond MgO:PPLN optical parametric oscillator," J. Opt. Soc. Am. B **29**, 144-152(2012).

5. T. Liu, L. Liu, X. B. Wang, X. Li, and J. Hou, "Cascaded synchronous terahertz optical parametric oscillations in a single MgO:PPLN crystal," Laser Phys. **22**, 678-683 (2012).

6. J. Lu, Y.-H. Liu, G. Zhao, X.-P. Hu, and S.-N. Zhu, "Generating a 2.4-W cw Green Laser by Intra-Cavity Frequency Doubling of a Diode-Pumped Nd:GdVO4 Laser with a MgO:PPLN Crystal," Chin. Phys. Lett. **29**, 094207 (2012).

7. Q. Sheng, X. Ding, C. Shi, S. Yin, B. Li, C. Shang, X. Yu, W. Wen, and J. Yao, "Continuous-wave mid-infrared intra-cavity singly resonant PPLN-OPO under 880 nm in-band pumping," Opt. Express **20**, 8041-8046 (2012).

8. J. Wallace, "PPLN upconversion advances single-photon detection," Laser Focus World **48**, (2012).

9. R. M. Koehl, S. Adachi, and K. A. Nelson, "Direct visualization of collective wavepacket dynamics," J. Phys. Chem. A **103**, 10260-10267 (1999).

10. R. M. Koehl, S. Adachi, and K. A. Nelson, "Real-space polariton wave packet imaging," J. Chem. Phys. **110**, 1317-1320 (1999).

11. K. L. Yeh, M. C. Hoffmann, J. Hebling, and K. A. Nelson, "Generation of 10 μJ ultrashort terahertz pulses by optical rectification," Appl. Phys. Lett. **90**, 171121 (2007).

12. S. B. Bodrov, D. I. Kulagin, Y. A. Malkov, A. A. Murzanev, A. I. Smirnov, and A. N. Stepanov, "Initiation and channelling of a microwave discharge by a plasma filament created in atmospheric air by an intense femtosecond laser pulse," J. Phys. D: Appl: Phys. **45**, 045202 (2012).

13. F. Jahangiri, M. Hashida, S. Tokita, T. Nagashima, K. Ohtani, M. Hangyo, and S. Sakabe, "Directional Terahertz Emission from Air Plasma Generated by Linearly Polarized Intense Femtosecond Laser Pulses," Appl. Phys. Express **5**, 026201 (2012).

14. F. Jahangiri, M. Hashida, S. Tokita, T. Nagashima, M. Hangyo, and S. Sakabe, "Directional elliptically polarized terahertz emission from air plasma produced by circularly polarized intense femtosecond laser pulses," Appl. Phys. Lett. **99**, 161505 (2011).

15. X.-L. Liu, X. Lu, J.-L. Ma, L.-B. Feng, X.-l. Ge, Y. Zheng, Y.-T. Li, L.-M. Chen, Q.-L. Dong, W.-M. Wang, Z.-H. Wang, H. Teng, Z.-Y. Wei, and J. Zhang, "Long lifetime air plasma channel generated by femtosecond laser pulse sequence," Opt. Express **20**, 5968-5973 (2012).

16. X. Yang, J. Wu, Y. Tong, L. e. Ding, Z. Xu, and H. Zeng, "Femtosecond laser pulse energy transfer induced by plasma grating due to filament interaction in air," Appl. Phys. Lett. **97**, 071108 (2010).

17. N. Zhang, Z. Wu, K. Xu, and X. Zhu, "Characteristics of micro air plasma produced by double femtosecond laser pulses," Opt. Express **20**, 5968-5973 (2012).

18. Z.-Q. Zhu, and X.-L. Wang, "Experimental study on emission spectra of air plasma induced by femtosecond laser pulses," Acta Phys. Sin. **60**, 085205 (2011).

19. R. Boyd, *Nonlinear Optics* (Elsevier, 2008).

20. S. A. Myers, and E. J. Robinson, "Kerr effect in CS_2, C_6H_6, and CCl_4," J. Chem. Phys. **58**, 3526 (1973).

21. J. Etchepare, G. Grillon, and A. Antonetti, "Comment on the subpicosecond kerr effect in CS_2," Chem. Phys. Lett. **107**, 489-489 (1984).

22. A. Idrissi, M. Ricci, P. Bartolini, and R. Righini, "Optical Kerr-effect investigation of the reorientational dynamics of CS2 in CCl4 solutions," J. Chem. Phys. **111**, 4148 (1999).

23. I. A. Heisler, R. R. B. Correia, T. Buckup, S. L. S. Cunha, and N. P. da Silveira, "Time-resolved optical Kerr-effect investigation on CS_2/polystyrene mixtures," J. Chem. Phys. **123**, 054509 (2005).

24. I. A. Heisler, R. R. B. Correia, and S. L. S. Cunha, "Molecular dynamics investigation with the time resolved optical Kerr effect on the CS_2-C6H6 mixtures," J. Chem. Phys. **125**, 7 (2006).

25. A. D. Slepkov, "Third-order nonlinearities of novel iso-polydiacetylenes studied by a differential optical kerr effect detection technique," in *Department of Physics* (University of Alberta, 2002).

26. E. Hecht, *Optics* (Addison-Wesley, 2002).

Chapter 8

Development of a free-standing, frameless carbon nanotube terahertz polarizer

A free-standing, frameless carbon nanotube terahertz polarizer was fabricated by cutting an ultralong carbon nanotube array pad with femtosecond laser pulses. The thickness of the polarizer is 0.35 mm, and the extinction ratio is 10^{-4} within the spectral range from 0.3 to 2.2 THz. The degree of polarization is higher than 0.999.

8.1 Introduction

The terahertz spectral range is situated between the infrared and microwave region of the electromagnetic spectrum. Due to its unique properties, it has gained lots of attention in the past two decades [1-8]. The demand for developing THz optics such as polarizers, filters, and phase plates is increasing [9-16]. However, most of the well-established techniques developed for neighboring frequencies cannot be shared in the THz region. For instance, unlike the optical frequencies, which have various types of polarizer, the most used polarizer in THz region is still the free-standing wire-grid polarizer [17, 18].

A commercial wire-grid polarizer is made by winding thin tungsten wires on a frame [17, 18], and the performance is determined by the polarizer's geometrical parameters including the wire diameter and spacing between two neighboring wires. Although such commercial free-standing tungsten wire-grid polarizers have very good extinction ratios and high transmission efficiency, they are very expensive due to the complex fabrication procedure. What's more, they need

frames and are also mechanical fragile.

In order to make an alternative THz polarizer, methods such as making birefringent type THz polarizers with liquid crystal [12], fabricating metallic wires patterns on a substrate to make wire-grid type polarizers with micro fabrication [11], nano fabrication [10], as well as inkjet printing [14] have been proposed and demonstrated.

Recently, instead of fabricating parallel metallic wires on substrate, highly aligned carbon nanotubes array (CNTA) is employed to make wire-grid polarizers [15, 16]. This is mainly due to its one-dimensional nature and strong anisotropy in electric and optical properties [19, 20].

So far two types of CNTA wire-grid polarizer have been demonstrated [15, 16]. The first one is to grow CNTA on a parallel line patterned catalyst and then transfer the grown CNTA onto a sapphire substrate to get a CNTA thin film [15]. The obtained CNTA thin film shows different THz transmission efficiency when the orientation of the carbon nanotube is parallel or perpendicular to the THz polarization. However, because the film is very thin, the extinction ratio is quite low. Furthermore, the complicated fabrication procedure, and requirement of substrate make it unsuitable for practical THz polarizer applications. The second approach, reported more recently, is to wind a carbon nanotube (CNT) sheet from a CNTA pad [16]. By controlling the round number in the winding process, the thickness of the free-standing CNT sheet is adjusted and the extinction ratio can be optimized as well. However, a drawable CNTA is required for this method [21], and also a frame is still required to support the polarizer.

Here, we make a free-standing, frameless CNTA THz polarizer by cutting an ultralong CNTA pad (provided by Prof. Weixing Chen's group) [22-25] into thin sheets using femtosecond (fs) laser pulses. The size of the polarizer is as large as 3.5 mm $\times$ 5.5 mm. The degree of the polarization (DOP) is close to 1 within the

spectral range from 0.3 THz to 2.2 THz, and the extinction ratio is as high as 10^{-4}.

8.2 Fabrication of the carbon nanotube polarizer

The ultralong CNTA pad with CNT length around 3.5 mm is grown on the P-type Si substrate with catalytic chemical vapor deposition (CCVD) method [22, 23].
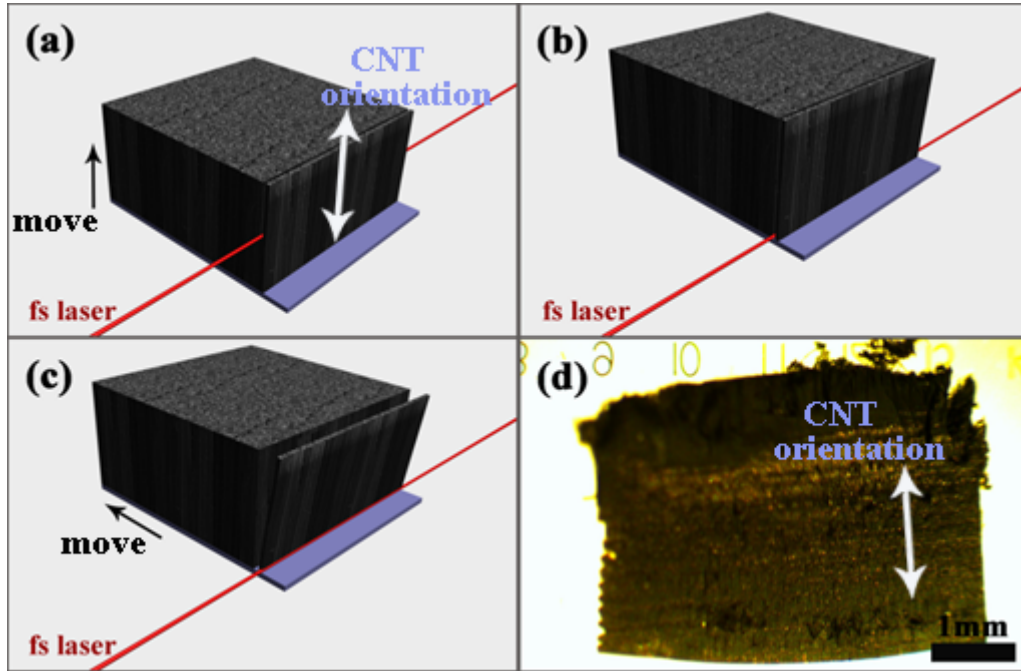

Figure 8.1: Illustration of the laser cutting procedure. (a) The CNTA pad is moved upward so that the CNTA gets cut by the laser beam along the CNT orientation direction. (b) The CNTA pad is stopped when the substrate reaches the laser beam. (c) The CNTA pad moves away from the laser beam horizontally so that the root of the CNTA sheet is cut and released. (d) Microscope image of the CNTA sheet.

The obtained CNTA pad (grown and provided by Prof. Weixing Chen's group) was cut into thin CNTA sheets with an amplified Ti: sapphire laser system (0.9 mJ, 100 fs, 800 nm, 1 kHz). The laser beam with optical power of 100 mW is focused on the CNTA pad with a depth of focus of the optical beam of 20 mm.

The CNTA pad is mounted on a three dimensional stage so that the CNTA pad can move relatively to the laser beam.
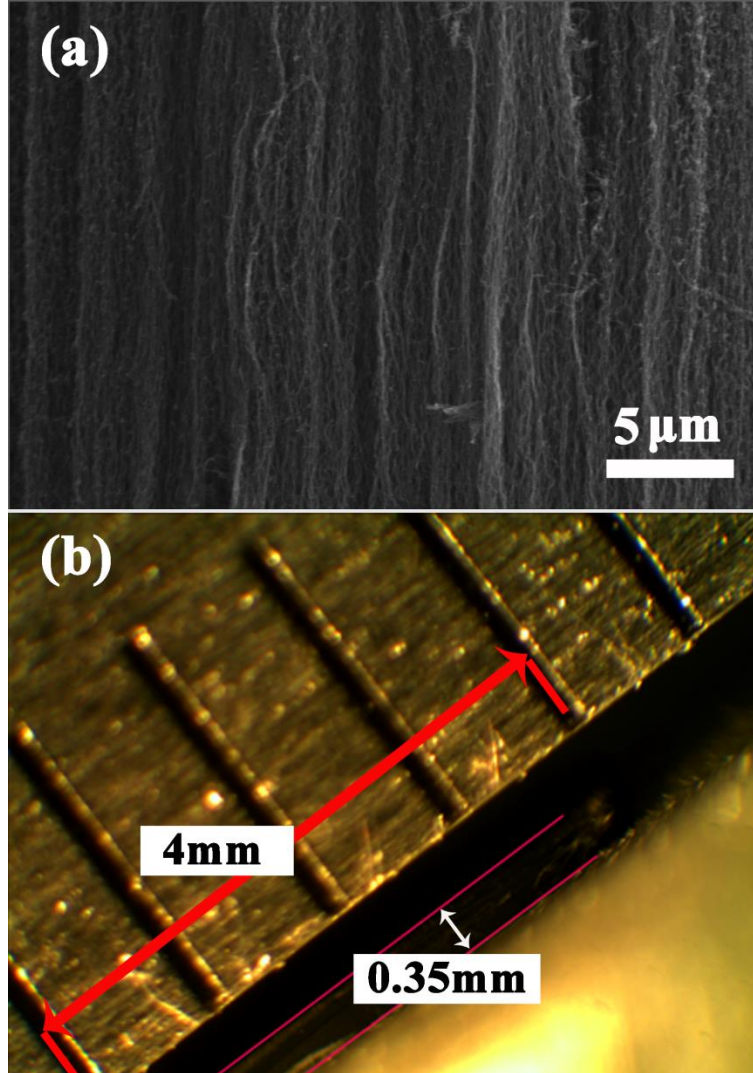
Figure 8.2: (a) SEM image of the cut CNTA polarizer, the CNT orientation is in the vertical direction. (b) Thickness measurement of the CNTA polarizer by a microscope. (1 mm divisions on ruler.)

Figure 8.1 illustrates the detailed cutting procedure. Firstly, as shown in Figure 8.1(a), the CNTA is moving upward until its bottom reaches the laser beam

(see Figure 8.1(b)) so that the CNTA pad gets cut from top to bottom. The CNTA pad is then moved away from the laser beam in the horizontal direction (Figure 8.1(c)) and the root of the CNTA is cut and one piece of highly orientated CNTA sheet is released from the CNTA pad. As shown in Figure 8.1(d), the obtained CNTA sheet is observed under a microscope. The size of the sheet is around 3.5 mm $\times$ 5.5 mm. The orientation of the nanotubes is in the vertical direction, and the horizontal stripe pattern is because the CNTA pad is moved vertically in the cutting process.

Figure 8.2(a) shows the SEM image taken by the JSM-6301FXV field emission scanning electron microscope (FESEM), and we find that the orientation of the CNTA is still aligned very well. The thickness of the obtained CNTA sheet is measured by a microscope, as shown in Figure 8.2(b), to be 0.35 mm.

8.3 THz polarizer test setup

The behavior of the CNTA polarizer was tested with a THz time-domain optical setup in air. The THz pulse is generated with a ZnTe crystal through optical rectification [26-28], and the THz pulse polarization is kept horizontal by a commercial THz tungsten grid wire polarizer.

As illustrated in Figure 8.3, the generated THz pulse on the CNTA polarizer with the focused spot size 1 mm by an off axis parabolic mirror (not shown). The CNTA polarizer is mounted on a sample holder, the nanotube orientation can be adjusted by rotating the sample holder. The transmitted THz pulse waveform is sampled by another femtosecond laser pulse in a second ZnTe crystal [26-29]. Because the nanotube orientation cannot be recognized by eye, we optimize the transmitted THz pulse amplitude by rotating the polarizer and define the CNT orientation in the vertical direction when the THz amplitude reaches the maximum value.
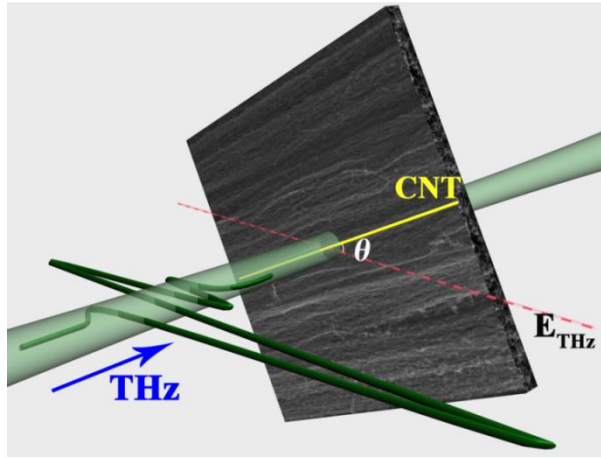
Figure 8.3: Illustration of the THz polarizer test scheme. The CNTA sheet is mounted on a rotational stage which can rotate the nanotube orientation along the THz propagation direction. The THz beam is focused by an off axis parabolic mirror on the CNTA sheet and its polarization is kept horizontal.

8.4 THz polarizer Test

8.4.1 Dynamic range of the THz test system

In order to determine the dynamic range of our THz test setup (in vacuum), the sample is taken away and a THz waveform is collected. The noise signal is also collected with the THz beam blocked.

Figure 8.4(a) shows the collected THz waveform as well as the background noise, and Figure 8.4(b) is the corresponding power spectral. According to the power ratio between the noise and THz signal (Figure 8.4(c)), the reliable frequency range for our THz test setup is from 0.3 THz to 2.2 THz.
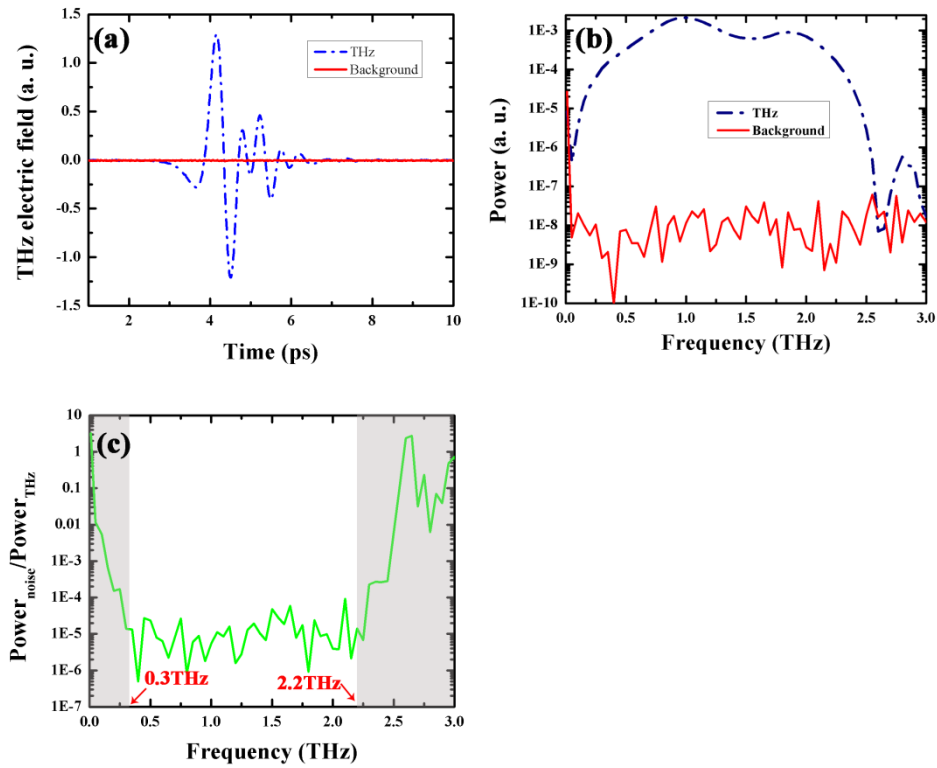
Figure 8.4: (a) THz waveform (blue slash dot line) measured in free space, and the noise (red solid line) measurement when the THz pulse is blocked. (b) FFT of the THz waveform and the noise signal. (c) The power ratio between the noise signal and THz signal in the frequency domain.

8.4.2 Commercial tungsten wire-grid polarizer test
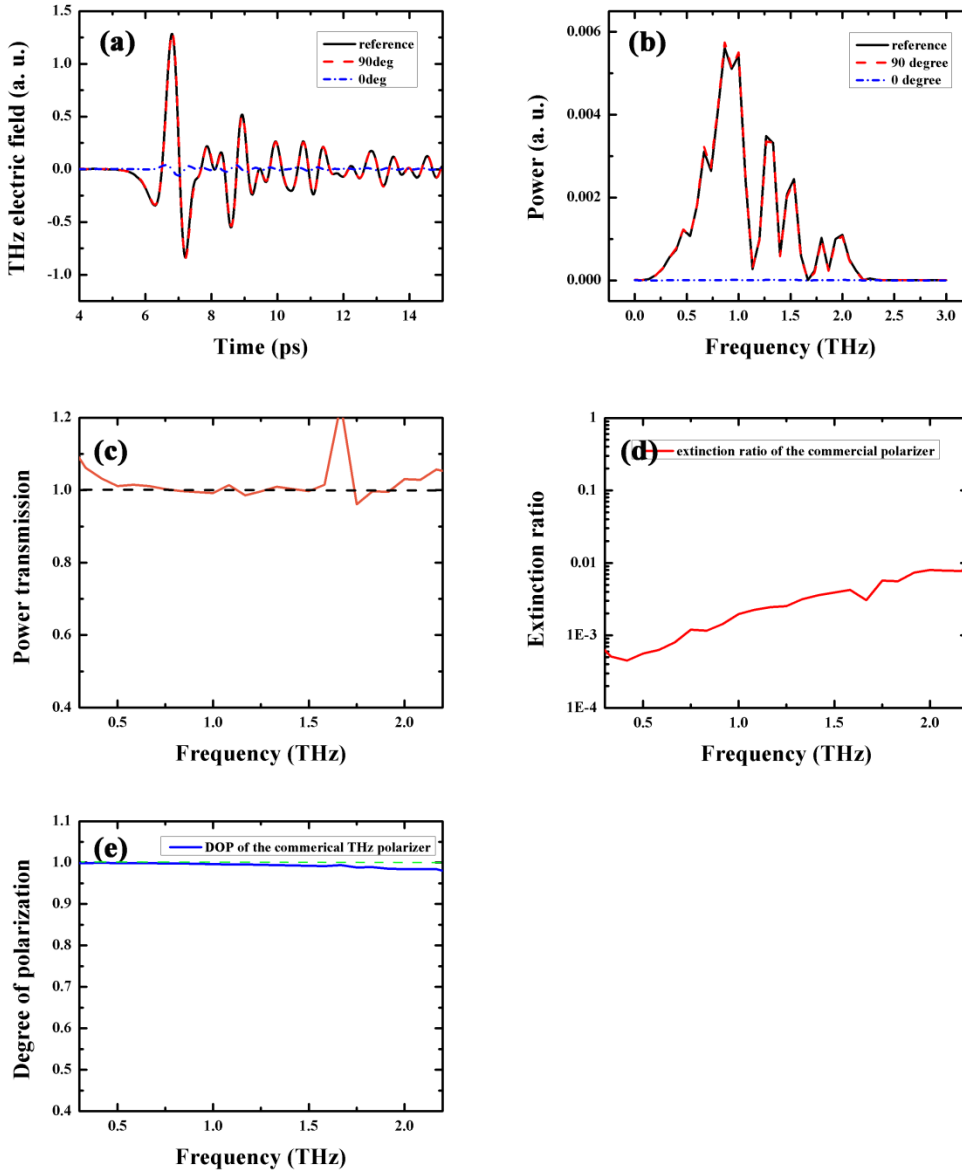
Figure 8.5: (a) THz wave from collected as reference signal when the sample is taken away, 90 degree means the orientation of the grid is perpendicular to the THz polarization, 0 degree means the THz pulse collected with the grid orientation parallel to the THz polarization. (b) The corresponding Fourier transform result of the THz waveform in (a). (c) Power transmission of the THz polarizer. (d) Extinction ratio of the THz polarizer. (e) Degree of the polarization.

For comparison, a commercial tungsten wire-grid polarizer from Microtech

Instruments, Inc. was tested in air. Figure 8.5(a) shows the transmitted THz waveforms sampled at a wire-grid orientation angle of $0\,°$ and $90\,°$ with respect to the horizontal direction. The reference THz waveform is taken without the sample. The corresponding power spectra are shown in Figure 8.5(b). Figure 8.5(c) shows that the transmission (calculated by $P_{90°}(\omega)/P_{ref}(\omega)$) is close to 100% when the grid orientation is perpendicular to the THz pulse polarization. The extinction ratio is also calculated with equation $P_{0°}(\omega)/P_{90°}(\omega)$. As shown in Figure 8.5(d), the extinction ratio is between 10^{-3} and 10^{-2} within the spectrum range from 0.3 THz to 2.2 THz. Finally, the degree of polarization (DOP) calculated with equation $\frac{|P_{0°}(\omega)-P_{90°}(\omega)|}{|P_{0°}(\omega)+P_{90°}(\omega)|}$ is shown in Figure 8.5(e).

8.4.3 THz CNTA polarizer test
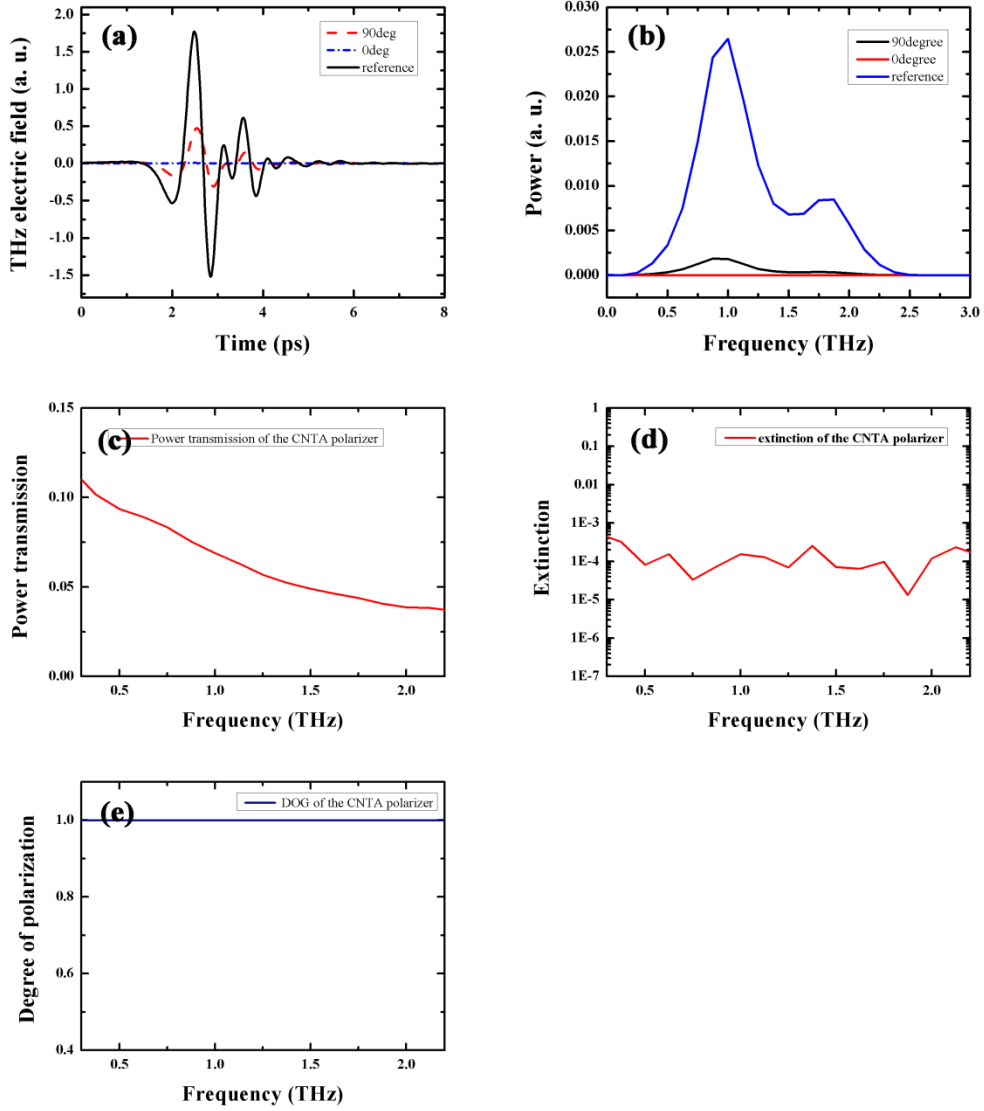
Figure 8.6: (a) The THz reference waveform (without CNT polarizer) and the transmitted waveforms at different CNTA orientations with respect to the THz polarization. (b) THz transmission through the CNTA sheet at different CNTA orientation angles. (c) Power transmission of the THz polarizer. (d) Extinction ratio of the THz polarizer. (e) Degree of the polarization.

Similar to the commercial tungsten wire-grid polarizer, a piece of 0.35 mm-thick CNTA sheet was tested. Figure 8.6(a) and (b) show the transmitted THz

pulse waveforms and the corresponding power spectral. We find that the maximum power transmission is between 5% and 10% (shown in Figure 8.6(c)). The low power transmission could be due to the existence of conductive amorphous carbon inside the CNTA sheet [23].

As shown in Figure 8.6(d), compared to the commercial THz wire-grid polarizer, the CNTA polarizer has a much higher extinction ratio (10^{-4}). The DOP shown in Figure 8.6(e) is also higher than the commercial THz polarizer, but the throughput is much worse.

8.5 Conclusions

A new method to make free-standing, frameless THz polarizer with an ultralong CNTA pad cut with femtosecond laser pulses was demonstrated. Compared to the commercial tungsten wire-grid polarizer, the obtained THz CNTA polarizer shows a higher degree of polarization and a better extinction ratio. The CNTA polarizer is free of frame or substrate, and making it a potential THz polarizer.

References:

1. M. Tonouchi, "Cutting-edge terahertz technology," Nat. Photonics **1**, 97-105 (2007).

2. B. Ferguson, and X.-C. Zhang, "Materials for terahertz science and technology," Nat. Mater. **1**, 26-33 (2002).

3. F. Blanchard, G. Sharma, L. Razzari, X. Ropagnol, H.-C. Bandulet, F. Vidal, R. Morandotti, J.-C. Kieffer, T. Ozaki, H. Tiedje, H. Haugen, M. Reid, and F. Hegmann, "Generation of Intense Terahertz Radiation via Optical Methods," IEEE J. Sel. Top. Quant. Electron. **17**, 5-16 (2011).

4. M. C. Beard, G. M. Turner, and C. A. Schmuttenmaer, "Transient photoconductivity in GaAs as measured by time-resolved terahertz spectroscopy," Phys. Rev. B **62**, 15764-15777 (2000).

5. B. B. Hu, and M. C. Nuss, "Imaging with terahertz waves," Opt. Lett. **20**, 1716-1718 (1995).

6. B. M. Fischer, M. Hoffmann, H. Helm, R. Wilk, F. Rutz, T. Kleine-Ostmann, M. Koch, and P. U. Jepsen, "Terahertz time-domain spectroscopy and imaging of artificial RNA," Opt. Express **13**, 5205-5215 (2005).

7. J. Federici, and L. Moeller, "Review of terahertz and subterahertz wireless communications," J. Appl. Phys. **107**, 111101(2010).

8. H.-W. Huebers, "Terahertz technology towards thz integrated photonics," Nat. Photonics **4**, 503-504 (2010).

9. J.-S. Li, "A novel terahertz wave reflective polarizer for THz communication," Opt. Commun. **284**, 957-960 (2011).

10. S.-Z. A. Lo, and T. E. Murphy, "Nanoporous silicon multilayers for terahertz filtering," Opt. Lett. **34**, 2921-2923 (2009).

11. I. Yamada, K. Takano, M. Hangyo, M. Saito, and W. Watanabe, "Terahertz wire-grid polarizers with micrometer-pitch Al gratings," Opt. Lett. **34**, 274-276 (2009).

12. C.-F. Hsieh, Y.-C. Lai, R.-P. Pan, and C.-L. Pan, "Polarizing terahertz waves with nematic liquid crystals," Opt. Lett. **33**, 1174-1176 (2008).

13. D.-B. Tian, H.-W. Zhang, W.-E. Lai, Q.-Y. Wen, Y.-Q. Song, and Z.-G. Wang, "Double wire-grid terahertz polarizer on low-loss polymer substrates," Chin. Phys. Lett. **27**, 104201 (2010).

14. T. Kondo, T. Nagashima, and M. Hangyo, "Fabrication of wire-grid-type polarizers for THz region using a general-purpose color printer," Jpn. J. Appl. Phys. Part 2-Lett. **42**, L373-L375 (2003).

15. L. Ren, C. L. Pint, L. G. Booshenri, W. D. Rice, X. Wang, D. J. Hilton, K. Takeya, I. Kawayama, M. Tonouchi, R. H. Hauge, and J. Kono, "Carbon nanotube terahertz polarizer," Nano Lett. **9**, 2610-2613 (2009).

16. J. Kyoung, E. Y. Jang, M. D. Lima, H.-R. Park, R. O. Robles, X. Lepro, Y. H. Kim, R. H. Baughman, and D.-S. Kim, "A reel-wound carbon nanotube polarizer for terahertz frequencies," Nano Lett. **11**, 4227-4231 (2011).

17. A. E. Costley, K. H. Hursey, G. F. Neill, and J. M. Ward, "Free-standing fine-wire grids - their manufacture, performance, and use at millimeter and submillimeter wavelengths," J. Opt. Soc. Am. B **67**, 979-981 (1977).

18. P. A. R. Ade, A. E. Costley, C. T. Cunningham, C. L. Mok, G. F. Neill, and T. J. Parker, "Free-standing grids wound from 5 mu-m diameter wire for spectroscopy at far-infrared wavelengths," Infrared Phys. **19**, 599-601 (1979).

19. S. Shoji, H. Suzuki, R. P. Zaccaria, Z. Sekkat, and S. Kawata, "Optical polarizer made of uniaxially aligned short single-wall carbon nanotubes embedded in a polymer film," Phys. Rev. B **77**, 153407 (2008).

20. Y. Murakami, E. Einarsson, T. Edamura, and S. Maruyama, "Polarization dependence of the optical absorption of single-walled carbon nanotubes," Phys. Rev. Lett. **94**, 087402(2005).

21. A. A. Kuznetsov, A. F. Fonseca, R. H. Baughman, and A. A. Zakhidov, "Structural model for dry-drawing of sheets and yarns from carbon nanotube forests," ACS Nano **5**, 985-993 (2011).

22. F. Hu, X. Cui, and W. Chen, "Ultralong-cnta-supported pd-based anodes for ethanol oxidation," J. of Phys. Chem. C **114**, 20284-20289 (2010).

23. X. Cui, W. Wei, C. Harrower, and W. Chen, "Effect of catalyst particle interspacing on the growth of millimeter-scale carbon nanotube arrays by catalytic chemical vapor deposition," Carbon **47**, 3441-3451 (2009).

24. X. Li, X. Zhang, L. Ci, R. Shah, C. Wolfe, S. Kar, S. Talapatra, and P. M. Ajayan, "Air-assisted growth of ultra-long carbon nanotube bundles," Nanotechnology **19**, 455609 (2008).

25. S. Chakrabarti, T. Nagasaka, Y. Yoshikawa, L. Pan, and Y. Nakayama, "Growth of super long aligned brush-like carbon nanotubes," Jpn. J. Appl. Phys. Part 2-Lett. & Express Lett. **45**, L720-L722 (2006).

26. F. H. Su, F. Blanchard, G. Sharma, L. Razzari, A. Ayesheshim, T. L. Cocker, L. V. Titova, T. Ozaki, J. C. Kieffer, R. Morandotti, M. Reid, and F. A. Hegmann, "Terahertz pulse induced intervalley scattering in photoexcited GaAs," Optics Express **17**, 9620-9629 (2009).

27. T. L. Cocker, L. V. Titova, S. Fourmaux, G. Holloway, H. C. Bandulet, D. Brassard, J. C. Kieffer, M. A. El Khakani, and F. A. Hegmann, "Phase diagram of the ultrafast photoinduced insulator-metal transition in vanadium dioxide," Phys. Rev. B **85**, 155120 (2012).

28. D. G. Cooke, A. N. MacDonald, A. Hryciw, J. Wang, Q. Li, A. Meldrum, and F. A. Hegmann, "Transient terahertz conductivity in photoexcited silicon nanocrystal films," Phys. Rev. B **73**, 193311 (2006).

29. P. C. M. Planken, H. K. Nienhuys, H. J. Bakker, and T. Wenckebach, "Measurement and calculation of the orientation dependence of terahertz pulse detection in ZnTe," J. Opt. Soc. Am. B **18**, 313-317 (2001).

Chapter 9
Conclusions and outlook

This thesis presents our contributions to the development of terahertz (THz) pulse generation, THz pulse sampling, and THz spectroscopy technique via ultrafast imaging methods. A novel carbon nanotube array (CNTA) THz polarizer was developed as well.

For the first time, by extracting the ac complex conductivity of photoexcited GaAs, we demonstrated that THz electric field waveforms obtained with a noncollinear imaging technique in E-mode are suitable for THz spectroscopy analysis. However, due to the low signal-to-noise ratio (SNR), multi-shots are required. In order to sample THz waveforms in single-shot with a reasonable SNR, E^2-mode is proposed and demonstrated to sample the square of the THz electric field waveforms. Although part of the phase information is lost in the square of the THz electric field waveforms, single-shot transmitted THz power spectra can still be obtained. Future work for single-shot THz spectroscopy is to employ an intense THz pulse source to overcome the low SNR in single shot in E-mode.

In order to develop intense THz sources based on $LiNbO_3$, a transverse imaging technique is employed to image THz generation and propagation in $LiNbO_3$ crystals.

The THz Cherenkov waves generated by point focused optical pump pulses are imaged in the side-view mode and the top-view mode. In both view modes, various THz Cherenkov wave parameters including the refractive indices of the THz pulse and optical pump pulse, as well as the Cherenkov angle are measured directly. The imaging distortion of the Cherenkov angle due to the transverse imaging geometry is simulated and calibrated. The THz Cherenkov angle is found

to be independent on the optical pump power or the optical pump beam size. The THz pulse dependence on the optical pump pulse polarization is imaged, and we find that the THz pulse is generated most efficiently when the optical pump pulse polarization is parallel to the optics axis (c-axis) of the LiNbO$_3$ crystal. We also find that the THz pulse generation efficiency is strongly determined by the optical pump pulse duration.

Transition-like radiation generated at the crystal surface is imaged for the first time. Because it's still controversial to explain the generation mechanism theoretically, future work should focus on proposing a new theory and then testing it experimentally with the transverse imaging technique.

Because LiNbO$_3$ THz pulse sources are one of most popular intense THz sources, we also imaged the THz pulse that is generated with the tilted-pulse-front excitation scheme. Based on the captured images, the optical pump beam width, the tilt angle of the optical pump pulse wavefront, and the THz Cherenkov angle can be measured directly. The measured THz Cherenkov angle in LiNbO$_3$ crystals is $60°$ (with a calibrated angle $64°$), and is found to be independent of the tilt angle of the optical pump pulse wavefront. On the other hand, the THz generation efficiency is strongly determined by the tilt angle. We find that the maximum generation efficiency is obtained when the optical pulse tilt angle is between $61°$ and $67°$. Because we can image THz pulses in real time with a good SNR, the transverse imaging technique enables us to optimize the THz pulse generation efficiency more efficiently.

Since detecting the output THz pulse energy and imaging the THz pulse inside LiNbO$_3$ crystals can be realized at the same time, the relationship between the imaging signal amplitude and the output THz pulse energy was studied, and we found that the square of the imaging signal amplitude was proportional to the THz pulse energy, implying that the imaging amplitude can be considered as the

THz pulse electric field quantitatively. On the other hand, it's interesting to note that the output THz pulse can be detected only when the optical pump pulse is incident on the crystal tip, where the output THz pulse is still mixed with the optical pump pulse before it's coupled to the air. It would be very interesting to figure out the reason for this in the future.

The 3D structure of THz Cherenkov waves that is generated by the optical pump pulse in full beam size was realized by scanning the slit along the probe pulse propagation direction. Based on the constructed 3D image, the distortion of the optical pump pulse wavefront can be checked.

We demonstrated a $180\,°$ phase change of the THz pulse that is reflected at the crystal-Au boundary with the transverse imaging method. Because the reflected THz pulse has no phase change at the crystal-air boundary, we investigated a possible THz antireflection coating by depositing an Au grating on the $LiNbO_3$ crystal surface. Future work should focus on parameter optimization with simulations and experimental tests using the transverse imaging method. Furthermore, THz pulse reflection, transmission, and tunneling in various conditions are imaged for physics teaching demonstrations. Besides the ultrafast imaging in $LiNbO_3$ crystals, potential applications of the transverse imaging technique to study THz generation in periodically poled lithium niobate (PPLN), air plasma generated by femtosecond laser pulses, Kerr signals induced by femtosecond laser pulses in CS_2, quartz, methanol, and water are explored. We believe that the transverse imaging technique will be a very powerful tool for understanding pulse propagation in nonlinear optics and physics educational demonstration.

Finally, by cutting a carbon nanotube array (CNTA) pad with femtosecond laser pulses, a new type of free-standing, frameless carbon nanotube array THz polarizer was developed.

Appendix A

ICCD camera operation and calibration

A.1 Introduction to the ICCD camera

(a)

(b)
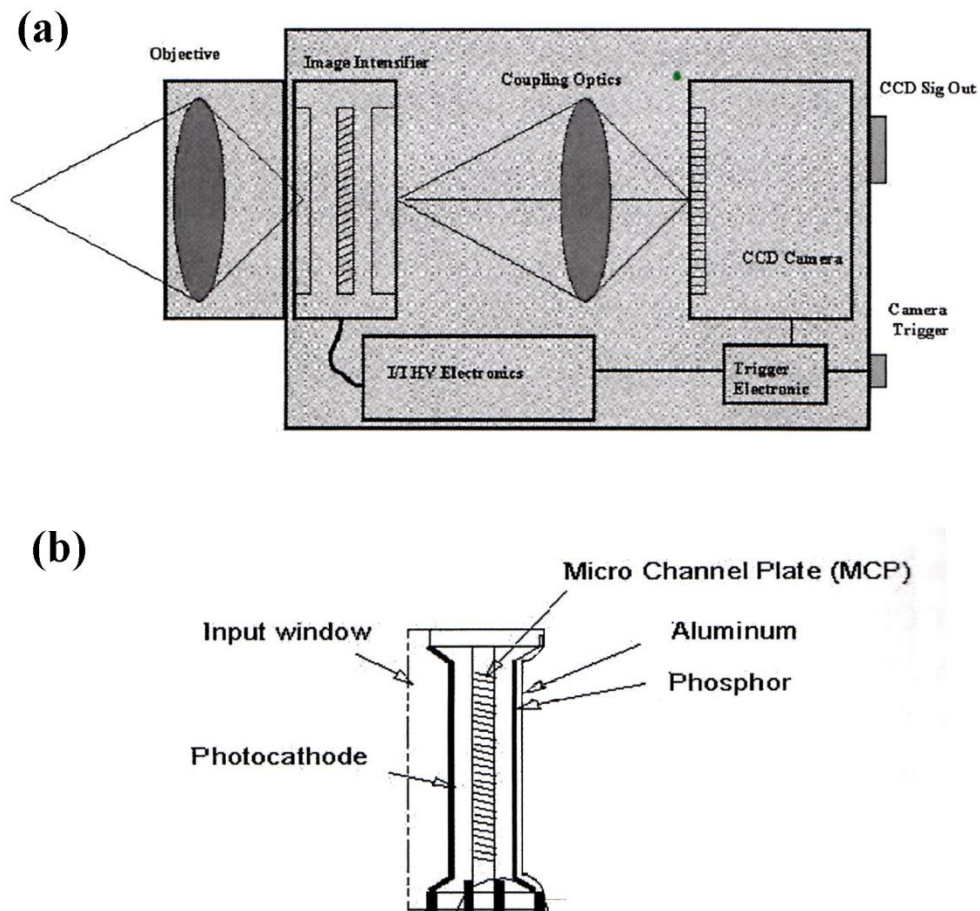
Figure A.1: (a) Scheme of the ICCD camera. (b) Scheme of the micro channel plate (MCP). (the figures are copied from LaVision ICCD camera menu [1])

The intensified CCD (ICCD) camera used in our lab is from LaVision. As shown in Figure A.1(a), the ICCD mainly consists of two devices: an image intensifier

and a CCD head. Here, a brief introduction to the ICCD camera is given. For detailed information, readers are directed to *ICCD menu_PicoStar HR_Charpter 8* [1].

The intensifier functions as a signal amplifier and a gate. As illustrated in Figure A.1(b), it consists of a photo cathode, a multi-channel plate (MCP), and a phosphor.

When an object is imaged on the photo cathode, the input photons are converted into photoelectrons though the photoelectric effect. The generated photoelectrons are controlled by a voltage bias, which functions as an electric gate. By changing the bias polarization, the photoelectrons can be sent to MCP for further amplification (gate open) or kept away from the MCP (gate closed). As illustrated in Figure A.2, the electric gate (with the gate width as short as 80 ps) is synchronized to the laser pulse, and the time delay between the gate and the laser pulse is controlled by an electronic circuit board (DEL-350).

When the gate is open, the photoelectrons are sent into MCP channels for amplification. A high electric potential exerted on the MCP is used to accelerate the photoelectrons. Because the channel orientation has a small angle deviation from the direction of the acceleration electric field. The high speed electrons collide with the MCP channel wall and generate new electrons when they travel through the whole channel, thus realize the signal amplification. When the amplified electrons come out of the MCP, they are accelerated in free space by another high voltage bias (in kV scale) to gain high kinetic energy. Finally, these accelerated electrons bombard the phosphor to generate photons, which are imaged by the CCD camera head.
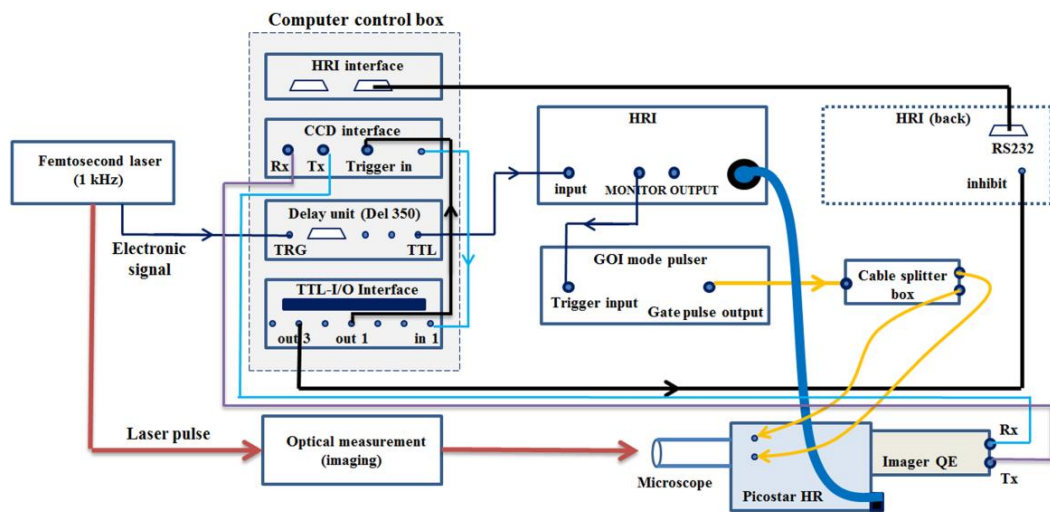
Note: The connection of Tx(interface)-Rx(CCD), Rx(interface)-Tx(CCD) can be seen in the menu.

Figure A.2: Schematic of the imaging using the ICCD camera

A. 2 Hardware connection of the ICCD camera system

Figure A.2 and A.3 show the cable connection of the whole ICCD camera system, the trigger signal comes from our femtosecond laser system.
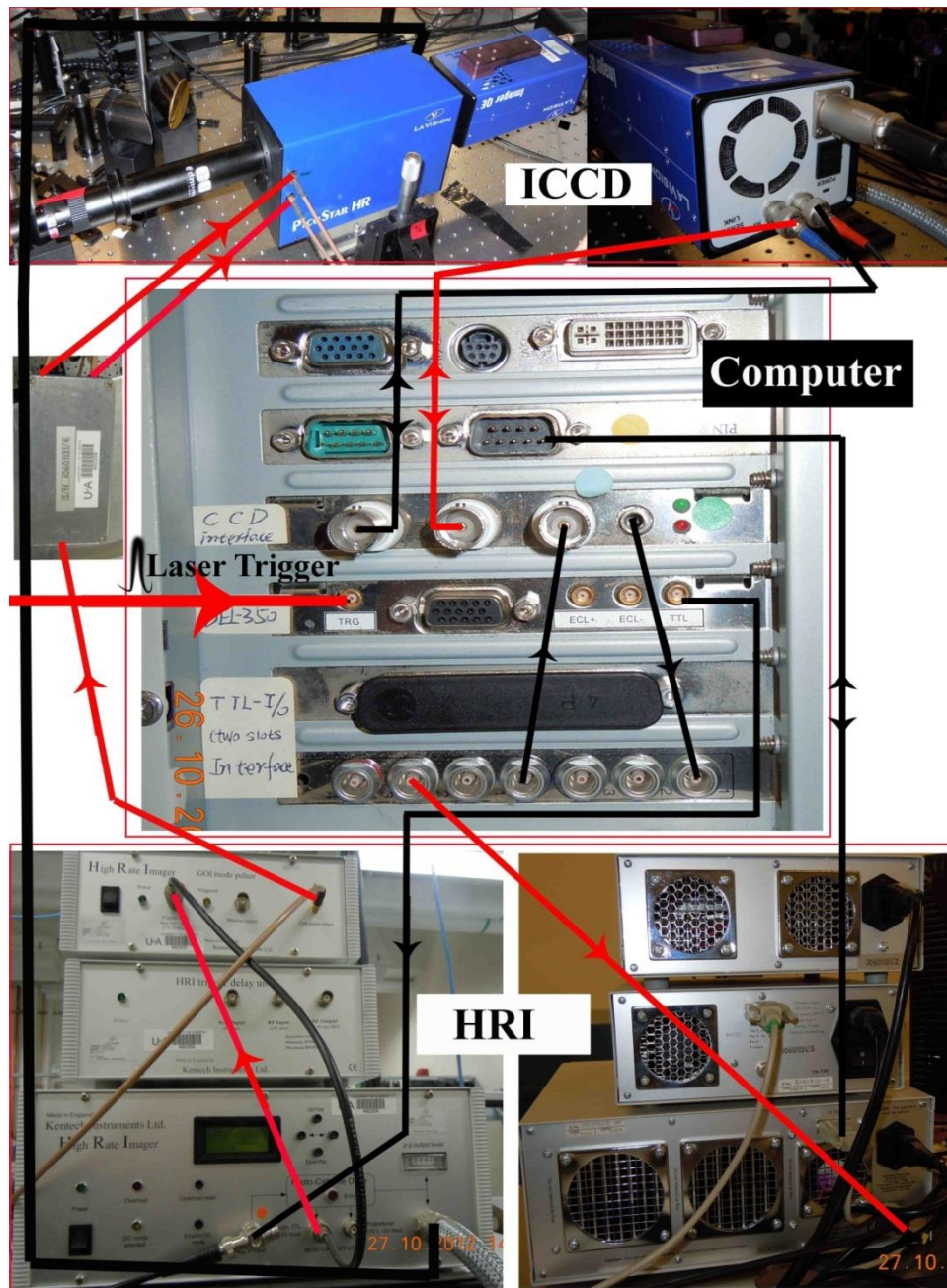
Figure A.3: Scheme of the cable connection of the ICCD camera system.

A.3 Example to operate the ICCD camera

The ICCD camera system is controlled by the software Davis 7.1. Parameters such as the time delay between the electronic gate and the laser trigger signal, MCP voltage, as well as the gate width can be adjusted.

In order to help future users to have a good start to run the ICCD camera, a simple imaging experiment is demonstrated. (the ICCD has a lot of powerful functions, future users are encouraged to explore them)

(1) Switch on the power of High Rate Imager (HRI) box and the ICCD camera.
(2) Click "Davis 7.1" to run the software (Figure A.4).

Figure A.4: Click icon "Davis 7.1" to run the software.

(3) Initialize devices by clicking "Init Devices", and then select the "Expert User" mode (Figure A.5).
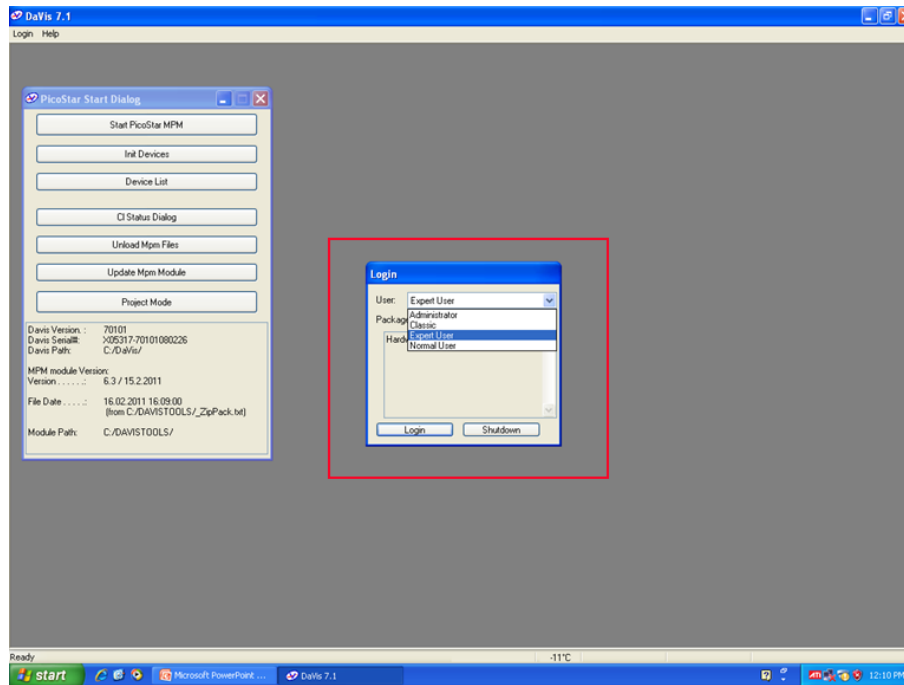
Figure A.5: Initialize devices, and then choose the "Expert user" mode.

(4) Create a new directory by clicking icon "New" (Figure A.6).
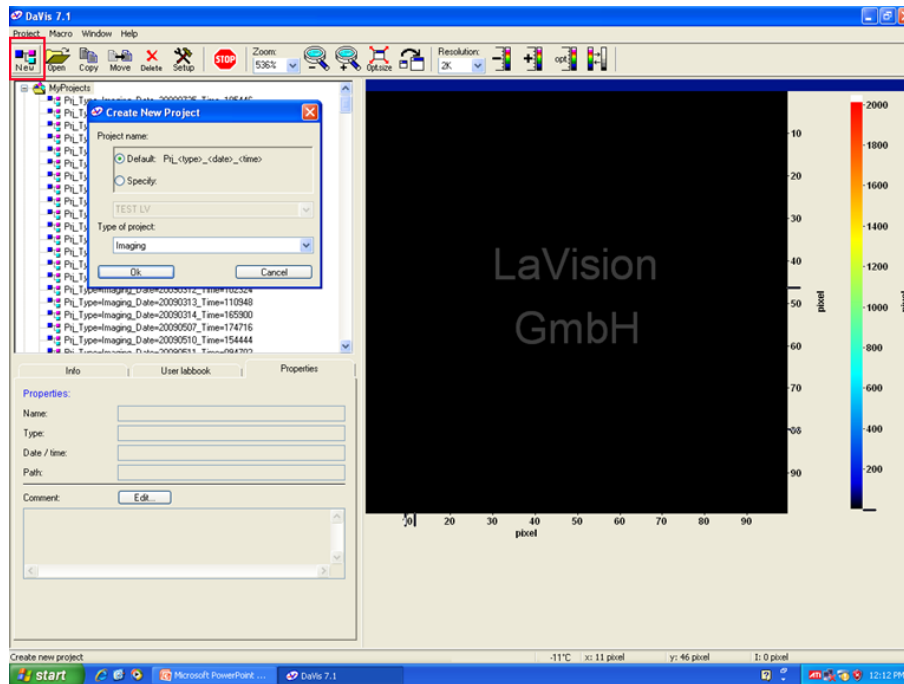
Figure A.6: Click icon "New" to create a new directory.

(5) Click icon "New" to show ICCD camera control interface (Figure A.7).
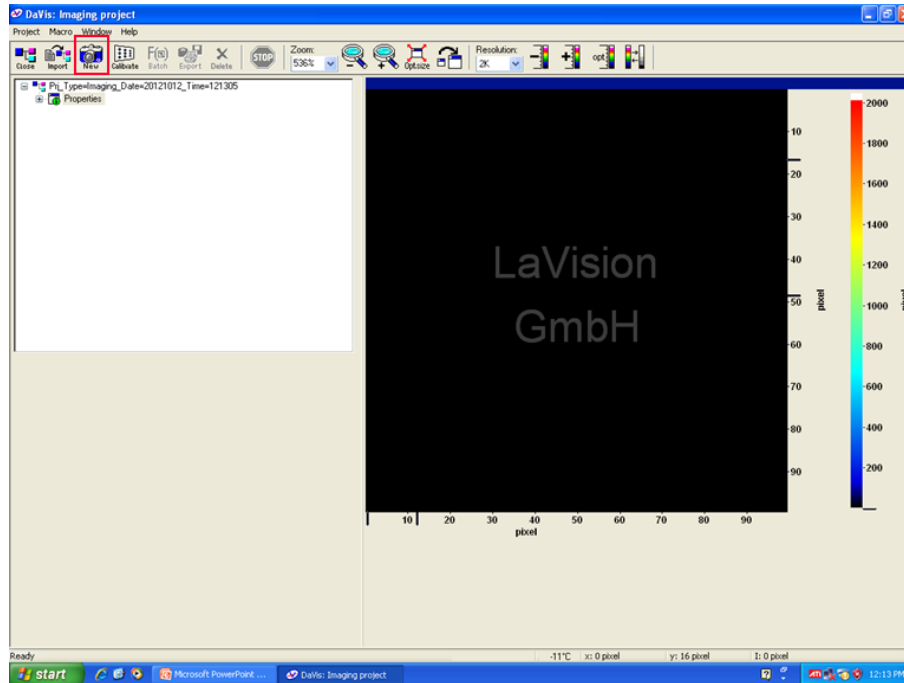
Figure A.7: Click icon 'New' to show ICCD camera control interface.

(6) Set synchronization parameters as shown in the red box in Figure A.8.
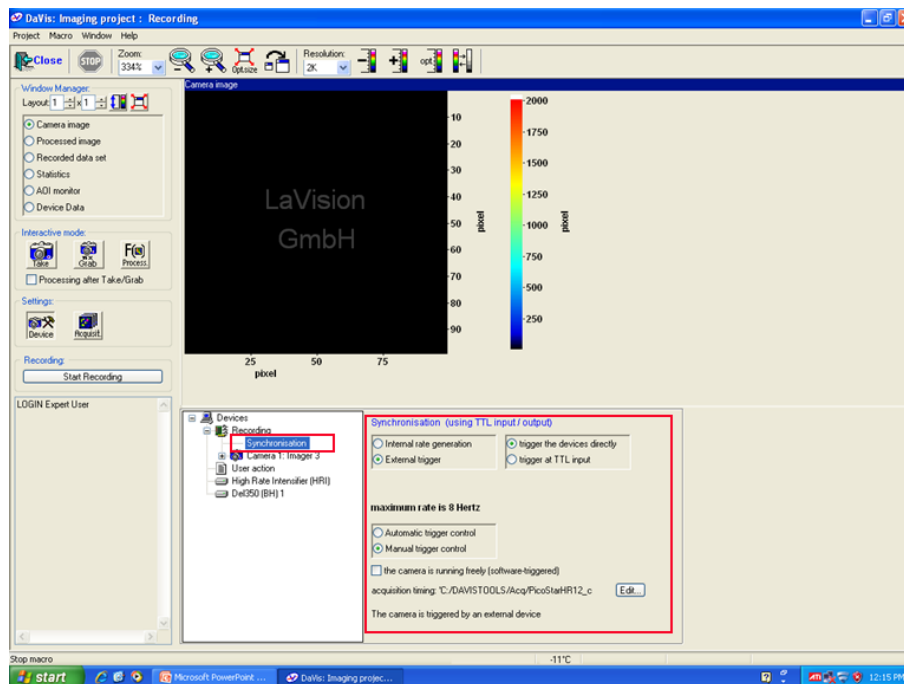
Figure A.8: Set parameters to synchronize the ICCD camera with laser trigger signals.

(7) Set CCD parameters as shown in the red box (Figure A.9).
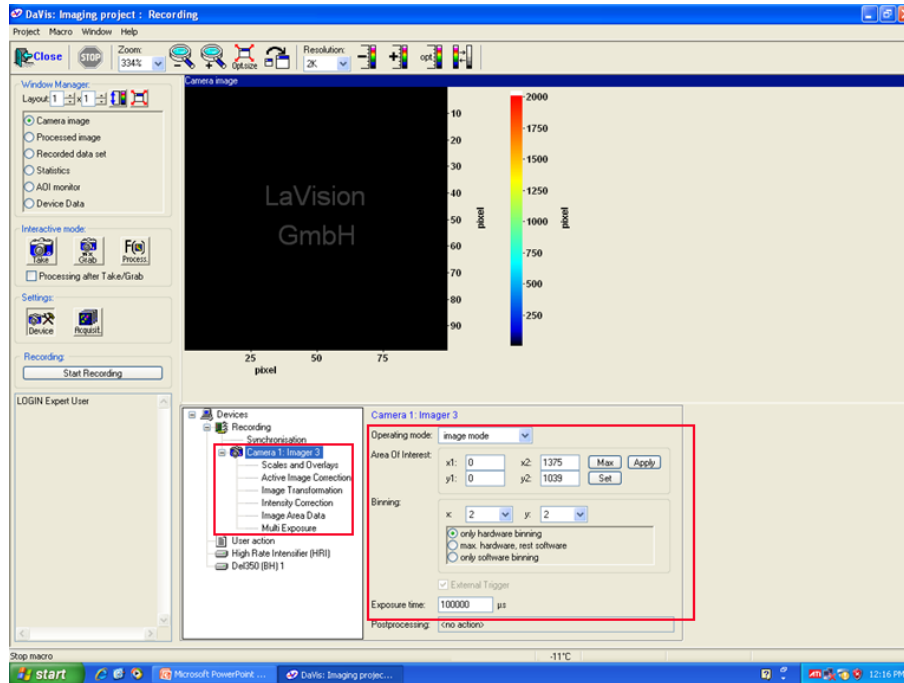
Figure A.9: Set CCD parameters to define the exposure time, the area of interest, and the binning.

(8) Set High Rate Intensifier parameters as shown in the red box in Figure A.10.
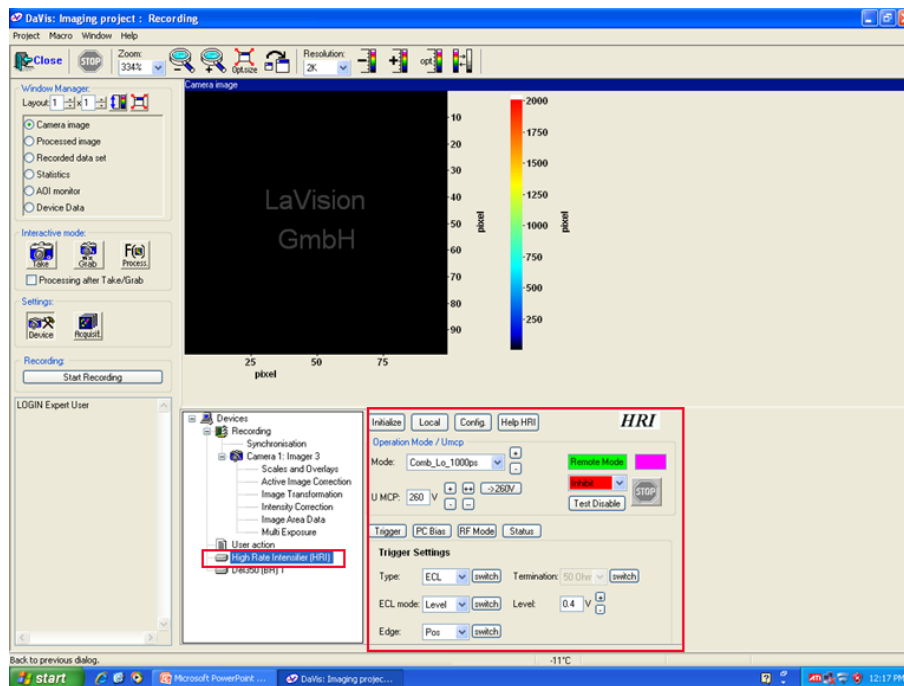
Figure A.10: Set High Rate Intensifier parameters to define the mode, U MCP, and trigger settings.

The UMCP is used to amplify the signal.

(9) Set parameters of DEL 350 as shown in the red box in Figure A.11.
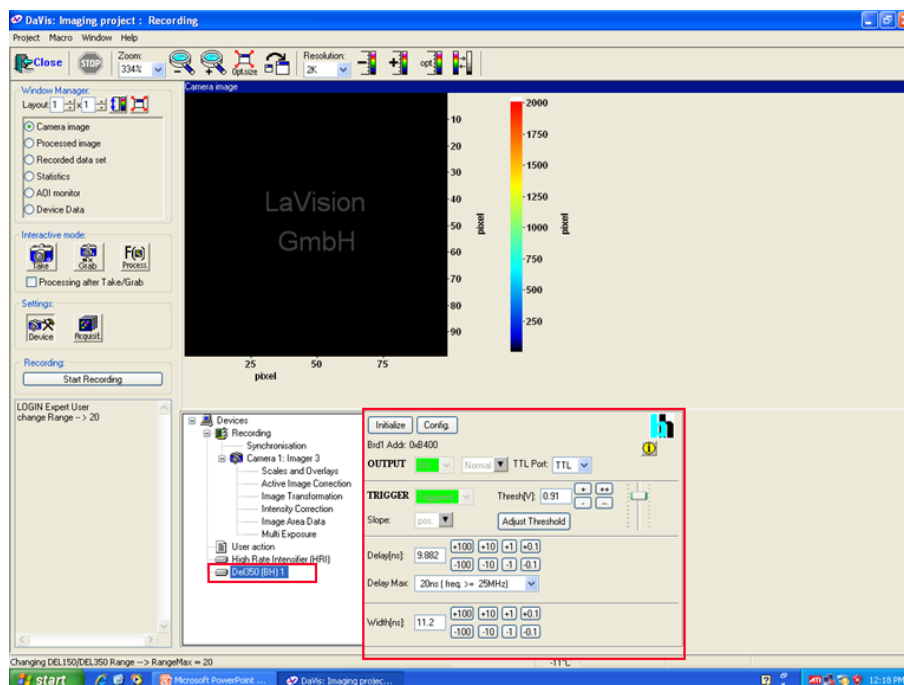
Figure A.11: Set DEL 350 parameters to synchronize the ICCD gate with the laser pulse. Leave "Grab" button on when scan the delay time.

(10) If necessary, collect the background image (Figure A.12).
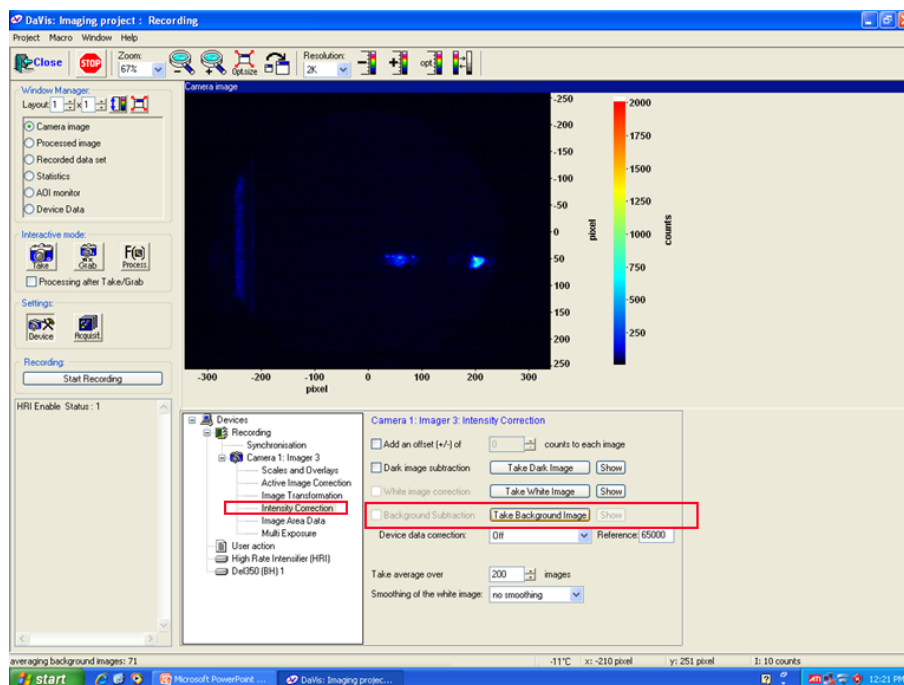
Figure A.12: Take background images by clicking button "Take Background Image". The number of the images can be set.

(11) If necessary, add an offset (Figure A.13).
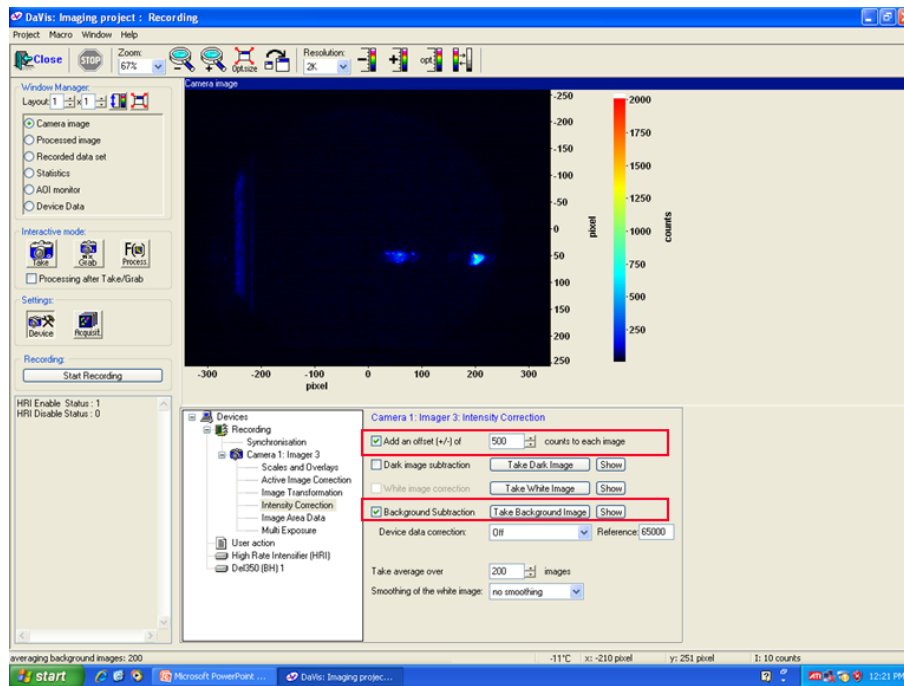
Figure A.13: Activate the "Take Background Image" function and add an offset.

(12) Capture images by clicking button "Take", "Grab", or "Acquits" (Figure A.14).
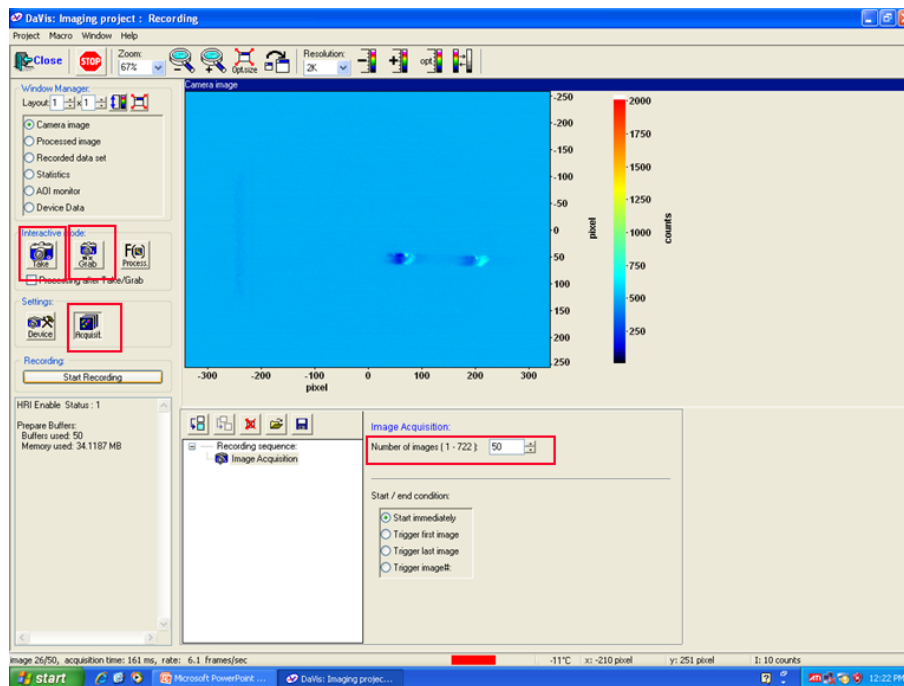
Figure A.14: Click "take" button to image, "grab" button to capture images continually, or "Acquits" button to record images into the computer. The Number of the images can be set. Click "close" to check the saved images.

(13) Check the saved data (Figure A.15).
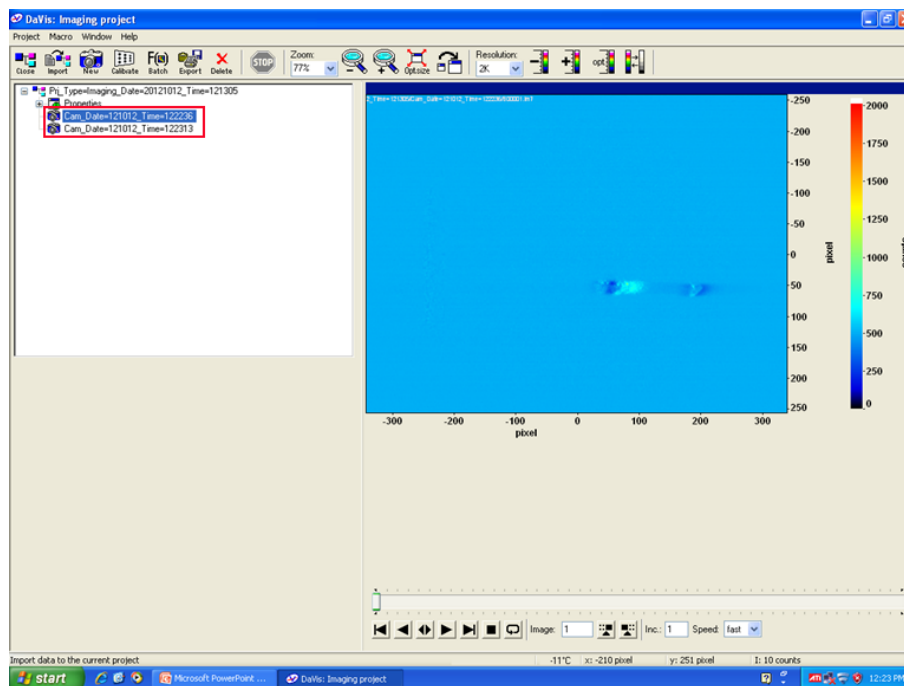
Figure A.15: Check the saved images data.

(14) Average the collected image (Figure A.16). **(Imaging processing)**
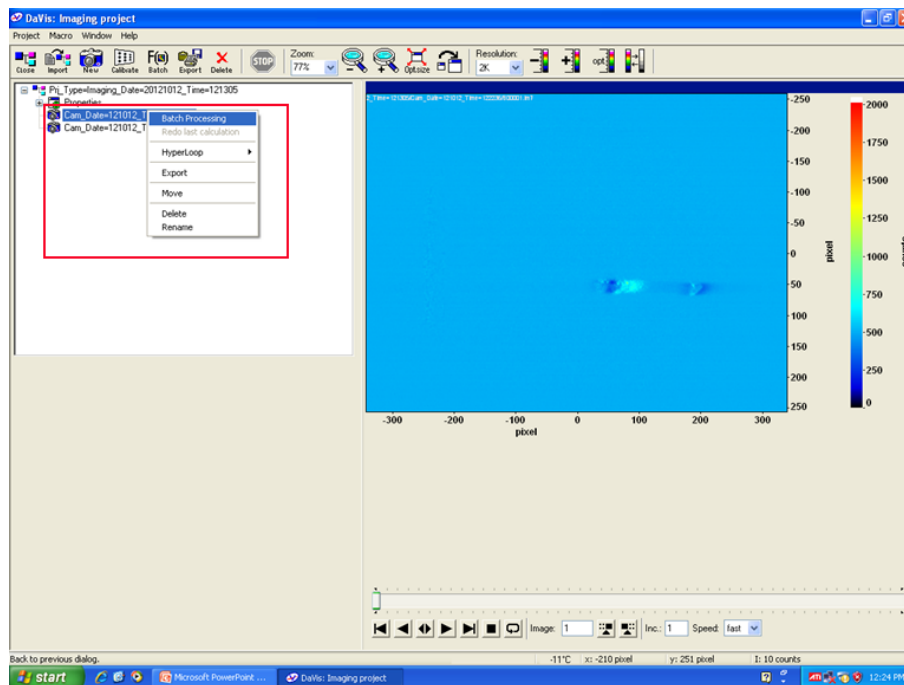
Figure A.16: Process the saved image by right clicking the image's name.

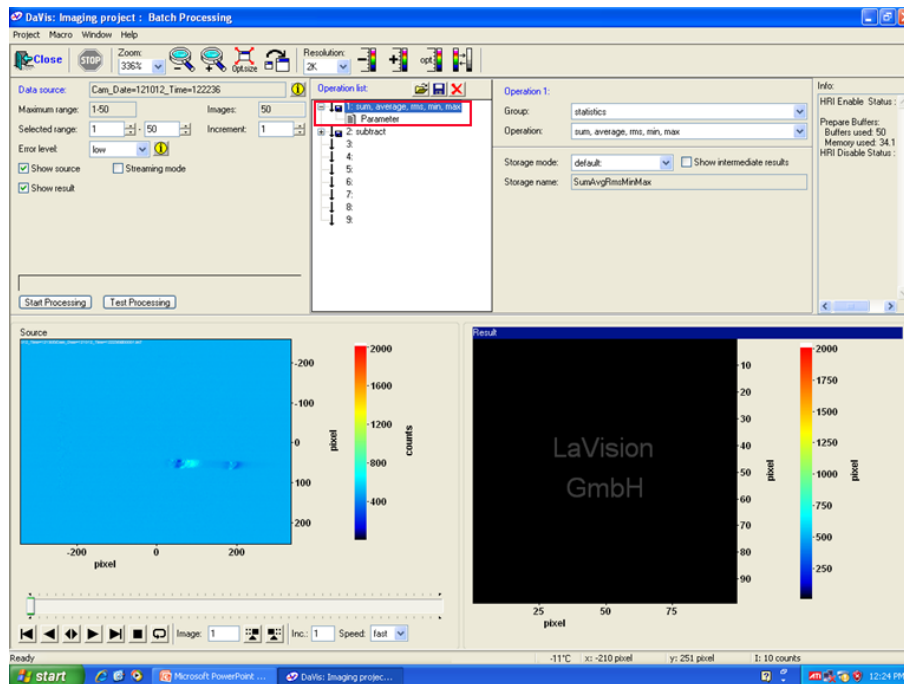(15) Set image processing parameters. (Figure A.17). **(Imaging processing)**

Figure A.17: Set image processing parameters.

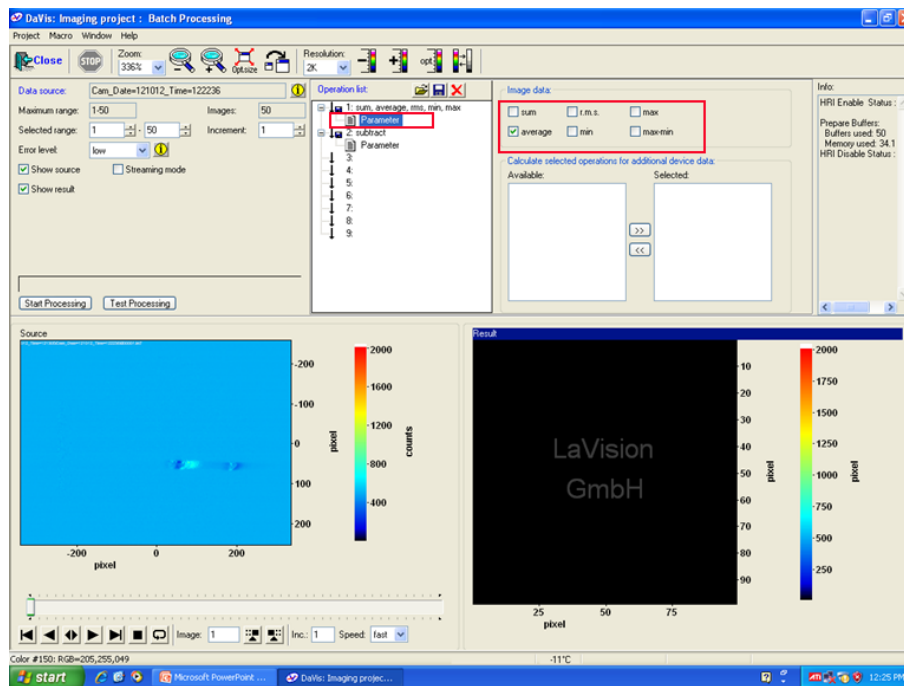(16) Choose the "average" setting. (Figure A.18). **(Imaging processing)**

Figure A.18: Select the "average" function to average the saved images.

206

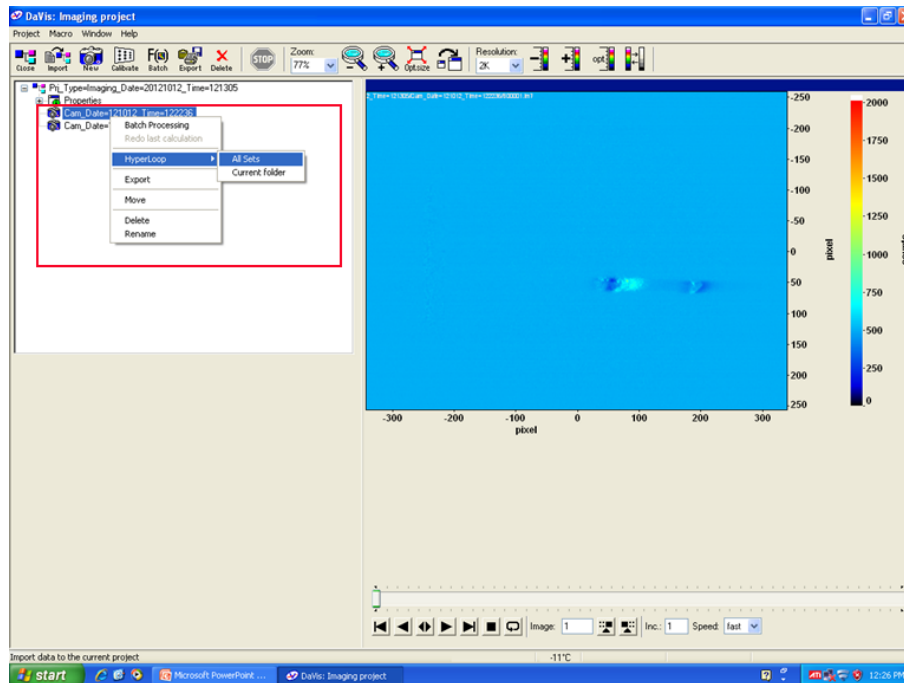(17) Treat all the data automatically using "Hyperloop" (Figure A.19). **(multi-images processing)**

Figure A.19: Process all the saved images with the "Hyperloop" function.

(18) Select files that need to be processed (Figure A.20). **(multi-images processing)**
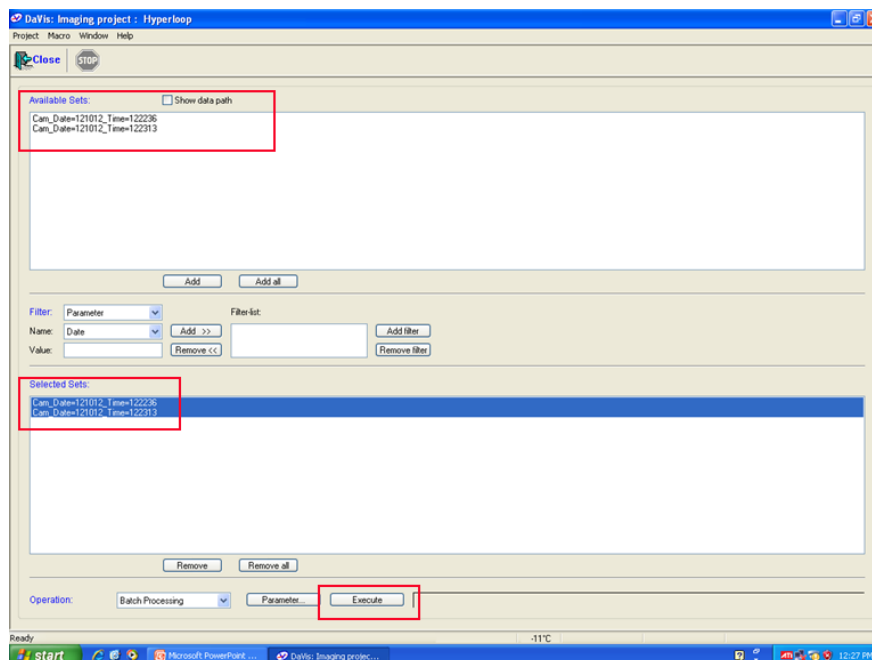

Figure A.20: Process all the saved images by selecting files. Clicking "Execute" button to process.

(19) Set image processing parameters, similar as steps (15) and (16).

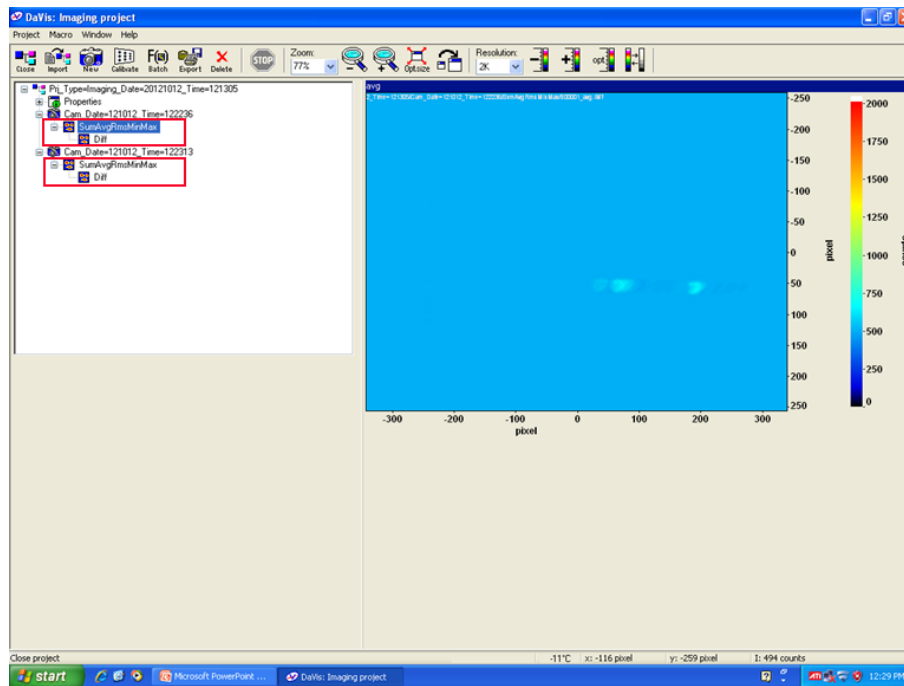(20) Export the saved images in various data formats (Figure A.21).

Figure A.21: Export the save images by right clicking image files.

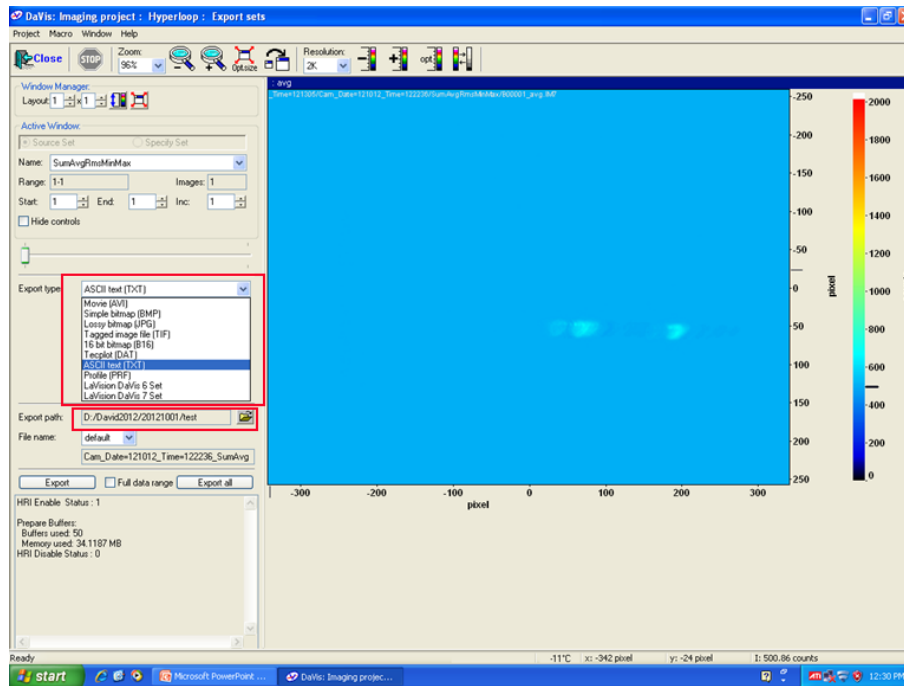(21) Edit export parameters to export the saved or processed images (Figure A.22).

Figure A.22: Edit export parameters to export the saved images.

A.4 Check image distortion of the ICCD camera

Figure A.23 shows the image of a protractor, the angle measured from the image matches with the real value, implying that the ICCD camera is free of the image distortion.
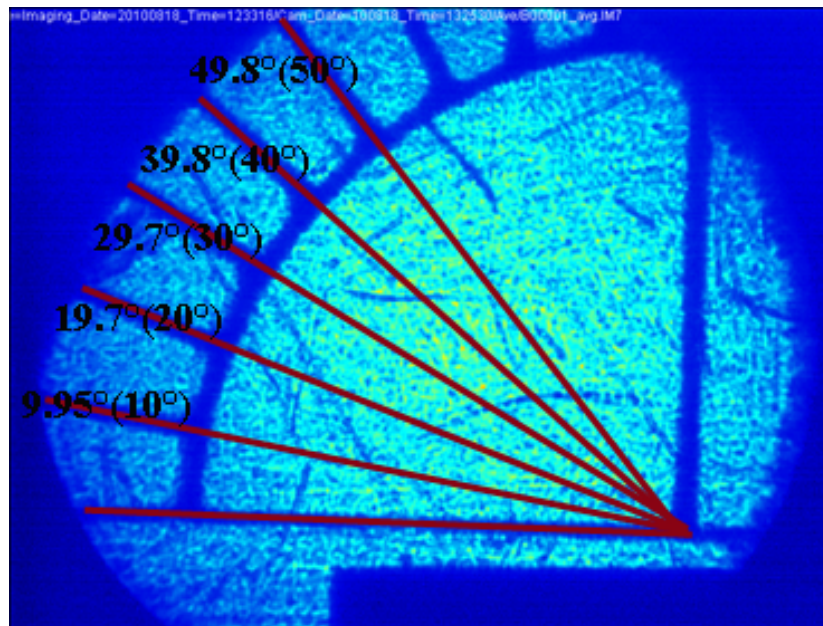

Figure A.23: Image of a protractor with the ICCD camera.

A. 5 Image scale calibration

Because most of our experimental images are collected with Talbot image method, in which the ICCD camera is out of focus and results in a smearing image, so calibrating the spatial scale of a blurred image is very important. In the following part, two methods are introduced.

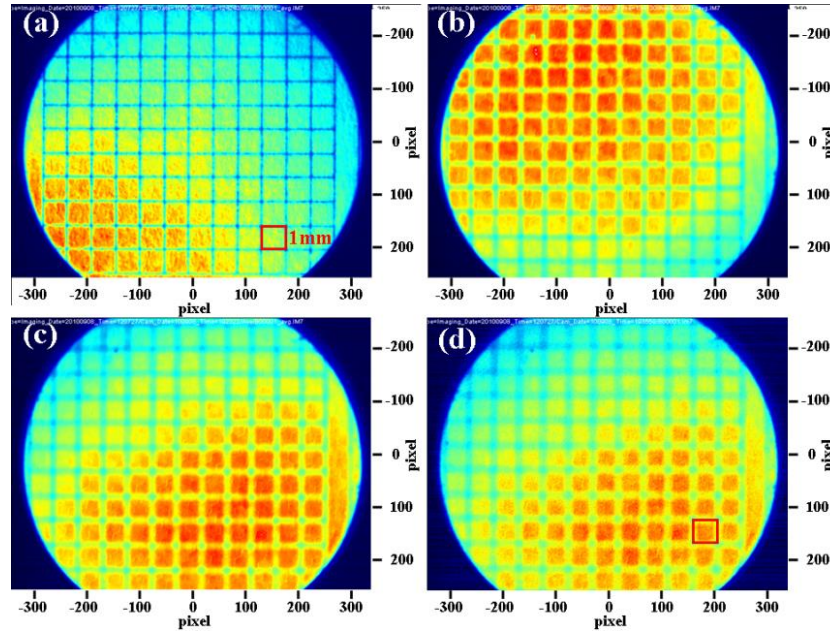## (a) Method 1: image scale calibration by a grid plate

Figure A.24: Images of a grid plate when the ICCD is (a) in focus, (b)-(d) out of focus.

As shown in Figure A.24, images of a grid plate (grid size is 1 mm) are captured by the ICCD camera that is in focus or out of focus to some extents. Although the image of the grid line becomes blurred when the camera is out of focus (Figure A.24 (b) − (d)), the distance between two neighbour grid lines is the same as that measured in a focused image. The calibrated image scales measured in the vertical as well as the horizontal directions in various camera focus conditions are listed in

Table A1. **The same calibration scale value tells us that the measured spatial distance between two objects (lines) is not affected by the image smearing.**

(b) Method 2: image scale calibration by shifting the ICCD camera

In order to calibrate the image scale more conveniently, we develop a new calibration method by shifting the ICCD camera. Figure A.25 (a)-(d) and Figure A.25 (e)-(h) are the images of a grid plate taken by the ICCD camera when the camera is shift horizontally or vertically.

As shown in Figure A.26, by plotting positions of the line (red lines are for the horizontal shift, blue line are for the vertical shift) and the camera displacements, the image scales are obtained.

With the same camera shifting method, scale calibration of the blurred images is also carried out. All the calibration image scales are summarized in Table A.1. We find that the image scale calibrated by moving the camera vertically is the same as the value measured with the grid plate method (method 1). On the other hand, the image scale obtained by moving the camera horizontally is different from the grid plate method. The reason could be that the ICCD camera is not aligned perfectly in horizontal direction.

In conclusion, the image scale can be calibrated by shifting the ICCD camera vertically. It's a very convenient method in the terahertz Cherenkov imaging experiments, and a sample calibration is shown in Figure A.27. (note: the different calibration value obtained in Figure A.27 is due to the different imaging magnification (zoom in) setting).
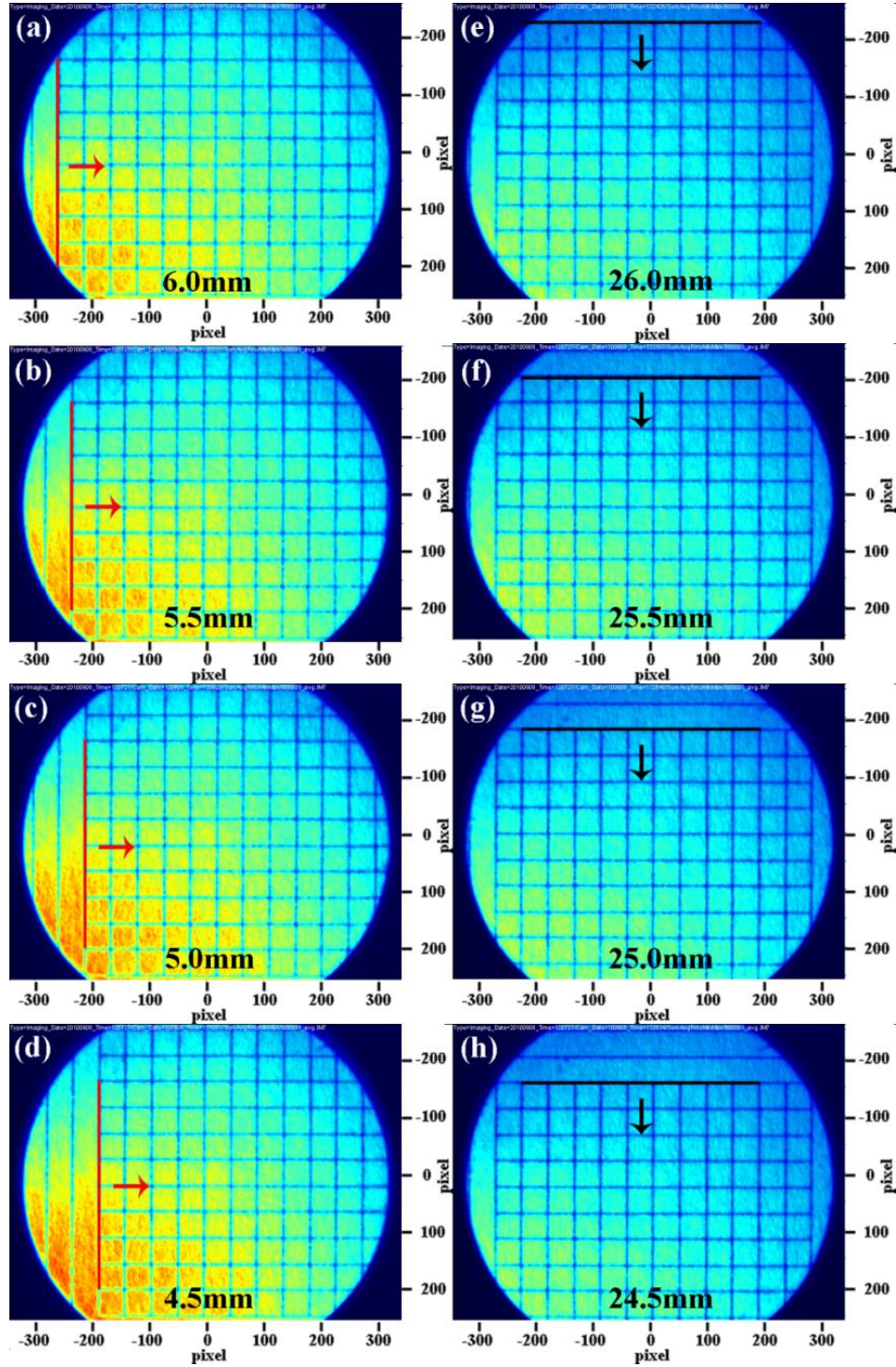
Figure A.25: (a)-(d) Images of the grid plate when the ICCD camera is moved horizontally. The values show the ICCD camera positions in the horizontal direction. (e)-(h) Images of the grid plate when the ICCD camera is moved vertically. The values show the ICCD camera positions in the
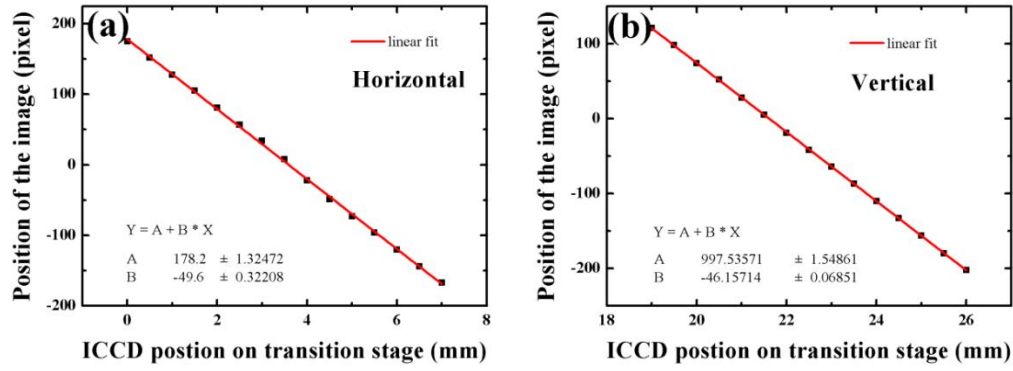
212

vertical direction.

Figure A.26: Plot between image positions with respect to ICCD positions in the (a) horizontal direction, and (b) vertical direction.

Table A.1: Summary of the image scales calibrated with the grid plate method and the ICCD camera shift method

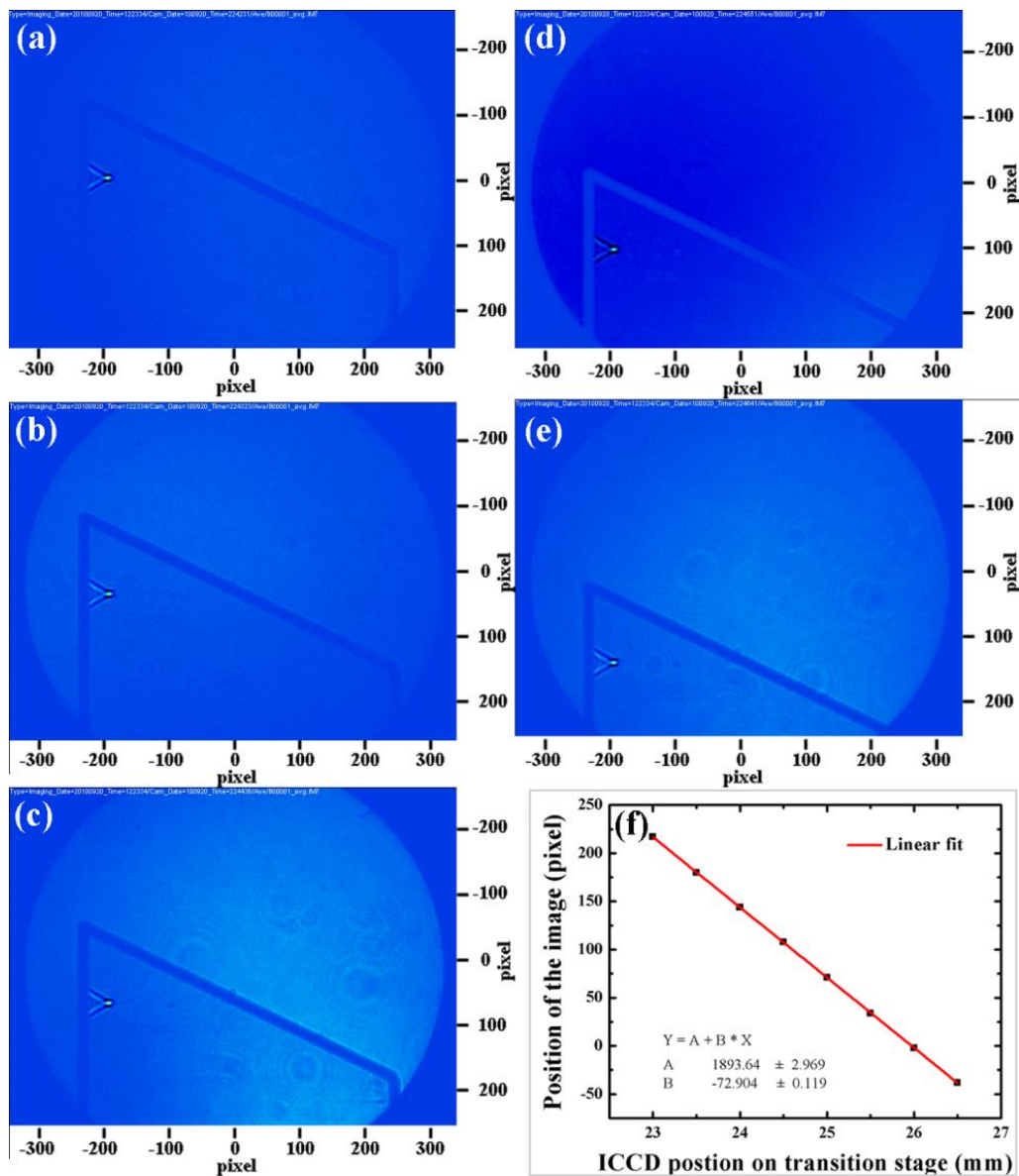|	calibration by plate directly (pixel/mm)		calibration by moving ICCD camera (pixel/mm)	
	horizontal	vertical	horizontal	vertical
Case a (well focused)	46.13	45.7	49.6±0.3	46.2±0.1
Case b (not focused)	47.08	46.38	50.6±0.8	47.0±0.2
Case c (not focused)	47.26	46.88	51.0±0.6	46.9±0.2
Case d (not focused)	47.5	47.1	51.3±0.6	47.0±0.3

Figure A.27: (a)-(e) Images of the THz Cherenkov wave when the ICCD camera is at different positions in the vertical direction. (f) Plot between the cone tip positions via the ICCD camera positions.

A. 6 Sample imaging of the background-subtracted image

(a) Introduction

As illustrated in Figure A. 28(a), after a probe pulse goes through the sample and gets phase modulated, the phase modulated probe pulse is converted into the light intensity object with various techniques and then is recorded by a CCD camera. The captured image is digitalized and saved into the computer memory.
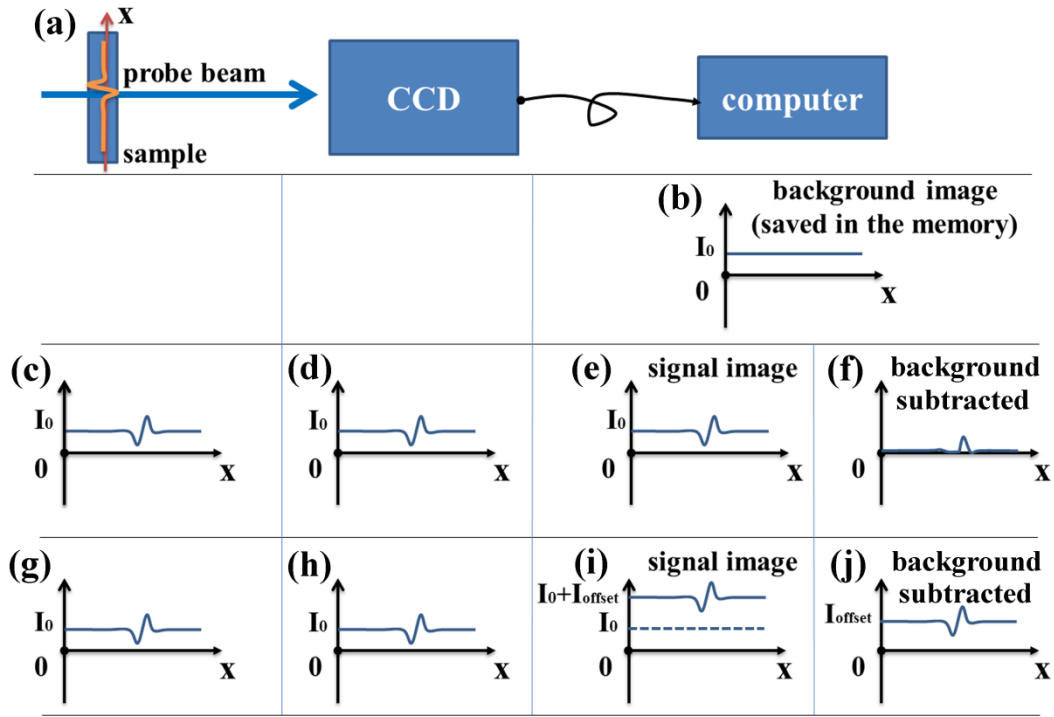

Figure A.28: (a) Illustration of the imaging process. The probe pulse goes through the sample and gets phase modulated. The phase modulated probe pulse is converted into light intensity object and then recorded by the CCD camera. The captured image is digitalized and saved into the computer memory. (b) Background image saved in the computer memory. (c)-(f) The process to obtain the background-subtracted image (with no image offset). (g)-(j) The process to obtain the background-subtracted image (with an offset).

Because background-subtracted images are required in the Talbot imaging and the noncollinear *E*-mode imaging, a brief introduction to the background-subtracted imaging is given here.

The background-subtracted image can be obtained in two different ways. The first one is to take the background image I_0 (with the optical pump beam blocked) and the signal image $I_{sig}=I_0+I_0\alpha$ (with the optical pump beam unblocked), respectively, where α is the modulation ratio. Then a subtraction operation is carried out manually between the background image and the signal image. Based on the captured background image and the signal image, the background-subtracted image $I_{sig}-I_0=I_0\alpha$ can be calibrated, and the modulation ratio α can be calculated as well.

The second method is to take the background-subtracted image directly in the imaging process. As shown in Figure A. 12 in section A. 3, block the optical pump beam, then click the button 'Take Background Image' to take the background image I_0 (with the button 'Add an offset(+/-)…' unselected). The background image I_0 (see Figure A. 28(b)) is temporarily saved into the computer memory. When we start to capture the background-subtracted image, unblock the optical pump beam and then take a signal image $I_{sig}=I_0+I_0\alpha$ (see Figure A. 28(e)). The computer will do the subtraction operation automatically and give a background-subtracted image $I_{sig}-I_0=I_0\alpha$. However, as illustrated in Figure A. 28(f), we find that the signal value of the negative sign is considered to be zero by the computer, and thus makes the obtained background-subtracted image wrong.

In order to overcome this problem, we add a positive offset (see Figure A. 28(i)) when we take the signal image to make the signal image $I_{sig}+I_{offset}$ $=(I_0+I_0\alpha)+I_{offset}$. As shown in Figure A. 28(j), if the offset is set appropriately, the background-subtracted image $I_0\alpha+I_{offset}$ won't have negative values. Once the background-subtracted image is saved into the computer, we can remove the

offset I_{offset} to make the baseline zero. We note that adding an offset keeps the image information complete and won't cause any distortion. This is because the optical probe pulse intensity and the ICCD amplification factor don't change no matter we add the offset or not.

In conclusion, the first method is more intuitive, but needs two images for one background-subtracted image. The second one is suitable for the real time observation once the background image is taken and the offset is set appropriately. Because the background-subtracted image can still be calibrated as well, the second method is preferred.

(b) Sample imaging

In this section, an example is given to show how to get a background subtracted image automatically (the second method) with the ICCD camera system.

Firstly, we make the signal strength level of the background image at about 2400 counts by adjusting the probe light intensity and ICCD intensifier. Then click the button 'Take Background Image' (see Figure A.12) to save the background image I_0 into the computer memory (with the button 'Add an offset (+/-)…' unselected). The saved background image can be checked by clicking the 'show' button and is displayed in Figure A.29(a).

Secondly, unblock the optical pump beam, add an offset of 200 counts, and take the image. If the 'Take Background Image' is not activated, the captured image is the signal image I_{sig} (see Figure A.29(b)). On the other hand, if the 'Take Background Image' is activated, a background-subtracted image $I_{background\text{-}subtracted}$ is then obtained (see Figure A. 29(c)).

As we can see in Figure A.29(c), the baseline of the background-subtracted image $I_{background\text{-}subtracted}$ is not zero due to the given imaging offset. We can correct the baseline of the image with Matlab, and the corrected background-subtracted

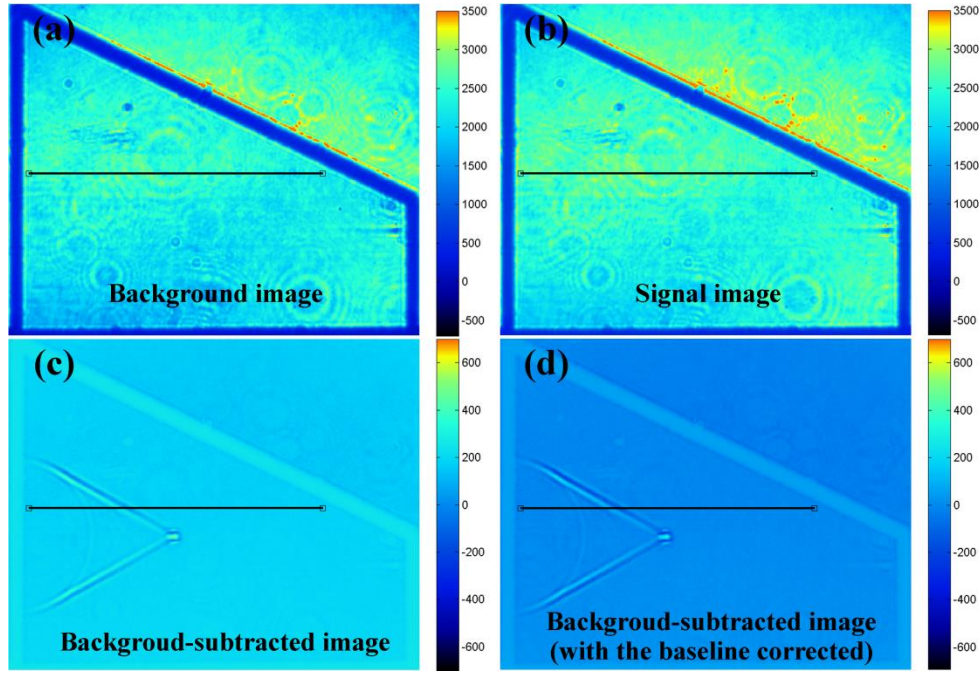image $I_{background\text{-}subtracted(baseline\ corrected)}$ is shown in Figure A. 29(d).

Figure A.29: (a) Background image. (b) Signal image taken with an offset. (c) Background-subtracted image. (d) The baseline corrected background-subtracted image.

Figure A.30(a) corresponds the profile plots from images shown in Figure A.29 along the black line. The modulation ratio is calculated by the formula I $_{background\text{-}subtracted(baseline\ corrected)}$ /I$_0$, and is shown in Figure A. 30(b).
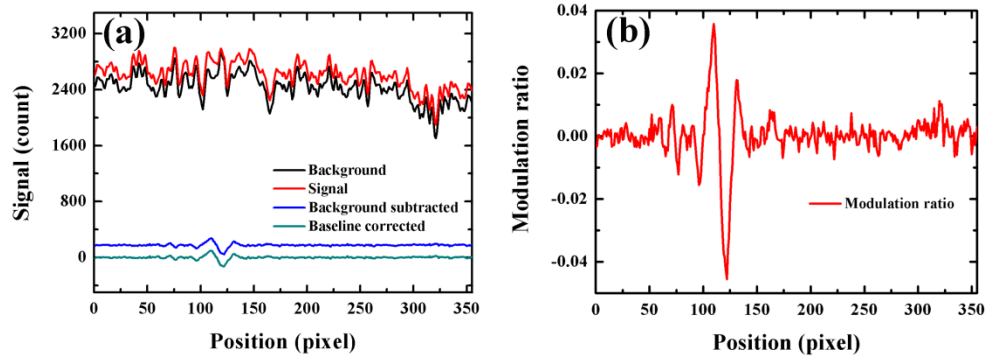

Figure A.30: (a) profile plot of the image along the black line in images shown in Figure A. 29. (b) Plot of the modulation ratio along the black line.

Appendix B

Optical setup for tilting the optical pulse wavefront

A couple of methods based on prism, echelon, and grating have been developed to tilt the wavefront of an optical pulse [2-4], and the grating method has been widely used for intense THz pulses generation in $LiNbO_3$ crystals recently [4, 5].

As illustrated in Figure B.1, when an optical beam gets diffracted from a grating, the relationship between the incident angle and the first-order diffraction angle is described by

$$N\lambda = \sin(\alpha) + \sin(\beta) \qquad (B.1)$$

where α and β are the incident angle and the first-order diffraction angle, N is the grating groove density, and λ is the optical wavelength. As illustrated in Figure B.1(a), after being diffracted by the grating, beam **1** has a longer propagation distance than that of beam **2**. The displacement of the beam and the diffracted beam width are

$$a + b = D\,\sin\alpha + D\sin\beta = D(\sin\alpha + \sin\beta) \qquad (B.2)$$

$$L = D\cos\beta \qquad (B.3)$$

As illustrated in Figure B.1(b), the tilt angle of the wavefront satisfies the following relationship

$$tan\gamma = \frac{a+b}{L} = \frac{sin\alpha + sin\beta}{cos\beta} \qquad (B.4)$$
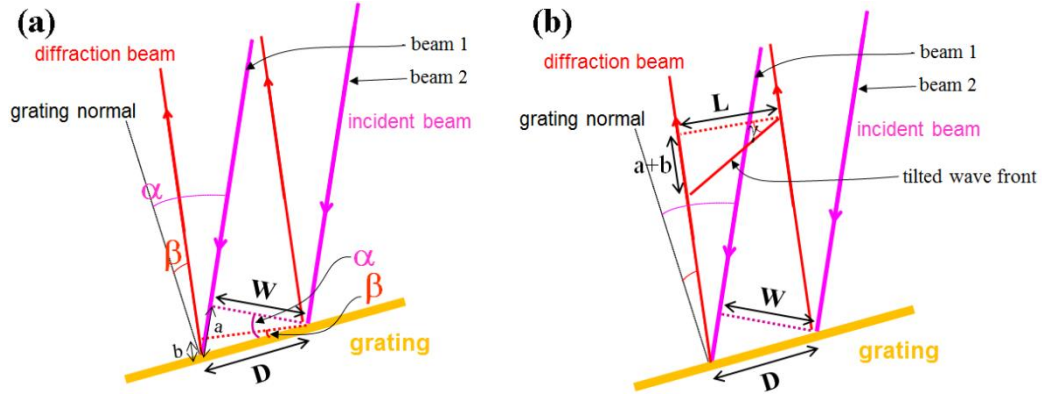
Figure B.1: (a) (b) Scheme of the optical beam diffraction on a grating.
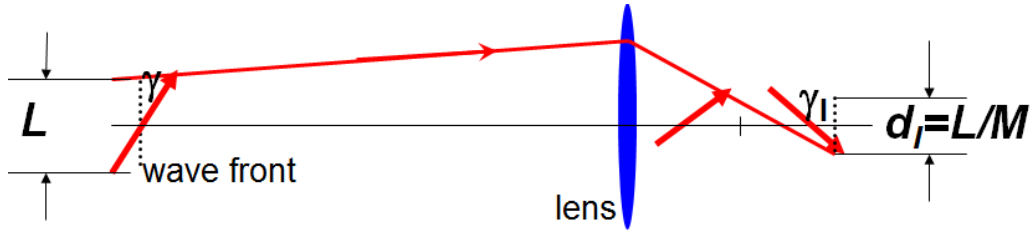

Figure B.2: Illustration of the tilt angle dependence on the demagnification M.

Due to the broad band width, the diffracted femtosecond optical pulse beam has a large angle dispersion and the tilted optical wavefront has to be imaged onto the LiNbO$_3$ crystal by a lens. As shown in Figure B.2, the tilt angle of the beam γ_I at the image plane and the imaging demagnification M has the following relationship

$$tan\gamma_I = -M \times tan\gamma \qquad (B.5)$$

where γ is the tilt angle at the grating, γ_I is the tilt angle at the image plane, and M is the imaging demagnification.

As illustrated in Figure B.3, when the optical beam is incident on the LiNbO$_3$ crystal, the tilt angle of the optical beam γ' inside the LiNbO$_3$ crystal is

determined by

$$tan\gamma_I = n \times tan\gamma' \qquad (B.6)$$

where n is the refractive index of the crystal.

In summary, from Equation B.4, Equation B.5, and Equation B.6. The relationship between the tilt angle γ' inside the crystal and the diffraction angle is

$$tan\gamma' = -\frac{N\lambda M}{ncos\beta} \qquad (B.7)$$

where γ' is the tilt angle inside the crystal, N is the groove density, λ is the wavelength in free-space, M is the imaging demagnification, n is the refractive index, and β is the diffraction angle.
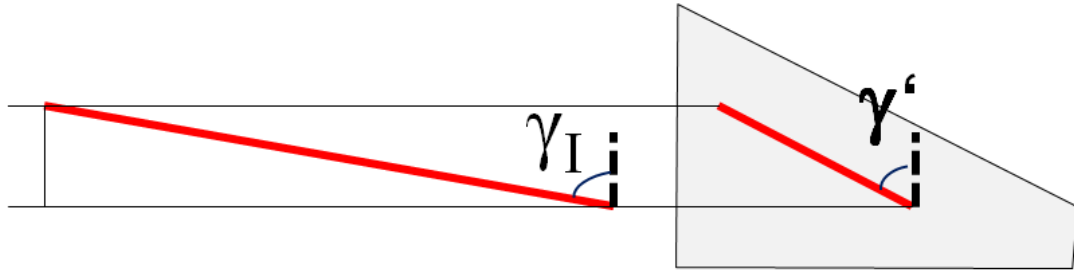

Figure B.3: Illustration of the tilt angle inside the crystal.

The tilted wavefront excitation optical setup used in our experiment is shown in Figure B.4, in which the grating groove density is 1800 mm^{-1}, the incident angle is 43°, and the refractive index is 2.25. According to Equation B.7, by changing the imaging demagnification M, the tilt angle γ' inside LiNbO$_3$ crystals can be adjusted. In order not to change the LiNbO$_3$ crystal position, the grating and lens are moved during the image demagnification adjustment. The imaging

demagnification, object distance, and image distance that correspond to various tilt angles inside the crystal is shown in Table B.1.

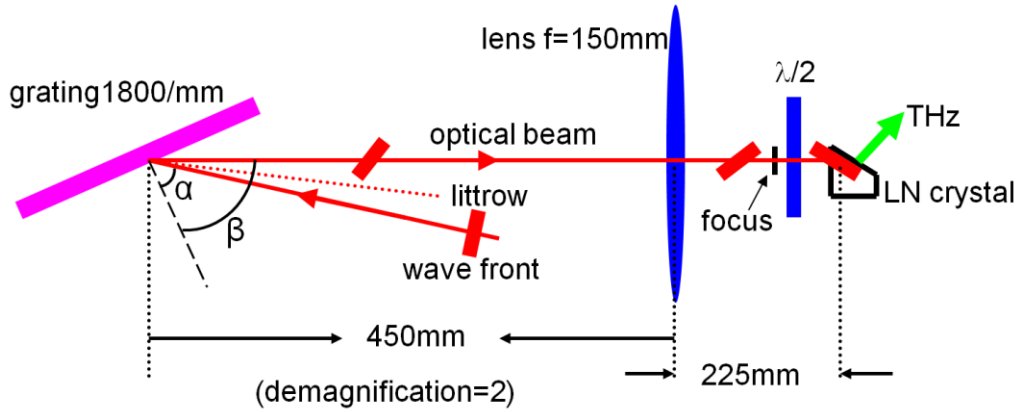As shown in Figure B.5, the diffraction efficiency of the grating is 84%.

Figure B.4: Optical setup of the tilted-pulse-front excitation technique in our lab.

Table B.1. Various tilt angles and their corresponding demagnification values, object distances and image distances.

| object distance (mm)	image distance (mm)	focus length (mm)	Demagnification	total distance (mm)	α(°)	β(°)	γ'(°)
495.0	215.2	150	2.3	710.2	43	49.29	66.10
480.0	218.2	150	2.2	698.2	43	49.29	65.15
465.0	221.4	150	2.1	686.4	43	49.29	64.11
450.0	**225.0**	**150**	**2.0**	**675.0**	**43**	**49.29**	**63.00**
435.0	229.0	150	1.9	664.0	43	49.29	61.79
420.0	233.3	150	1.8	653.3	43	49.29	60.48
405.0	238.2	150	1.7	643.2	43	49.29	59.06
390.0	243.8	150	1.6	633.8	43	49.29	57.51
375.0	250.0	150	1.5	625.0	43	49.29	55.81
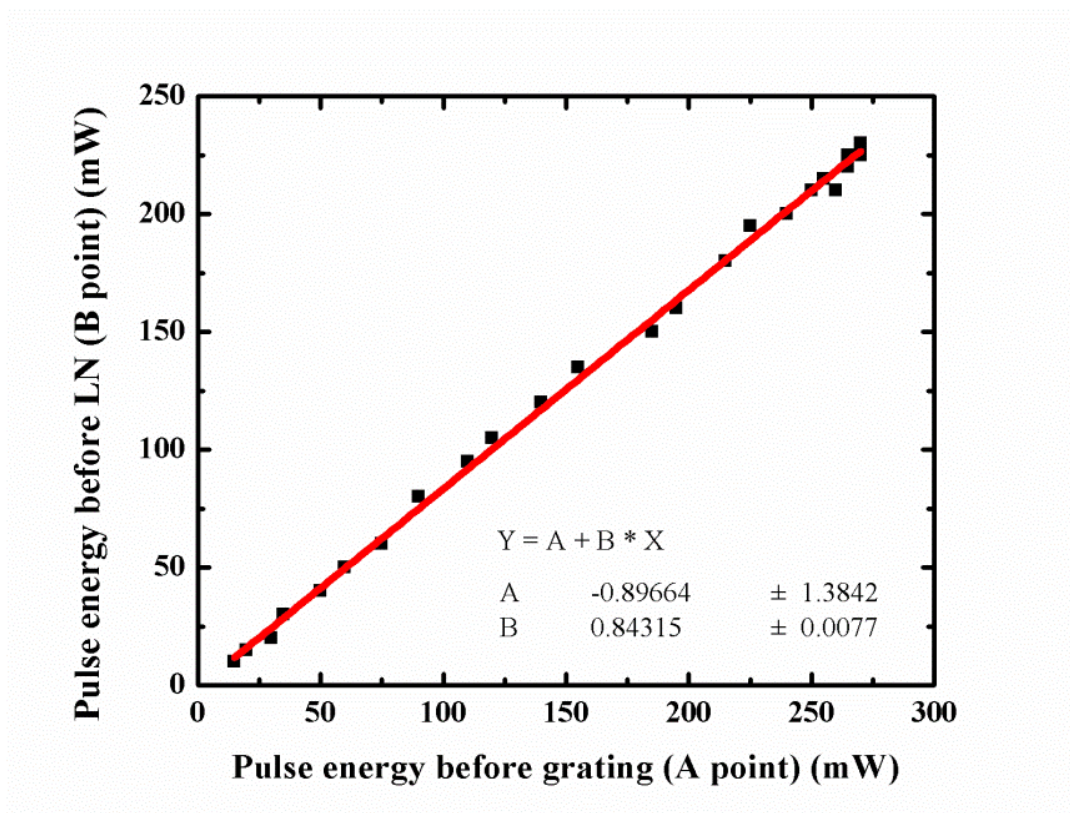
Figure B.5: The efficiency of the diffraction grating.

Appendix C

Ac complex conductivity calculation with terahertz time-domain spectroscopy and the Drude model fitting

C. 1 Ac complex conductivity of a thin film with the THz time-domain spectroscopy
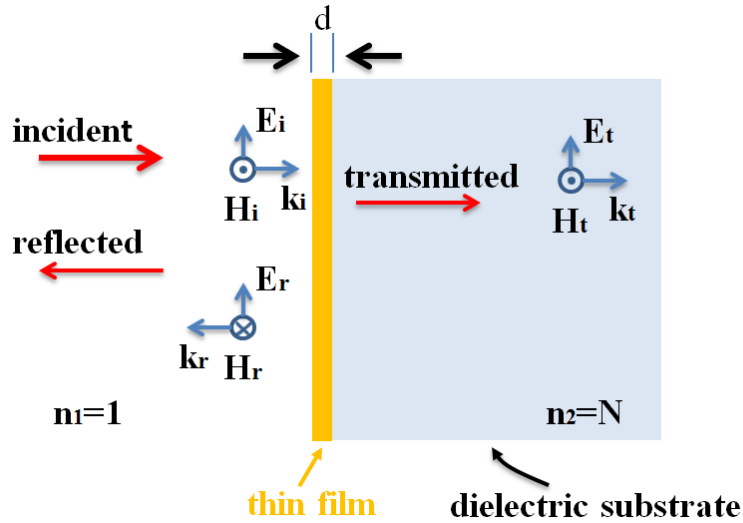

Figure C.1: Illustration of the electromagnetic wave that propagates through a thin conductive film that locates between the free space and the dielectric substrate. The thickness of the film is d.

As illustrated in Figure C.1, an electromagnetic wave is incident on a thin conductive film which locates between the free space and the dielectric media. If the approximation $d \ll \frac{\lambda}{n}$ is satisfied (d is the thickness of the conductive film, λ is the wave length of the incident electromagnetic wave in free space, and n is the refractive index of the thin film), the ac complex conductively can be calculated

through Tinkham equation [6]:

$$t_{film}(\omega) = \frac{\widetilde{E_{t\_film}}(\omega)}{\widetilde{E_i}(\omega)} = \frac{2}{N+1+Z_0 d\tilde{\sigma}(\omega)} \qquad \text{(C.1)}$$

where $\widetilde{t_{film}}(\omega)$ is the complex electric field transmission, N is the refractive index of the dielectric media, $Z_0 = 377\Omega$ is the impendence of the free space, ω is the frequency, $\tilde{\sigma}(\omega)$ is the ac complex conductivity of the thin film. $\widetilde{E_i}(\omega)$ and $\widetilde{E_{t\_film}}(\omega)$ are the complex electric field of the incident and transmitted electromagnetic waves.

On the other hand, if there is no thin film, the complex electric field transmission becomes

$$t_{no-film} = \frac{\widetilde{E_{t\_nofilm}}(\omega)}{\widetilde{E_i}(\omega)} = \frac{2}{N+1} \qquad \text{(C.2)}$$

From Equation C.1 and Equation C.2, we can get

$$\frac{\widetilde{E_{t\_film}}(\omega)}{\widetilde{E_{t\_nofilm}}(\omega)} = \frac{N+1}{N+1+Z_0 d\tilde{\sigma}(\omega)} \qquad \text{(C.3)}$$

In Summary, according to Equation C.3, if we get the transmitted time-domain waveforms of the THz pulses that propagate though a substrate with and without a thin conductive film, respectively, the ac complex conductively of the thin film can be extracted.

C. 2 Drude model

Drude model is perhaps the simplest and most commonly used model to describe ac conductivity of free electric carriers. The motion of electric carriers in an applied electric field is described as

$$m\frac{d\vec{v}}{dt} = -m\frac{\vec{v}}{\tau} - e\vec{E}(t) \qquad\qquad (C.4)$$

where m is the mass of the carrier, $\vec{v}$ is the drift velocity of the carrier, τ is the scattering time, $-e$ is the charge of the electron, and $\vec{E}(t)$ is the applied electric field, and t is the time.

For a steady electric (dc) field, the current density $\vec{J} = ne\vec{v}$ is a constant (n is the free carrier density), implying that

$$\frac{d\vec{J}}{dt} = \frac{d\vec{v}}{dt} = 0 \qquad\qquad (C.5)$$

From Equation C.4 and Equation C.5, the dc conductivity can be expressed as

$$\sigma_{dc} = \left|\frac{\vec{J}}{\vec{E}}\right| = \frac{ne^2\tau}{m} \qquad\qquad (C.6)$$

On the other hand, if an ac electric field $\vec{E}(t) = \vec{E}(\omega)e^{-i\omega t}$ is applied, where ω is the angle frequency, the drift velocity $\vec{v}$ in Equation C.4 is in the form of $\vec{v} = \vec{v}(\omega)e^{-i\omega t}$, and Equation C.4 becomes

$$(-i\omega)m\vec{v}(\omega) = -m\frac{\vec{v}(\omega)}{\tau} - e\vec{E}(\omega) \qquad (C.7)$$

So
$$\vec{v}(\omega) = \frac{e\tau}{m}\frac{1}{1-i\omega\tau}\vec{E}(\omega) \qquad \text{(C.8)}$$

From Equation C.6 and Equation C.8, the complex ac conductivity of the electric carrier can be presented as

$$\sigma_{ac} = \frac{\vec{J}(t)}{\vec{E}(t)} = \frac{ne\vec{v}(t)}{\vec{E}(t)} = \frac{ne^2\tau}{m}\frac{1}{1-i\omega\tau} = \sigma_{dc}\frac{1}{1-i\omega\tau} \qquad \text{(C.9)}$$

The real and imaginary ac conductivity are

$$\sigma_1(\omega) = \sigma_{dc}\frac{1}{1+(\omega\tau)^2} \qquad \text{(C.10)}$$

$$\sigma_2(\omega) = \sigma_{dc}\frac{\omega\tau}{1+(\omega\tau)^2} \qquad \text{(C.11)}$$

where $\sigma_{dc} = \frac{ne^2\tau}{m}$ is the DC conductivity, $\sigma_1(\omega)$ and $\sigma_2(\omega)$ are the real and imaginary ac conductivity.

By fitting the experimental ac conductivity that is obtained from the THz time-domain spectroscopy with Equation C.10 and Equation C.11, the dc conductively σ_{dc} and the scattering time τ can be extracted.

Appendix D

Matlab codes for image processing

D 1. Image rotation and profile plotting

As illustrated in Figure D.1, we want to plot the averaged THz waveform along the red arrow direction in the defined red box area. Because the arrow is not in the horizontal direction, the image is rotated to make the arrow horizontal and then the waveform is plotted.
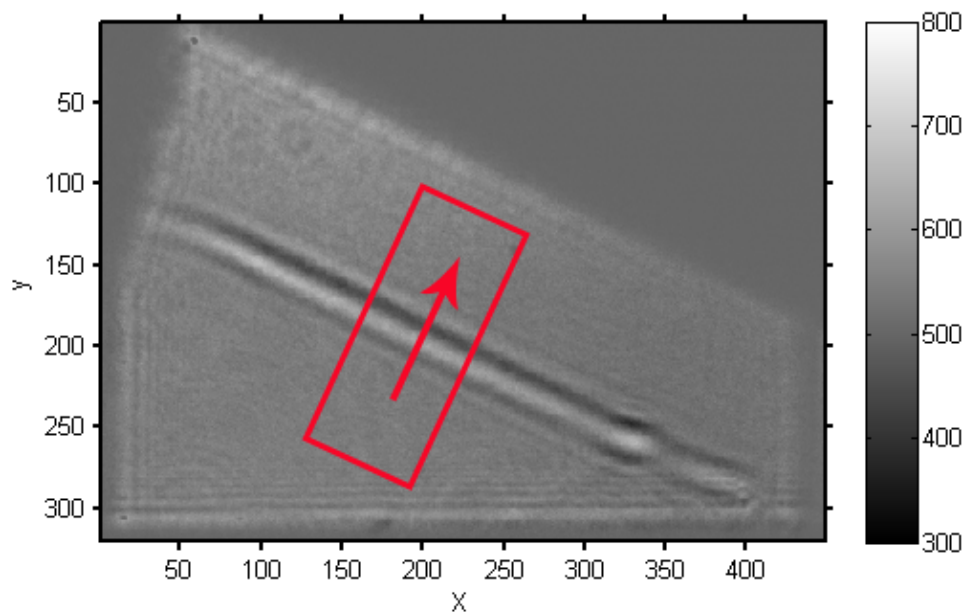

Figure D.1: The averaged THz waveform plot along the arrow direction in the defined red square area.

The MatLab code is (with a given image file *thzimage.txt*):

```
function rotate_image_profile_plot
% purpose: make a plot from an image, the format of the image file is in .txt
%%_STEP 1: load image in .text format and display it _%%
```

```matlab
 I=load('thzimage.txt'); %load the image file (in .txt format), it's named as
thzimage.txt
size(I)                 % check the image size
figure
colormap('default')
imshow(I,'DisplayRange',[300 800]),colorbar   %display the image.
xlabel('X'),ylabel('y')
axis on
%%%%%%%%%%_PART 2: rotate the image _%%%%%%%%
J=imrotate(I,-63.8);   % rotate the image by 63.6 degree.
figure
colormap('default')
imshow(J,'DisplayRange',[300 800]),colorbar   %display the rotated image.
xlabel('X'),ylabel('y')
axis on
%%%%%%%%%%_PART 3: plot the image in a given area_%%%%%%%%
                xstart=80;
                xend=320;        %set the range for the ploting in horizontal direction
                ystart=200;
                yend=280;         %set the range for the average in vertical direction
waveform=zeros(xend-xstart,yend-ystart+1);
for k=ystart:1:yend
x=[xstart xend];
y=[k k];
waveform(:,k-ystart+1)=improfile(J,x,y);
end
 h = imline(gca,[xstart xend],[ystart, ystart]) % define the plot area
setColor(h,[0 1 0])
 h = imline(gca,[xstart xend],[yend, yend])
setColor(h,[0 1 0])
 h = imline(gca,[xstart xstart],[ystart, yend])
setColor(h,[0 1 0])
 h = imline(gca,[xend xend],[ystart, yend])
 setColor(h,[0 1 0]) %% show the averaged plot in the defined area %%
 avergewaveform=zeros(xend-xstart,2);
for k=1:1:xend-xstart
   averagewaveform(k,1)=k;
end
averagewaveform(:,2)=mean(waveform,2); %Final averaged plot
figure
plot(averagewaveform(:,2))
```

229

D 2. 3D visualization of the terahertz pulse generated with the full beam optical pump pulse

Similar to the 3D MRI visualization, Figure D.2 shows a series of images collect at different depth. A code is written to process images for 3D visualization.
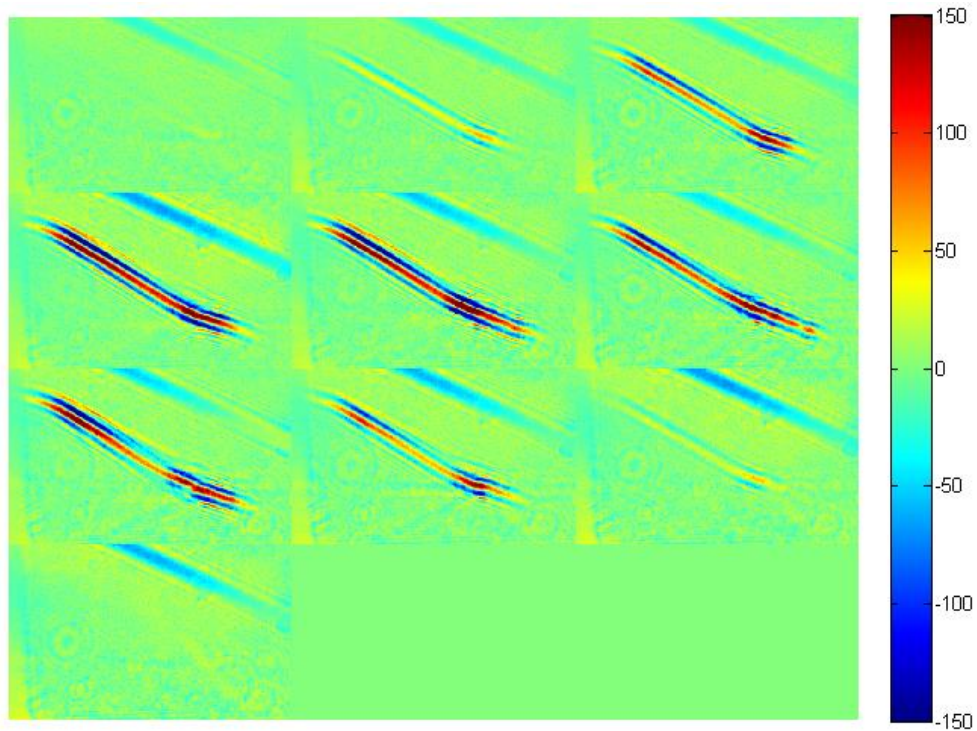

Figure D.2: Images of the THz pulse collected at different depths.

```
function THz3D_Analysis_tilted
%% set parameters%%%%
ICCDscale=56.8;%tell the ICCD scale in pixel/mm
STEPdistance=0.215;%tell the distance between two neighbouring images
SCALE=ICCDscale*STEPdistance;% pixel distance between two neighbour frames
colorstyle=('jet');
scalemax=150;%define scale bar range
scalemin=-150;
%% Load data
load('THz1.txt'),load('THz2.txt'),load('THz3.txt'),load('THz4.txt'),load('THz5.txt'),
```

```matlab
load('THz6.txt'),load('THz7.txt'),load('THz8.txt'),load('THz9.txt'),load('THz10.txt'),
size(THz1);%check the image size
x1=110; %define the range to make matrix more compact
x2=370;
y1=120;
y2=540;
D(:,:,1,1)=THz1(x1:x2,y1:y2); D(:,:,1,2)=THz2(x1:x2,y1:y2);
D(:,:,1,3)=THz3(x1:x2,y1:y2);
D(:,:,1,4)=THz4(x1:x2,y1:y2); D(:,:,1,5)=THz5(x1:x2,y1:y2);
D(:,:,1,6)=THz6(x1:x2,y1:y2);
D(:,:,1,7)=THz7(x1:x2,y1:y2);
D(:,:,1,8)=THz8(x1:x2,y1:y2);D(:,:,1,9)=THz9(x1:x2,y1:y2);
D(:,:,1,10)=THz10(x1:x2,y1:y2);
E=squeeze(D); %change matric from M*N*1*K to M*N*K
%% Display original images
figure,
Montage(D,'DisplayRange',[scalemin scalemax]), colorbar
title('FRONT VIEW');
colormap(colorstyle)
xlabel('X')
ylabel('Y')
zlabel('Z')
%% 3D visualization
D=squeeze(D);
D(:,1:70,:) = [];
figure,
clims = [-100 100];
p1 = patch(isosurface(D, 50),'FaceColor','green',...
 'EdgeColor','blue');
p2 = patch(isocaps(D, 5),'FaceColor','interp',...
 'EdgeColor','none');
alpha(.1);% set the degree of transperency
view(3);
xlabel('X'),ylabel('Z (c axis)'),zlabel('Y'),axis tight,daspect([1,1,1/SCALE])
view (-9,18);
box on
grid on
set(gca,'DataAspectRatio',[1 1 0.082]) % set the scale ratio. number means one unit
```

Appendix E

Electric field distribution of the THz Cherenkov wave induced by optical rectification

As discussed in Chapter 2, femtosecond optical pulses are used to generate THz pulses in $LiNbO_3$ and $LiTaO_3$ with optical rectification effect [4, 7]. Since the optical pulse travels faster than that of the generated THz pulse, a THz Cherenkov wave is formed [4, 7]. Here, we calculate the electric field distribution on the THz Cherenkov cone. In order to make the calculation simple, the medium in which the THz Cherenkov wave propagates is assumed to be homogenous.
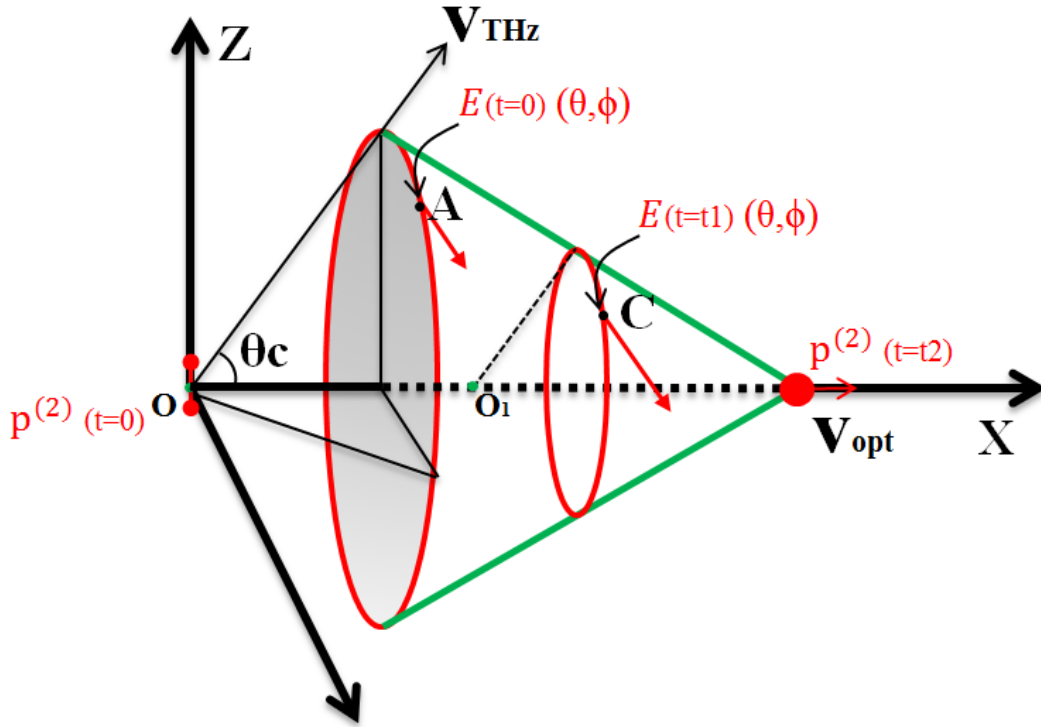

Figure E.1: Illustration of the THz Cherenkov wave. On the Cherenkov cone, the THz ring **A** and **C** are generated by optical pulse at point **O** and **O₁**, respectively.

As illustrated in Figure E.1, the THz Cherenkov cone is formed by rings that are generated by optical pulse at different locations. For example, the THz wave ring **A** is generated by the optical pulse that is at point **O**, and the ring **C** is by optical pulse at point O_1. By calculating THz electric field of the ring, the electric field distribution on the whole cone can be finally obtained.
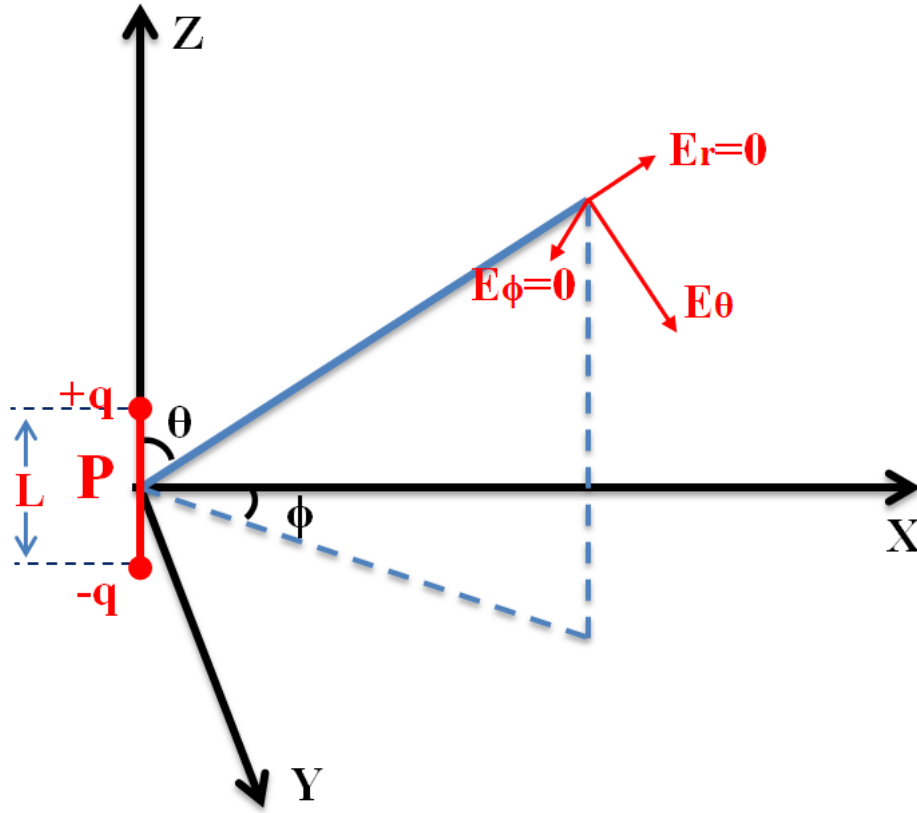

Figure E.2: Illustration of electric field of the radiation generated by a short dipole.

In the case of r>>L and λ>>L, where r is the distance between the point of interest and the dipole, L is the length of the dipole, and λ is the wavelength of radiation, a short dipole approximation can be employed to calculate the electric field of the radiation by the following equation [8],

$$E_r = 0$$

$$E_\theta = \frac{i60\pi I_0 e^{i(\omega t - kr)} \sin\theta}{r} \frac{L}{\lambda} \qquad \text{(E.1)}$$

$$E_\phi = 0$$

where (as illustrated in Figure E.2) E_r, E_θ, E_ϕ are 3 electric field components, r is the distance between the point of interest and the dipole, L is the length of the dipole, I_0 is the current of the dipole (proportional to the polarization $P^{(2)}$), λ, ω and k are the wavelength, angular frequency, and wave vector of the radiation, respectively, θ and ϕ are the polar angle and azimuth angle, respectively. For simplicity, E_θ is rewritten as

$$E_\theta = M \frac{\sin\theta}{r} \qquad \text{(E.2)}$$

where $M = \frac{i60\pi I_0 e^{i(\omega t - kr)} L}{\lambda}$. The corresponding components of the electric field at point (x, y, z) in the x, y, and z directions are,

$$E_x = E_\theta \cos\theta \cos\phi$$

$$E_y = E_\theta \cos\theta \sin\phi \qquad \text{(E.3)}$$

$$E_z = -E_\theta \sin\theta$$

As illustrated in Figure E.3, for the ring that is defined by the radiation propagation distance $|OA| = R_0$, the x, y, z , θ, and ϕ follow,

$$x = R_0 \cos\theta_c$$

$$x^2 + y^2 + z^2 = R_0{}^2 \qquad \text{(E.4)}$$

$$\cos\theta = z/R_0$$

$$\cos\phi = y/\sqrt{R_0{}^2 - z^2}$$

where θ_c is the Cherenkov angle. According to Equations E.2, E.3, and E.4, the electric field in the x, y, and z directions are,

$$E_x = M\frac{zx}{R_0{}^3}$$

$$E_y = M\frac{zy}{R_0{}^3} \qquad\qquad (E.5)$$

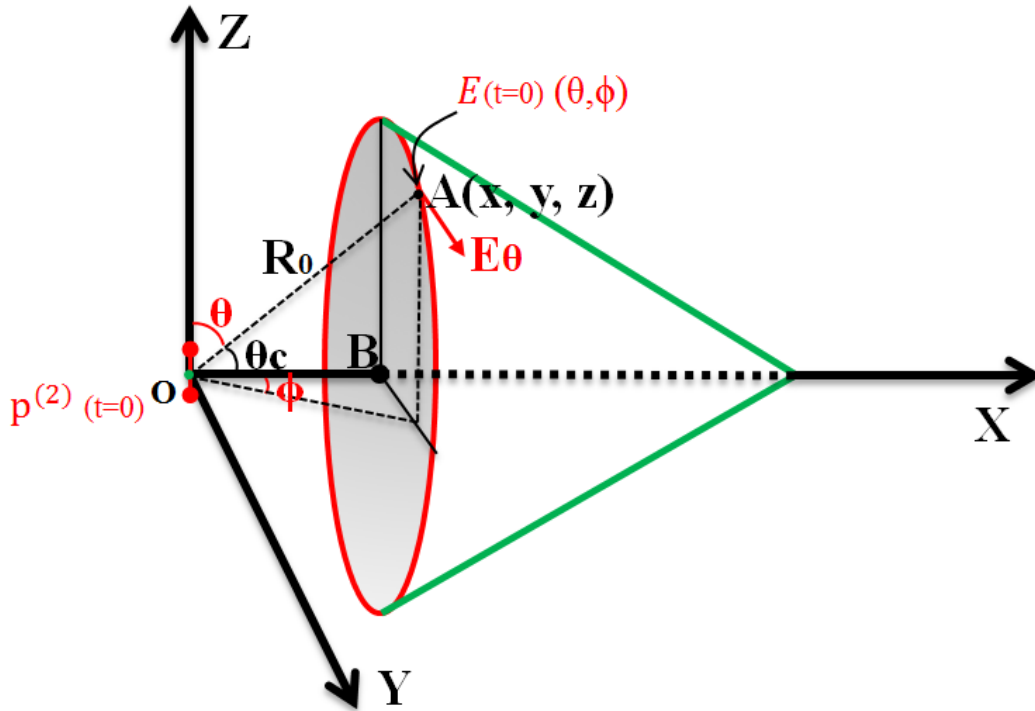$$E_z = -M\frac{x^2+y^2}{R_0{}^3}$$

Figure E.3: Illustration of electric field of the radiation generated by a short dipole.

So far, the electric field that comes from the dipole which is at point **O** at time t=0 is calculated. As shown in Figure E.4, when the dipole moves to point **O'** by Δx at time t=t₁, the electric field on the ring **C** is,

235

$$E_x = M \frac{z\cos\theta_c}{(R_0 - \Delta x\cos\theta_c)^2}$$

$$E_y = M \frac{zy}{(R_0 - \Delta x\cos\theta_c)^3} \qquad (E.5)$$

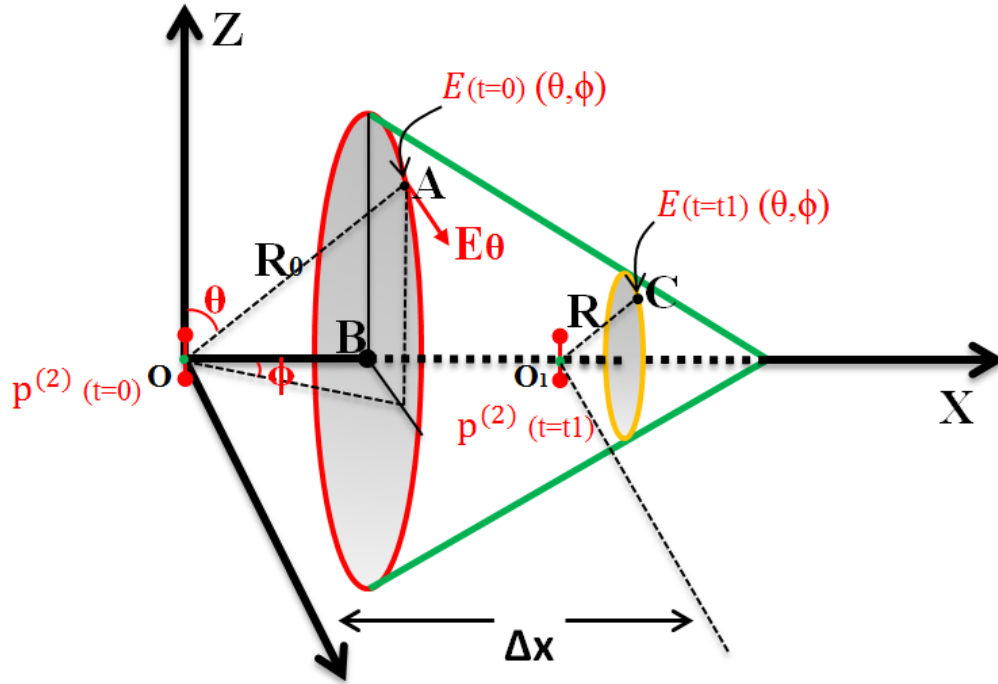$$E_z = -M \frac{[(R_0 - \Delta x\cos\theta_c)\cos\theta_c]^2 + y^2}{(R_0 - \Delta x\cos\theta_c)^3}$$
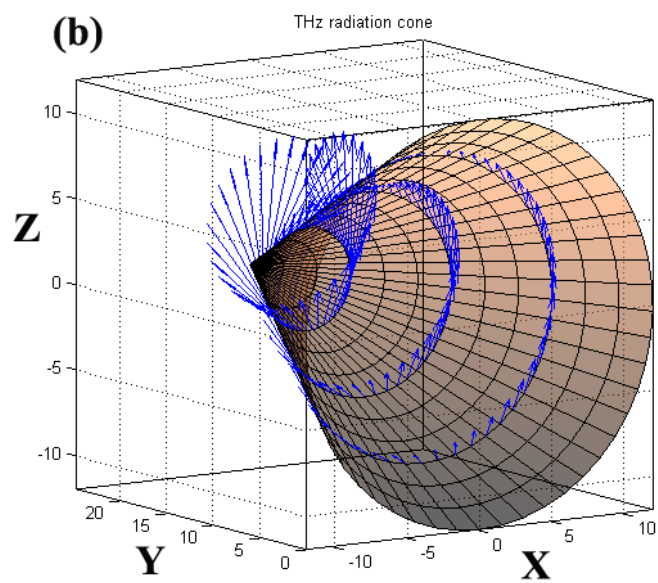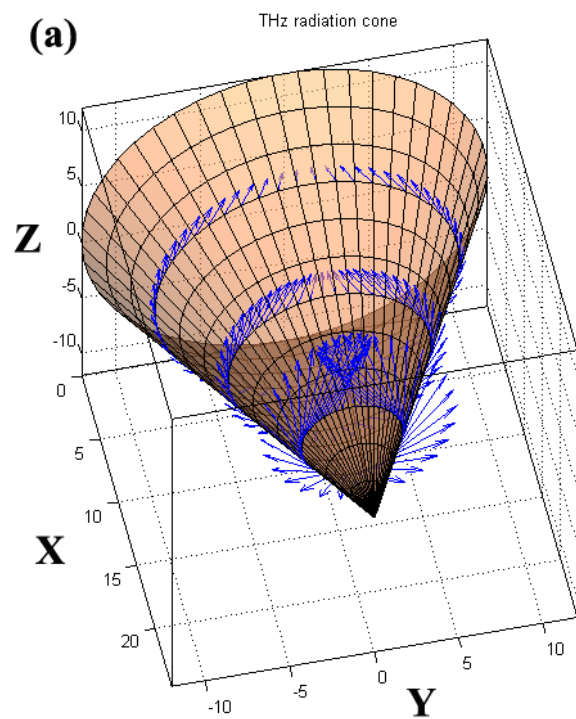

Figure E.4: Illustration of electric field of the radiation generated by a short dipole that moves from point **O** to **O₁**.

Based on Equation E.5, by changing the displacement Δx, the electric field on the THz Cherenkov cone is drawn with MATLAB, as shown in Figure E.5 (the same figure as shown in Chapter 2).

(a)

THz radiation cone
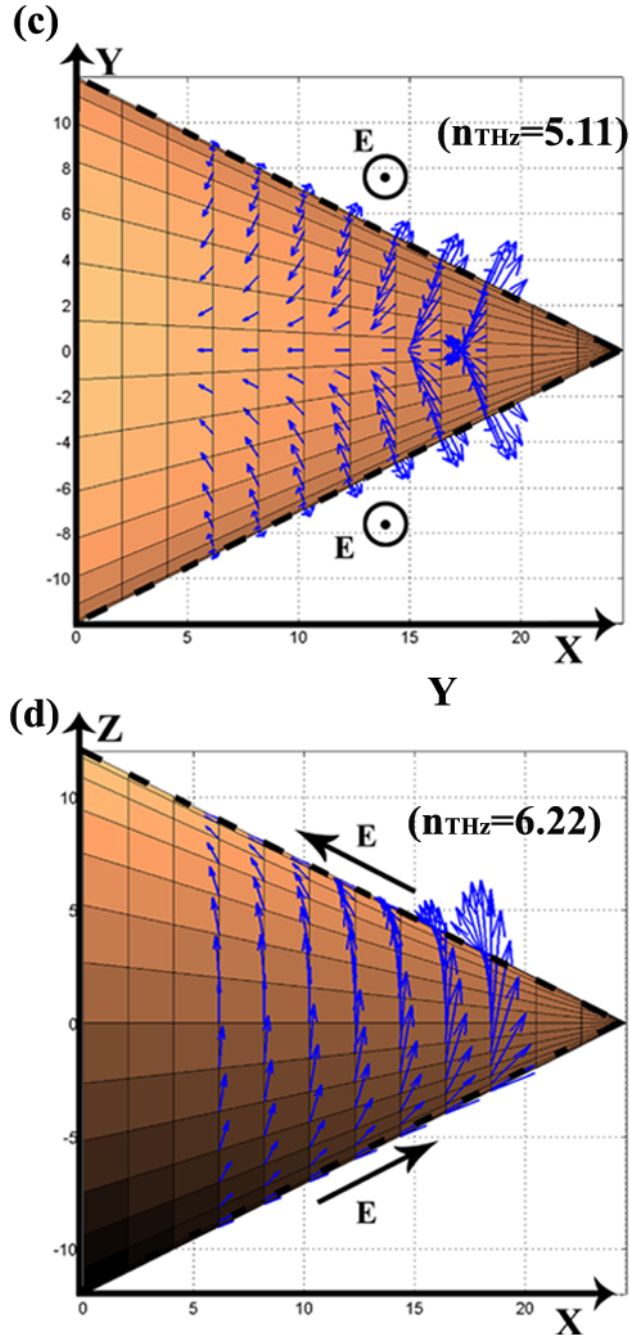
(b)

THz radiation cone

237

Figure E.5: (a) and (b), Distribution of the THz electric field on the THz Cherenkov cone in different view angle. (c), (d) Illustration of the THz pulse propagating in the XY plane with polarization in z axis (c-axis) direction (c) and in the XZ plane with polarization parallel to the THz pulse wavefront (d).

The MATLAB code is:

```matlab
function Quivercone
m = 2.0503; %define the cone ratio=height/radius,tan64deg
r_step = 1; %define the step,r=1
h = m*r_step; %h=2.0503 makes the chrenkov angle 64deg
circle_radius=12;%define the radius of the circle at x=0 position
R0=circle_radius*0.898794 % raidus calculate with circle_radius*sin64deg
[r,A] = meshgrid([-1*circle_radius:r_step:0],linspace(0,2*pi,50)); % R is a 2D matrix, A is a 2D matrix
size(r)
size(A)
Z = r.* cos(A);
Y = r.* sin(A);
X = m*(r+circle_radius); %make the largest circle at x=0 position

R=(m*circle_radius-X)*0.438371;% cos64deg=0.438371
size(R)
%%
%----------draw the cone-------------------
% Cone around the x-axis, point at the origin
figure(1) % add (1), or (2) can keep the figure stay at the same position
surf(X,Y,Z); % mesh(X,Y,Z) %meshc(X,Y,Z) give a projection image.
colormap(copper) %% This will change the color
alpha(0.6) %% This will make transparent
grid on
box on
axis equal % equal scale
xlabel('X','fontsize',10),ylabel('Y','fontsize',10),zlabel('Z','fontsize',10),
title('THz radiation cone'),
%%
%----------draw the electric field vector on the cone-------------------
  %%%we will remake matrix X,Y,Z to make it less dense%%%%%
[r2,A2] = meshgrid([-1*circle_radius:3*r_step:-3],linspace(0,2*pi,50)); % R is a 2D matrix, A is a 2D matrix
Z2 = r2.* cos(A2);
Y2 = r2.* sin(A2);
X2 = m*(r2+circle_radius); %make the largest circle at x=0 position
R2=(m*circle_radius-X2)*0.438371;% cos64deg=0.438371
```

```matlab
hold on; %put the cone and quvier vector together

%%--- define the electric field x,y,z component--start--

U2=-0.438371*Z2.*(R2.^-2);% -B*Z*cos64deg/(R^2), R is the radius along the THz propagation angle, and B is a
constant

V2 = -1*Z2.*Y2.*(R2.^-3);

W2 =((R2*0.438371).^2+Y2.^2).*(R2.^-3); % W = X+Y.^2+Z.^3;

%%--- define the electric field x,y,z component--end--

quiver3(X2,Y2,Z2,U2,V2,W2,2)

axis square

xlabel('X','fontsize',10),ylabel('Y','fontsize',10),zlabel('Z','fontsize',10),

title('THz radiation cone')
```

Appendix F

THz absorption spectroscopy analysis in E^2-mode

As discussed in Chapter 3, the THz electric field waveform can be sampled in E-mode with multi shots, and the square of the THz electric field waveform can be sampled in E^2-mode in single shot.
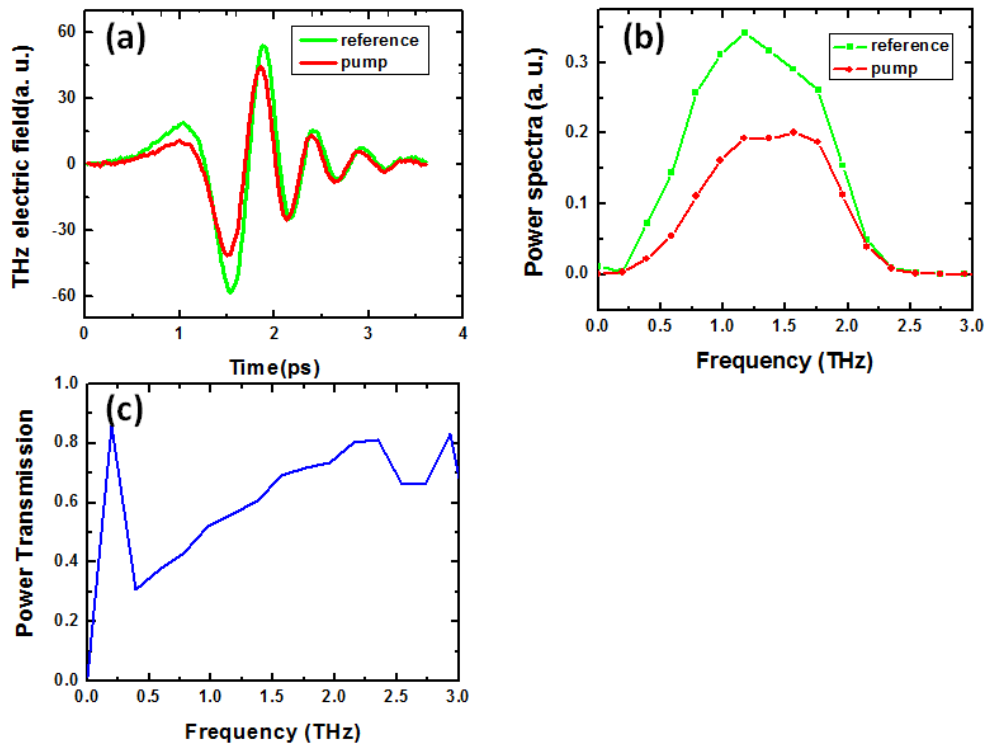

Figure F. 1: Illustration of how to do THz absorption spectroscopy analysis in E-mode. (a) THz electric field waveforms obtained as reference signal and pump signal. (b) The power spectra obtained from THz electric field waveforms in (a). (c) The power transmission spectrum.

For THz electric field waveforms obtained in E-mode, the THz absorption spectroscopy can be performed easily. As shown in Figure F. 1(a), the reference and pump signal are obtained, and the corresponding power spectra (see Figure F.

1(b)) can be calculated with Fast Fourier Transform (FFT). The THz power transmission spectrum (shown in Figure F. 1(c)) can thus be calculated by dividing the pump signal power spectrum with the reference signal spectrum.
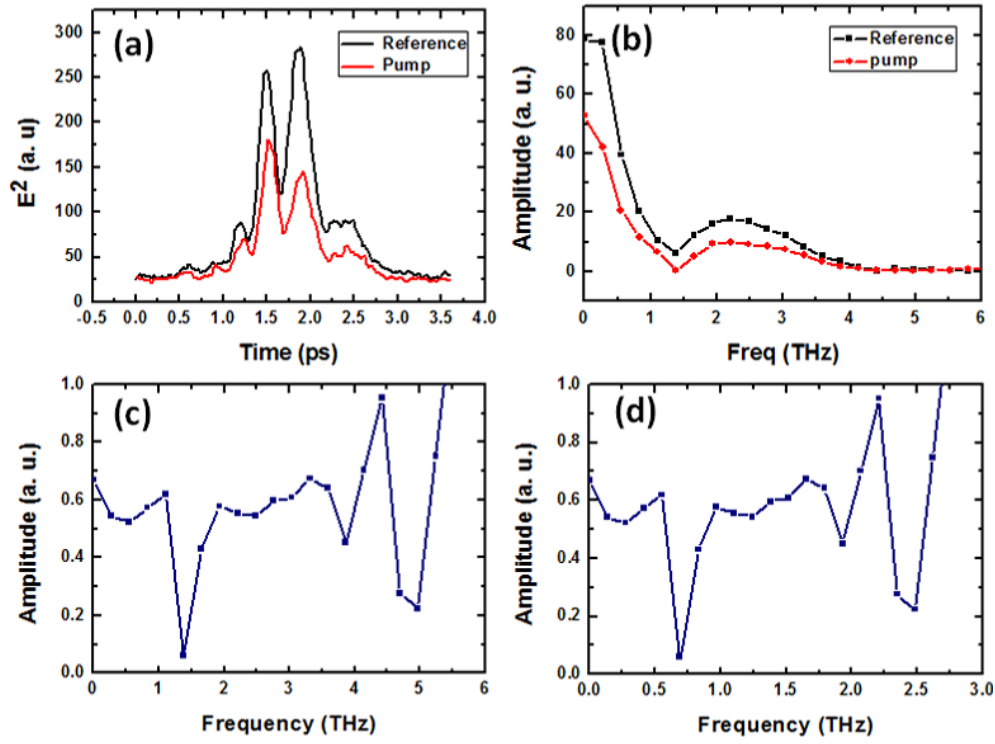

Figure F. 2: Illustration of how to do THz absorption spectroscopy analysis in E^2-mode. (a) The square of the THz electric field waveforms are obtained as reference signal and pump signal. (b) The amplitude spectra from waveforms in (a). (c) The amplitude transmission spectrum. (d) The amplitude transmission spectrum obtained by dividing frequency with a factor of 2.

Mathematically, the squared THz electric field waveforms obtained in E^2 mode cannot be employed for THz absorption spectroscopy, but we can obtain an approximated absorption spectrum that is very close to the THz absorption spectrum extracted in E-mode by using the following procedure: (1) obtain the squared THz electric field waveforms (see reference and pump signal in Figure F.

2(a)), (2) perform FFT to get amplitude spectra (see Figure F. 2(b)), (3) get THz transmission spectrum by dividing the pump signal spectrum with the reference signal spectrum (see Figure F. 2(c)), (4) divide the frequency with a factor of 2 (see Figure F.2(d)).

Besides using the experiment data to test our method, we also played around with a set of simulated waveforms. As illustrated in Figure F. 3(a), a reference waveform y= sin(t)*exp(-0.007*t^2) and a pump waveform y=0.9*sin(t-0.5)*exp(-0.007*t^2) are provided as E-mode data. Figure F. 3(c) and (e) show the corresponding power spectra and the power transmission. On the other hand, the square of the reference and pump waveforms in Figure F. 3(a) is shown in Figure F. 3(b), and is considered as the waveforms obtained in E^2-mode. As shown in Figure F. 3(d) and (f), the amplitude spectra are obtained through FFT transform. After dividing the frequency with a factor of 2 (see Figure F.3 (g)), we find that the obtained transmission spectrum in E^2-mode is very close to the power transmission in E-mode (see Figure F. 3(h)).
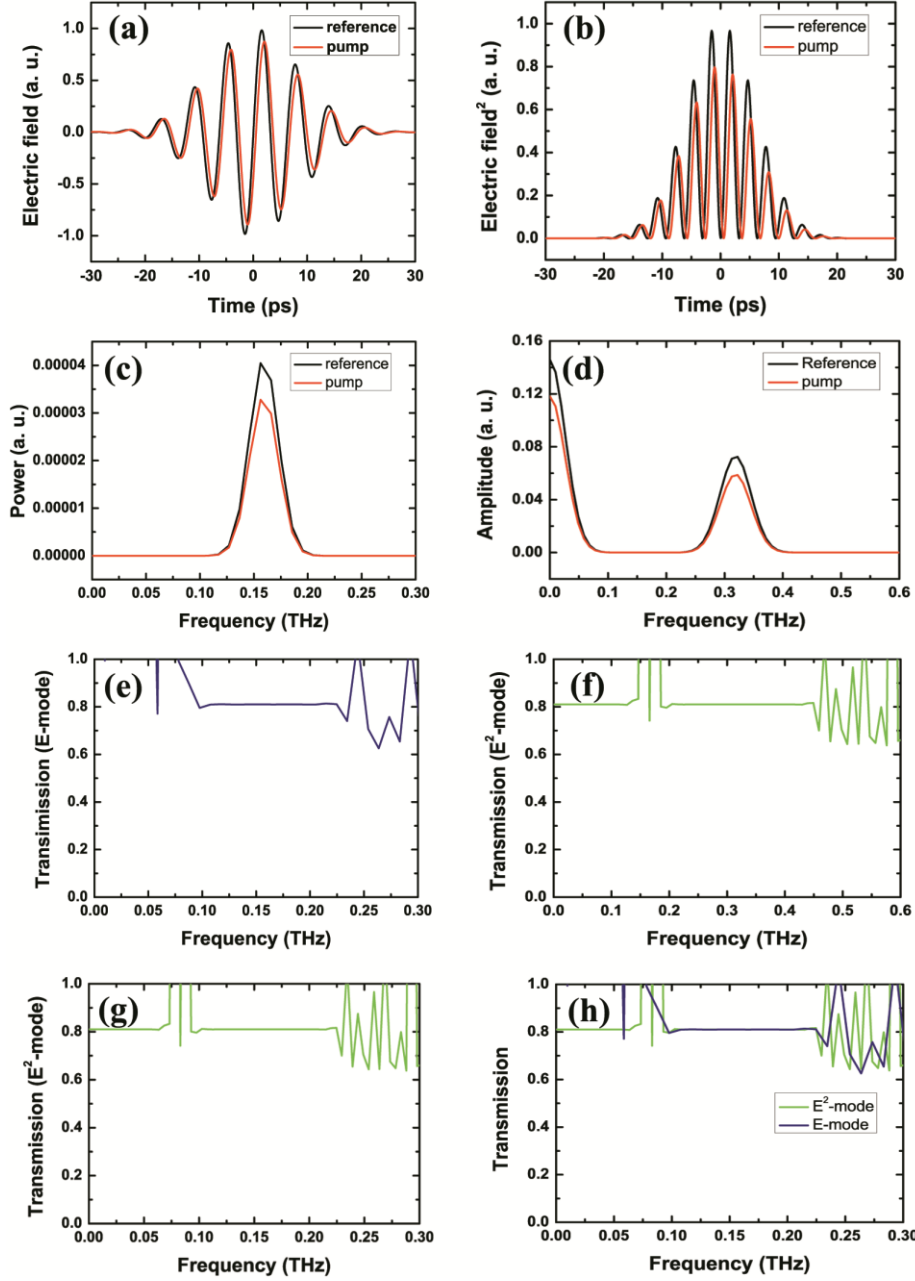
Figure F. 3: (a) The reference and pump waveforms obtained in E-mode. (b) The square of waveforms obtained in E^2-mode. (c) The power spectra obtained from waveforms in (a). (d) The amplitude spectra obtained from waveforms in (b). (e) The power transmission spectrum calculated based on (c). (f) The amplitude transmission spectrum calculated based on (d). (g) The amplitude transmission spectrum after dividing the frequency axis with a factor of 2 in (f). (h) Comparison between the transmission spectra obtained in E-mode and E^2- mode

244

Appendix G

Transition-like radiation and THz index measurement using terahertz time-domain spectroscopy

G. 1 Measurement of THz index in LiNbO$_3$ with a THz time-domain spectroscopy method
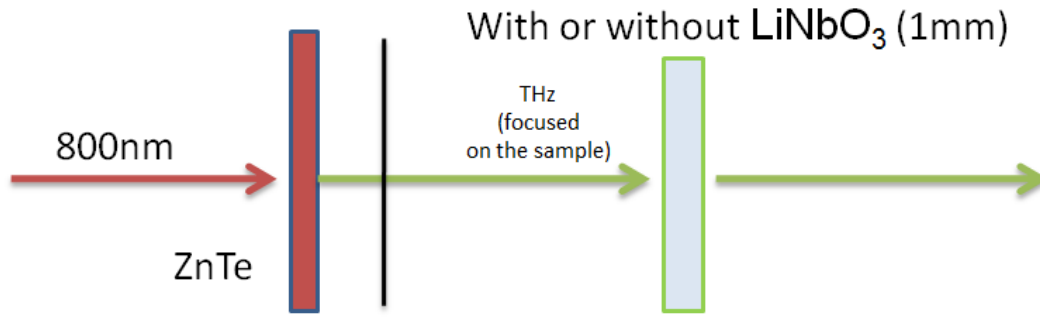

Figure G. 1: Illustration of how to measure the THz refractive index of a LiNbO$_3$ crystal. A THz pulse is generated in ZnTe crystal, and the generated THz pulse propagates through a 1 mm thick LiNbO$_3$ slab and its electric field waveform is then sampled in the time domain.

As illustrated in Figure G. 1, a THz pulse (centre frequency = 1 THz) is generated in a ZnTe crystal and finally is sampled in the time domain. By adding a 1 mm thick LiNbO$_3$ slab and measuring the time delay induced by the LiNbO$_3$, we can calculate the THz index of LiNbO$_3$ crystal. As shown in Figure G. 2, the time delay between the reference signal (without LiNbO$_3$ crystal inserted) and LiNbO$_3$ signal (with LiNbO$_3$ crystal inserted) is 13.84 ps. The calculated THz index is 5.1 (at 1 THz).
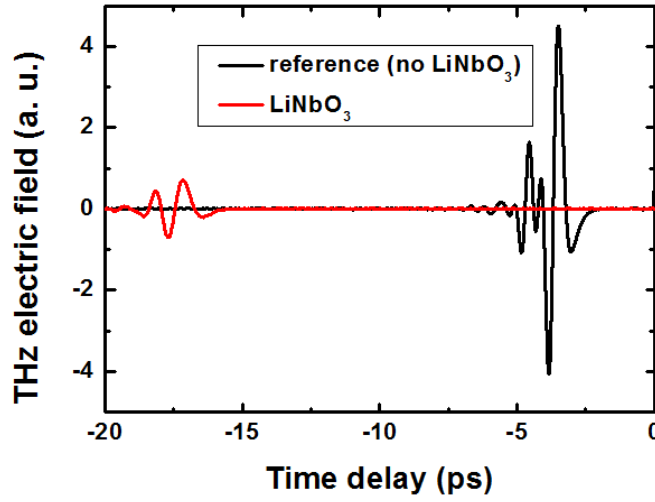
Figure G. 2: THz pulses that propagate through free space (reference) and a 1mm thick LiNbO$_3$ crystal (LiNbO$_3$) are sampled in the time domain. The time delay between the two waveforms is 13.84 ps.

G. 2 Measurement of the transition-like radiation generated on the front and back surfaces of the LiNbO$_3$ crystal

As illustrated in Figure G. 3, an optical pump pulse (800 nm) is focused onto a 1 mm thick LiNbO$_3$ slab. The generated transition-like radiation from the front surface (A) and the back surface (B) is sampled in a ZnTe crystal. As shown in Figure G. 4, compared to the waveform generated from the front surface (A), the waveform from the back surface (B) is reversed in phase. Based on the time delay (9.03 ps) between signal A and B, the THz index of LiNbO$_3$ crystal can be calculated and is found to be 4.959 at central frequency of 0.5 THz.
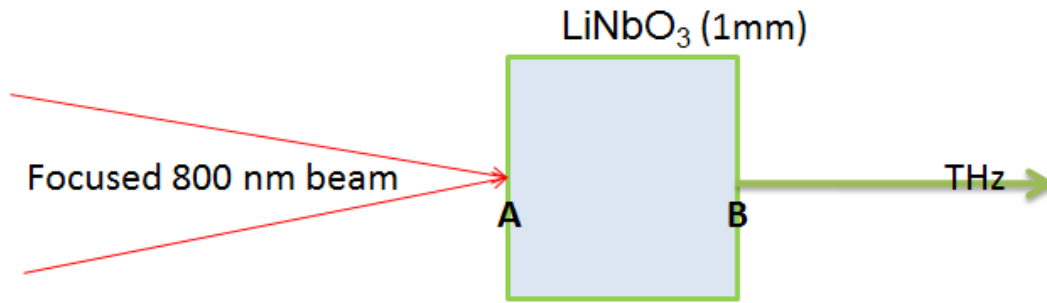
Figure G. 3: Illustration of the experimental setup to generate transition-like radiation on the front (A) and back (B) surfaces of the LiNbO$_3$ crystal. The generated THz pulses are finally sampled in a ZnTe crystal.
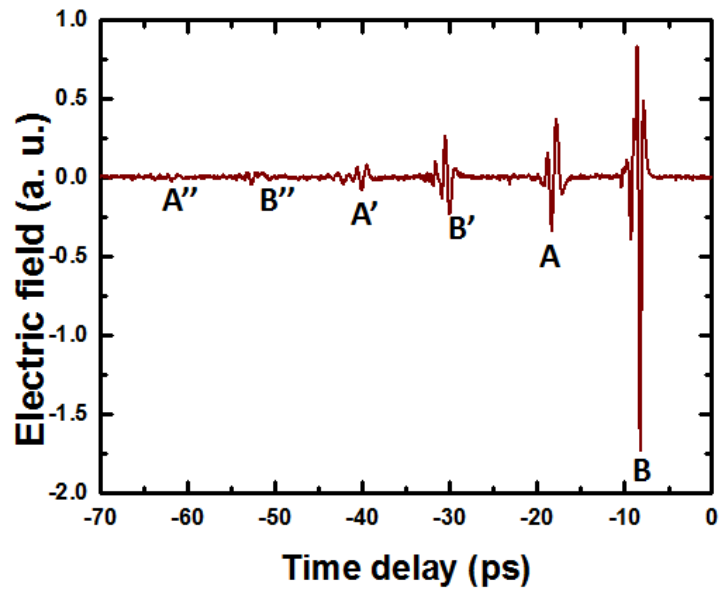

Figure G. 4: Transition-like radiation generated on the front (A) and back (B) surfaces. Signals A', A", B' and B" are due to the multi reflection of THz signal A and B inside the detection ZnTe crystal, respectively.

Appendix H

Is the imaging distortion due to Lorentz contraction of the THz Cherenkov wave?

As discussed in Chapter 4, when a LiNbO$_3$ crystal is pumped by an optical pump pulse, a THz Cherenkov wave is generated. The generated THz Cherenkov wave is in a cone shape and its Cherenkov angle is determined by the velocities of THz pulse and optical pump pulse [4, 7].

As illustrated in Figure H. 1(a), because the whole Cherenkov cone structure travels at the same velocity ($0.444c$) of the optical pump pulse in the optical pulse propagation direction (x direction), Lorentz contraction should happen in the x direction when we measure the cone with the transverse imaging method [9].
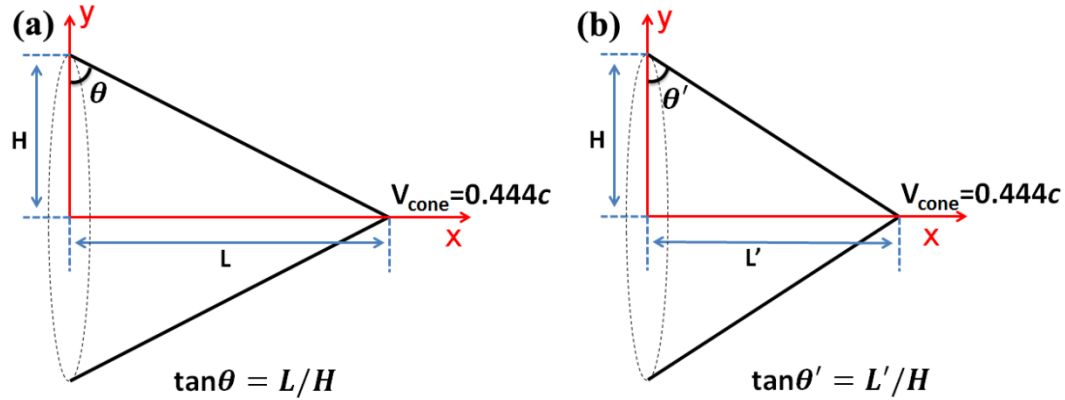

Figure H. 1: (a) Illustration of the THz Cherenkov wave cone. (b) Illustration of the observed THz Cherenkov cone.

According to Lorentz contraction theory, the measured length L' (illustrated in Figure H. 1(b)) of the cone can be calculated using the formula [9]:

$$L' = \frac{L}{\gamma(v)} = L\sqrt{1 - v_{cone}^2/c^2} \quad \text{(H. 1)}$$

where L is the proper length of the cone (see Figure H. 1(a)), L' is the length imaged by a CCD camera, v is the velocity of the cone, c is the speed of light, $\gamma(v)$ is the Lorentz factor. As illustrated in Figure H. 1(b), because the cone size in y direction does not change, the observed THz Cherenkov cone has a smaller THz Cherenkov angle. For the case of a THz Cherenkov wave with Cherenkov angle 64° and cone travelling speed $0.444c$, the Lorentz factor is 1.1163, and the corresponding measured THz Cherenkov angle is 61.4^{o}, which is pretty close to the experimental value 60.2^{o}.

In conclusion, because the THz Cherenkov wave cone structure travels at a speed close to the speed of light, Lorentz contraction could be the reason for the observed THz Cherenkov wave imaging distortion.

References:

1. Lavision Inc., *System-Manual: PicorStar HR* (2003).

2. Y. Kawada, T. Yasuda, H. Takahashi, and S.-i. Aoshima, "Real-time measurement of temporal waveforms of a terahertz pulse using a probe pulse with a tilted pulse front," Opt. Lett. **33**, 180-182 (2008).

3. K. Y. Kim, B. Yellampalle, A. J. Taylor, G. Rodriguez, and J. H. Glownia, "Single-shot terahertz pulse characterization via two-dimensional electro-optic imaging with dual echelons," Opt. Lett. **32**, 1968-1970 (2007).

4. J. Hebling, G. Almasi, I. Z. Kozma, and J. Kuhl, "Velocity matching by pulse front tilting for large-area THz-pulse generation," Opt. Express **10**, 1161-1166 (2002).

5. M. C. Hoffmann, and J. A. Fulop, "Intense ultrashort terahertz pulses: generation and applications," J. Phys. D: Appl. Phys. **44**, 17 (2011).

6. R. E. Glover, and M. Tinkham, "Conductivity of superconducting films for photon energies between 0.3 and 40k-tc," Phys. Rev. **108**, 243-256 (1957).

7. D. H. Auston, K. P. Cheung, J. A. Valdmanis, and D. A. Kleinman, "Cherenkov radiation from femtosecond optical pulses in electro-optic media," Phys. Rev. Lett. **53**, 1555-1558 (1984).

8. J. D. Kraus, and K. R. Carver, *Electromagnetics* (McGraw-Hill, 1973).

9. P. A. Tipler, and R. A. Llewellyn, *Modern Physics* (W. H. Freeman and Company, New York, 2000).